Dense Small Cell Networks for Next-Generation Wireless Systems

Amir Hossein Jafari

Supervisor: Professor Jie Zhang

Advisor: Dr David Lopez-Perez

Department of Electronic and Electrical Engineering
University of Sheffield

This dissertation is submitted for the degree of
Doctor of Philosophy

Faculty of Engineering November 2016

This thesis is dedicated to my mother for her love, pride, and devotion.

-Amir H. Jafari

Declaration

I hereby declare that except where specific reference is made to the work of others, the contents of this dissertation are original and have not been submitted in whole or in part for consideration for any other degree or qualification in this, or any other university. This dissertation is my own work and contains nothing which is the outcome of work done in collaboration with others, except as specified in the text and Acknowledgements. This dissertation contains fewer than 65,000 words including appendices, bibliography, footnotes, tables and equations and has fewer than 150 figures.

Amir Hossein Jafari
November 2016

Acknowledgements

First and foremost, I like to express my sincerest gratitude to Professor Geraint Jewell and Professor John David, the current and former heads of the department of Electronic and Electrical Engineering who greatly supported me during all my years at the University of Sheffield.

I am truly grateful to my university adviser, Professor Jie Zhang for his trust and great support during my Ph.D. studies. I truly appreciate the freedom he gave me and to let me explore a variety of problems.

I also like to express my sincere gratitude to my Nokia Bell Labs adviser Dr David Lopez-Perez who most importantly helped me to mature as a researcher. Working with David has been a wonderful experience and I could never accomplish my Ph.D. studies without his insight, guidance, and persistent help. One simply could not wish for a better adviser. Special thanks goes to members of Nokia Bell Labs Small Cell Research Department, Dr Holger Claussen and Dr Lester Ho with whom we had many hours of fruitful discussions.

I would like to appreciate Dr Ming Ding from Data61, CSIRO, Australia. Chapter four of this thesis is the result of collaboration with Ming. I learned a lot from Ming's great experience and adept ability to come up with simple improvisations to tackle complicated problems.

I would also like to thank Dr Vijay Vankateswaran from Huawei Technologies, who was a research engineer at Nokia Bell Labs during my second year of studies. Vijay has been very helpful to me with his knowledge and patience. The fifth chapter of this thesis is the result of collaboration with him.

I have been very fortunate to join Professor Robert W. Heath Jr. research group at the University of Texas at Austin as a visiting Ph.D. student during my last year. My time at Austin has been really one of my best experiences on both academic and personal levels.

I would also like to thank my Ph.D. committee members Prof. Ismail Güvenc, and Dr. Jonathan Rigelsford for their comments, insights, and guidance that greatly improved my Ph.D. thesis.

My journey as a Ph.D. student involved some travelling around the world from Sheffield, United Kingdom to Dublin, Ireland and to Austin, United States of America. I am very grateful for the generous financial support from the University of Sheffield Faculty of Engineering without which these would have never been possible.

Last but not least, words can’t express my heartfelt appreciation to my family for their encouragement, patience, and unfailing love during all these years. They taught me the most important lesson of my life; be ambitious, take challenges, and never surrender.

List of Publications

[P1] D. López-Pérez, M. Ding, H. Claussen, and A. H. Jafari, "Towards 1 Gbps/UE in cellular systems: understanding ultra-dense small cell deployments," *IEEE Commun. Surveys and Tutorials*, vol. 17, no. 4, pp. 2078-2101, Fourthquarter 2015. [Impact Factor: 17.188]

[P2] A. H. Jafari, V. Venkateswaren, D. López-Pérez, and J. Zhang, "Diversity Pulse Shaped Transmission in Ultra-Dense Small Cell Networks," *IEEE Transactions on Vehicular Technology*, vol. 66, no. 7, pp. 5866-5878, Jul. 2017. [Impact Factor: 4.066]

[P3] A. H. Jafari, M. Ding, D. López-Pérez, and J. Zhang, "Performance Analysis of Dense Small Cell Networks with Practical Antenna Heights under Rician Fading," *IEEE Access*, vol. 6, pp. 9960-9974, 2018. [Impact Factor: 3.244]

[P4] A. H. Jafari, D. López-Pérez, H. Song, H. Claussen, L. Ho, and J. Zhang, "Small Cell Backhaul: Challenges and Prospective Solutions," *EURASIP Journal on Wireless Communications and Networking*, pp. 1-18, Aug. 2015. [Impact Factor: 1.588]

[P5] A. H. Jafari, M. Ding, D. López-Pérez, and J. Zhang, "Performance Impact of LoS and NLoS Transmissions in Dense Cellular Networks under Rician Fading Channel," *Wiley*, Jan. 2018.

[P6] A. H. Jafari, D. López-Pérez, M. Ding, and J. Zhang, "Study on Scheduling Techniques for Ultra Dense Small Cell Networks," *IEEE 82nd Vehicular Technology Conference (VTC Fall)*, Sep. 2015. [22 Google Scholar Citations]

[P7] A. H. Jafari, V. Venkateswaren, D. López-Pérez, and J. Zhang, "Pulse Shaping Diversity to Enhance Throughput in Ultra-Dense Small Cell Networks," *IEEE 17th Workshop on Signal Processing Advances in Wireless Communications*, Jul. 2016.

[P8] L. Li, A. H. Jafari, X. Chu, and J. Zhang, "Simultaneous Transmission Opportunities for LTE-LAA Small Cells Coexisting with WiFi in Unlicensed Spectrum," *IEEE International Conference on Communications (ICC)*, May 2016.

[P9] A. H. Jafari, J. Park, and Robert W. Heath Jr, "Analysis of Interference Mitigation in mmWave Communications," *IEEE International Conference on Communications (ICC)*, May 2017.

[P10] M. Ding, D. López-Pérez, A. H. Jafari, G. Mao, and Z. Lin, “Ultra-Dense Networks: A New Look at the Proportional Fair Scheduler,” *IEEE Global Communications Conference (Globecom)*, Dec. 2017.

Abstract

Today's heterogeneous networks comprised of mostly macrocells and indoor small cells will not be able to meet the upcoming traffic demands. Indeed, it is forecasted that in comparison to today's network capacity, at least a 100× network capacity increase will be required to meet the traffic demands in 2020. As a result, researchers are now looking at using every tool at hand to improve network capacity. In this epic campaign, three main directions are noteworthy, i.e., enhance spatial reuse through network densification, use of larger bandwidths by exploiting higher spectrum frequencies both in licensed and unlicensed spectrum and enhance spectral efficiency through multi-antenna transmissions and cooperative communications.

In this thesis, special attention is paid to network densification and its implications when transiting to ultra-dense small cell networks.

First a simulation based analysis of ultra-dense small cell networks is presented. In this analysis, it is aimed to investigate how each of the three discussed capacity enhancement paradigms contributes to achieve the required 1 Gbps data rate. It is shown that network densification with an average inter-site distance (ISD) of 35 m can increase the average user equipment (UE) throughput by 7.56×, while the use of the 10 GHz band with a 500 MHz bandwidth can further increase the network capacity up to 5×, resulting in an average of 1.27 Gbps per UE. It is further shown that the use of beamforming with up to 4 antennas per small cell base station (BS) lacks behind with average throughput gain of up to 1.45×. It is also examined how idle mode feature (the capability to switch off small cell BSs with no active UEs) plays a key role in the performance of ultra-dense small cell networks.

Next, the impact of network densification on multi-user diversity is explored and it is demonstrated that as a result of densification the proportional fair alike schedulers can lose their advantages over round robin schedulers. It is shown that at low ISDs, the proportional fair scheduling gain over the round robin one in terms of cell throughput is only around 10% and, therefore, it is suggested that due to significantly lower complexity of round robin schedulers, they could be an alternative to proportional fair ones in ultra-dense small cell networks. Furthermore, the energy efficiency of ultra-dense small cell networks is analysed and it is elaborated that in order to make the deployment of ultra-dense small

cell networks more energy-efficient, it is important to develop advanced idle mode algorithms than cause the small cell BSs to consume zero power in idle mode. It is further explained that future small cell networks should benefit from energy harvesting technologies to reap their required energy from environmental resources.

Next, it is expressed that in order to cost-effectively deploy dense small cells networks, it is necessary to acquire an in-depth theoretical understanding of the implications brought by dense small cell networks. Due to proximity of UEs to small cell BSs in ultra-dense small cell networks, there is a high probability of line-of-sight (LOS) communication which causes a transition from non-line-of-sight (NLOS) to line-of-sight (LOS) for many communication links. It is explained that the simplistic single slope path loss models that only consider a single path loss exponent and do not differentiate among LOS and NLOS transmissions are not applicable in ultra-dense small cell networks and, therefore, a distance based piecewise path loss model featuring piecewise path loss functions that consider probabilistic LOS and NLOS transmissions is proposed. In addition to the proposed path loss model, distance-dependent Rician fading with a variant Rician K factor is also considered to assess the performance of ultra-dense small cell networks. The analysis demonstrates that the network coverage probability first increases with the increase in small cell BS density, but as network becomes denser the coverage probability decreases and the impact of multi-path fading is almost negligible. This implies that in contrary to previous conclusion, in dense small cell networks, the small cell BS density does matter.

Finally, it is proved that spatial multiplexing (SM) gains in multiple input multiple output (MIMO) cellular networks are limited when used in combination with ultra-dense small cell networks. In ultra-sense small cell networks, due to dominant LOS communication between UE and BS and insufficient spacing between antenna elements at both UE and BS, spatial channel correlation is considerably enhanced and, therefore, spatial multiplexing gain is suffered. To overcome this challenge, a new transmission technique entitled diversity pulse shaped transmission (DPST) is proposed. In DPST, transmit signals at adjacent antenna elements are shaped with distinct interpolating filters where each antenna transmits its own data stream with a relative time offset with respect to its adjacent antenna. The time offset which must be a fraction of symbol period generates deterministic inter-symbol-interference (ISI) into the channel, allowing to increase the diversity among different channel pairs. At the receiver,

a fractionally spaced equalizer (FSE) is exploited and it is shown that the combined effects of DPST and FSE enable the receiver to sense a less correlated channel. Simulation results demonstrate that in 2×2 and 4×4 MIMO systems, DPST can enhance the UE throughput by almost 2× and 4×, respectively.

Table of contents

List of figures

List of tables

Chapter 1

Introduction

1.1 Introduction

Over the period of last century, the society has witnessed long distance communications being freed from wires and operated through air at the speed of light; wireless and mobile communications made available to over 6 billion users worldwide [1]; new types of communications and social interactions emerging through the Internet and social networking [2] [3]; and many other breakthroughs that have certainly changed the everyday lives. These developments, although of great importance today, but will probably appear as small steps towards a new era to future generations. The new era of communications, still in its infancy, will continue to change the world in unpredictable and fascinating ways. Even though there is uncertainty on how such future advancements will look like, it is expected that they follow the same trends as previous communication systems and technology breakthroughs, and require more and more capacity, bits per second (bps), as time goes by. Voice services [4] were the killer applications at the beginning of this century, demanding tens of kbps per user equipment (UE), while high quality video streaming [5] is the most popular one today, needing tens of Mbps per UE [6]. Future services such as augmented reality, 3D visualisation and online gaming may use multiple displays requiring hundreds of Mbps each, resulting in a total sum of up to 1 Gbps per UE, and who knows what else tomorrow will bring? In view of such significant future traffic demands, the mobile industry has set its targets high, and has decided to improve the capacity of today's networks by a factor of 100× or more over the next 20 years—1000× the most ambitious [7].

In order to achieve these goals [8], mobile operators are already evolving their networks from the traditional macrocell-only networks to heterogeneous networks (HetNet) [9] [10], in which small cells reuse the spectrum locally and provide most of the capacity while macrocells provide a blanket coverage for mobile UEs. Currently, small cells are deployed

Table 1.1 Cell tier types and their characteristics.

Cell Type No.	Cell Type	Spectrum	Relationship with the Macrocell Tier	Typical Use Case
1	low-frequency macrocell tier	around 1∼2GHz, licensed	-	umbrella coverage
2	low-frequency small cell tier	around 1∼2GHz, licensed	co-channel deployment, CRE & ABS	capacity enhancement in hotspots
3	mid-frequency small cell tier	around 5GHz, unlicensed	non-co-channel deployment, dual connectivity	high traffic offloading
4	high-frequency small cell tier	>10GHz, unlicensed	non-co-channel deployment, dual connectivity	very high traffic offloading

in large numbers. Indeed, according to recent surveys, in 2012, the number of small cell base stations (BSs) was already larger than that of macrocell BSs [11]. These small cell deployments are mainly in the form of home small cells, known as femtocells [12] [13] [14], but many operators have also already started to deploy outdoor small cell solutions to complement their macrocell coverage [15].

1.2 Small Cells in Heterogeneous Networks

Given the different approaches to enhance network capacity, it may be worth understanding how network capacity has been improved in the past and which have been the lessons learnt to make sure the best choices are taken. To this end, Prof. Webb analysed the different methods used to enhance network capacity from 1950 to 2000 [16]. According to his study, the wireless capacity has increased around a 1 million fold in 50 years. The breakdown of these gains is as follows: 15× improvement was achieved from a wider spectrum, 5× improvement from better media access control (MAC) layer and modulation schemes, 5× improvement by designing better coding techniques, and an astounding 2700× gain through network densification and reduced cell sizes. According to this data, it seems obvious that if the industry is looking for a 1000× improvement in network performance, network densification through ultra-dense small cell deployments is the most appealing approach, and today's networks have already started going down this path.

Most of the existing small cell deployments, particularly femtocells, are configured to transmit on a dedicated carrier different from that of the macrocells [13]. While this avoids inter-tier interference, it also limits the available radio spectrum that each cell can access, and is less efficient than co-channel deployments, in which small cells and macrocells share the same frequency bands [17]. However, while co-channel operation provides better frequency utilisation, the additional inter-tier interference can result in coverage and handover issues for mobile UEs [18], [19]. This interference issue is particularly severe in femtocell deployments with closed subcarrier group (CSG) access, in which UE cannot connect to the strongest cell; the latter thus becoming a strong interferer [18].

In order to take advantage of the benefits of both orthogonal and co-channel network deployments – interference mitigation and spectrum reuse, respectively – and further enhance

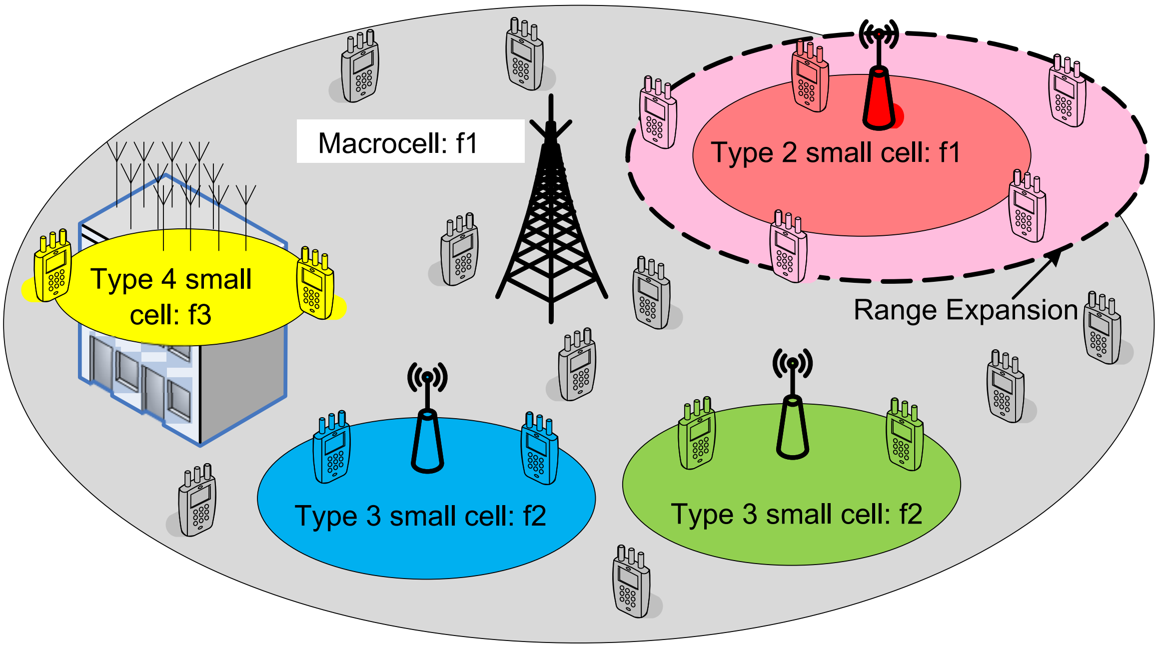

Fig. 1.1 Cell tier types.

network capacity, it is anticipated that future networks will be comprised of different small cell tiers with different types of small cell BSs. These different types of small cell BSs will be targeted at different types of environments and traffic. Fig. 1.1 and Table 1.1 summarise the classification of future network tiers. Note that to make the framework more complete, the macrocell tier is treated as a special case of the small cell tiers in Table 1.1.

1.2.1 Classification of Future Network Tiers

Cell Type 1 is essentially the conventional macrocell tier that provides an umbrella coverage for the network. Although this cell type will not be treated in this thesis, it is important to mention that a noteworthy enhancement for Cell Type 1 that is currently being investigated, is the 3D multi-user multiple-input-multiple-output (MU-MIMO) transmission, which is expected to enhance the indoor penetration and spectral efficiency of macrocells, especially for the scenarios with high-rise buildings [20] [21].

Cell Type 2 features today's state of the art co-channel deployments of small cells with the macrocell tier. Cell Type 2 is conceived as an add-on to Cell Type 1 for capacity enhancement through cell splitting gains in hotspots. Long Term Evolution (LTE) Release 10 features such as cell range expansion (CRE) and enhanced inter-cell interference coordination (eICIC) are critical for this small cell type to provide efficient macrocell off-loading and cope with the inter-tier interference issue [10]. Besides, advanced receivers with interference cancellation capabilities are an enhancement for small cell UEs to remove the residual interference from cell specific reference signal (CRS) [22]. Moreover, multi-cell cooperation among nodes with different power levels has been proved to be beneficial in recent works [23] [24]. Important technologies in this cell type such as CRE and eICIC via almost blank sub-frame (ABS) will be discussed later, together with its drawbacks and need for new cell types.

Cell Type 3 features dense orthogonal deployments of small cells with the macrocell tier, which are envisaged to be the workhorse for network capacity boosting through extensive spatial reuse in the near future. Due to its small size, Cell Type 3 is not appropriate to support mobile UEs and is targeted at static UEs, which represent a vast majority of the UEs population with more than 80 % of today's data traffic carried indoors [25]. In order to ensure a smooth inter-working between Cell Type 3 and Cell Type 1, dual-carrier (DC) is a promising technology currently being investigated in the LTE framework [26] [27] [28] [29], where a given UE may use radio resources provided by at least two different network points (Master and Secondary BSs) connected with non-ideal backhaul. The typical usage of DC is the splitting of traffic flows [30]. In more detail, it is beneficial to let macrocells provide the voice service for a UE and outsource its data service to small cells. In addition, DC also improves the robustness of the mobility management since UEs are now connected to two cell tiers [30].

It is important to note that DC is not suitable for Cell Type 2 because its compatibility with eICIC is challenging. In essence, eICIC tries to make macrocells invisible to small cell UEs in certain subframes using the ABS mechanism to eliminate inter-tier interference. In contrast, DC tries to maintain both connections, one to the macrocells and one to the small cells. As a result, eICIC is mainly used in the co-channel deployment where the macrocell to small cell interference is a major issue, while DC is mainly suitable for the orthogonal deployment where the traffic flow splitting or the mobility management is a major issue. Other new emerging technologies in Cell Type 3 include dynamic small cell idle modes [31] [32] [33], dynamic time division duplex (TDD) transmission [34] [35] [36] (which have attracted a lot of momentum in both the academia and the industry in the last years), high-order MIMO techniques [37] [38], etc.

Cell Type 4 finally, will push the technology frontier even further by using a very wide spectrum in high-frequency bands, e.g., millimeter wave [39] [40] [41], and exploiting massive MIMO techniques to achieve beamforming and spatial multiplexing [42] [43], etc.

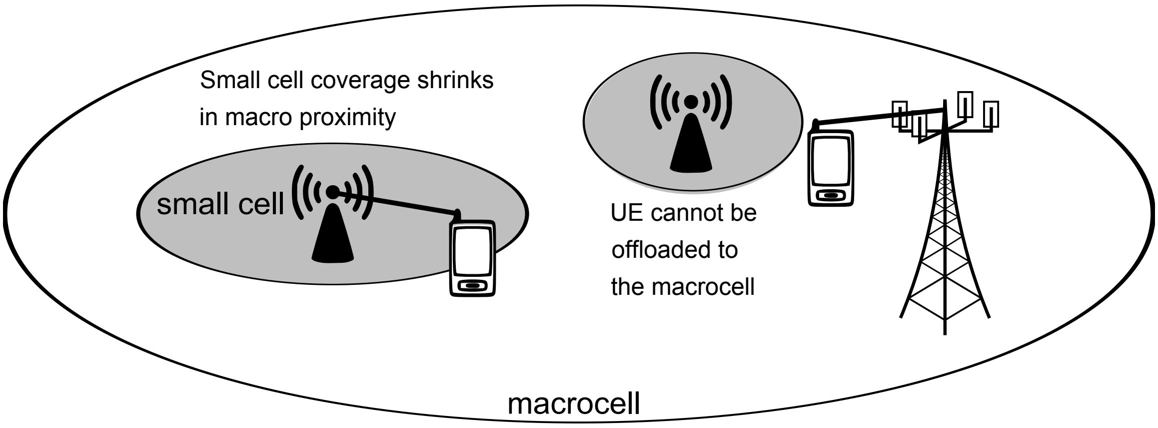

Fig. 1.2 Small cell coverage shrinks in the proximity of a macrocell BS leading to poor offloading.

1.3 Why Are Today's Small Cells Not Practical to Meet Future Capacity Demands?

In contrast to CSG, open access helps to minimise inter-tier interference since UEs are always allowed to connect to the strongest cell, thus avoiding the CSG interference issue [18]. However, in a co-channel deployment of small cells with the macrocell tier, due to the large difference in transmission power between both types of BSs, being attached to the cell that provides the strongest pilot received signal strength (RSS) may not always be the best strategy. UEs will tend to connect to macrocells rather than to small cells, even if they are at a shortest path loss distance. This effect is aggravated as the distance between small cell and macrocell BSs becomes smaller. As shown in Fig. 1.2, the closer the small cell BS is to the macrocell BS, the smaller is the resulting small cell coverage due to macrocell BS power dominance. This leads to a poor macrocell off-load [9] [10]. Moreover, as shown in Fig. 1.3, due to this server selection procedure based on pilot RSS, the transmissions of UEs connected to macrocells will also severely interfere with all small cells located in their vicinity in the Uplink (UL). Note that due to the lower path loss, if a macrocell UE would connect to the small cell with the smallest path loss, this UE would transmit with a much lower UL power. This would allow load balancing as well as UL interference mitigation, thus improving network performance.

In order to address these problems arising from the significant power difference between co-channel BSs in HetNets, new cell selection methods that allow UE association with cells that do not necessarily provide the strongest pilot RSS are necessary. In this regard, CRE has been proposed in the 3rd generation partnership project (3GPP) for increasing the Downlink (DL) coverage footprint of small cells by adding a positive cell individual offset to

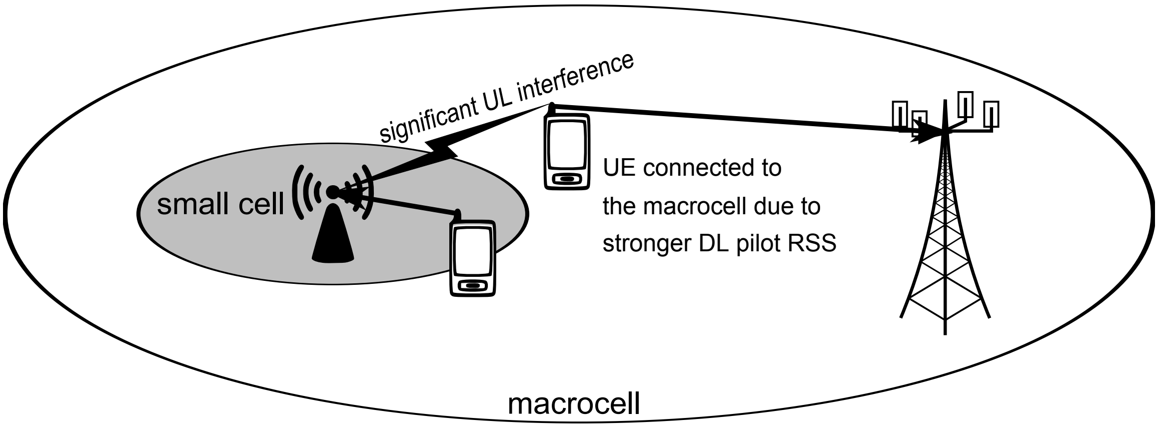

Fig. 1.3 Macrocell UE jamming the UL of a nearby small cell.

the pilot RSS of the small cells during the serving cell selection procedure [44] [15]. CRE mitigates UL interference and facilitates offloading. With a larger Range Expansion Bias (REB), more UEs are offloaded to the small cells, at the cost of increased co-channel DL interference for the range-expanded UEs, since they are not connected to the strongest server anymore (see Fig. 1.4). CRE without interference management has been shown to degrade the throughput of the overall network, but improves the sum capacity of the macrocell UEs due to offloading. In [45], closed form analytical expressions of outage probability with CRE in HetNets corroborate that CRE without interference management degrades the outage probability of the overall network.

In order to address this issue, the use of eICIC schemes has been proposed to guarantee the proper operation of CRE [9] [10]. In such schemes, special attention is given to the mitigation of inter-cell interference in the control channels transmitted in the DL. If control channels are unreliable due to severe interference, UEs may declare radio link failure and experience service outage. Among the proposed eICIC schemes, time-domain eICIC methods have received a lot of attention, particularly ABS [46]. In an ABS mechanism, no control or data signals, but only reference signals are transmitted, thus significantly mitigating interference since reference signals only occupy a very limited portion of the whole subframe. As shown in Fig. 1.5, ABS can be used to mitigate interference problems in open access small cells that implement CRE. A macrocell can schedule ABS while small cells can schedule its range-expanded small cell UEs within the subframes that are overlapping with the macrocell ABS. ABS can also be used to mitigate interference problems in CSG small cells. CSG small cells can schedule ABS while macrocells can schedule their victim macrocell UEs located nearby a CSG small cell within the subframes that are overlapping with the small cell ABS. Moreover, ABS can be scheduled at the small cell BSs to allow fast moving macrocell UEs to move through it. The benefits provided by ABS do not come for free, but at the expense of

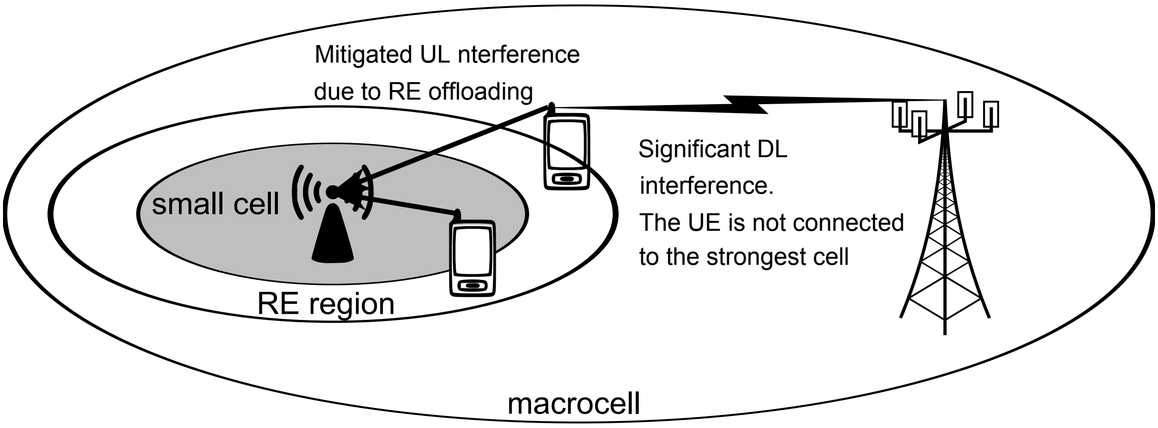

Fig. 1.4 Range expansion mitigates UL interference and facilitates offloading at the expense of increasing DL interference.

blanking radio resources and the associated capacity loss. In order to minimise the capacity loss at the BSs scheduling ABS, the agreement in [47] generalises ABS from completely blank data and control symbols to the transmission of such symbols at a reduced-power level, implying that the aggressing BS may also be able to transmit information. In [48], the network performance improvement due to CRE and ABS was analysed showing the merits of ABS. Moreover, analytic expressions for average capacity and 5%-tile throughput were derived in [49], while considering ABS and power reduced subframes as a function of BS densities, transmit powers and interference coordination parameters in a two-tier HetNet scenario. The results confirm the benefits of power reduced subframes over ABS.

The proper operation of eICIC at network level also depends on synchronisation issues. In order to enable efficient interference mitigation, REB and ABS schemes (reduced power subframes also included in this category) should be able to dynamically adapt to the number of small cells at various geographical locations and different traffic conditions. A dynamic adaptation of ABS patterns can be realised through X2 backhaul inter-BS coordination, where neighbouring macrocell BSs agree on a given ABS pattern, and then each macrocell BS informs its overlaid small cell BSs of the subframes that it will use for scheduling macrocell user equipments (MUEs) and which ones will be blanked for interference mitigation. Finding the appropriate ratio of ABS to non-ABSs is also tricky. The larger the REB for a given small cell BS, the more expanded-region small cell UEs connect to it, which requires a larger macrocell ABS duty cycle to provide a desired quality of service to these UEs. In contrast, the larger the ABS duty cycle, the lower the macrocell performance may be due to subframe blanking.

In [50], a mathematical framework to efficiently compute UE association and corresponding REBs together with ABS duty cycles is proposed. The solution is provably within a

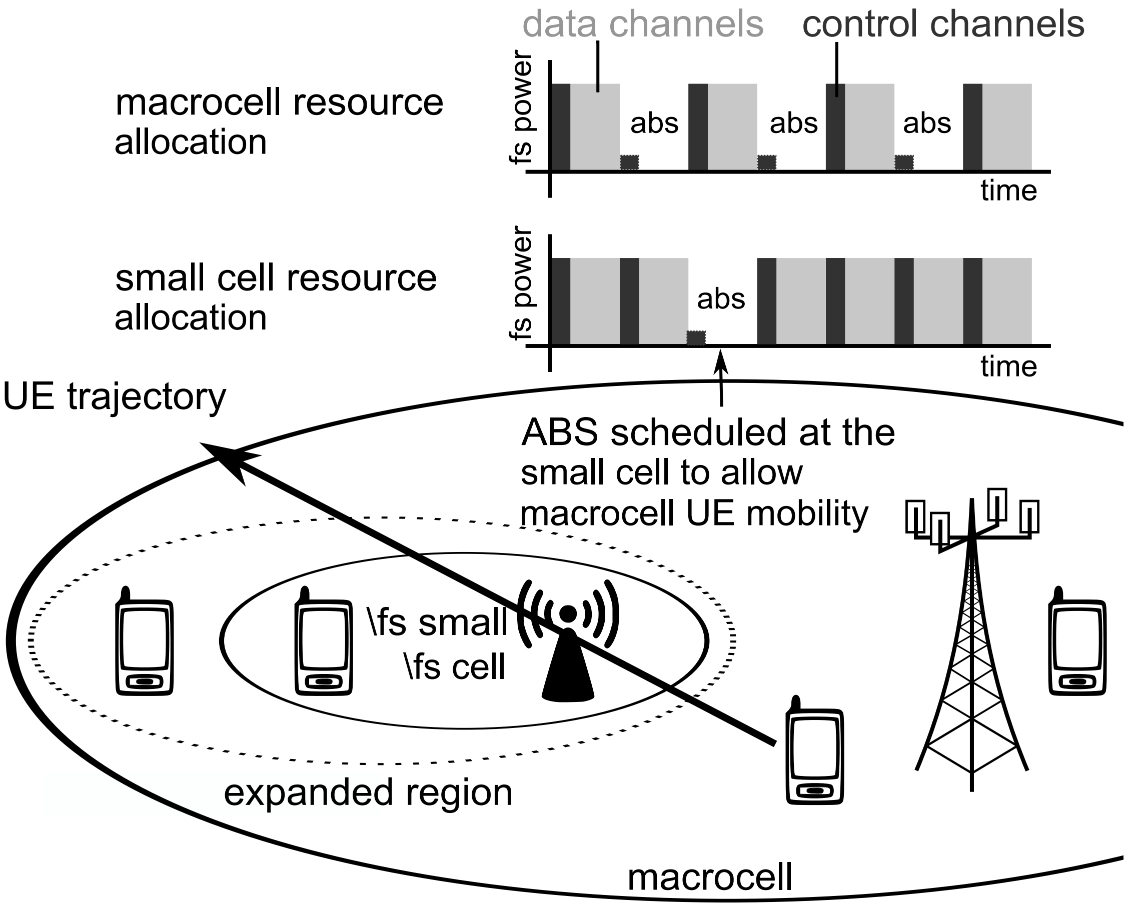

Fig. 1.5 ABS concept. ABS scheduled at the macro BS to helps pico range-expanded UEs. ABS scheduled at small cells to help mobile macro UEs.

constant factor of the optimal solution, scales linearly with the number of cells and is also amenable to distributed optimisation. However, it requires extensive input information from each UE with respect to its best macrocell and small cell BSs, which may be difficult to obtain since a UE cannot be simultaneously connected to multiple cells. In addition, for an efficient interference mitigation, inter-macrocell BS coordination should be considered [51]. If neighbouring macrocells do not coordinate their ABS patterns and they are not fully time aligned, this will cause additional interference fluctuations in the network, resulting in less efficient link adaptation and radio-aware packet scheduling.

From the previous discussion, it can be derived that a joint optimisation of REBs, ABS patterns, power reduction factors in reduced power subframes, scheduling thresholds and frequent inter-BS coordination may be required to achieve a good performance in a co-channel deployment of small cells with the macrocell tier. The complexity of these optimisation procedures will be aggravated with the number of cells, and thus it is anticipated that Cell

Type 2 is not suitable for ultra-dense small cell networks, where network planning should be completely avoided. This suggests that co-channel deployments of small cells with the macrocell tier should be aimed at hotspot locations with a reasonable low number of small cells (less than 10 per macrocell sector), while ultra-dense networks should use dedicated carriers to circumvent interference problems and the planning stage. This gives rise to Cell Type 3, which is the focus of research in this thesis.

1.4 Transition to Ultra-Dense HetNets

In this section, the main differences between regular HetNets and ultra-dense HetNets are highlighted.

Difference 1 - BS to UE density: In regular HetNets, the UE density is larger than the BS density, while in ultra-dense HetNets, the UE density is smaller than the BS density. As a result, and in contrast to regular HetNets where the BSs are powered on most of the times, in ultra-dense HetNets, BSs with no active UEs should be powered off to reduce unnecessary interference as well as to save power.

Difference 2 - Propagation conditions: In regular HetNets, non-line-of-sight (NLOS) interferers count for most cases, while in ultra-dense HetNets, line-of-sight (LOS) interferers count for most cases. As a result, and in contrast to regular HetNets where simple single-slope path loss model is usually assumed to obtain the numerical/analytical results, in ultra-dense HetNets, more sophisticated and practical multi-slope path loss models should be considered.

Difference 3 - Diversity loss: In regular HetNets, there is a rich UE diversity, while in ultra-dense HetNets there is a limited UE diversity. As a result, and in contrast to regular HetNets where independent shadowing and multi-path fading among UEs in one cell is usually assumed to obtain the numerical/analytical results, in the ultra-dense HetNets, such assumption is not valid. Thus, new results for ultra-dense HetNets should be derived.

Because of these differences, the numerical/analytical results for regular HetNets cannot be directly applied to ultra-dense HetNets due to different assumptions for the fundamental characteristics of the networks.

1.5 Challenges in Ultra-Dense Small Cell Networks

On the way to ultra-dense small cell networks, the following challenges must be addressed.

Challenge 1 - Backhaul: Recent surveys show that 96 % of the operators consider backhaul as one of the most important challenges to small cell deployments, and this issue is exacerbated in ultra-dense ones [52] [53] [54]. While today's wireless backhaul solutions may be a good choice in higher network tiers, it is anticipated that they will only be a solution up to a certain extent in ultra-dense small cell networks. Due to the high capacity requirements, wired backhaul will likely be a key requirement for these networks, and thus this type of network only makes sense in dense urban scenarios, where the traffic demands are the highest and the city infrastructure can provide dense fibre and/or digital subscriber line (DSL) connectivity to operators. The existing backhaul capability may well influence the deployment of the small cell BSs. Massive MIMO multicast is also a promising solution to provide backhaul to a large number of underlaid small cells [43]. However, this technology still faces its own challenges, implying that architecture and hardware impairments [55], pilot contamination [56] and accurate channel state information (CSI) acquisition [57] may be still an issue to provide a global solution. Other wireless backhaul technologies include two-way relaying [58], or even four-way relaying [59]. However, as explained earlier, such solutions might not be scalable to ultra-dense small cell networks. Hence, their usage is envisaged to be limited in practice.

Challenge 2 - Mobility: It is anticipated that future network architecture is comprised of different small cell tiers with different types of small cell BSs, targeted at different types of environments and traffic, where dedicated channel mid-frequency small cell deployments with the macrocell tier may be ultra-dense to enhance network capacity. Within this architecture, mobile UEs should be kept in the macrocell tier, while static UEs should be handed over to the ultra-dense small cell tier. In order to realise this, a new mobility management approach is needed, in which UEs only take measurements and access the cells of the appropriate network tier according to their velocity. Accurate mobility state estimation is key to realise this [60]. Splitting the transmission of the UE control and data planes will also provide mobility robustness, allowing the larger cells to transmit and manage control/mobility related information, while the smaller cells provide the majority of the data traffic [27]. However, this new architecture poses challenges in the management of data bearers towards the core network, since in order to realise the mobility benefits, the data bearer should be anchored at the cell in the higher network tier (e.g., macrocells), and this one forwards the information to the cell in the lower network tier (e.g., small cells) [61]. If many small cells anchor to the same macrocell, the latter may become a bottleneck.

Challenge 3 - Reducing costs: In order to improve the cost efficiency of network deployments, it is important that small cell BSs are developed in enormous numbers to take advantage of an economies of scale. Moreover, capital expenditure (CAPEX) and operating expenditure (OPEX) should be brought to a minimum. In order to reduce CAPEX, the price of small cell BS should be considered, which may require the use of cheap filters, power amplifiers and other components. Small cell BSs may also be deployed by the end users themselves to leverage existing power and back-haul infrastructure, thus reducing OPEX [62]. Moreover, in order to deploy a larger number of cells cost effectively in a short period of time, it is required that the cells can be deployed in a plug & play manner and do not require any human involvement for optimisation. Self-organisation capabilities are thus key to manage an ultra-dense small cell deployment. For example, the approach in [63] ensures that the small cell coverage is confined within the targeted household through power control and antenna switching techniques, thus minimising necessary handovers. The approach in [64] maximises capacity by using machine learning techniques at the small cell to learn where the UEs are clustered and then use of beamforming techniques to point its antenna beam towards such hotspot. Neighbouring cell list optimisation is also a key issue in ultra-dense small cell networks where neighbouring cells are switched on and off in a dynamic manner [65].

Challenge 4 - Small cell location planning: Finding hotspots and characterising their traffic is of crucial importance in order to deploy the right number of small cells in the right positions according to UEs' needs. Misunderstanding this information can result in an under- or over-estimated number of deployed cells, which will affect both energy and cost efficiency as well as network performance. However, finding and characterising hot spots is not an easy task since UEs' traffic is not usually geolocated, and currently network operators mostly rely on inaccurate proximity or triangulation approaches. Fingerprinting approaches are a possible solution to enhance the accuracy of geolocation [66].

Challenge 5 - Smart idle mode capabilities: Considering the large number of deployed small cell BSs, the availability of an efficient idle mode capability at the small cell BSs is key in order to mitigate inter-cell interference and save energy. In idle mode, it is important that small cell BSs minimise signalling transmissions and consume as little power as possible. Indeed, to achieve the most energy efficient deployments, a small cell BS in idle mode should not consume any power. To realise this, aside from the LTE solution based on demodulation reference signal (DRS) [26], another feasible solution would be to equip the small cell BSs with a sniffing capability, as proposed in [67], such that the small cell BS is idle and switches off most of the small cell BS modules when it is not serving active UEs. When the small cell is idle, it transmits no signalling, and wakes up upon the detection of uplink signalling from the UEs towards the macrocell tier. However, this solution does not allow selective wake-ups, where only the most adequate cell in a cluster of idle cells wakes up to serve the incoming UEs. Moreover, it is important to note that smart idle mode capabilities imply UE-oriented operations, and thus should be performed in a dynamic manner, considering the traffic dynamics of large variety of UEs. Dynamic small cell idle mode control also poses new challenges such as the ping-pong cell re-selection. To be more specific, a suddenly powered-on BS might confuse idle UEs since they need to re-select cells according to the best reference signal received power (RSRP) rule, and then go back to their previous cells when the small cell BS returns to idle mode. The ping-pong cell re-selection greatly consumes UE battery life and should be avoided.

Challenge 6 - Modulation and coding schemes: Deploying higher order modulation and coding schemes is critical to take advantage of the high signal-to-interference-plus-noise ratio (SINR) resulting from ultra-dense small cell networks. Even higher modulation schemes than currently used in LTE and Wireless Fidelity (Wi-Fi), i.e., 256-quadrature amplitude modulation (QAM), may be required, e.g., 1024-QAM. However, this brings about the need for accurate CSI for coherent de-modulation. However, the implementation feasibility of 1024 or higher QAMs is still unclear due to the error vector magnitude (EVM) issues at transmitters [68]. In addition, peak to average power ratio (PAPR) problem should also be re-considered for 1024 or higher QAMs.

Challenge 7 - Radio resource management: In terms of radio resource management, current scheduling and other network procedures have to be revisited since due to the lower number of UEs per cell, the current approaches used in macrocell BSs may not be optimum anymore. For example, proportional fair scheduling may not be the best solution for very small cells, since there are not many UEs to be fairly served and channel fluctuations may be low due to LOS channel conditions. Simpler solutions such as round robin scheduling may be more appealing. This will be discussed in further details in chapter 3.

Challenge 8 - Spatial multiplexing: Using spatial multiplexing techniques, multiple streams of data can be transmitted simultaneously and successfully decoded at the receiver, provided that the channels corresponding to every pair of transmit and receive antennas are uncorrelated. However, the small cell sizes in an ultra-dense small cell deployment may result in large spatial correlation among different channel pairs, thus limiting the available degrees of freedom and rendering spatial multiplexing less useful. Therefore, further research is needed in order to understand which is the optimum number of antennas per small cell BS according to the small cell density, so that beamforming and spatial multiplexing can be exploited in a cost effective manner. Multiuser MIMO is another avenue that should be explored in order to benefit from spatial multiplexing, which as a by-product may bring down BS power consumption. This will be discussed in further details in chapter 5.

Challenge 9 - Dynamic TDD transmissions: It can be envisaged that in future networks, small cells will prioritise TDD schemes over frequency division duplex (FDD) ones, since TDD transmissions are particularly suitable for hot spot scenarios with traffic fluctuations in both link directions [69]. In this line, a new technology has recently emerged, referred to as dynamic TDD, in which TDD DL and UL subframes can be dynamically configured in small cells to adapt their communication services to the fast variation of DL/UL traffic demands in either direction. The application of dynamic TDD in homogeneous small cell networks has been investigated in recent works with positive results [34], [35], [70]. Gains in terms of UE packet throughput and energy saving have been observed, mostly in low-to-medium traffic load conditions. However, up to now, it is still unclear whether it is feasible to introduce the dynamic TDD transmissions into HetNets, because it will complicate the existing CRE and ABS operations and its advantage in the presence of macrocells in terms of UE packet throughput is currently being investigated [36] [69]. Some pioneering work on the application of dynamic TDD in small cell HetNets can be found in [36]. It is important to note that dynamic TDD serves as the predecessor of the full duplex transmission, which has been identified as one of the candidate technologies for the next generation of mobile communications (5G). In a full duplex system, interference comes from both the DL and the UL, which is also the case in dynamic TDD.

Challenge 10 - Coexistence with Wi-Fi: In order to gain access to more frequency resources, LTE small cells may be deployed in unlicensed bands, where they are required to coexist with Wi-Fi networks [71]. However, when LTE and Wi-Fi nodes are deployed in the same frequency band, Wi-Fi nodes may tend to stay in listening mode waiting for a channel access opportunity, due to their courteous Carrier Sensing Multiple Access/Collision Avoidance (CSMA/CA) protocol and the high-power interference from the LTE network. Simulation results have shown that when coexisting with LTE nodes, if these ones do not implement any coexistence mechanism, Wi-Fi nodes in some indoor scenarios may spend even up to 96 % of the time in listening mode due to inter-radio access technology interference and the poor performance of CSMA/CA mechanisms. This significantly degrades Wi-Fi performance [72]. New coexistence solutions have to be devised to enhance LTE and Wi-Fi coexistence and ensure that those two networks share the unlicensed bands in a fair manner. Moreover, it is desirable that the coexistence schemes to be as much frequency agnostic as possible so that a global solution can be achieved. In the 3GPP, a prevailing view is that in the near future, unlicensed operation in 5 GHz should be considered first with focus on DL-only operations assisted by licensed carriers, which is also referred to as license assisted access (LAA) [73] [74].

1.6 Contributions and Organization of the Thesis

As technology walks down the path of network densification, and gradually enters the realm of ultra-dense small cell networks, things start to deviate from the traditional understanding. In this thesis, it is aimed to provide a better understanding towards the implications of network densification and in particular ultra-dense small cell networks. Considered as one of the main approaches to drive the 5th-generation of mobile communications (5G), vendors and mobile operators must acquire a thorough vision towards the implications brought by network densification in order to achieve a cost-effective deployment of small cell networks. Therefore, it is of great significance to persistently work to model and analyse dense and ultra-dense deployment of small cell BSs. The main contributions of this thesis can be summarized as follows:

- Most prior studies on small cell networks have concluded that coverage probability would linearly increase with BS density which has been founded based on using path loss models that do not differentiate line-of-sight (LOS) and non-LOS (NLOS) communications. However, in ultra-dense small cell networks, due to the proximity of UEs and BSs, the probability of LOS communication is considerably increased and so it is vital to exploit path loss models that incorporate both LOS and non-LOS (NLOS) transmissions. A novel piecewise path loss model to capture the dependence of the path loss exponent on the link distance between UE and BS is proposed and the impact of multi-path fading on the performance of ultra-dense small cell networks in terms of both coverage probability and area spectral efficiency (ASE) is investigated. Indeed, this work is the first to offer a simultaneous analysis of the performance of dense small cell networks by integrating a piecewise distance-based path loss model that features probabilistic LOS and NLOS path loss functions and a distance-dependent Rician fading model with a variant Rician K factor based on the distance between UE and BS. The full derivations for the analytical results on both the coverage probability and the ASE are presented and it reveals that in dense small cell networks where the UE and BS are deployed at the same height, once the BS density exceeds a certain threshold the coverage probability starts to decline. It is further found out that multi-path fading has a negligible impact and is not able to mitigate the performance degradation, which implies that the LOS/NLOS path loss characteristics and not the *the multi-path fading* dominate the performance. This important remark indicates that in ultra-dense small cell networks BS density does matter which sheds valuable insights on the deployments of future dense small cell networks. The results of this work were presented in publications [P3] and [P5].

- Moreover, for the first time the performance of radio resource management (RRM) and in particular scheduling algorithms in the context of ultra-dense small cell networks is assessed. Proportional fair scheduling has been conceived as an effective and widely used RRM method in macrocell networks. However, it is important to assess whether the proximity of UEs and BSs and the dominance of LOS path loss affect the choice of scheduling algorithms in ultra-dense small cell networks. The theoretical analysis of proportional fair scheduler in time and frequency domains is presented and it is demonstrated that the proportional fair scheduling has a negligible gain ($\approx 10\%$) over round robin scheduling algorithm in ultra-dense small cell networks. The analysis reveals that this limitation is due to the smaller number of UEs per small cell BS as well as the reduced diversity among the channel conditions of different UEs. Therefore, due to significantly lower computational complexity of round robin scheduling, it is perceived as a more appropriate scheduling algorithm in dense small cell networks. This major remark has a significant impact in the manufacturing of future small cell BSs where the digital signal processing (DSP) cycles saved due to the adoption of round robin scheduling, can be used to enhance the performance of other technologies such as advanced idle mode algorithms. The results of this work were presented in publications [P1] and [P6].

- Furthermore, the deployment of large number of small cell BSs leads to massive power consumption and in order to have sustainable small cell networks, it is necessary to analyse the energy efficiency of ultra-dense small cell networks. For the first time, two new and futuristic idle mode models are proposed which are used along with the power model by the GreenTouch project to conduct a comprehensive investigation on the energy efficiency of ultra-dense small cell networks under various BS densities. Simulation results prove that the lower the power consumption in the idle mode, the larger the energy efficiency of the network would be since less energy is required to transmit the same amount of bits at the network level. The simulation results also reveal a major remark which states that increasing the number of antennas at the small cell BSs always decreases the energy efficiency of the network. This analysis helps to obtain the following key insights: To make the deployment of a very large number of small cell BSs feasible, it is crucial to develop advanced idle mode algorithms that cause the small cell BSs to consume zero energy in the idle mode to not only mitigate the interference, but also to enhance the network energy efficiency, which can serve as a guideline for mobile operators for future ultra-dense small cell deployments. The results of this work were presented in publication [P1].
- Finally, due to remarkable advantages of multiple input multiple output (MIMO) systems, the performance of multi antenna systems in the context of ultra-dense small cell networks is evaluated. MIMO spatial multiplexing helps to simultaneously transmit and decode multiple data streams equal to the minimum number of transmit/receive antennas. However, due to both dominant LOS communication between UE and BS in ultra-dense small cell networks and the small spacing between antenna elements of a

MIMO system (due to small cell BS form factor), the wireless channel suffers from high spatial correlation which causes the channel to be ill-conditioned and renders the opportunity to achieve spatial multiplexing gain. To overcome the challenge to achieve spatial multiplexing gain, for the first time diversity pulse shaped transmission (DPST) is proposed as a multi-stream transmission technique where adjacent antenna element signals are shaped with slightly different band limited pulse shaping filters followed by a fractionally spaced equalizer (FSE) at the receiver that operates at a rate significantly greater than the symbol rate. From the receiver point of view, the combined effects of DPST and FSE generate a virtual MIMO channel that benefits from a condition number of close to one. Considering 2×2 and 4×4 MIMO systems between UE and small cell BS, it is shown through theoretical analysis and simulation results that in spite of the initially highly correlated MIMO channels, exploiting DPST helps to significantly enhance the UE's throughput and compensate for the loss of spatial multiplexing gain. The results of this work were presented in publications [P2] and [P7].

The rest of this thesis is organized in detail as follows:

Chapter 2 conducts the first in-depth survey on network densification, use of higher frequency bands, and use of multi-antenna technologies as the three main paradigms to achieve the desired average UE throughput of 1 Gbps for next generation of mobile communications. Assuming a 500 m × 500 m outdoor simulation scenario, the small cell BSs are placed in a uniform hexagonal grid and extensive simulations are performed assuming various scenarios in terms of ISD, frequency band of operation, antenna implementation, UE distribution, UE density, etc to not only understand the potential gains and limitations of these three paradigms, but also to derive the Pareto set of network configurations that help to reach the desired average UE throughput. The simulation results reveal some key remarks which state that one UE per small cell BS is the fundamental limit of network densification and that utilization of idle mode capability at small cell BSs is critical for future ultra-dense small cell deployments. The results also show that for a realistic non-uniformly distributed UE density of 300 active UE per square km, an average 1 Gbps per UE is achieved with an ISD of 35 m, 250 MHz bandwidth, and 4 antennas per small cell BS. The results of this chapter have been published in publication [P1].

Chapter 3 elaborates that the high density of BSs and the relative proximity of UEs to their serving BSs in ultra-dense small cell networks have substantial impact on the energy efficiency as well as the choice of scheduling algorithms in ultra-dense small cell networks. To evaluate the performance of scheduling algorithms in ultra-dense small cell networks, Rician fading is selected as the appropriate multi-path fading model and for the first time the Rician K factor is derived according to the probability of LOS communication between UE and BS. For the first time, the performances of proportional fair and round robin scheduling algorithms in the context of ultra-dense small cell networks are analysed. A major remark from the analysis is that as network becomes denser, the multi-user diversity is considerably reduced and so the computationally complex proportional fair scheduling offers marginal gain over the low complexity round robin scheduling. In order to assess the energy efficiency of ultra-dense small cell networks, for the first time a comprehensive survey is conducted on network energy efficiency assuming different ISDs and number of antennas at small cell BSs using the idle mode models provided by the GreenTouch project as well as two novel and futuristic idle mode models. The assessment indicates that the only way to enhance the energy efficiency of ultra-dense small cell networks is to develop advanced idle mode capabilities where the small cell BS has zero power consumption from the energy grid in the idle mode. The results of this chapter have been published in publications [P1] and [P6].

Chapter 4 discusses that previous studies have claimed that the signal-to-interference-plus-noise ratio (SINR) distribution monotonically increases with BS density, however, that conclusion has been founded based on many assumptions such as single slope path loss models and UE's freedom in BS association which are not necessarily true in ultra-dense small cell networks since they are not able to precisely capture the dependency of path loss exponent on the link distance between UE and BS to differentiate between LOS and NLOS transmissions. It is also explained that most of prior studies on small cell networks have considered Rayleigh fading which is not an accurate multi-path fading model in ultra-dense small cell networks. Consequently, a distance-based piecewise path loss model that incorporates probabilistic LOS and NLOS transmissions is proposed and for the first time its impact along with the impact of a distance-dependent Rician fading with variant Rician K factor on the performance of ultra-dense small cell networks in terms of coverage probability and ASE are analysed. The analytical derivations and simulation results demonstrate the key remark that in ultra-dense small cell networks the BS density does matter since beyond a certain BS density due to enhanced interference, the SINR degrades and multi-path fading is not able to mitigate the SINR degradation. The results of this chapter have been published in publications [P3] and [P5].

Chapter 5 investigates how to achieve MIMO spatial multiplexing gain in ultra-dense small cell networks. It is explained that due to limited beamforming gains, the use of spatial multiplexing is more appealing since the throughput can be increased by the minimum number of transmit/receive antennas. However, applying MIMO spatial multiplexing technique to ultra-dense small cell networks is very challenging since due to existence of strong LOS component and insufficient spacing between antenna elements at both UE and BS sides, the spatial correlation among channel pairs of a MIMO system is significantly increased.

The enhanced spatial correlation hinders the opportunity to achieve spatial multiplexing gain through simultaneously transmitting and decoding multiple data streams. To overcome this challenge, for the first time a new transmission scheme entitled diversity pulse shaped transmission (DPST) is proposed which generates deterministic inter-symbol-interference (ISI) which is exploited to increase the diversity of the channel. At the receiver, a fractionally spaced equalizer (FSE) is used which operates in an oversampled domain to extract the channel diversity. The performance of DPST in a single tier hexagonal small cell layout is evaluated and it is shown that DPST can compensate for the loss of spatial multiplexing gain in ultra-dense small cell networks. The results of this chapter have been published in publications [P2] and [P7].

Chapter 6 concludes the thesis by summarizing the results and presenting some important future research directions.

The following notations are used throughout this thesis. Bold and lowercase letters denote vectors, whereas bold and capital letters denote matrices. The notations $()^{-1}$, $()^{H}$, $()^{*}$ and $()^{T}$ denote the inverse, Hermitian, conjugate and transpose of a vector or matrix, respectively. The $*$ also refers to the convolution operation.

Chapter 2

Simulation Based Analysis of Network Densification

2.1 Introduction

As discussed in chapter 1, the mobile data traffic that is currently observed on mobile operators' networks will keep growing towards 2030 and, therefore, mobile service providers are facing more pressure to provide higher data rate, higher spectral efficiency, and lower latency services. In order to achieve this goal, network densification, utilization of higher frequency bands, and multi-antenna technologies have been designated as the main approaches to drive the next generation of mobile communications. In this chapter, it is aimed to cast a new look on the Pareto set of network configurations in terms of small cell BS density, frequency band of operation, and number of antennas per small cell BS to achieve an average throughput exceeding 1 Gbps per UE. A comprehensive analysis of the potential gains and limitations of network densification and its implications when transiting to ultra-dense small cell networks along with the impacts of use of higher frequency bands (non-millimetre wave) and use of multi-antenna technologies are presented for the first time. Considering a 500 m-by-500 m simulation scenario, the analysis in this chapter looks into different combinations of network densification (different inter-site-distances (ISDs)), different carrier frequencies, and different number of antennas at the small cell BSs to meet the target UE throughput of 1 Gbps. The impacts of UE distribution, UE density, and small cell BS idle mode capability are also taken into account. An important takeaway message from this chapter is that network densification with an average ISD of 35 m, can increase the cell-edge UE throughput up to 48×, while the use of the 10 GHz band can increase the network capacity up to 5×, and the use of LTE codebook beamforming with up to 4 antennas per small cell BS only offers cell-edge

UE throughput gains of up to 2×. To the author's best knowledge, this chapter is the first to present an in-depth analysis on network densification and the main contributions are summarized as follows:

- It is proved that 1 UE per small cell BS concept is the fundamental densification limit since the bandwidth available per UE cannot be further increased through cell splitting. This key remark states that once this limit is met, network densification can only enhance network capacity at a lower pace in a logarithmic manner which may not be cost effective.

- Simulation results show that when the density of small cells is larger than a specific threshold, many interfering signals transit from NLOS to LOS causing the UE SINR to degrade with small cell BS density. This major observation leads to propose idle mode capability at small cell BSs in order to mitigate the interference. It is demonstrated that once the idle mode capability is activated, the UE SINR is significantly boosted with the cell density.

- Analysis demonstrates that in realistic deployments, switching off a large number of small cell BSs does not lead the network to transit from an interference limited one to a noise limited one and, therefore, the small cell BS transmit power should be simply configured to just guarantee a targeted coverage range.

- Simulation results show that a uniform UE distribution requires more active BSs than a non-uniform distribution to provide full coverage to a given UE density. In contrast, due to more active BSs, the uniform distribution results in a lower number of active UEs per active BS for a given UE density, which tends to provide a better UE performance at the expense of an increased number of deployed active cells, and thus cost.

- Simulation results reveal that while the gains provided by *higher (non millimetre Wave) frequency bands* and *multiple antenna technology* represent a significant increase in network performance, but these gains are not as large as the gains provided by network densification. A major remark is that as network densifies, the beamforming gain is reduced.

- A takeaway message from the numerous simulation results in this chapter is that all these three paradigms have their own fundamental limitations and cannot be infinitely exploited and the target average UE throughput of 1 Gbps is only achievable via a synergy of all three paradigms.

The extensive simulation results in this chapter can be served as a guideline for a cost effective deployment of future dense small cell networks.

2.2 System Model

In this section, the system model to analyse ultra-dense small cell networks is introduced. Note that due to the insufficient capacity provided by Cell Types 1 and 2-which were discussed in chapter 1- and in order to meet the forecasted mobile traffic demands, in this thesis, the focus is on Cell Type 3, i.e., non-co-channel mid-frequency small cell deployments in combination with a macrocell tier for area coverage. It is important to mention that this cell type has the potential to significantly enhance network performance through high network densification and the usage of relatively high frequency bands, while avoiding interference and coordination issues with the macrocell tier, designed to support fast moving UEs. Consider a dense network of small cells. In this system model, a 500 m-by-500 m scenario is used, and small cells are placed outdoors in a uniform hexagonal grid with different inter-site-distances (ISDs) of 200, 150, 100, 75, 50, 35, 20, 10 or 5 m, which result in 29, 52, 116, 206, 462, 943, 2887, 11548 or 46189 small cell BSs per square km deployed in the scenario, respectively.

Two scenarios for UE distribution are considered, with three different UE densities of 600, 300 or 100 active UEs per square km:

- **Uniform:** UEs are uniformly distributed within the scenario.
- **Non-uniform:** Half of the UEs are uniformly distributed within the scenario, while the other half are uniformly distributed within circular hot spots of 40 m radius with 20 UEs each. Hot spots are uniformly distributed, and the minimum distance between two hotspot centres is 40 m.

Note that 300 active UEs per square km is the density usually considered in dense urban scenarios, such as Manhattan [75].

In terms of frequency bands, four carrier frequencies are considered, i.e., 2.0, 3.5, 5.0, and 10 GHz, where the available bandwidth is 5 % of the carrier frequency, i.e., 100, 175, 250, and 500 MHz, respectively.

In terms of antenna implementation and operation, each small cell BS has 1, 2, 4, and 8 antennas deployed in a horizontal array forming a linear antenna array (see Appendix A), while the UE has only 1 antenna.

The standardised LTE code book beamforming is adopted, targeted in this case at maximising the received signal strength of the intended UE (quantised maximum ratio transmission

(MRT) beamforming with no inter-BS coordination required). It is important to note that the power per antenna remains constant and that beamforming is only applied to the data channels and not to the control channels, which defines the small cell coverage and UE cell association. The transmit power of each active BS is configured such that it provides a signal-to-noise ratio (SNR) of 9, 12 or 15 dB at the targeted coverage range also known at cell-edge, which is $\frac{\sqrt{3}}{2}$ of the ISD [13].

UEs are not deployed within a 0.5 m range of any BS, and all UEs are served by the BS from which they can receive the strongest received pilot signal strength, provided that the pilot signal-to-interference-plus-noise ratio (SINR) is larger than -6.5 dB. A BS with no associated active UE is switched off. This is the idle mode capability presented in [67], and adopted in this chapter. It is also envisioned that because of the use of mid- to high-frequency bands and due to the importance of the LOS component in small cells, the time spread of the channel impulse response (CIR) will be very small, typically in the order of several μs, and hence the impact of multi-path fading will become less significant in the future. Therefore, multi-path fading is not considered in this chapter's analysis. For details on path loss, antenna gain, shadow fading, SINR computation and capacity mapping, please refer to Appendix A.

For the sake of clarity, it is also important to mention that in the legend of the figures and within the context of this chapter, i indicates the ISD of the scenario in meter, d indicates the density of UE per square km, ud indicates the type of UE distribution ($ud = 0$ uniform; $ud = 1$ non-uniform), s indicates whether the idle mode capability of the small cell BS is deactivated or activated ($s = 0$ deactivated; $s = 1$ activated), f indicates the carrier frequency in GHz, a indicates the number of antennas, and t indicates the SNR target of the small cell BS at its cell-edge, which is located at $\frac{\sqrt{3}}{2}$ of the ISD.

2.3 Network Densification

Network densification has the potential to significantly increase the capacity of the network with the number of deployed cells through spatial spectrum reuse, and is considered to be one of the key enablers to provide the capacity gains in future networks. In order to better understand the implications of network densification on network capacity, the network capacity is defined based on the framework developed by Claude Shannon [76] as

$$C[\text{bps}] = \sum_{m}^{M} \sum_{u}^{U_m} B_{m,u}[\text{Hz}] \log_2(1 + \gamma_{m,u}), \tag{2.1}$$

where $\{1, \ldots, m, \ldots, M\}$ is the set of BSs deployed in the network, $\{1, \ldots, u, \ldots, U_m\}$ is the set of UEs connected to BS m, B[Hz] is the total available bandwidth, and $B_{m,u}$[Hz] and

$\gamma_{m,u}$ refer to the bandwidth granted to and the SINR experienced by UE u when connected to BS m. Note that the interference is assumed to be Gaussian. At the network level, network densification increases the number of geographically separated BSs M that can simultaneously reuse the available bandwidth B, thus linearly improving spatial reuse and increasing network capacity with M.

At the cell level, a consequence of network densification is cell size reduction, which directly translates into a lower number of UEs U_m connected per BS m and thus a larger bandwidth $B_{m,u}$ is available per UE. In this way, network capacity linearly increases with the number of offloaded UEs. Moreover, at the cell level too, the average distance between a UE and its serving BS reduces, while the distance to its interfering BSs does not necessarily reduce at the same pace assuming idle mode capabilities. This leads to an increased UE signal quality $\gamma_{m,u}$, and thus the network capacity logarithmically increases with the $\gamma_{m,u}$.

As can be derived from the above discussions, network densification increases M and in turn improves both $B_{m,u}$ and $\gamma_{m,u}$, resulting in an increase of the network capacity. However, the impact of UE density and distribution should not be forgotten. If network densification is taken to an extreme, and the number of deployed BSs is larger than the number of existing active UEs, this ultra-dense small cell deployment may reach a fundamental limit in which the number of average active UEs per cell is equal or lower than one, i.e., $U_m \leq 1$.

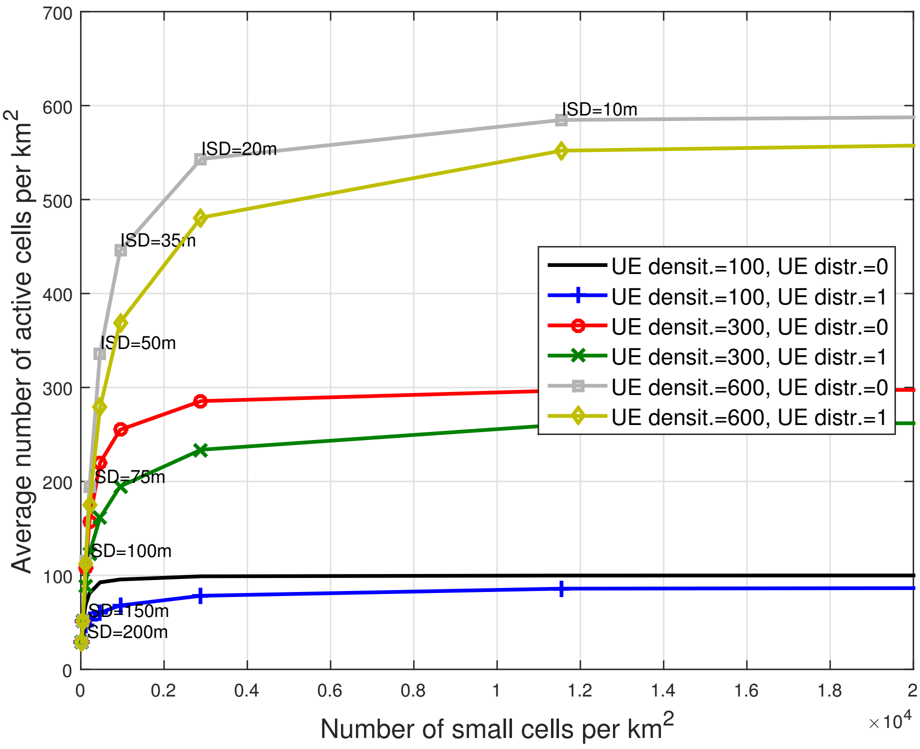

(a) Average number of active BSs in the network per square km.

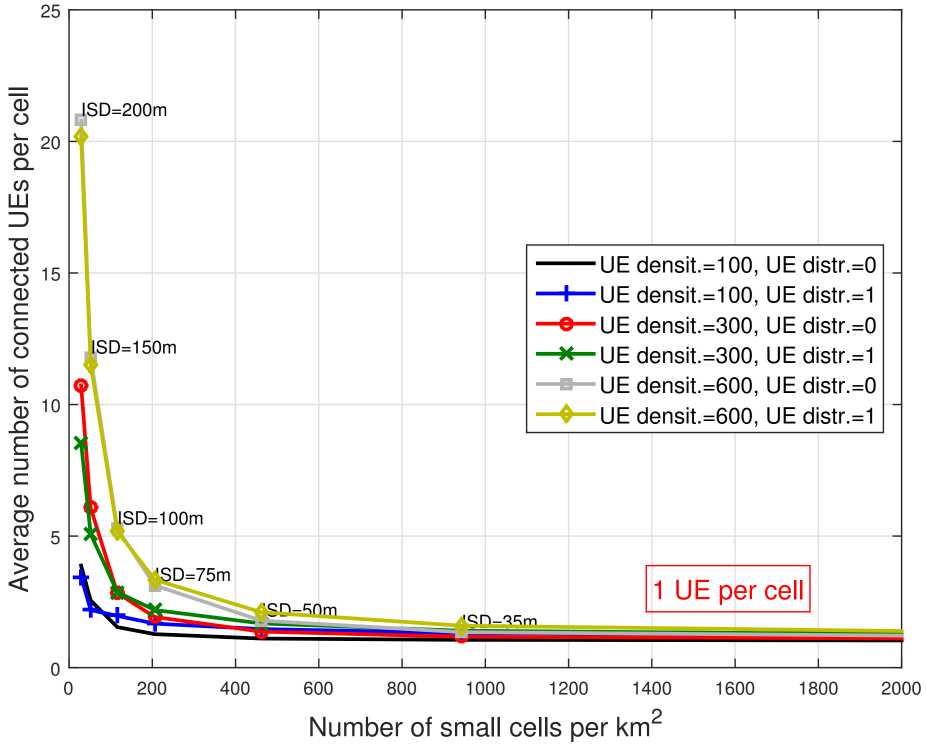

(b) Average number of active UEs per active BS.

Fig. 2.1 Average number of active BSs in the network per square km and average number of active UEs per active BS. The UE densities are 100, 300, and 600 active UEs per km^2, the carrier frequency is f = 2 GHz, the cell-edge SNR target is t = 12 dB, and the idle mode is activated.

At this point, the bandwidth $B_{m,u}$ available per UE cannot be further increased through cell splitting, and thus network densification can only enhance network capacity at a lower pace in a logarithmic manner by bringing the network closer to the UE and improving the UE signal quality $\gamma_{m,u}$, which may not be cost-effective. As a result, *one UE per cell* may be the operational sweet spot from a densification view point.

An important note is that even if the supply of UEs is infinite, and thus the spatial reuse gain increases linearly with the small cell density, it is still premature to claim that network capacity will increase linearly with the BS density. In chapter 4, a sophisticated multi-slope path loss model will be introduced into the stochastic geometry analysis incorporating both LOS and NLOS transmissions to study their performance impact in dense small cell networks. The performance impact of LOS and NLOS transmissions in small cell networks in terms of network capacity is shown to be significant both quantitatively and qualitatively, compared with previous works. In particular, it will be demonstrated that when the density of small cells is larger than a threshold, $\gamma_{m,u}$ will *decrease* as small cells become denser due to NLOS to LOS transition of the interfering signals, which in turn makes the network capacity suffer from a slow growth or even a notable *decrease* in practical regime of small cell density.

2.3.1 Idle mode capability and the 1 UE per cell concept

One important advantage of having a surplus of cells in the network is that a large number of them could be switched off if there is no active UE within their coverage areas, which reduces interference to neighbouring UE as well as energy consumption. Provided that a surplus of cells exists and as a result of an optimal idle mode capability [67], the network would have the key ability of adapting the distribution of active BSs to the distribution of active UEs, and thus the number of active cells, transmit power of the network, and interference conditions would strongly depend on the UE density and distribution.

According to the system model, Fig. 2.1 shows the average number of active BSs in the network per square km and the average number of active UEs per active BS, with the aforementioned idle mode capability where a BS with no associated UE is switched off. It is worth noting that in Fig. 2.1, both uniform and non-uniform UE distribution with UE densities of 100, 300, and 600 active UEs per km^2 has been considered. It helps to remind that in uniform distribution, UEs are uniformly distributed within the scenario whereas in non-uniform distribution half of the UEs are uniformly distributed within the scenario, while the other half are uniformly distributed within circular hot spots of 40 m radius with 20 UEs each. Hot spots are uniformly distributed, and the minimum distance between two hotspot centres is 40 m. The small cell BSs operate at carrier frequency of $f = 2$ GHz, and the SNR target of the small cell BS at its cell-edge is $t = 12$ dB. From Fig. 2.1(a), it is realized that the lower the UE density, the lower the average number of active BSs in the scenario and the lower the average number of active UEs per active BS. With regard to UE distribution, a uniform distribution requires more active BSs than a non-uniform distribution to provide full coverage to a given UE density. This is because UEs are more widely spread in the former. In contrast, due to the more active BSs, the uniform distribution results in a lower number of active UEs per active BS for a given UE density, which tends to provide a better UE performance at the expense of an increased number of deployed active cells, and thus cost. This indicates the importance of understanding the UE density and distribution in specific scenarios to realise efficient deployments.

An important result that can be extracted from Fig. 2.1(b) is that an ISD of 35 m can already achieve an average of 1.1 active UE per active BS or smaller, approaching the fundamental limit of spatial reuse. Reaching such limit has implications for the network and UE performance, as it has been qualitatively explained before, and as it will be quantitatively shown in Section 2.4. Moreover, it also has implications for the cost-effectiveness of the network, since densifying further than the 1 UE per cell sweet spot requires an exponential increase in investment to achieve a diminishing logarithmic capacity gain through signal quality enhancement. In other words, when the network is dense enough, a large number of cells have to be added to the network to enhance the UE throughput in a noticeable manner, and this may not be desired since the operator may have to pay exponentially more money to carry on with the deployment.

2.3.2 Transmit Power and UE SINR Distribution

Combining ultra-dense small cell deployments together with an efficient idle mode capability has the potential to significantly reduce the transmit power of the network. This is because active cells transmit to UEs with a lower power due to their reduced cell size and empty cells with no active UEs can be put into idle mode until a UE becomes active [67]. Moreover, by turning off empty cells, the interference suffered by UEs from always on channels, e.g., synchronisation, reference and broadcast channels, can also be removed, neutralising some neighbouring cells and thus improving UE SINR distributions.

Working in this direction, LTE Release 12 networks have defined periodic demodulation reference signal (DRS) to facilitate UEs the discovery of small cells that are turned off [26]. DRS are transmitted sparsely in the time domain and they consist of multiple types of reference signals (RS), based on which UEs are able to perform synchronisation, detect cell identity and acquire coarse CSI, etc. Due to the low periodicity of DRS, the impact of DRS on UE SINR distribution is marginal, and thus it can be ignored.

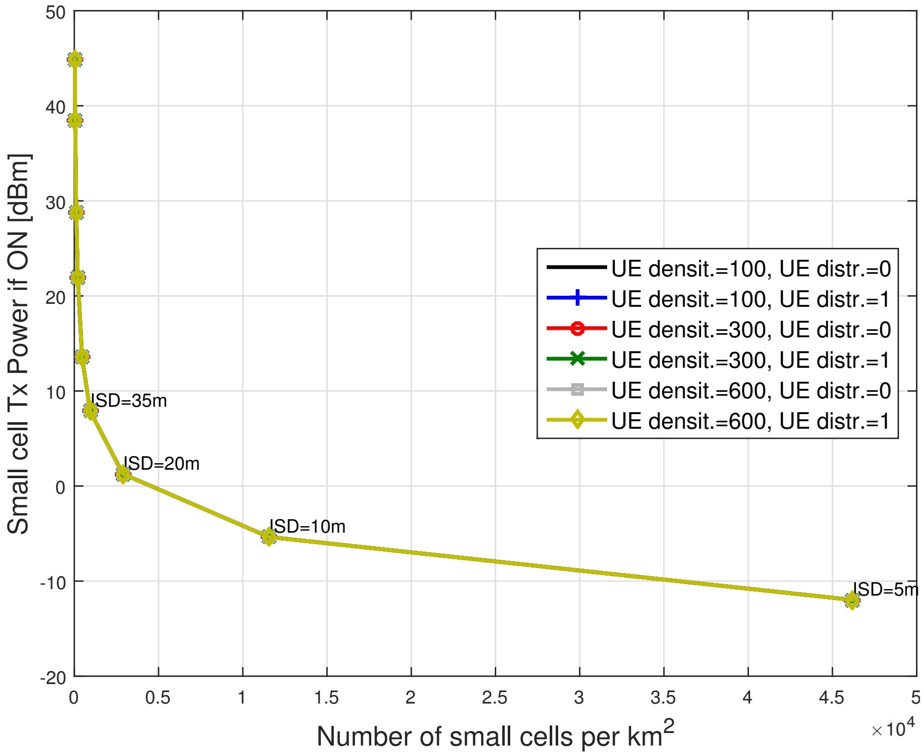

(a) Transmit power per active BS.

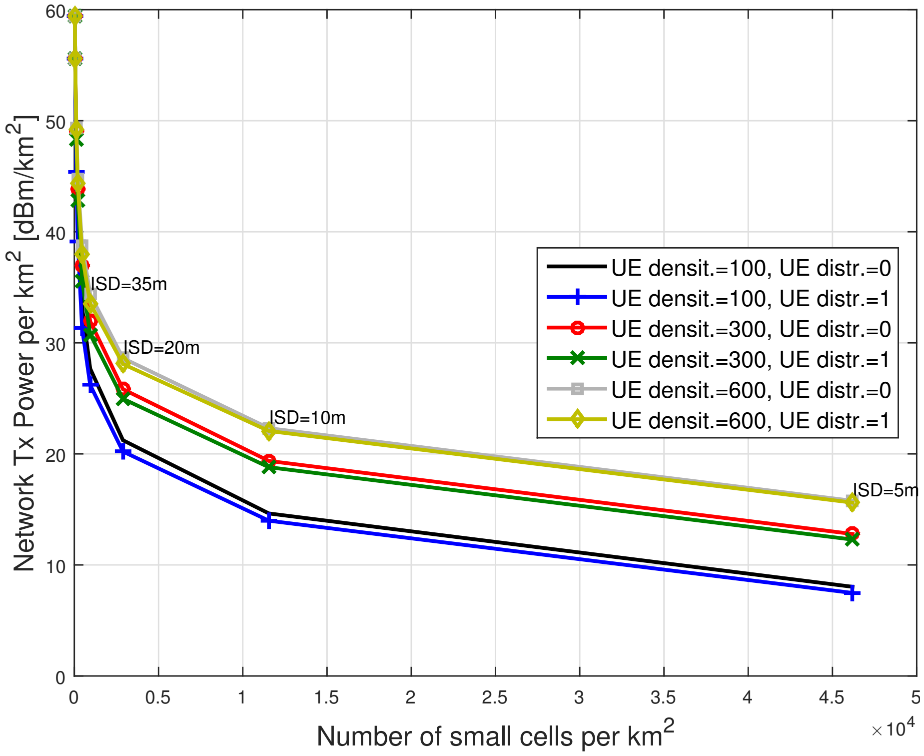

(b) Transmit power of the network per km^2.

Fig. 2.2 Transmit power per active BS and transmit power of the network per km^2. The UE densities are 100, 300, and 600 active UEs per km2, the carrier frequency is f = 2 GHz, the cell-edge SNR target is t = 12 dB, and the idle mode is activated. In Fig. 2.2(a) there are 6 overlapping curves since the power used by the small cell BS if it is activated does not depend on the UE density.

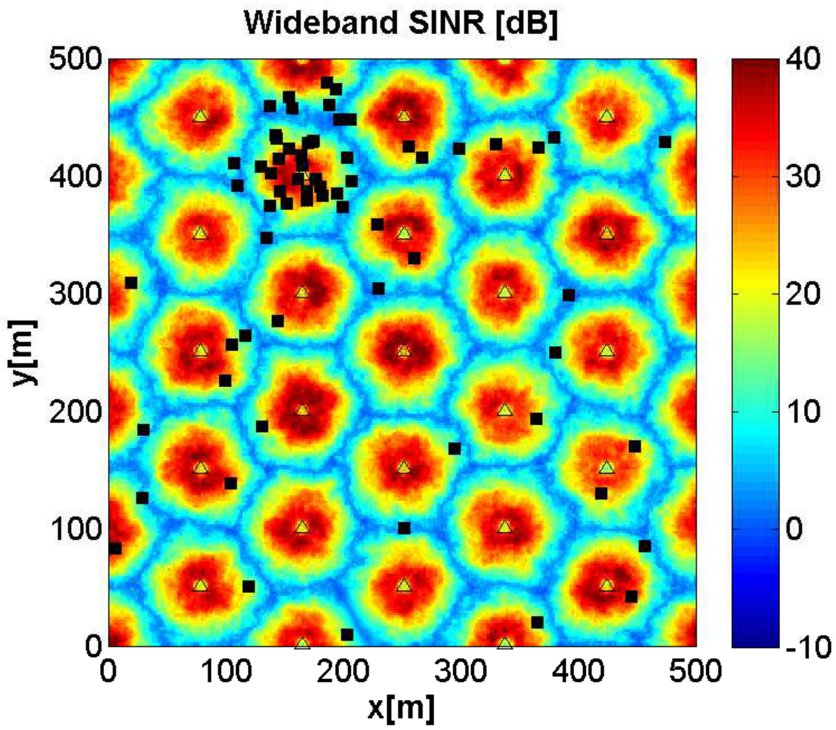

(a) ISD of 100 m & idle mode capability deactivated.

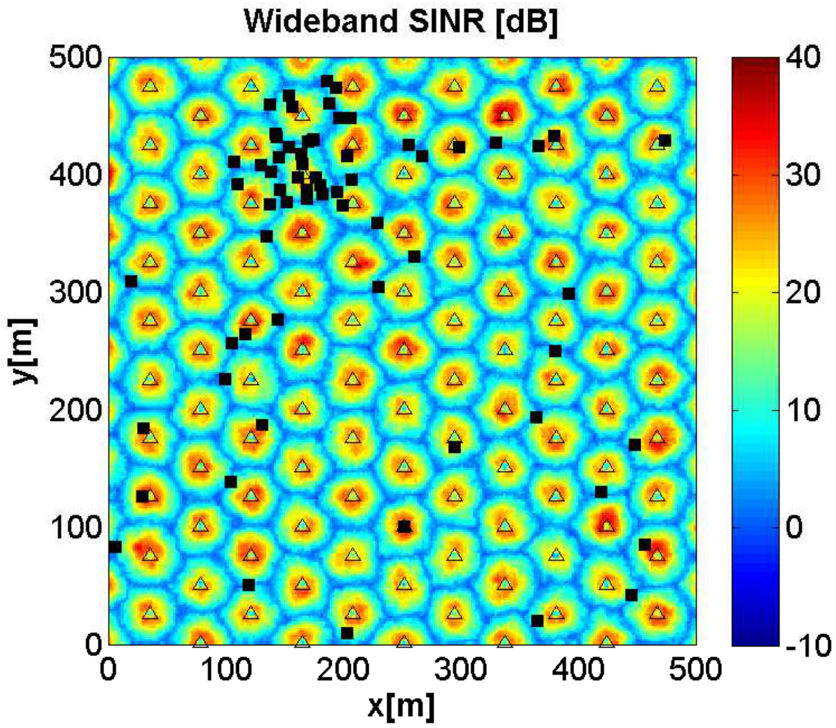

(b) ISD of 50 m & idle mode capability deactivated.

Fig. 2.3 SINR spatial distributions of small cell deployments with ISDs of 50m and 100m assuming deactivated idle mode capabilities. The rest of the parameters are non-uniform UE distribution with UE density of d = 300 UE/km^2, carrier frequency of f = 2 GHz, and cell-edge SNR target of t = 12 dB. The triangles represent BSs and the squares represent active UEs.

Having discussed the impact of idle mode capability, an important question that might arise, i.e., if a small cell BS has no UE in its proximity to serve, can the small cell BS serve a UE from a highly loaded nearby small cell BS for a fairer load distribution instead of entering the idle mode to mitigate the interference? Answering this question refers to an alternative UE association scheme based on throughput maximization which is a non-convex optimisation problem and is very difficult to analyse. That is the main reason that the received signal strength (RSS) based UE association is often adopted in most studies. Detailed discussions on alternative UE association schemes is beyond the scope of this thesis and is left for future investigations.

2.3.2.1 Transmit Power

In terms of transmit power, Fig. 2.2(a) shows how the transmit power per active BS significantly reduces with the small cell BS density in the studied scenario. In the simulation settings, both uniform and non-uniform distribution with UE densities of 100, 300, and 600 active UEs per km^2 has been assumed. The operating carrier frequency is $f = 2\,\text{GHz}$, and idle mode is activated. In this case, the transmit power of each active BS is configured such that it provides a SNR of 12 dB at the targeted coverage range, which is $\frac{\sqrt{3}}{2}$ of the ISD. Note that here the required transmit powers are significantly lower compared to co-channel deployments where the small cells should exceed the received macrocell power in the intended coverage area. It is important to note that in Fig. 2.2(a) there are 6 overlapping curves and this is because the power used by the cell when being activated does not depend on the UE density. In addition, due to idle mode capability being activated, Fig. 2.2(b) shows how the overall transmit power used by the network also significantly reduces with the small cell BS density in the studied scenario. This is because the reduction of transmit power per cell outweighs the increased number of active cells, and this fact holds true for both the uniform and non-uniform UE distributions, with network transmit power reductions of up to 43 dB.

2.3.2.2 UE SINR Distribution

Traditional understanding has led to the conclusion that the UE SINR distribution and thus outage probability is independent of BS density. The intuition behind this phenomenon is that the increase in signal power is exactly counter-balanced by the increase in interference power, and thus increasing the number of BSs does not affect the coverage probability. This is a major result in the literature [77] [78], which only holds under the assumption of a single-slope path loss model more suited for rural areas. However, conclusions are different for urban and dense urban scenarios where NLOS to LOS transitions may occur.

Table 2.1 Simulation Settings for SINR distribution

Parameter	**Value [80]**
Simulation scenario	Outdoor warp-around
Scenario dimension	500 m × 500 m
Deployment	Hexagonal
Inter-site-distance	5, 10, 20, 50, 75, 100, 200 m
No. of small cell BSs	46189, 11584, 2887, 462, 206, 116, 20
Carrier Frequency	2 GHz
UE distribution	Non-Uniform
UE density	300 UE/km^2
Circular hotspot radius	40 m
No. of UEs per hotspot	20
Minimum distance between two hotspots	40 m
Cell-edge SNR target	12 dB
Path loss model	LOS/NLOS gains with spline interpolation
Scheduler	Round Robin

In order to show this, Fig. 2.3 and Fig. 2.4 show the SINR spatial distribution with and without idle mode capability for ISDs of 50 m and 100 m that refer to 462 and 116 small cell BSs, respectively. Moreover, Fig. 2.5 shows the UE SINR cumulative distribution functions (CDFs) for both activated and deactivated idle mode capabilities at ISDs of 5 m, 10 m, 20 m, 50 m, 75 m, and 200 m corresponding to 46189, 11584, 2887, 462, 206, and 20 small cell BSs. Recall that the path loss models the NLOS to LOS transition with the probabilistic function defined for urban microcell environments defined in [79]. Table. 2.1 presents the detailed simulation settings. In the simulation settings, an outdoor wrap-around 500 m-by-500 m scenario is considered where small cell BSs are distributed in a uniform hexagonal grid with ISDs of 50 m and 100 m resulting in 462 and 116 small cell BSs per square km, respectively. It is further assumed the small cell BSs to operate at carrier frequency of $f = 2\,\text{GHz}$. In terms of UE distribution, the focus is on non-uniform distribution with UE density of $d = 300\,\text{UE/km}^2$ where the term non-uniform means that half of the UEs are uniformly distributed within the 500 m-by-500 m scenario and the other half are uniformly distributed within circular hot spots of 40 m radius with 20 UEs per hot spot. The hot spots are uniformly distributed, and the minimum distance between each two hotspot centres is 40 m. The SNR target of the small cell BS at its cell-edge which is defined as $\frac{\sqrt{3}}{2}$ of the ISD is also $t = 12\,\text{dB}$. Note that in Figs. 2.3 and 2.4, triangles represent BSs and squares represent active UEs.

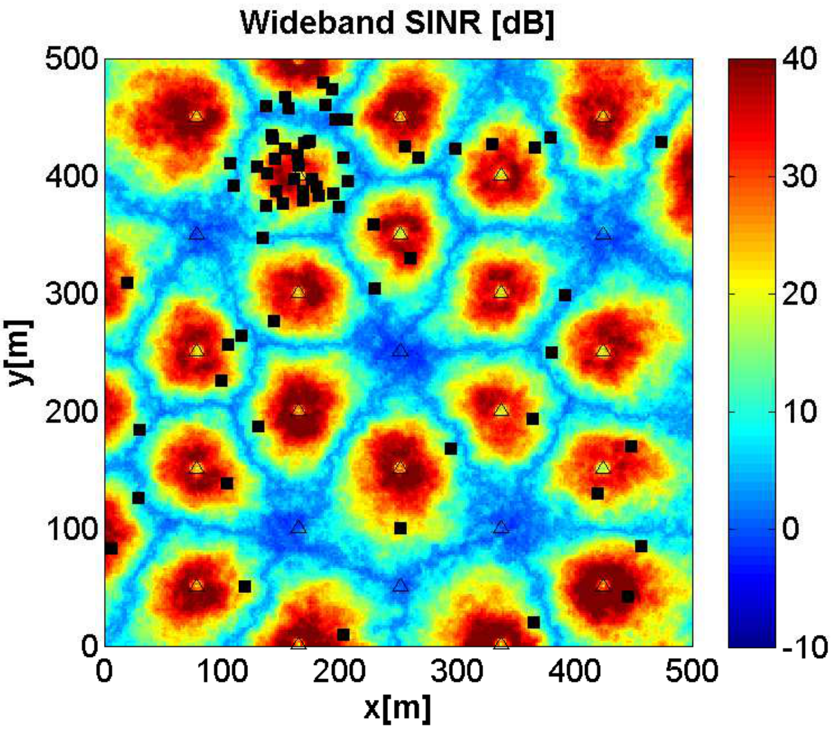

(a) ISD of 100 m & idle mode capability activated.

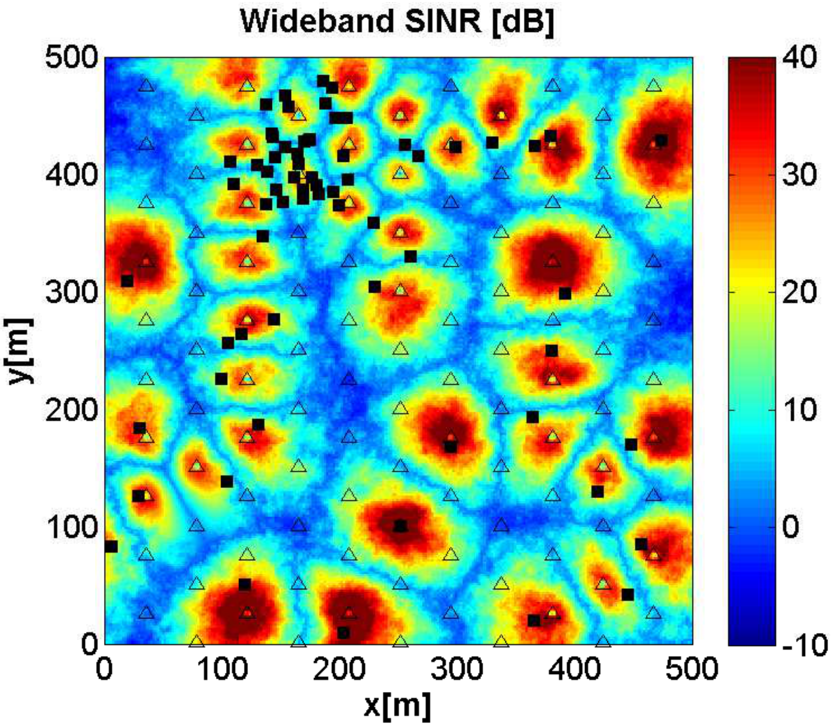

(b) ISD of 50 m & idle mode capability activated.

Fig. 2.4 SINR spatial distributions of small cell deployments with ISDs of 50m and 100m assuming activated idle mode capabilities. The rest of the parameters are non-uniform UE distribution with UE density of d = 300 UE/km^2, carrier frequency of f = 2 GHz, and cell-edge SNR target of t = 12 dB. The triangles represent BSs and the squares represent active UEs

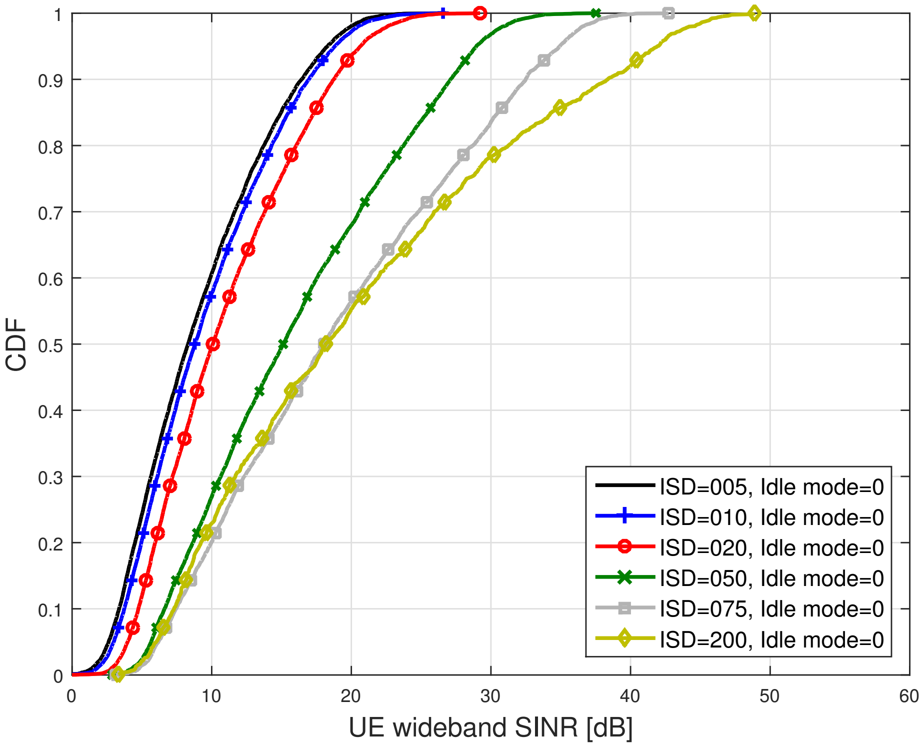

(a) CDF of UE SINR with idle mode capability deactivated.

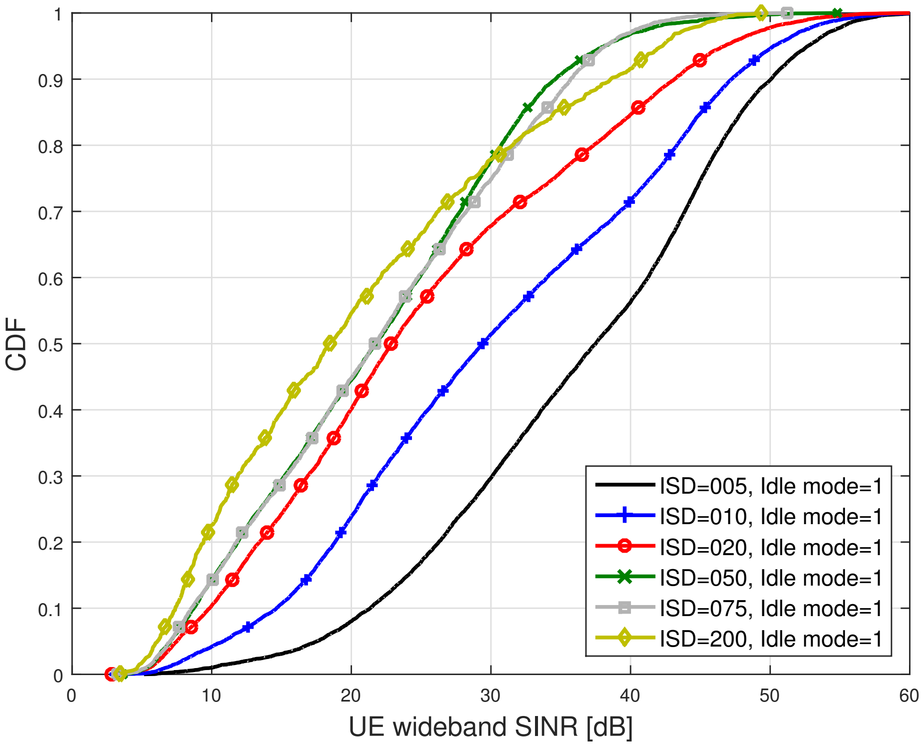

(b) CDF of UE SINR with idle mode capability activated.

Fig. 2.5 UE SINR CDF in ultra-dense small cell networks with ISDs of 5 m , 10 m , 20 m, 50 m, 75 m, and 200 m. The rest of the parameters are non-uniform UE distribution with UE density of d = 300 UE/km^2, carrier frequency of f = 2 GHz, and cell-edge SNR target of t = 12 dB.

When the idle mode capability is deactivated, Fig. 2.5(a) shows that the UE SINR CDF degrades with the small cell density, contradicting the results in [77] [78] where the authors have claimed that UE SINR CDF it is independent of BS density. As the network becomes denser, the ISD is reduced and the LOS component starts to dominate the path loss model for the interfering signals. While in traditional networks with large ISDs, the carrier signal may be subject to LOS depending on the distance between the UE and its serving BS, the interfering signal is not usually subject to LOS due to the large distance between the serving BS and its interfering BS. However, with the smaller ISDs, LOS starts dominating the interfering signal too and this brings down the UE SINR, thus lowering the UE and cell throughputs. In other words, the interference power increases faster than the signal power with densification due to the transition of the former from NLOS to LOS, and thus the BS density matters.

This new conclusion should significantly impact network deployment strategies, since the network capacity no longer grows linearly with the number of cells, based on previous understandings. However, as shown in Fig. 2.5(b) when the idle mode capability is activated, the trend is just the opposite, and the UE SINR CDF is significantly boosted with the cell density as a result of interference mitigation. The denser the BS deployments, the larger the capacity increase, since more BSs can be turned off, which reduces interference. When the ISD among BSs is 35 m, the median SINR improvement with idle mode capability is activated compared to the case when the idle mode capability is deactivated is around 8.76 dB, while for an ISD of 10 m the median SINR improvement due to benefiting from idle mode activation is around 20.62 dB. As conclusion, it is important to note that an optimum idle mode capability not only plays a significant role both in transmit power savings, but also in interference mitigation technique.

2.3.3 Transition from Interference to Noise Limited Scenarios

As shown in Fig. 2.1, in ultra-dense small cell networks, a large number of small cell BSs should be switched off when the BS density is large and the UE density is low; this combination leads to the most effective interference mitigation. However, is this interference mitigation through small cell deactivation large enough in order to cause a transition from an interference limited scenario to a noise limited scenario? In an interference limited scenario, the signal quality of a UE is independent of the transmit power of the serving and the interfering BSs, provided that they all use the same transmit power. However, this is not the case in a noise limited scenario where the signal quality of a UE improves with the transmit power of the serving BS, as the noise remains constant. Therefore, if such transition takes place, the tuning of the small cell BS transmit power becomes even more important, since the transmit power will not only determine the coverage radius of the cell, but will also affect the capacity of the network.

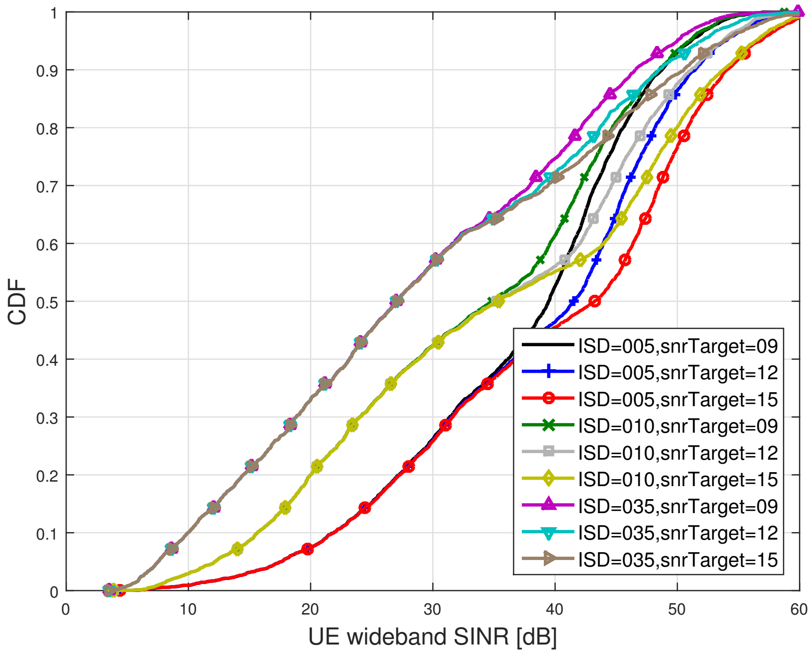

(a) 100 active UE per km^2.

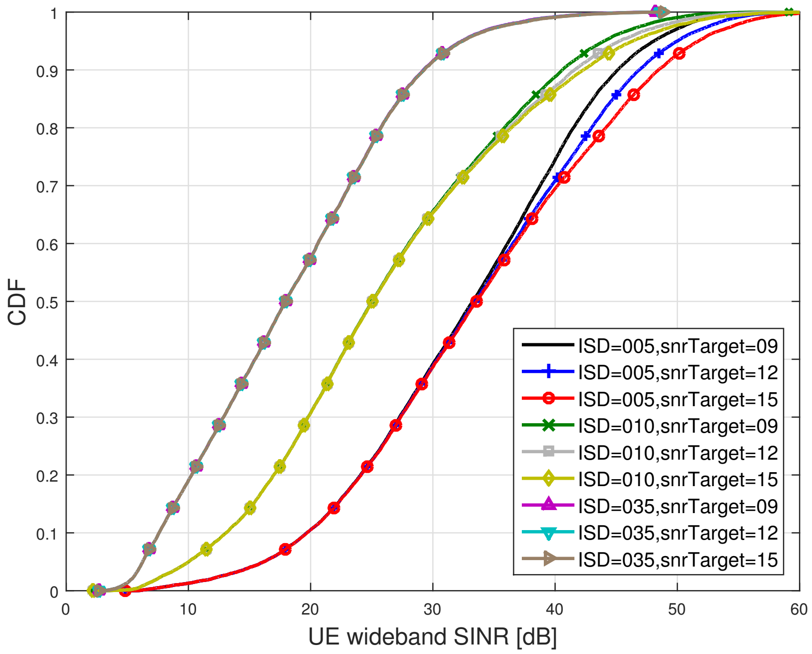

(b) 600 active UE per km^2.

Fig. 2.6 UE SINR CDF in ultra-dense small cell networks with ISDs of 5 m , 10 m , 35 m, non-uniform UE distribution with UE densities of 100 and 600 UEs per km^2, and cell-edge SNR targets of 9 dB, 12 dB, and 15 dB. The carrier frequency is f = 2 GHz and the idle mode capability is activated.

In order to answer this question, Fig. 2.6 shows the UE SINR CDF in different ultra-dense small cell networks, while considering different transmit power for the small cell BSs. In the simulations, non-uniform distribution with UE densities of 100 and 600 UEs per square km has been assumed in which half of the UEs are uniformly distributed within the 500 m-by-500 m simulation scenario and the other half are uniformly distributed within circular hot spots of 40 m radius with 20 UEs per hot spot. Hot spots are uniformly distributed, and the minimum distance between each two hotspot centres is 40 m. The carrier frequency of operation is $f = 2\,\text{GHz}$ and the targeted SNR at $\frac{\sqrt{3}}{2}$ of the ISD is set to 9 dB, 12 dB, and 15 dB. The idle mode capability is also activated. The results show that the change in transmit power only has an impact on the SINR distribution of the scenario with the largest BS densities, ISDs of =5 m and ISD=10 m, and the lowest UE densities, 100 active UE per km^2. Otherwise, the SINR distribution is independent of the transmit power, indicating that this transition does not occur in representative scenarios.

It is important to note that even in the indicated cases the decoupling of the UE SINR CDF only happens at the high SINR regime, whose SINRs belong to non-cluster UEs suffering from low interference. As a result, since the decoupling only happens for a very extreme BS density, it can be concluded that such transition from interference limited to noise limited does not occur in realistic deployments, and that the small cell BS transmit power should be configured to guarantee a targeted range.

2.4 Higher Frequency Bands

As shown by the Shannon-Hartley theorem presented in (2.1), the network capacity linearly increases with the available bandwidth. Therefore, increasing the available bandwidth is an appealing proposition to enhance network capacity. However, spectrum is a scare resource, especially at the lower frequency bands, [500-2600] MHz, which are in use today by radio and TV stations as well as the first wireless communication systems due to their good propagation properties. These frequency bands are thus heavily regulated, and it is unlikely that large bandwidths become available from them in the very near future. As a result, in the quest to increase network capacity, vendors and operators have started to look at the usage of higher frequency bands, $\geq$3500 MHz, where large bandwidths $\geq$100 MHz are available.

Due to the higher path losses at higher frequency bands, these bands were never appealing for large macrocells, but now suit well the operation of small cells, targeted at short ranges. These higher path losses should not only be considered as a disadvantage, but also as an opportunity, since they effectively mitigate interference from neighbouring cells, and thus allow a better spatial reuse. Moreover, it allows using smaller antennas and packing more of them per unit of area, which benefits multi-antenna techniques. In the following, the capacity gains provided by and the challenges faced when using higher frequency bands are discussed.

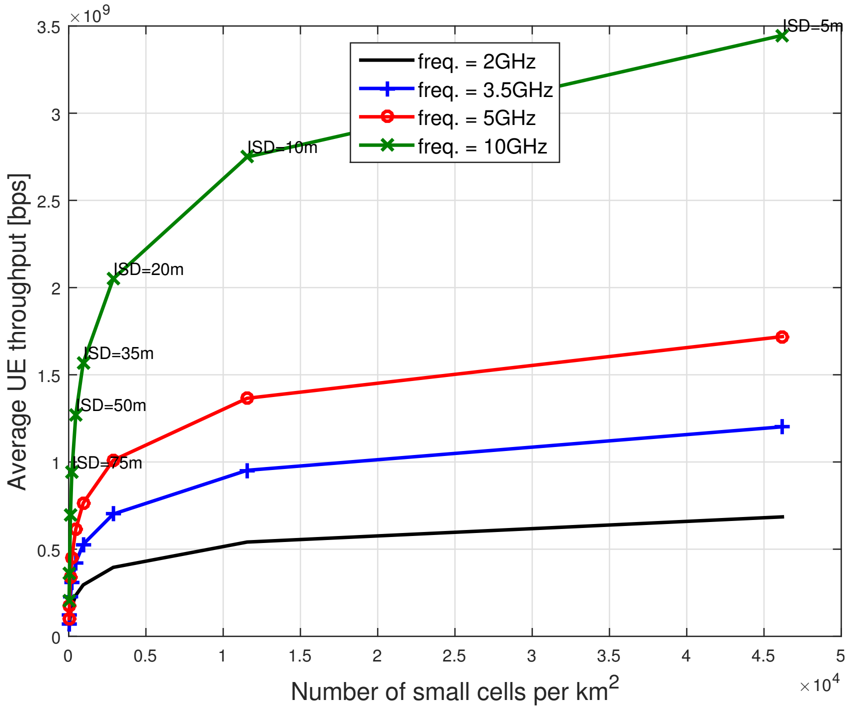

(a) Average UE throughput for different frequency bands.

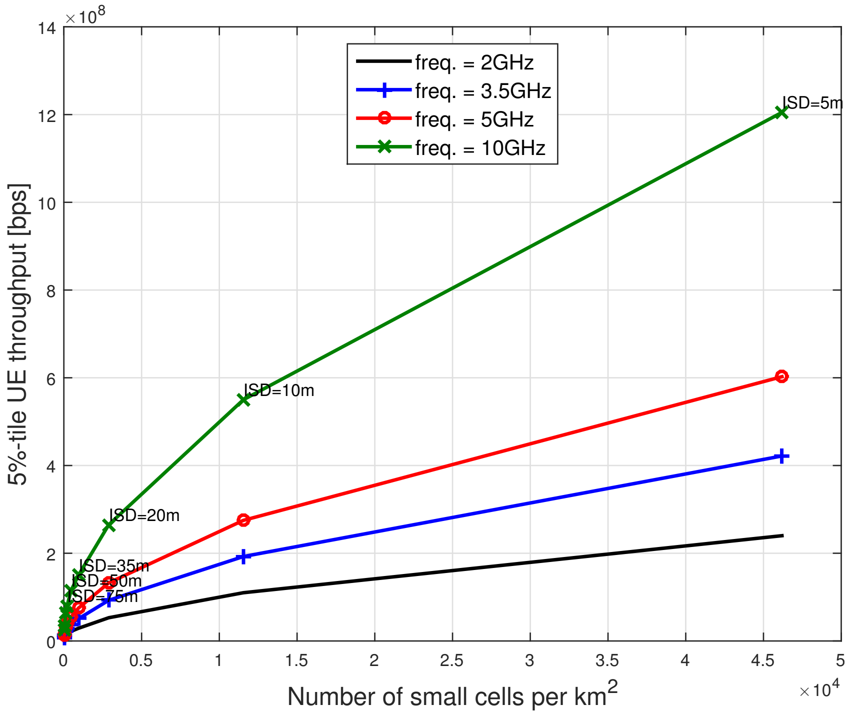

(b) 5 %-tile UE throughput for different frequency bands.

Fig. 2.7 Average and 5%-tile UE throughput at carrier frequencies of 2.0, 3.5, 5.0, and 10 GHz. The UEs are non-uniformly distributed with UE density of of d = 300 UE/km^2 and the SNR target at the cell-edge is 12 dB.

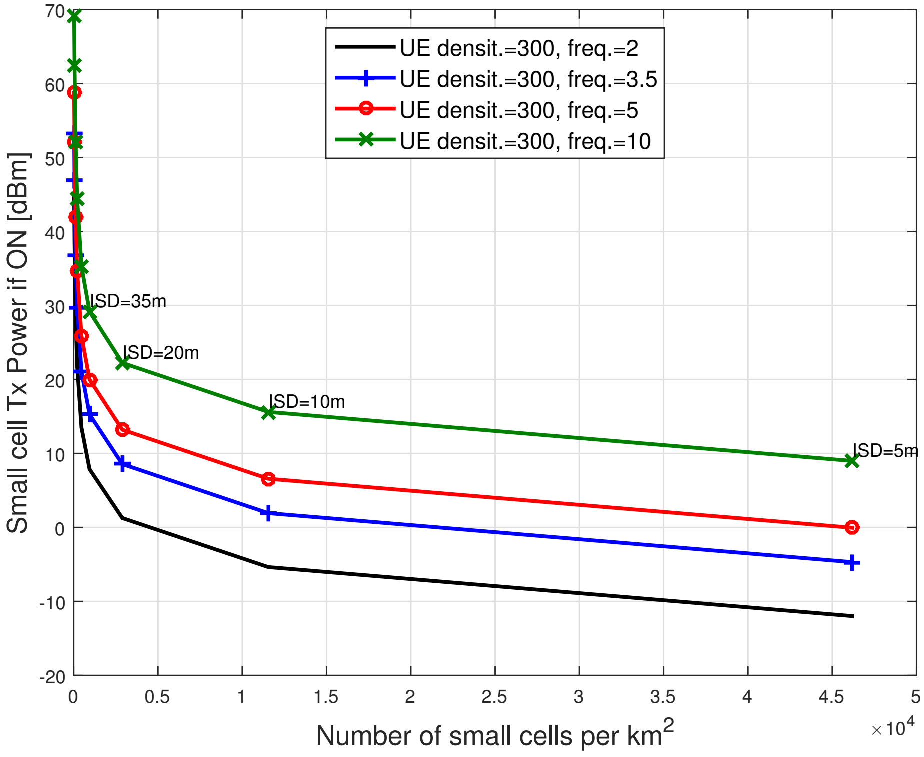

(a) Transmit power per active BS for different frequency bands.

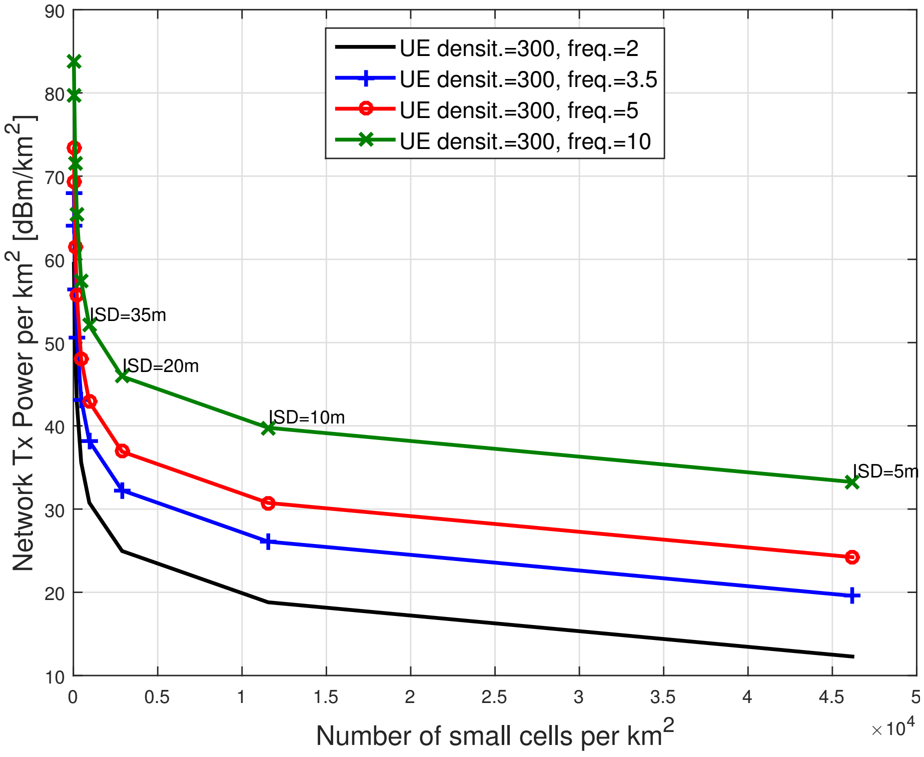

(b) Transmit power of the network per km^2 for different frequency bands.

Fig. 2.8 Transmit power per active BS and transmit power of the network per km^2 at carrier frequencies of 2.0, 3.5, 5.0, and 10 GHz. The UEs are non-uniformly distributed with UE density of of d = 300 UE/km^2 and the SNR target at the cell-edge is 12 dB.

In order to assess the capacity gains provided by ultra-small cell deployments and the use of higher frequency bands, Fig. 2.7 shows the average and 5%-tile UE throughput for different densification levels and four different network configurations where the carrier frequencies are 2.0, 3.5, 5.0, and 10 GHz and the available bandwidth is 5 % of the carrier frequency, i.e., 100, 175, 250, and 500 MHz, respectively. Note that in the simulations, it has been assumed that UEs are non-uniformly distributed with UE density of $d = 300\,\text{UE/km}^2$ and that the targeted SNR by the small cell BSs at the cell-edge which is $\frac{\sqrt{3}}{2}$ of the ISD is $t = 12\,\text{dB}$ in order to assure a constant coverage area regardless of the frequency band. Idle mode capability is also activated. From Fig. 2.7, different observations can be made.

In the following and based on Fig. 2.7, first the impact of densification on network capacity is analysed and then the improvements brought by the use of higher frequency bands are discussed. In terms of densification, the average and 5 %-tile UE throughput do not increase linearly with the number of deployed BSs, but with diminishing gains. This is due to the finite nature of UE density and the characteristic of its distribution. In the first phase, with a low BS density and up to an ISD of 35 m, the UE throughput rapidly grows, almost linearly with the number of cells, due to cell splitting gains and spatial reuse.

Subsequently, in the second phase, once the fundamental limit of spatial reuse is reached – *one UE per cell* – the UE throughput continues growing, but at a lower pace with the network densification. This is due to the combined effect of both, bringing the UE closer to the serving cell BS through densification and further from the interfering BSs through idle modes. These two effects together result in a SINR enhancement, which improves network performance in a logarithmic manner (see (2.1). These transition and two regimes are more obvious for the average than for the 5 %-tile UE throughput, since cell-edge UEs are the ones that suffer from significant interference and hence benefit more from proximity gains and interference mitigation.

Looking at the average and 5 %-tile UE throughput shown in Fig. 2.7, the case corresponding to ISD of 200 m with a 100 MHz bandwidth is used as a baseline which offers an average and 5 %-tile UE throughputs of 3.902×10^7 bps and 5×10^6 bps, respectively. Looking at the case of 35 m ISD with a 100 MHz bandwidth, it is seen that it can provide an average and cell-edge UE throughputs of 2.952×10^8 bps and 2.9×10^7 bps, respectively which results in corresponding gains of 7.56× and 5.80×. Further densification to reach an ISD of 5 m enhances the average and cell-edge UE throughputs to 6.852×10^8 bps and 2.4×10^8 bps which leads to gains of 17.56× and 48.00×, respectively. This shows that a significant increase in network performance can be achieved through network densification. In terms of frequency bands, the average and 5 %-tile UE throughput increase linearly with the carrier frequency due to the larger available bandwidth, showing the use of larger bandwidths as a key to achieve very high UE throughputs.

Furthermore, from Fig. 2.7 and by looking at the average and 5 %-tile UE throughput with the 35 m ISD case with a 100 MHz bandwidth as a baseline, a bandwidth of 250 MHz by using the carrier freqeuncy of 5 GHz can provide an average and cell-edge gain of 2.59× and 2.58×, respectively, while the gains provided by using the carrier frequency of 10 GHz with bandwidth of 500 MHz are 5.31× and 5.17×, respectively. Although smaller than the gains provided by network densification, this linear gains also represent a significant increase in network performance.

It is important to highlight that the capacity gains seen through using higher frequency bands do not come for free. The costs of the UE and BS equipments increase with the carrier frequency, as more sophisticated analogue circuit components are needed. Moreover, a larger transmit power is required for both lighting up the more subcarriers existing in a wider bandwidth and compensating for the higher path losses at higher frequency bands [81]. In this regard, Fig 2.8 shows the transmit power consumption in the network. Note that the simulation setting is similar to previous setting where idle mode is activated and UEs are distributed non-uniformly with UE density of $d = 300$ UE/km^2, and the cell-edge SNR target is $t =$12 dB. Fig 2.8 shows how both the transmit power per active BS and the overall transmit power used by the network increases with the wider bandwidth and the larger path losses, where this increase is not negligible and up to 24.34 dB. This transmit power increase is prohibitive in macrocell BSs where the required power would be up to 70 dBm, but it is still well suited to ultra-dense small cell deployments where BSs could operate this large bandwidth with less than 20 dBm of transmit power. In order to reduce transmit power, the identification and characterisation of hot spots becomes critical [82], [83]. Deploying small cell BSs where they are most needed, where the UEs are, for example, in the middle of a hot spot, will decrease the average UE path loss to the serving BS, and reduce this transmit power. Lighting up only those subcarriers with good channel quality that are necessary to achieve the required UE throughput targets will also help to reduce transmit power.

From above discussions, one can see that, when combining network densification with increased bandwidth, the targeted average 1 Gbps per UE is reachable with an ISD of 50 m and 500 MHz bandwidth, or 35 m ISD and 250 MHz bandwidth. The first and the second combination result in an average of 1.27 Gbps and 1.01 Gbps per UE, respectively. Thus, it can be concluded that the usage of larger cellular bandwidth than today's 100 MHz is required to meet the targeted high data rates of around 1 Gbps or larger. Taking the usage of higher frequency bands to an extreme, vendors and operators have also started to look at exploiting millimetre wave (mmWave) with carrier frequencies on 22, 60 and 77 GHz, where the available bandwidth is enormous, $\geq$1 GHz. However, diffraction and penetration through obstacles are hardly possible at these high frequency bands, and thus only LOS or near—LOS links seem more feasible. In addition, the range of the cell may be confined by high atmospheric phenomena. Water and oxygen absorption significantly increase path losses, especially at 22 GHz and 60 GHz, respectively. As a result, providing the required coverage range through larger transmit powers is not feasible anymore, as it is in the sub-10 GHz bands. Thus, it is expected that active antenna arrays and beamforming techniques become essential to overcome the increased path losses at these high frequency bands.

2.5 Multi-antenna Techniques and Beamforming

Previous results showed that for a single antenna small cell BS, the targeted average 1 Gbps per UE is only reachable with an ISD of at least 50 m and a bandwidth of 500 MHz (or alternatively with an ISD of 35 m and a bandwidth of 250 MHz). In order to enhance UE performance and bring down this still relatively large BS density, the usage of multiple antennas at the small cell BS is discussed in the following. Multiple antenna systems provide a number of degrees of freedom for transmitting information, which may vary from one to a number upper bounded by the minimum number of transmit/receive antennas. The higher the number of degrees of freedom available, the better spectral efficiency can be expected. However, how many effective degrees of freedom are available is mostly related to the spatial correlation of the channels. Given a number of degrees of freedom available, two multi-antenna techniques stand out. Beamforming makes use of only one of the degrees of freedom available, while spatial multiplexing may use all of them. Beamforming benefits from a low complexity implementation, together with its ability to extend the cell range by focusing the transmit power in a certain direction. However, it may be suboptimal in terms of spectral efficiency. In contrast, spatial multiplexing has the potential to approach the maximum channel capacity, linearly increasing the capacity of the channel with the minimum of number of transmit and receive antennas. However, it is significantly more complex to implement. Partly due to its simplicity and partly due to the fact that the small cell sizes in an ultra-dense deployment may suffer from a large spatial correlation of the channels, which limits the degrees of freedom available and renders spatial multiplexing infeasible, in this chapter the focus is on beamforming. In more detail, it focuses on quantised maximal ratio transmission (MRT) beamforming, using the standardised LTE code book beamforming approach [84]. Note that spatial multiplexing for ultra-dense small cell networks will be thoroughly discussed in chapter 5.

In the model, it is assumed that each BS is equipped with a horizontal linear antenna array comprised of 1, 2, 4, and 8 antenna elements, and each UE has a single antenna. The existing transmit power is equally distributed among antennas. Based on measurements over BS pilots signals, the UE suggests to the BS the precoding weights specified in the LTE code book [85] that maximise its received signal strength, and the BS follows such suggestion. It is worth mentioning that in case of 8 antenna elements, the LTE codebook is called double precoder. This horizontal beamforming helps to shape the horizontal antenna pattern at the BS and thus focuses the energy towards the UE in the horizontal plane. The characteristics of the antenna elements used in this analysis are described in Appendix A. Interference mitigation is also achieved in an opportunistic manner [86]. Real-time inter-BS coordination required for cooperation is not supported.

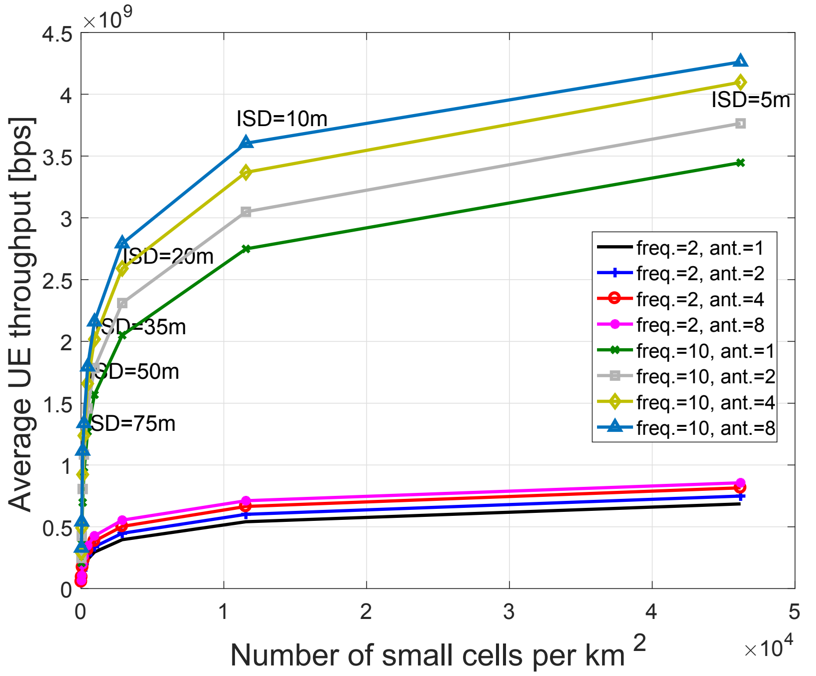

(a) 5 %-tile UE throughput for different number of antennas at 2 GHZ and 10 GHz frequency bands.

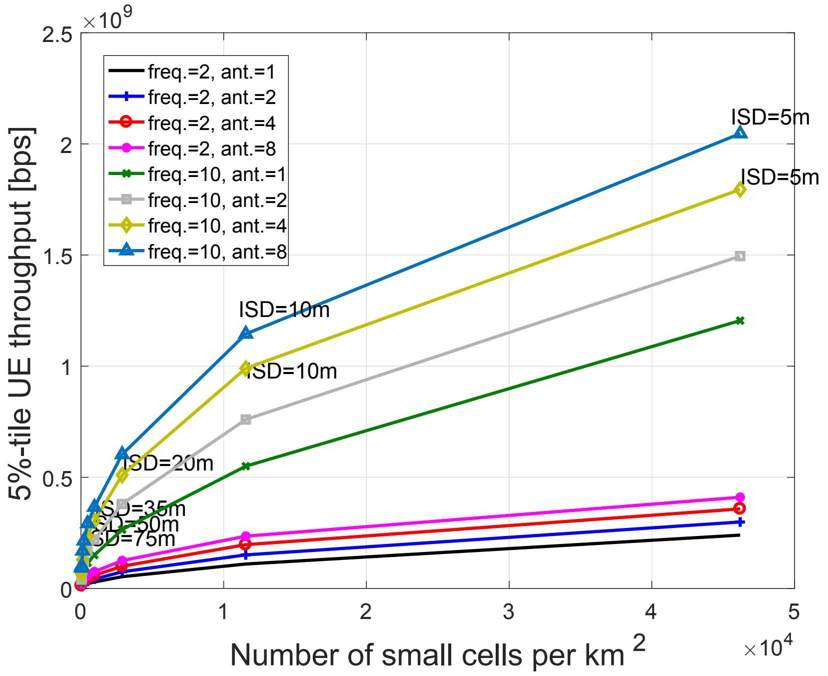

(b) Average UE throughput for different number of antennas at 2 GHZ and 10 GHz frequency bands.

Fig. 2.9 Average and 5%-tile UE throughput using different number of antennas per BS. UEs are non-uniformly distributed with UE density of d = 300 UE/km^2 and the SNR target at the cell-edge is 12 dB.

Fig. 2.9 and Tables 2.2-2.5 show the average and 5%-tile UE throughput for different network configurations where the carrier frequencies are 2.0 and 10 GHz and the number of antennas per small cell BS are 1, 2, 4, and 8. Control channels are not beamformed. The density of UE per square km is $d = 300\,\text{UE/km}^2$ and the UE distribution is assumed to be non-uniform. Moreover, it has been assumed that the idle mode is activated and that the targeted SNR by the small cell BS at cell-edge is 12 dB, thus assuring a constant coverage area regardless of the frequency band at the expense of larger transmit power.

From Fig. 2.9(b) and Table. 2.4, it is realised that for the 35 m ISD and 10 GHz carrier frequency case, the average UE throughput from using 2 antennas is 1.885×10^9 bps while the average UE throughput from using 1 antenna is 1.569×10^9 bps and hence the average gain of using 2 antennas over 1 antenna is 20.01 % (1 more antenna is needed). Increasing the number of antenna to 4 results in average UE throughput of 2.018×10^9 bps which implies that the gain of using 4 antennas over 2 antenna is 07.05 % (2 more antennas are needed) and the overall average gain from 1 to 4 antennas is 28.61 %.

Comparing the average UE throughput and 5%-tile UE throughput where the latter refers to the cell-edge throughput presented in Tables. 2.2-2.5, it is realized that beamforming gains are larger at the cell-edge. The higher beamforming gain at cell edge is because of the interference mitigation provided by the beamforming, which is more noticeable at the cell-edge. For instance, for the 35 m ISD and 10 GHz carrier frequency case, the 5%-tile UE throughput is 2.42×10^8 bps and 1.5×10^8 bps for 2 and 1 antennas, respectively, which results in a gain of 61.33 %. Using 4 antennas results in 5%-tile UE throughput of 3.05×10^8 bps and, therefore, the gain of using 4 antennas over 2 and 1 antennas is 26.03 % and 103 %, respectively.

It is further perceived that beamforming gains are larger for larger cell sizes. This is because beamforming helps improving the received signal strength of the UE, which may receive only a poor received signal strength if beamforming is not in place. From Table. 2.4, it is seen that for ISDs of 200 m and 5 m with carrier frequency of 10 GHz, the average UE throughput using 1 antenna is 2.084×10^8 bps and 3.446×10^9 bps, respectively. Using 2 antennas results in the average UE throughputs of 2.491×10^8 bps and 3.794×10^9 bps, respectively and using 4 antennas improves the average UE throughput to 2.902×10^8 bps and 4.012×10^9, respectively. Therefore, for the ISDs of 200 m and 5 m, the gains of using 2 antennas over 1 antenna are 19.52 % and 10.11 %, respectively, while the gains of using 4 over 2 antennas are 16.49 % and 5.74 %, respectively. This shows the beamforming gains increase in a diminishing manner with the number of antennas which is also in line with the linear antenna array theory indicating that beamforming antenna gains increase logarithmically with the number of antennas [87].

Table 2.2 Average UE throughput at carrier frequency of 2 GHz.

Inter-Site-Distance	1 Antenna	2 Antennas	4 Antennas
5 m	6.852×10^8	7.488×10^8	8.154×10^8
10 m	5.409×10^8	6.009×10^8	6.346×10^8
20 m	3.957×10^8	4.775×10^8	5.033×10^8
35 m	2.952×10^8	3.581×10^8	3.844×10^8
50 m	2.355×10^8	2.822×10^8	3.113×10^8
75 m	1.729×10^8	2.01×10^8	2.115×10^8
100 m	1.277×10^8	1.49×10^8	1.622×10^8
150 m	6.756×10^7	7.98×10^7	9.077×10^7
200 m	3.902×10^7	4.698×10^7	5.256×10^7

Table 2.3 5%-tile UE throughput at carrier frequency of 2 GHz

Inter-Site-Distance	1 Antenna	2 Antennas	4 Antennas
5 m	2.4×10^8	2.99×10^8	3.38×10^8
10 m	1.1×10^8	1.51×10^8	1.77×10^8
20 m	5.3×10^7	8.5×10^7	1×10^8
35 m	2.9×10^7	4.2×10^7	5.5×10^7
50 m	2.2×10^7	3.2×10^7	4.1×10^7
75 m	1.6×10^7	2.3×10^7	3.2×10^7
100 m	1.3×10^7	1.9×10^7	2.4×10^7
150 m	7×10^6	9.3×10^6	1.4×10^7
200 m	5×10^6	8.6×10^6	1.3×10^7

Table 2.4 Average UE throughput at carrier frequency of 10 GHz.

Inter-Site-Distance	1 Antenna	2 Antennas	4 Antennas
5 m	3.446×10^9	3.794×10^9	4.012×10^9
10 m	2.719×10^9	3.049×10^9	3.268×10^9
20 m	2.051×10^9	2.31×10^9	2.49×10^9
35 m	1.569×10^9	1.885×10^9	2.018×10^9
50 m	1.27×10^9	1.498×10^9	1.659×10^9
75 m	9.315×10^8	1.089×10^9	1.218×10^9
100 m	6.968×10^8	8.058×10^8	9.031×10^8
150 m	3.619×10^8	4.356×10^8	4.715×10^8
200 m	2.044×10^8	2.491×10^8	2.902×10^8

Table 2.5 5%-tile UE throughput at carrier frequency of 10 GHz

Inter-Site-Distance	1 Antenna	2 Antennas	4 Antennas
5 m	1.205×10^9	1.495×10^9	1.695×10^9
10 m	5.2×10^8	7.78×10^8	9.79×10^8
20 m	2.61×10^8	3.89×10^8	5.04×10^8
35 m	1.5×10^8	2.42×10^8	3.05×10^8
50 m	1.12×10^8	1.79×10^8	2.25×10^8
75 m	8×10^7	1.2×10^8	1.63×10^8
100 m	6.5×10^7	9.5×10^7	1.21×10^8
150 m	3.5×10^6	5×10^7	7.42×10^7
200 m	2.5×10^6	4.1×10^7	6.4×10^7

Table. 2.5 also shows that for the 5 m ISD and 10 GHz carrier frequency case, using 1, 2, and 4 antennas results in 5%-tile UE throughputs of 1.205×10^9 bps, 1.495×10^9 bps, and 1.695×10^9 bps, respectively. Increasing the ISD to 200 m can enhance the 5%-tile UE throughputs to 2.5×10^7 bps, 4.1×10^7 bps, and 6.4×10^7 bps, respectively. This demonstrates that beamforming gains are most effective at the *cell-edge of larger cell sizes* due to beamforming effects on both the interference mitigation and the improvement of the received signal strength.

From the results shown in Tables. 2.2-2.5, one can see that the targeted average throughput of 1 Gbps per UE is now reachable by operating at carrier frequency of 10 GHz and deploying 206 small cell BSs per square km at ISD of 75 m where each BS is equipped with 4 antennas. Alternatively, the 1 Gbps average UE throughput can also be achieved by using 4 antennas at each BS while reducing the carrier frequency to 5 GHz and deploying 943 small cell BSs per square km at ISD of 35 m. These two scenarios verify that multi-antenna techniques enhance the UE performance and are able to bring down the BS density to meet the targeted average UE throughput demands. However, beamforming gains are estimated to be of the order of up to 2x, which are low compared to the larger gains provided by network densification and use of higher frequency bands. Therefore, since the larger path loss at the frequency bands between 2 and 10 GHz could be compensated via larger transmit powers, the existing antennas at the small cell BSs may be better exploited by using spatial multiplexing, which has the potential to linearly increase the throughput with the minimum number of transmit/receive antennas provided that the required degrees of freedom exists in the channel which will be discussed in chapter 5. Finally, it is important to note that although the beamforming gains are the lowest in absolute values, it may be the most cost-effective solution since implementing more antennas at the small cell BSs is cheaper than deploying more BSs or purchasing more spectrum.

2.6 Conclusion

The objective of this chapter has been to shed new light on main approaches to manage the exponentially growing data deluge by conducting an in-depth survey on the Pareto set of network configurations in terms of small cell BS density, frequency band of operation, and number of antennas per small cell BS which can bring the next generation of mobile communications to reality to achieve an average throughput exceeding 1 Gbps per UE. For the first time, using simulation based analysis the gains and limitations of network densification along with the use of higher frequency bands (non-millimetre wave) and multi-antenna techniques were extensively presented. This analysis helped to advance the state of the art through following key novel insights: It was derived that one UE per small cell BS is the fundamental limit of network densification and once this limit is met, any further densification is not cost-effective since there will not be any linear gain increase with network densification which emphasizes the necessity to have a clear understanding of UE density and distribution prior to the deployment of small cell BSs. Moreover, it was demonstrated that extreme network densification by deploying 46189 small cell BSs per square km with an ISD of 5 m provides the most of UE throughput gains of up to 48x at the cell-edge, followed by a linear scale up to 5x attained by moving from the carrier frequency of 2 GHz to 10 GHz. It was further proved that cell-edge beamforming gains of around 2x can be achieved by using LTE codebook beamforming and increasing the number of antennas at small cell BSs from one to four. It was also discovered that the beamforming gains are larger at the cell-edge of larger cells. In addition to above insights, an important remark to underline is the relatively lower gain of beamforming in comparison to the gains from network densification and the gain from the use of higher frequency bands which implies that network densification through ultra-dense small cell deployments is the most appealing approach for the next generation of mobile communications. The final pivotal point from this chapter is that the remarkable gains of network densification are only achievable when network densification is accompanied by utilization of idle mode capability at small cell BSs in order to mitigate the interference.

Chapter 3

Analysis of Multi-User Diversity and Energy Efficiency of Dense Small Cell Networks

3.1 Introduction

An ultra-dense small cell network refers to a cellular network where the BS density is larger than UE density. Such large deployment of small cell BSs has implications on channel conditions experienced by UEs and UE density per BS as well as network power consumption and, therefore, it is imperative to assess their consequences. In this chapter, for the first time the impact of transition to an ultra-dense deployment of small cell BSs is evaluated from two prospects. Firstly, the effect of network densification on channel diversity - which affects the choice of scheduling algorithm for ultra-dense small cell networks - is studied. A systematic view towards the trade-offs of network densification in terms of radio resource management and in particular channel sensitive scheduling is presented and it is demonstrated that round robin scheduling could be considered as an alternative to proportional fair scheduling in ultra-dense small cell networks. Secondly, the energy efficiency of ultra-dense small cell networks - which plays a very significant role in better understanding the impact of network densification on the power consumption of ultra-dense small cell networks in terms of throughput per Watt ([bps/W]) - is investigated and it is deduced that dynamic algorithms are crucial to enhance the energy efficiency of ultra-dense small cell networks.

In the first section, it is stated that proportional fair scheduling has been discerned as an effective technique to efficiently utilize the available spectrum in sparse networks. However, in the context of ultra-dense small cell networks due to different propagation conditions, its gain may be limited. In this chapter, for the first time the performances of proportional fair and round robin scheduling algorithms under both activated and deactivated idle mode capabilities with different densification levels are compared, and fundamental trade-offs of network densification are analysed. The analysis reveals a key remark implying that as network densifies and the UEs locate closer to the BS, the LOS communication becomes stronger and so the multi-user diversity starts to diminish. The loss in the multi-user diversity for both the proportional fair and round robin schedulers is quantified and it is discovered that proportional fair scheduling offers a negligible gain in comparison to round robin scheduling in ultra-dense small cell networks and hence round robin scheduling may be a better choice in dense small cell deployments considering its lower complexity. This novel finding casts a new look at the role of the scheduling algorithms in ultra-dense small cell networks and has a significant impact in the manufacturing of small cell BSs where the digital signal processing (DSP) cycles saved due to the adoption of round robin scheduling, can be used to enhance the performance of other components, i.e., advanced idle mode algorithms with zero power consumption in idle mode.

In the second section, the energy efficiency of ultra-dense small cell networks is analysed. It is elaborated that while the power consumed by small cell BSs is much less than the power consumed by macro BSs, however, the installation of small cell BSs in large numbers will significantly enhance the aggregated energy consumption. The energy consumption of the network under different network configurations assuming different number of antennas and various idle modes based on the GreenTocuh Project is investigated and a detailed analysis of the effect of densification on energy efficiency of the network is presented. In addition to the slow idle mode and the shut-down mode models provided by the GreenTouch project, two futuristic idle modes are also proposed, where their energy consumption are 15% and 0% of the GreenTouch slow idle mode power consumption model. The analysis reveals a major remark which indicates that regardless of the idle mode profile, the beamforming gain due to addition of a new antenna is not large enough to cope with the increase in power consumption of the antenna chain at the small cell BS, causing a degradation in energy efficiency. It is also discovered that a small cell BS that is in idle mode may still consume a non-negligible amount of energy, thus impacting the energy efficiency of the network. This key observation casts the necessity to develop advanced idle mode capabilities with zero small cell BS power consumption in idle mode. In this regard, for the first time the use of energy harvesting technologies in the context of small cell networks is proposed which can derive energy from external sources such as solar power to supply sufficient power to keep the small cell BSs alive during the idle mode. The main contributions of this chapter are summarized as follows:

- A novel model has been proposed to derive the Rician K based on the probability of LOS communication. The Rician K factor has been derived as a function of the distance between UE and BS to capture the impact of distance between UE and BS on the strength of LOS multi-path fading.
- A new cross-correlation shadow fading model has been proposed as a function of the distance among BSs. This new model shows that the 50% cross-correlation among shadow fadings of different sites is not realistic and proves that as network densifies (lower values of ISD), the spatial correlation between shadow fadings of nearby small cell BSs increases.
- A major finding shows that when the network moves towards an ultra-dense deployment of small cell BSs, the proportional fair scheduling as an effective and widely used radio resource management method in traditional macrocell networks offers a negligible gain over round robin scheduling and so less computationally complex round robin scheduling may be used in dense deployments.
- A critical matter in an ultra-dense deployment of small cell BSs is to use small cell BSs with *zero energy consumption in idle mode* to enhance the energy efficiency of the network. This important feature serves as a guideline for the development of future ultra-dense small cell networks.

3.2 Analysis of Scheduling in Dense Small Cell Networks

Scheduling has been conceived as an effective technique to efficiently use the available spectrum and improve network throughput in macrocell networks with a large number of UEs per macrocell BS. In more detail, proportional fair (PF) scheduler is used as an appealing scheduling technique that offers a good trade-off between maximising throughput and improving fairness among UEs with diverse channel conditions. However, the gains of proportional fair may be limited in ultra-dense small cell networks, partly because the number of UEs per small cell BS is considerably reduced in comparison to macrocell ones, and partly because UEs may not experience very different channel conditions on different subcarriers due to the dominance of LOS propagation as UEs may be really close to their serving BS. These changes give rise to the question of whether the proportional fair scheduling is as efficient for dense small cell networks as it is for macrocell scenarios, or if it can be substituted by scheduling algorithms of lower complexity.

3.2.1 Small Scale Multi-Path Fast Fading Model

In this section, the multi-path fast fading is modelled as a function of distance between the UE and the BS, incorporating the probability of LOS communication.

Considering the cell size and the relative proximity of UEs to their serving BSs, there is a high probability of LOS communication in ultra-dense small cell networks, which indicates that Rician fading channel models may be more appropriate than Rayleigh ones to model multi-path fading in these types of deployments. The Rician fading model considers a dominant, non-fluctuating strong path in addition to a number of reflections and scatterings, referred to as LOS and NLOS components, respectively [88].

The probability distribution function (PDF) of Rician fading is given as

$$f(x) = \left[\frac{2(K+1)x}{\gamma} \exp(-K - \frac{(K+1)x^2}{\gamma})\, I_0(2\sqrt{\frac{K(K+1)}{\gamma}}x) \right] \tag{3.1}$$

where γ refers to the total power in LOS and NLOS components, and I_0 is the first kind zero-th order modified Bessel function. The Rician K factor denoted by K is the ratio of power distribution in the specular LOS to the NLOS multi-path components, and ranges between 0 and ∞, with both extremes corresponding to the Rayleigh channel and the non-fading channel, respectively. The Rayleigh fading occurs when there is no dominant LOS path.

In this chapter, a new model is presented where the Rician K factor is derived according to the probability of LOS communication. Considering micro urban scenarios, the probability of LOS communication as a function of distance is given as

$$P_{\text{LOS}} = \min(\frac{18}{d}, 1) \times (1 - e^{\frac{-d}{36}}) + e^{\frac{-d}{36}}, \tag{3.2}$$

where d is the distance between the UE and the BS [89]. According to this model, within 18 m from the BS, the P_{LOS} is equal to 1. UEs that are positioned up to 18 m from the BS location have a guaranteed strong LOS component and as they locate further away from the BS, the probability of LOS communication exponentially decreases.

In order to comply with the P_{LOS} of 1, the value of 32 ($\sim$15 dB) is assigned to the Rician K factor to secure the existence of a strong LOS component within the LOS zone. This value is derived based on dictating an upper bound of 0.5 dB–flat fading–for the standard deviation of the Rician fading. Now, as UEs locate further away from the BS, the P_{LOS} exponentially decays and so should the Rician K factor in order to comply with the proposed one-to-one correspondence. Accordingly, the Rician K factor is approximated as

$$\mathrm{K} = \frac{\mathrm{P_{LOS}}}{\mathrm{P_{NLOS}}} \tag{3.3}$$

where P_{NLOS} is equal to $1 - P_{\mathrm{LOS}}$ and hence for the Out-of-LOS zone (UEs that are located further than 18 m from their BSs), the Rician K factor is modelled by the exponentially decaying function shown in (3.4).

$$\mathrm{K} = \begin{cases} 32 & \text{if } d < 18m \\ 140.10 \times \exp(-0.107 \times d) & \text{otherwise,} \end{cases} \tag{3.4}$$

This is interpreted as a distance dependant transition from Rician to Rayleigh fading for UEs that are located further away from their BSs where the LOS component gradually fades. Fig. 3.1 shows the derived Rician K factor and the corresponding probability of LOS communication P_{LOS}. It is important to note that this new model can be further extended and calibrated with measurements.

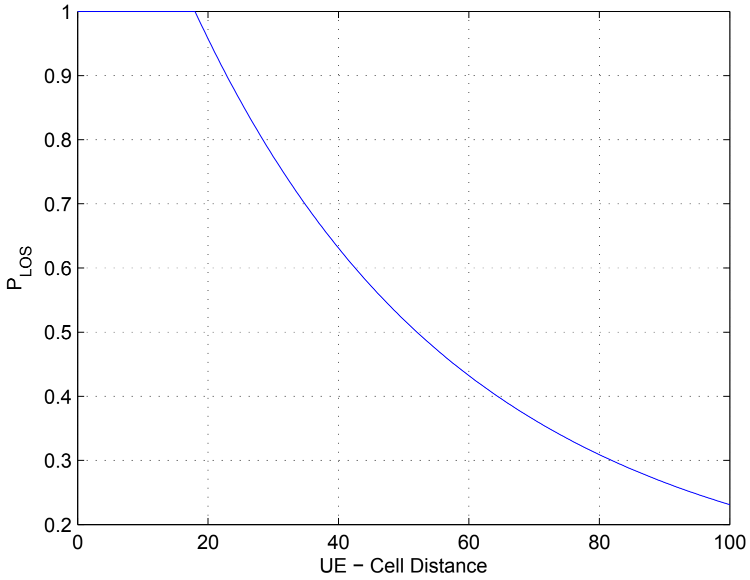

(a) Probability of LOS versus UE-Cell distance.

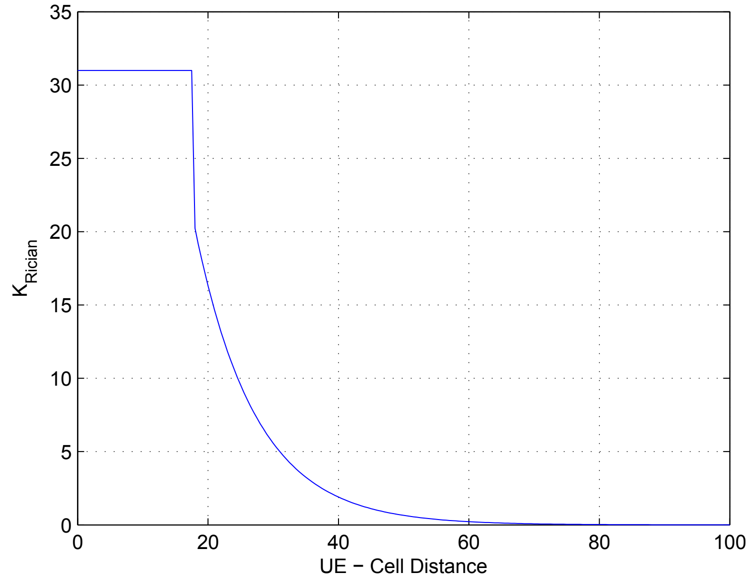

(b) Rician K factor versus UE-Cell distance.

Fig. 3.1 The one-to-one correspondence between probability of LOS communication and the Rician *K* factor.

3.2.2 Scheduling Algorithms for Small Cells

In LTE, a resource block (RB) refers to the basic time/frequency scheduling resource unit to which a UE can be allocated. Each RB expands 180 KHz in the frequency domain and has a duration of 1 ms in the time domain. The RB consists of 12 subcarriers of 15 KHz and its 1 ms transmission time interval (TTI) is referred to as one sub-frame. 10 sub-frames form one single frame.

Unlike other diversity techniques that aim to average the signal variations to mitigate the destructive impact of multi-path fading, multi-user diversity, also known as channel sensitive scheduling, takes advantage of multi-path fading by allocating to each resource block the UE which has the best channel conditions to enhance network performance [90]. Such type of scheduling leads to multi-user diversity gains, which have been shown to roughly follow a double logarithm scaling law in terms of capacity with regard to the number of UEs per BS for macro cell networks [91]. It is important to note that in order to aid the channel sensitive scheduling and exploit multi-user diversity gains, UEs need to report Downlink (DL) channel quality indicators (CQI) back to their serving BSs, which allows the scheduler to asses the UEs channel qualities and perform the scheduling according to a specific metric.

In a network with N UEs, each UE may undergo varying channel conditions where better channel quality generally refers to higher signal quality and higher throughput. Sharing the resources fairly between UEs that experience different channel qualities is a challenging task [92]. There are different types of scheduling algorithms that are concisely described as following:

- *Opportunistic scheduler* selects the UE with the best channel quality at each time and frequency resource, aiming to solely maximise the overall throughput. Opportunistic scheduling can remarkably increase system throughput at the expense of fairness, implying that UEs with relatively low channel qualities may be never served [93]

- *Round Robin scheduler* treats the UEs equally and give the same amount of time and frequency resources to all UEs irrespective of their channel qualities. Different types of round robin schedulers are summarised in Table 3.1.

- *Proportional Fair scheduler* exploits multi-user diversity based on UEs CQI, attempting to maximise the throughput while simultaneously forcing a degree of fairness in serving all the UEs. This scheduling will be further discussed in detail in the following.

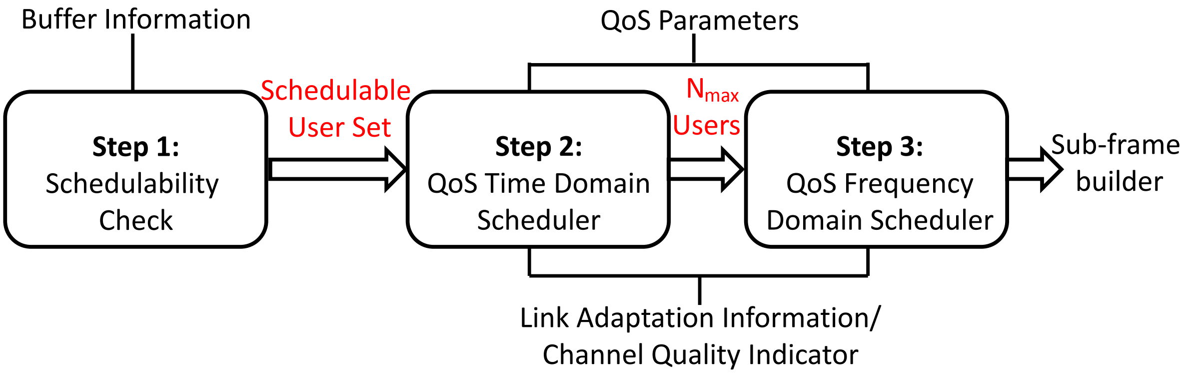

Fig. 3.2 Packet scheduling structure diagram.

3.2.2.1 Proportional Fair Scheduling

The proportional fair scheduling basically aims at weighting the potential instantaneous performance of a UE by its average performance, and this process consists of three stages. In the first stage, according to buffer information, the schedulable set of UEs is specified. The second stage is the time domain scheduling, which is in charge of reinforcing fairness and selecting the N_{max} UEs that will be input to the frequency domain scheduler. The last stage corresponds to the frequency domain scheduling, i.e., allocation of the resource blocks to the UEs. Fig. 3.2 shows the three steps of packet scheduling. Note that the complexity of the frequency domain scheduler highly depends on the number of its input UEs [94] [95], and thus the time domain scheduler has a major impact on the complexity of the frequency domain scheduler. A proportional fair scheduling metric in time domain can be defined as

$$M_{\mathrm{PF-TD}} = \frac{\hat{D}[n]}{R[n]}, \tag{3.5}$$

where $R[n]$ and $\hat{D}[n]$ are the past average throughput and potential instantaneous throughput of n-th UE, respectively [94]. The past average throughput can be computed using a moving average as

$$R_i(t+1) = (1-\frac{1}{T_c})R_i(t) + \frac{1}{T_c} \times r_i(t), \tag{3.6}$$

where $\mathrm{T_c}$ is the length of the moving average window and should be larger than the time elapsed between multiple schedules of the individual UE, and r_i is the current data rate of the serving UE. It is worth noting that the current data rate of a non-serving UE is considered to be zero. The UEs will be ranked constantly according to the metric in (3.5), and the

Table 3.1 Comparison of Proportional Fair and Round Robin schedulers

Scheduling Algorithm	**Time Domain**	**Frequency Domain**	**Complexity**
Proportional Fair	UE selection according to Eq. (3.5)	Resource blocks allocation according to Eq. (3.7)	$N^{\mathrm{UE}} \times N^{\mathrm{RB}}$
Round Robin 1	Single UE (in an iterative mode)	Entire bandwidth	1
Round Robin 2	—	Bandwidth equally divided among all UEs	1
Round Robin 3	Single UE selection according to Eq. (3.5)	Entire Bandwidth for single UE	N^{UE}
Round Robin 4	Multiple UEs selection according to Eq. (3.5)	Bandwidth equally divided among specified UEs	N^{UE}

N_{max} UEs with maximum preference are passed on to the frequency domain scheduler. A proportional fair scheduling metric in frequency domain can be defined as

$$M_{\mathrm{PF-FD}} = \frac{SINR[n,k,t]}{\sum_{k=1}^{\mathrm{N_{RB}}} SINR[n,k,t]}, \tag{3.7}$$

where the numerator is the SINR of the n-th UE on the k-th resource block and the denominator is the sum of the n-th UE SINRs over all resource blocks, which represents its average channel quality at sub-frame t [94]. The UEs will be ranked constantly according to the metric in (3.7), and the one with highest preference is selected to be served on the k-th resource block at each sub-frame.

The SINR of n-th UE over k-th resource block at sub-frame t is expressed as

$$SINR_{(n,k,t)} = \frac{P_{(n,k,t,i)} h_{(n,k,t,i)}}{\sum_{j=1 \ \& \ j \neq i}^{\mathrm{N_{BS}}} P_{(n,k,t,j)} h_{(n,k,t,j)} + N_0}, \tag{3.8}$$

where P is the BS transmit power over the k-th resource block, i, j and N_{BS} refer to the index of the serving BS, index of interfering BSs, and the total number of BSs, respectively, $h_{(n,k,t,m)}$ is the total channel gain between the n-th UE and the m-th BS, comprising antenna gain, path loss gain, shadow fading gain and multi-path fast fading gain and N_0 represents the noise power.

3.2.3 Performance Evaluation of Scheduling Algorithms

3.2.3.1 Impact of Rician K Factor

In order to study the impact of the Rician K factor on the scheduling algorithm performance, the Rayleigh fading channel model for which the Rician K factor is zero, is also inspected. Fig. 3.3 shows the ratio (gain) of cell throughput under the Rayleigh channel model to the Rician one. The UE-Cell distance varies when using various ISDs which based on (3.4), will result in different Rician K factors.

Moreover, for a given ISD, the higher the number of UEs that are being served, the higher the Rayleigh gain, since under the Rayleigh model there is more fluctuations in channel conditions and, therefore, there will be more multi-user diversity. For example, for an ISD of 20 m, the Rayleigh model boosts the cell throughput by 1.3x when having 5 UEs, while the boost is 1.41x when having 10 UEs. However, according to (3.4), as the ISD increases the Rician K factor decreases and the Rician channel model tends more towards a Rayleigh one, thus the Rayleigh over Rician gain diminishes. Fig. 3.3 shows that when serving 5 UEs, the Rayleigh over Rician gain drops by nearly 23% when the ISD is increased from 20 m to 70 m.

In ultra-dense small cell networks, due to the presence of LOS communication, exploiting the Rayleigh distribution to model the multi-path fading is unrealistic as it overestimates the multi-user diversity and results in very optimistic performances. Therefore, in the sequel, the Rician channel model is adopted.

3.2.3.2 Proportional Fair versus Round Robin Scheduling Algorithms

In this section, the performance of round robin and proportional fair schedulers are compared considering the Rician channel model considering both activated and deactivated idle mode capability. Note that the Rician K factor is computed based on (3.4) which depends on the distance between UE and BS. Since all round robin schedulers have similar performance with a $\sim 2\%$ variance, only the one that provided the best performance (round robin 4) is considered in the following discussion.

Fig. 3.4 shows the performances of round robin and proportional fair schedulers in terms of cell throughput with respect to the number of served UEs for different ISDs with both the idle mode capability of the small cell BS is deactivated or activated where idle model indicates that a small cell BS with no associated active UE is switched off. It can be seen from both Figs. 3.4(a) and 3.4(b) that when using round robin the number of served UEs per small cell BS does not impact the cell throughput, since round robin does not take into account the UE channel quality and, therefore, does not take advantage of multi-user diversity.

In contrast, proportional fair is able to benefit from multi-user diversity, and the cell throughput increases with the number of served UEs. However, it is important to realize that proportional fair can only exploit multi-user diversity until a given extent, as it is analysed in the following. In terms of number of served UEs per BS, there is a point in which a further increase in such number does not bring any significant cell throughput gain. For example, for an ISD of 200 m and when idle model capability is deactivated, having more than 8 UEs per cell small cell BS does not noticeably increase cell throughout, while for an ISD of 20 m, this number is reduced to 6 UEs. This shows how multi-user diversity gains vanishes with network densification due to stronger LOS propagation as well as less fluctuating channel conditions.

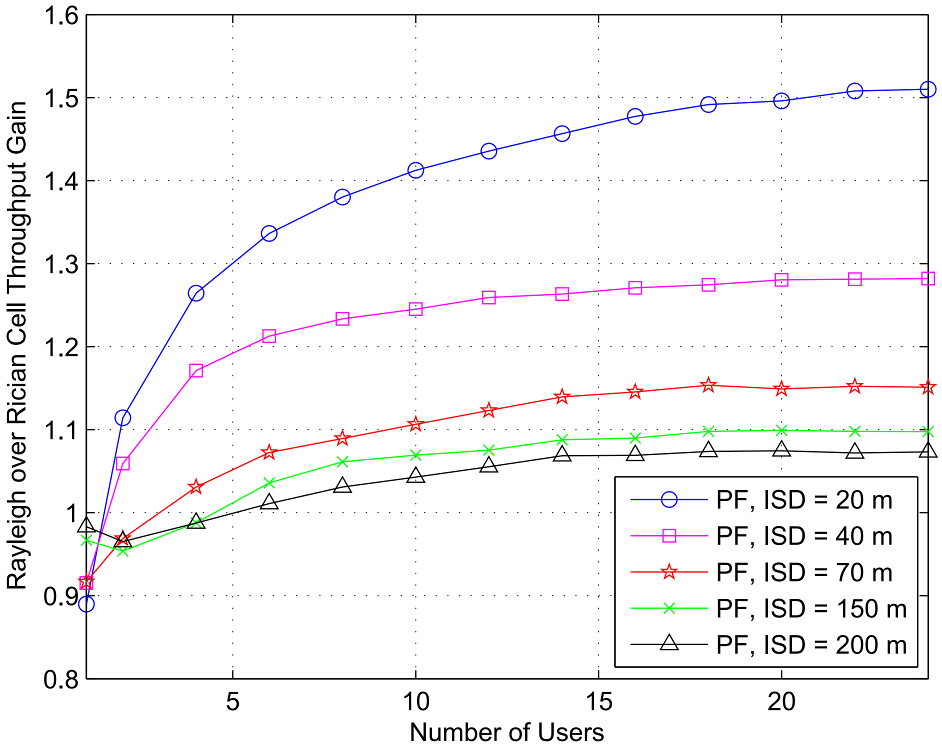

Fig. 3.3 The gain of Rayleigh over Rician fading using proportional fair scheduling.

Simulation results also show how the proportional fair scheduler starts losing its advantage in terms of cell throughput with the reduced cell size. For a given number of UEs per small cell BS, let's say 4, the proportional fair gain over round robin with deactivated idle mode capability is about 10.5 %, 12.4 % and 21.2 % for dense deployments with ISDs of 20 m, 40 m and 150 m, respectively. Investigating the impact of idle mode on cell throughput, it is seen from Fig. 3.4(a) that when the idle mode capability is deactivated, the overall cell throughput degrades with the small cell BS density. As the network becomes denser, the ISD is reduced and the LOS component starts to dominate the path loss model for the interfering signals which bring down the UE SINR, thus lowering the cell throughput. However, as demonstrated in Fig. 3.4(b), when the idle mode capability is activated, the trend is just the opposite, and the cell throughput is significantly boosted with the small cell BS density as a result of interference mitigation. The lower the ISD, the BS deployment will be denser and the larger the capacity increase, since more BSs can be turned off, resulting in reduced interference. This efficiency loss of proportional fair with the cell size makes us wonder if it is the suitable scheduler in dense small cell deployments.

Shrinking the cell size not only reduces the cell throughput, but also reduces the UE throughput. Applying the proportional fair scheduler, Fig. 3.5(a) shows that when the idle mode capability is deactivated, due to both interference enhancement (due to transition of NLOS interference to LOS interference as discussed in chapter two) as well as multi-user diversity loss (see Fig. 3.4), the average UE throughput for a given number of served UEs drops down with network densifucation. For instance, keeping 4 UEs per BS and reducing the ISD from 150 m to 40 m and 20 m, the average UE throughput drops by $\sim$ 42.2 % and 59.8 %, respectively. However, Fig. 3.5(b) shows that once the idle mode capability is activated due to interference mitigation, the trend is completely opposite and the UE throughput is significantly boosted with densification for both proportional fair and round robin schedulers. Comparing proportional fair and round robin performances, for an ISD of 20 mm, the gain of the former is almost negligible, around 5 %.

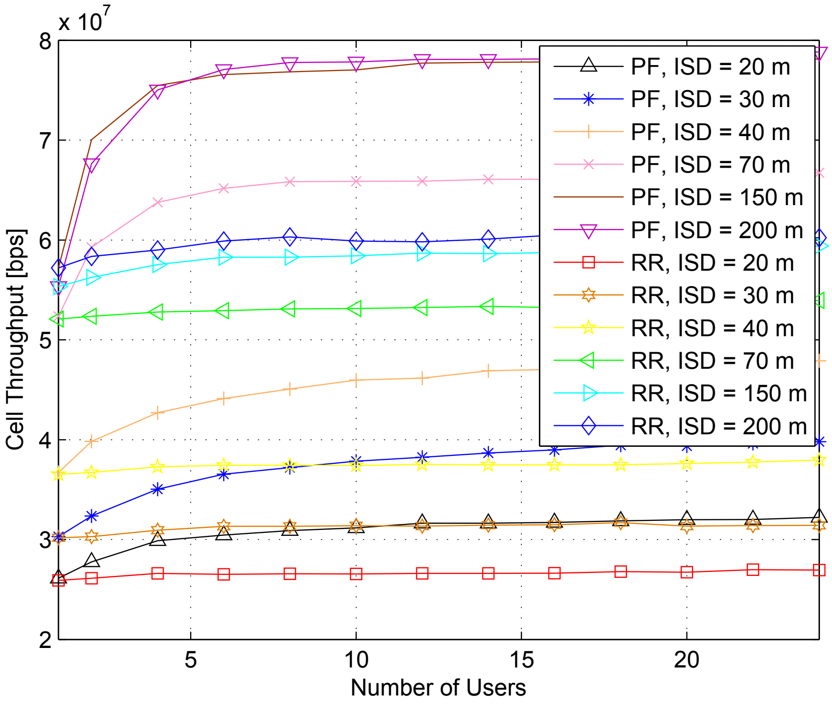

(a) Idle mode capability deactivated.

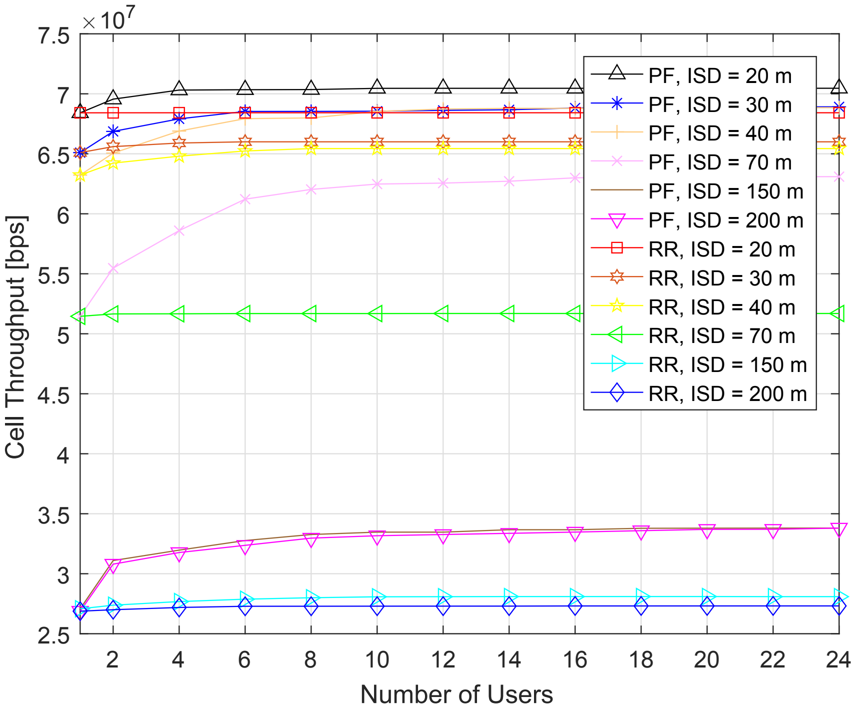

(b) Idle mode capability activated.

Fig. 3.4 Comparison of mean cell throughput at different ISDs with proportional fair and round robin schedulers.

The minor gains of proportional fair scheduler over the round robin one at low ISDs in terms of cell and UE throughputs suggests that round robin scheduler may be a better choice in ultra-dense small cell networks considering the higher complexity of proportional fair scheduler. This conclusion may have a significant impact in the manufacturing of small cell BSs where the digital signal processing (DSP) cycles that are saved due to the adoption of round robin scheduling, can be used to enhance the performance of other technologies. Table 3.1 shows the complexity comparison of the discussed scheduling schemes, where N^{UE} and N^{RB} refer to number of UEs and resource blocks, respectively. The complexity of the proportional fair lies in the evaluation of each UE on each resource block considering a greedy proportional fair that operates on a per resource block and subframe basis and is equal to $N^{\mathrm{UE}} \times N^{\mathrm{RB}}$. It is worth noting that proportional fair complexity with exhaustive search is considerably higher.

Until now it has been shown how network densification affects cell and UE performances for a given number of UEs per BS. In contrast, it is important to note that shrinking the cell size naturally leads to a lower number of UEs per BS, which increases UE throughput. Fig. 3.5 shows that the mean UE throughput is significantly increased by lowering the number of UEs per BS. At an ISD of 70 m, the mean UE throughput is increased by $\sim 1.30\times$, $1.42\times$ and $1.75\times$ when the number of served UEs is lowered from 4 to 3, 2, and 1 UE per cell, respectively. This UE throughput gain is due to the larger portion of spectrum that each UE can assess, and is larger than the UE throughput degradation due to loss in multi-user diversity and interference enhancement. Fig. 3.6 also shows the CDF of the UE throughput for various ISDs for both proportional fair and round robin schedulers. It can be realized that reducing the ISD from 200 m to 40 m and 20 m, the UE 5%-tile throughput drops by 40.8% and 36.7%, respectively. Comparing the UE 5%-tile throughput of proportional fair and round robin schedulers at the ISD of 20 m, the gain of the former is almost negligible, around 9%.

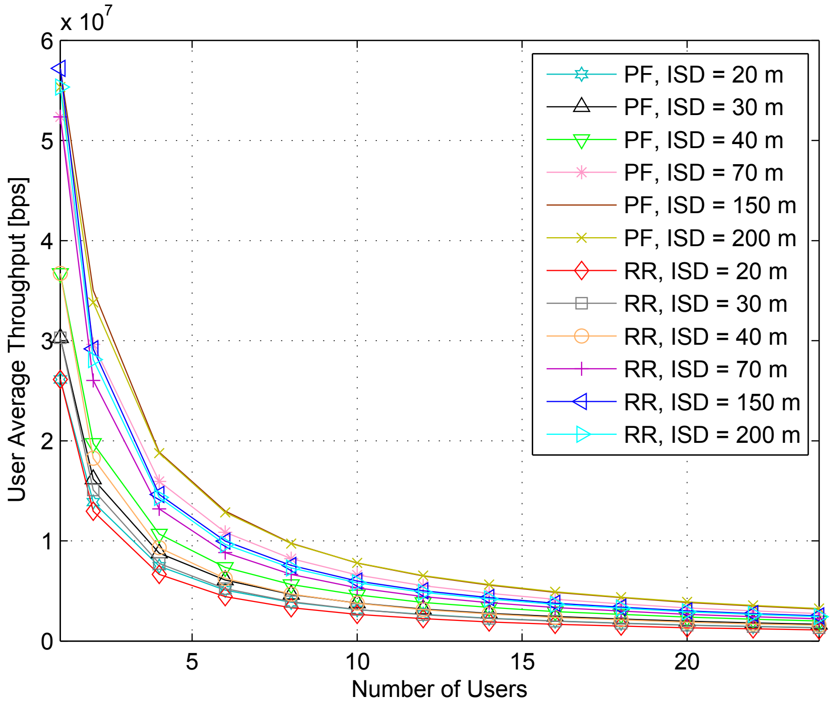

(a) Idle mode capability deactivated.

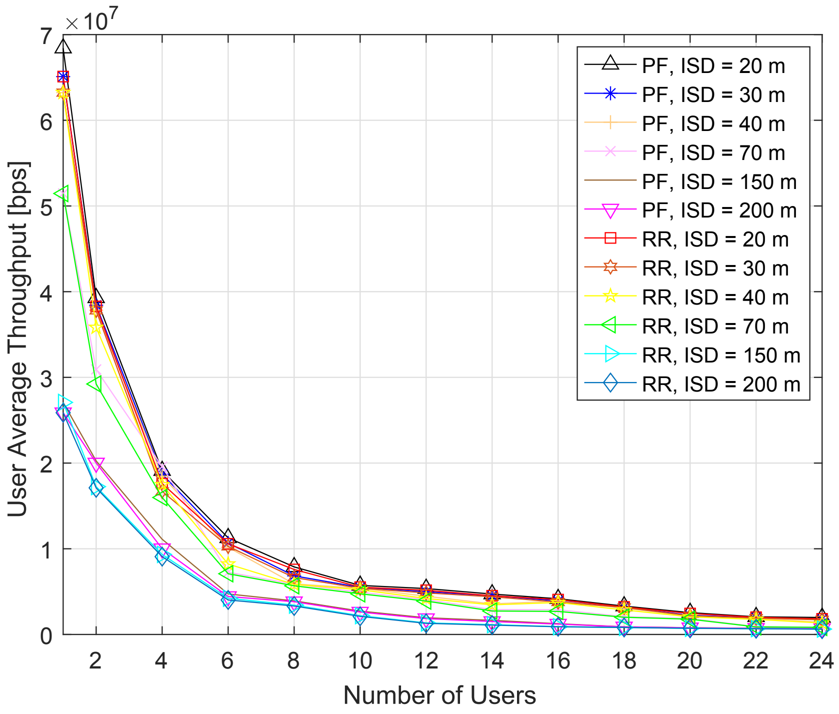

(b) Idle mode capability activated.

Fig. 3.5 Comparison of User mean throughput at different ISDs with proportional fair and round robin schedulers.

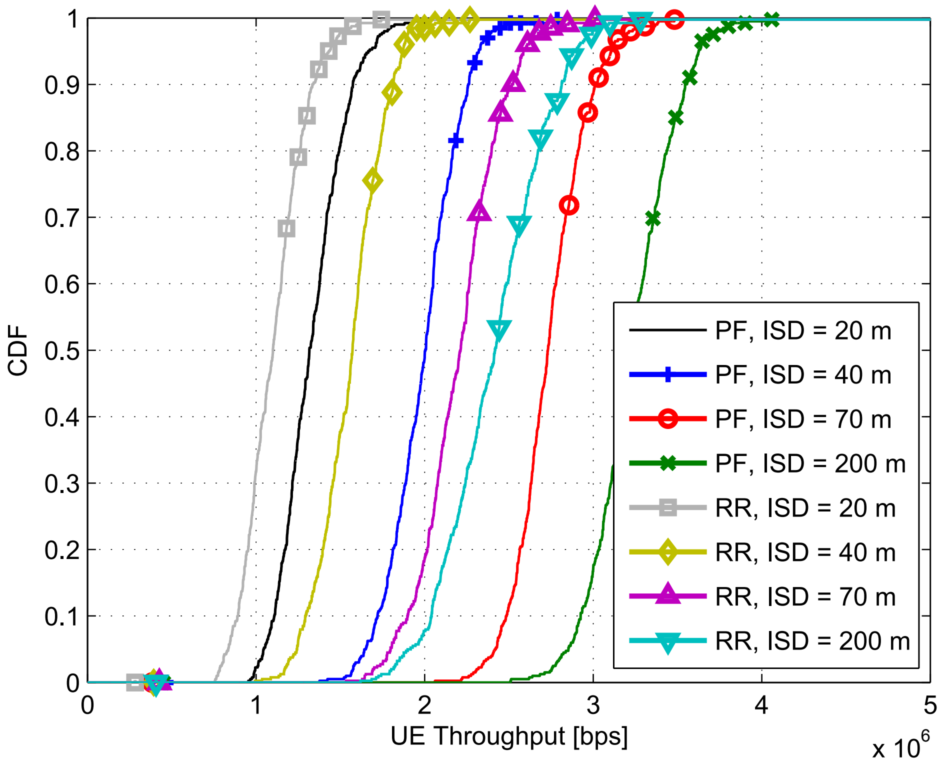

Fig. 3.6 Compariosn of the CDF of UE throughput at different ISDs with proportional fair and round robin schedulers.

It is realized as the cell size reduces, multi-user diversity gains also vanish and serving more UEs does not bring any further gain in cell throughput and, therefore, round robin schedulers may be used in ultra-dense small cell networks considering the extra complexity of proportional fair ones.

3.3 Analysis of Energy-Efficiency in Ultra-Dense Small Cell Networks

Deploying a large number of small cells, millions, tens of millions, poses some concerns in terms of energy consumption. For example, the deployment of 50 million femtocells consuming 12 Watts each will lead to an energy consumption of 5.2 TWh/a, which is equivalent to half the power produced by a nuclear plant [96]. This approach does not scale, and thus the energy efficiency of ultra-dense small cell networks should be carefully considered to allow the deployment of sustainable networks.

It was shown in chapter 2, that the overall transmit power used by the network significantly reduces with the small cell BS density when an efficient idle mode capability is used. This is because the reduction of transmit power per cell outweighs the increased number of active cells. However, this observation may not hold when considering the total power consumption of each small cell BS, since a non-negligible amount of energy may still be consumed by a BS in an idle mode which impacts the energy efficiency of the network. In order to better understand the impact of network densification on the power consumption, the energy efficiency of ultra-dense small cell networks in terms of throughput per Watt ([bps/W]) is analysed in this section.

In the study on the energy efficiency of ultra-dense small cell networks, it is required to model the BS power consumption. In this regard, Green Radio [97] and GreenTouch [98] projects are amongst the prominent ones that have analysed the energy efficiency of cellular networks. The Green Radio project discussed the architecture of current BSs and studied new techniques that can be exploited at key parts of BSs to obtain significant energy savings. The GreenTouch project proposed new BS architectures that can be extended upto 2020 to meet the ambitious energy efficiency target of $1000\times$. In this chapter, the power model developed in the GreenTouch project with different optimised idle mode states is used. The main motivation to use the GreenTouch model over other models [99–101] - which also compute the overall energy consumption based on BS size, antenna height, UE density and mobility, traffic scenario, etc - is that GreenTouch project has been designed for good accuracy, simplicity, and flexibility to describe the detailed power models of the BS components/sub-components and focuses on how the power is scaled over various scenarios, even if fully accurate absolute power numbers cannot be guaranteed. Indeed, the power model presented in GreenTouch project estimates the power consumption of a BS based on tailored modelling principles and scaling rules for each BS component, i.e., power amplifier, analogue front-end, digital base band, digital control, backhaul interface, and power supply. Moreover, GreenTouch project considers different types of BSs that includes macro, micro, pico, and femto cells and uses power instead of energy since power is a more natural metric to use as a function of required throughput or system load. Additionally, GreenTouch project allows the BS to be configured with multiple parameters, i.e., bandwidth, transmit power, number of antenna chains, and system load. In this chapter, since the focus is on the energy efficiency of ultra-dense small cell networks, the most efficient idle mode states which are GreenTouch slow idle mode and GreenTouch shut-down mode are considered where most or all components of the BSs are deactivated, respectively.

Table 3.2 shows the estimated power consumption for different small cell BS types with different transmit powers, where such power consumption is given for the active mode (full load) as well as the slow idle mode and the shut-down state, and for BS with 1, 2 or 4 antennas. Note that the 2020 small cell BS type is used in the model and that the presented analysis considers a carrier frequency of 2 GHz with 20 MHz bandwidth. In contrast to macrocell BS, it is important to indicate that the power consumption of a small cell BS linearly scales with the number of antenna chains, since it is the most contributing component to power consumption in a small cell BS.

Based on the values of Table 3.2 and the throughput analysis in chapter 2, Fig. 3.7 shows the energy efficiency in bps/W for different network configurations with 1, 2 or 4 antennas per BS. Note that it is considered that UEs are non-uniformly distributed with UE density of 300 $\frac{UE}{km^2}$ and activated idle model capability aiming for SNR target of 12 dB. In addition to the slow idle mode ($sm = 1$) and the shut-down mode ($sm = 2$) models provided by the GreenTouch project, two futuristic idle modes are considered, where their energy consumption is 15 % ($sm = 3$) or 0 % ($sm = 4$) of the GreenTouch slow idle mode power consumption model ($sm = 1$). The former model accounts less energy consumption than the shut-down mode ($sm = 2$), and the latter model assumes that the BS consumes nothing in idle mode.

For any given idle mode, results show that increasing the number of antennas at the small cell BS always decreases the energy efficiency. This is because the performance gain provided by adding a new antenna through beamforming is not large enough to cope with the increase in power consumption resulting from adding a new antenna chain at the small cell BS. A different conclusion may be obtained for the macrocell case, where adding a new antenna chain does not lead to a large increase in the total power consumption of the BS, since other components consume much more energy. Conclusions for the small cell BS case may also be different when considering spatial multiplexing instead of beamforming. Indeed, provided that the required degrees of freedom exists in the channel, the performance of spatial multiplexing in terms of capacity can follow a linear scaling law with the minimum number of transmit and receive antennas, and this capacity boost will enhance energy efficiency. Spatial multiplexing in ultra-dense small cell networks will be looked at in chapter 5.

When comparing the performance of the different idle modes in terms of energy efficiency, it can be seen that the lower the power consumption in the idle mode, the larger the energy efficiency of the network. This is because less energy is required to transmit the same amount of bits at the network level. When using the idle mode models provided by the GreenTouch project, idle modes 1 and 2, energy efficiency decreases with densification. This is because the increase in throughput provided by adding more cells is not large enough compared to the increase in their power consumption, mostly because idle cells following the GreenTouch project model still consume a non-negligible amount of energy. When

Table 3.2 Power consumption.

Small cell ISD ([m])	**Tx Power ([dBm/mW])**	**Consumed Power ([W])**								
		Full load			**idle mode 1 (*sm*=1)**			**idle mode 2 (*sm*=2)**		
		1 antenna	**2 antenna**	**4 antenna**	**1 antenna**	**2 antenna**	**4 antenna**	**1 antenna**	**2 antenna**	**4 antenna**
200	23.27/212.32	1.8923	2.5848	4.4560	0.2324	0.3105	0.4959	0.1881	0.2478	0.4073
150	20.52/112.72	1.3405	2.0316	3.9015	0.2191	0.2971	0.4825	0.1748	0.2345	0.3939
100	16.64/46.13	0.9793	1.6696	3.5386	0.2104	0.2884	0.4738	0.1661	0.2257	0.3852
75	13.90/24.55	0.8643	1.5544	3.4231	0.2076	0.2856	0.4710	0.1633	0.2230	0.3824
50	10.02/10.05	0.7853	1.4752	3.3437	0.2057	0.2837	0.4691	0.1614	0.2210	0.3804
35	6.61/4.58	0.7558	1.4456	3.3141	0.2050	0.2830	0.4683	0.1607	0.2203	0.3797
20	1.27/1.34	0.7383	1.4281	3.2965	0.2046	0.2826	0.4679	0.1603	0.2199	0.3793
10	-5.20/0.30	0.7326	1.4224	3.2908	0.2044	0.2824	0.4678	0.1601	0.2198	0.3792
5	-11.89/0.06	0.7314	1.4211	3.2895	0.2044	0.2824	0.4678	0.1601	0.2197	0.3791

considering the energy consumption of the futuristic idle mode 3, this trend starts changing. First, the energy efficiency increases with densification, and then starts decreasing when the number of deployed cells becomes large and many cells are empty. When considering the energy consumption of the new idle mode 4, idle cells do not consume anything, and the trend significantly changes. Energy efficiency always increases with densification, and it is done in a significant manner. This is because the increase in throughput provided by adding more cells comes now at no or very low energy cost since idle cells do not consume power from the energy grid.

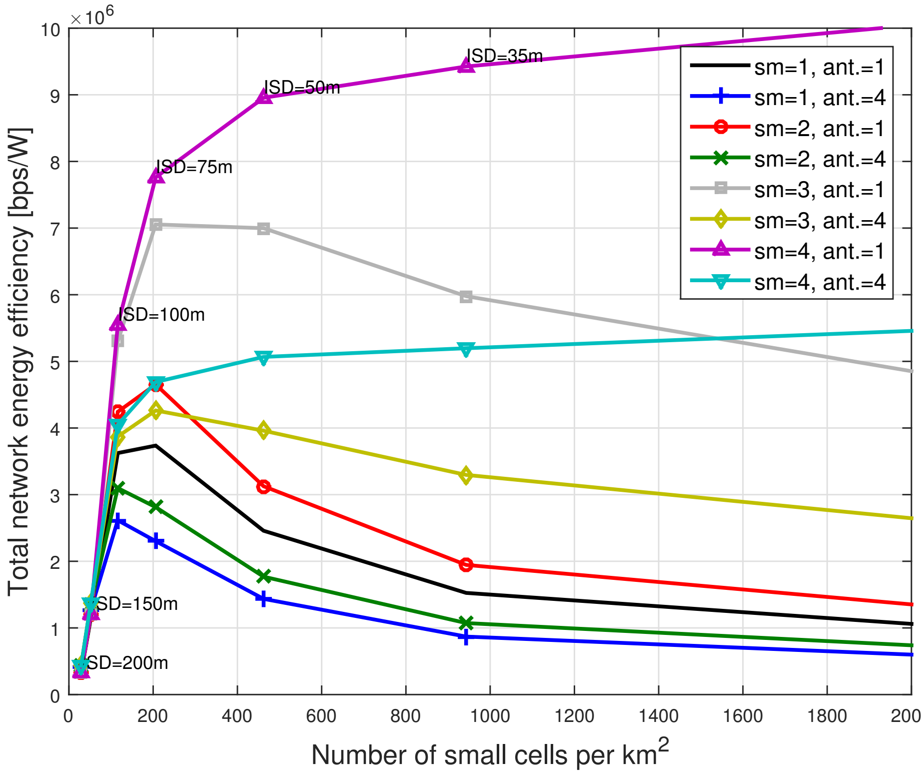

Fig. 3.7 Energy efficiency in bps per Watt for different network configurations with activated idle mode capability.

This last observation shows the need for the development of more advanced idle mode capabilities, where the power consumption of a small cell BS from the energy grid in idle mode is zero. This can be optimally realised by using energy harvesting approaches that are able to supply sufficient power to keep the small cell BS alive when it is in idle mode. For instance, assuming the use of idle mode 2, and 4 antennas at the small cell BS, the energy harvesting mechanism would need to provide the affordable amount of 0.4073 W per cell to make ultra-dense small cell networks highly energy efficient. In this area, researchers are looking at both thermoelectric as well as mechanical energy harvesting techniques. An example of the latter is the research in [102] and [103], based on vibration energy harvesting techniques for powering wireless sensors and small cell infrastructure. Moreover, an issue with all ambient environment energy sources, to varying degrees, is their intermittent nature. For instance, harvesting useable levels of solar and wind power depends on the time of the day, the season and the local weather conditions. For this reason, an efficient and cost-effective energy storage system is also key [104]. These are important areas of research, whose results are vital to deploy energy efficient and green telecommunications networks that have a minimal impact in the ecosystem.

3.4 Conclusion

In this chapter, it was discussed that the high density of BSs and the relative proximity of UEs to their serving BSs in ultra-dense small cell networks has implications on the multi-path channel fluctuations experienced by UEs as well as the network power consumption. Therefore, for the first time the performance of ultra-dense small cell networks has been studied in terms of both channel sensitive scheduling and multi-user diversity as well as the network energy efficiency. Firstly, it has been proved that in ultra-dense small cell networks, due to significant decrease in the number of UEs served per BS and the increase in the proximity of UEs and their serving BSs, the multi-path fading is dominated by LOS fading and hence the multi-user diversity is considerably reduced. This important remark indicates that considering the negligible gain ($\approx$ % 10) of the more complex channel-dependent proportional fair scheduling in ultra-dense small cell networks over the simpler and channel-independent round robin scheduling, it is highly recommended to adopt round robin scheduler in ultra-dense small cell networks to greatly simplify the radio resource management, and thus reduce the network complexity. Secondly, an extensive survey has been conducted for the first time to examine the impact of different idle modes from GreenTouch project on the energy efficiency of ultra-dense small cell networks. In addition to the idle mode models provided by the GreenTouch project, two new futuristic idle modes were also proposed and their impacts on network energy efficiency were investigated. The study has led to an important remark which states that the lower the power consumption in the idle mode, the more energy efficient the network would be and hence has articulated that developing advanced idle mode capabilities that have zero power consumption from the energy grid in the idle mode is critical for energy sustainable ultra-dense small cell networks. In this regard, it has been proposed to benefit from energy harvesting technologies that aim to reap energy from radio frequency signals as well as environmental energy sources, i.e., development of new interference management techniques that allow treating interference as a source of electromagnetic power to recharge the batteries of small cell BSs and to supply sufficient power to keep the small cell BSs alive when it is in idle mode in order to be able to immediately restart the transmission when required. Analysis of effectiveness of energy harvesting technologies on the energy efficiency of ultra-dense small cell networks is beyond the scope of this thesis and is left as part of future study.

Chapter 4

Performance Impact of LOS and NLOS Transmissions under Rician Fading

4.1 Introduction

Before 2015, the common understanding on small cell networks was that the density of BSs would not affect the per-BS coverage probability performance in interference-limited fully loaded wireless networks, and so the area spectral efficiency (ASE) would scale linearly with BS density. However, this conclusion was obtained with considerable simplifications on the propagation environment, which may not hold when evaluating ultra-dense small cell networks since they are fundamentally different from sparse macrocell ones. In ultra-dense small cell networks the distance between UEs and BSs is considerably reduced which in turn increases the probability of LOS communication which in turn brings a change in the channel characteristics, i.e., the channel may become LOS dominated with the subsequent loss of channel diversity. Unfortunately, most of the prior studies on ultra-dense small cell networks have only considered simplistic (single slope) path loss models that do not discriminate among LOS and NLOS transmissions and hence they are unable to capture these important channel properties. In this chapter, for the first time the performance of ultra-dense small cell networks is studied using distance-dependent models for both path loss and multi-path fading in order to more accurately capture the channel properties in ultra-dense small cell networks. Incorporating a multi slope piecewise path loss function with probabilistic NLOS and LOS transmission and assuming a distance dependent Rician multi-path fading model that exploits a variant Rician K factor based on the UE-BS distance, it is shown that as the density of small cell BSs increases, the area spectral efficiency will initially increase but as the small cell BS density exceeds a certain threshold, the SINR degrades and so the ASE may grow at a much slower pace or even decrease. This major remark proves that the small cell BS density has a key impact on network performance and further demonstrates that the impact of multi-path fading on the overall system performance is minor, and does not help to mitigate the performance loss caused by SINR degradation. From theoretical analysis point of view, it indicates that in ultra-dense small cell networks Rayleigh fading can be used to model the multi-path fading to ease the theoretical analysis. The main contributions of this chapter are as follows:

- For the first time, analytical results are derived for both the coverage probability and the area spectral efficiency of the network under Rician fading channel with variant Rician K factor using a general path loss model that considers both LOS and NLOS transmissions.

- Furthermore, integral-form expressions for the coverage coverage probability and the area spectral efficiency using a 3GPP path loss model with a *linear* LOS probability function are obtained. It is worth noting that using a linear LOS probability function allows to obtain more tractable results. It also helps to consider path loss models of further complexity which can be approximated by piecewise linear functions.

- Based on the theoretical analysis and simulation results, it is discovered that due to the dominance of path loss in ultra-dense small cell networks, the impact of the multi-path fading is negligible. This key finding indicates that when the density of small cell BSs exceeds a certain threshold, multi-path fading does not help to mitigate the user SINR degradation.

4.2 Prior Work

Stochastic geometry is a useful tool to analyse system performance in conventional cellular networks. In stochastic geometry, the BS locations in a conventional cellular network are modelled as a Poisson point process (PPP) on the plane and then using mathematical tools the aggregate coverage probability is derived in a simple closed form expression. Note that a general treatment of stochastic geometry can be found in [105]. Prior works on small cell networks [106, 105, 107] have exploited stochastic geometry to study the performance of small cell networks and have concluded that neither the number of small cell BSs nor the number of small cell BS tiers changes the coverage probability and that the area spectral efficiency will linearly increase with network densification in interference-limited fully-loaded wireless networks. However, this is a misleading conclusion, or a conclusion that does not apply to the full spectrum of small cell BS densities because they have used a simplistic path loss model that does not consider the probability of LOS communication and does not differentiate LOS and NLOS transmissions.

In this chapter, a more complete path loss model incorporating both LOS and NLOS transmissions to study their impact on the performance of ultra-dense small cell networks is proposed. However, it is important to remind that notions which are quite similar to LOS and NLOS transmissions have been previously explored in the building blockage study in [108] and the indoor communication network in [109]. In [108], the authors have proposed a microscopic performance analysis framework to model the random blockage effect of buildings, and analysed its impact on the performance of cellular networks. However, refinement and verification of the proposed model in [108] is necessary in order to consider reflections which are an important contributor to coverage in urban areas. In [109], the authors have presented an analytical study of indoor propagation through walls, and have shown that the throughput did not linearly scale with the density of small cell BSs. Note that different from [109], in this thesis, the focus is on outdoor dense small cell networks. Other relevant works to the work in this chapter are [110], [111], and [112]. In [110], the authors have assumed a multi-slope piece-wise path loss function. Specifically, denoting the distance between a BS and a UE by r in km, then the path loss associated with distance r has been formulated as

$$\zeta(r) = \begin{cases} \zeta_1(r), & \text{when } 0 \leq r \leq d_1 \\ \zeta_2(r), & \text{when } d_1 < r \leq d_2 \\ \vdots & \vdots \\ \zeta_N(r), & \text{when } r > d_{N-1} \end{cases}, \tag{4.1}$$

where the path loss function $\zeta(r)$ has been segmented into N pieces, with each piece and each segment break point have been denoted by $\zeta_n(r)$ and $d_n, n \in \{1, 2, \ldots, N-1\}$, respectively. In another study, Bai and Heath in [111], has considered the events of LOS or NLOS transmissions as probabilistic events for millimetre wave communications scenario. Specifically, the path loss associated with distance r has been formulated as

$$\zeta(r) = \begin{cases} \zeta^{\mathrm{L}}(r), & \text{with probability } \Pr^{\mathrm{L}}(r) \\ \zeta^{\mathrm{NL}}(r), & \text{with probability } \left(1 - \Pr^{\mathrm{L}}(r)\right) \end{cases}, \tag{4.2}$$

where $\zeta^{\mathrm{L}}(r)$, $\zeta^{\mathrm{NL}}(r)$ and $\Pr^{\mathrm{L}}(r)$ have been used to denote the path loss function for the case of LOS transmission, the path loss function for the case of NLOS transmission and the LOS probability function, respectively. To simplify their analysis, they have approximated the LOS probability function $\Pr^{\mathrm{L}}(r)$ by a moment matched equivalent step function in [111].The authors in [112] have also used the same path loss model as in (4.2) and considered the approximation of $\Pr^{\mathrm{L}}(r)$ as an exponentially decreasing function. The results in [112] are less tractable than those in [110] and [111]. This is due to the fact that the exponentially decreasing LOS probability function, although being more practical than the step function in [111], is still difficult to deal with in the theoretical analysis.

In this chapter, the works in [110] [111][112] are extended to a more general scenario to improve certain aspects of previous works. In [110], the multi-slope piece-wise path loss model in (4.1) does not fit well with the practical path loss model defined by the 3GPP, in which the path loss function is not a one-to-one mapping to the distance. In [111], the single-piece path loss model and the proposed step function are not compatible with the practical piece-wise path loss functions. In [112], the considered path loss model is very practical. However, the generality of the study and the tractability of the analysis need to be significantly improved. To overcome the challenges discussed in prior works, the path loss model presented in this chapter features piece-wise path loss functions with probabilistic LOS and NLOS transmissions and benefits from being applicable to different channel models that capture LOS and NLOS transmissions. Comparing the work in this chapter to some of the prior works, it can be claimed that in comparison to [112], the derivations in this chapter are more simple and tractable and there is no approximation such as the step function used in [111]. In comparison to the results in [110], it can be claimed that due to the consideration of probabilistic LOS events and a linear LOS probability function, the analysis in this chapter can more accurately characterize practical networks. Moreover, in terms of multi-path fading all prior works have considered Rayleigh fading for both LOS and NLOS components. For instance, while the work in [113] has used the piecewise path loss model, but the study has not been accurate because the fading in LOS transmissions is well known to be non-Rayleigh distributed. In this chapter, the multi-path fading is modelled as Rician fading with a variant distance dependent Rician K factor for both LOS and NLOS transmissions which is a more realistic multi-path fading model for dense small cell networks. To the author's best of knowledge, the analysis in this chapter is the first to combine a distance dependent Rician fading with a piecewise path loss function to investigate the performance of dense small cell networks.

4.3 System Model

In the following, the system model is discussed. Note that in this chapter, the focus is on downlink (DL) cellular networks.

BS Distribution: It is assumed that the small cell BSs form a Homogeneous Poisson point process(HPPP) Φ of intensity λ BSs/km^2.

User Distribution: UEs also form another stationary HPPP with an intensity of λ^{UE} UEs/km^2 which is independent from the small cell BSs distribution. Note that λ^{UE} is assumed to be adequately larger than λ so that each small cell BS has a minimum of one associated UE in its coverage. A typical UE that is located at the origin is assumed which is a common assumption in the stochastic geometry analysis.

Path Loss: The distance between the typical UE and an arbitrary BS is denoted by r in km. Furthermore, assuming practical LOS and NLOS transmissions, it is proposed to model the path loss with respect to distance r as (4.3).

$$\zeta(r)=\begin{cases}\zeta_1(r)=\begin{cases}\zeta_1^{\mathrm{L}}(r), & \text{with probability } \Pr_1^{\mathrm{L}}(r)\\ \zeta_1^{\mathrm{NL}}(r), & \text{with probability } \left(1-\Pr_1^{\mathrm{L}}(r)\right)\end{cases}, & \text{when } 0\le r\le d_1\\ \zeta_2(r)=\begin{cases}\zeta_2^{\mathrm{L}}(r), & \text{with probability } \Pr_2^{\mathrm{L}}(r)\\ \zeta_2^{\mathrm{NL}}(r), & \text{with probability } \left(1-\Pr_2^{\mathrm{L}}(r)\right)\end{cases}, & \text{when } d_1< r\le d_2\\ \vdots & \vdots\\ \zeta_N(r)=\begin{cases}\zeta_N^{\mathrm{L}}(r), & \text{with probability } \Pr_N^{\mathrm{L}}(r)\\ \zeta_N^{\mathrm{NL}}(r), & \text{with probability } \left(1-\Pr_N^{\mathrm{L}}(r)\right)\end{cases}, & \text{when } r> d_{N-1}\end{cases}. \tag{4.3}$$

As can be seen, the path loss function $\zeta(r)$ is divided into N pieces where each piece is represented by $\zeta_n(r)$. Moreover, $\zeta_n^{\mathrm{L}}(r)$, $\zeta_n^{\mathrm{NL}}(r)$ and $\Pr_n^{\mathrm{L}}(r)$ represent the n-th piece of path loss function for the LOS transmission, the NLOS transmission, and the LOS probability function, respectively. Moreover, $\zeta_n^{\mathrm{L}}(r)$ and $\zeta_n^{\mathrm{NL}}(r)$ in (4.3) are modelled as

$$\zeta_n(r)=\begin{cases}\zeta_n^{\mathrm{L}}(r)=A_n^{\mathrm{L}}r^{-\alpha_n^{\mathrm{L}}}, & \text{for LOS}\\ \zeta_n^{\mathrm{NL}}(r)=A_n^{\mathrm{NL}}r^{-\alpha_n^{\mathrm{NL}}}, & \text{for NLOS}\end{cases}, \tag{4.4}$$

where A_n^{L} and $A_n^{\mathrm{NL}}, n\in\{1,2,\ldots,N\}$ are referred to as reference path losses since they represent path losses at a reference distance of $r=1$ for the LOS and the NLOS cases in $\zeta_n(r)$, respectively. α_n^{L} and $\alpha_n^{\mathrm{NL}}, n\in\{1,2,\ldots,N\}$ also denote the path loss exponents for the LOS and the NLOS cases in $\zeta_n(r)$, respectively. Typical values of reference path losses and path loss exponents can be found in [69], [114]. Furthermore, $\left\{\zeta_n^{\mathrm{L}}(r)\right\}$ and $\left\{\zeta_n^{\mathrm{NL}}(r)\right\}$ are stacked into piece-wise functions as

$$\zeta^s(r)=\begin{cases}\zeta_1^s(r), & \text{when } 0\le r\le d_1\\ \zeta_2^s(r), & \text{when } d_1< r\le d_2\\ \vdots & \vdots\\ \zeta_N^s(r), & \text{when } r> d_{N-1}\end{cases}, \tag{4.5}$$

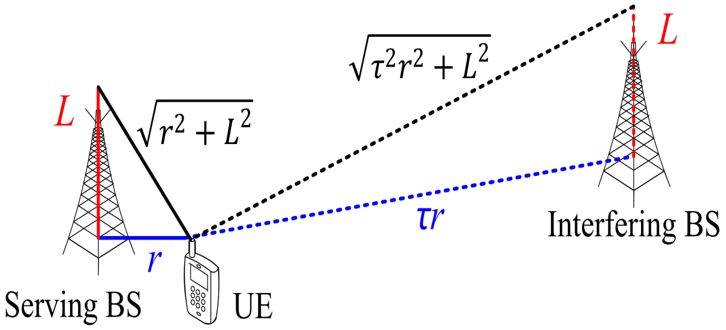

Fig. 4.1 Illustration of a dense small cell network with two small cell BSs.

where $s \in \{\mathrm{L}, \mathrm{NL}\}$, refers to LOS and NLOS transmissions. Note that in (4.3), $\mathrm{Pr}_n^{\mathrm{L}}(r), n \in \{1,2,\ldots,N\}$ denotes the n-th piece LOS probability function corresponding to a BS and UE that are separated by the distance r. Fig. 4.1 shows a schematic dense small cell network consisting of two small cell BSs where the distance between UE and its serving and interfering BSs are represented by r and τr, respectively, where $(1 < \tau < \infty)$ and L is the antenna height at the small cell BS. As one can see, as network densifies, the distance between UE and interfering BS is reduced implying the possibility of LOS communications for the interfering BS. As a result, unlike traditional cellular networks where the interfering signals are mostly NLOS, network densification results in transition of many interfering signals from NLOS to LOS. Therefore, as represented in (4.5) it is critical to divide the path loss into N pieces each with probabilistic LOS and NLOS to capture the impact of the distance between UE and BS on the LOS probability function and the path loss exponent.

User Association Strategy (UAS): The UE is associated with the BS which could be either LOS or NLOS that has the smallest path loss.

Antenna Radiation Pattern: It is assumed that each BS and the typical UE are equipped with an isotropic antenna.

Small Scale Fading: The multipath fading between an arbitrary BS and the typical UE is modelled as distance dependant Rician fading channel. As discussed in chapter 3, the Rician K factor is defined as the ratio of the power in the specular LOS component to the power in all NLOS components. For the LOS case, a distance dependant Rician K factor in *dB* scale as shown in (4.6) is used and for the NLOS case the Rician K factor is set to zero.

$$K(r) = 13 - 0.03r \tag{4.6}$$

where r denotes the distance between the BS and UE in meter. Note that $K(r)$ is denoted by K hereafter for notational simplicity, but it is critical not to interpret K as a constant value.

4.4 Analysis Based on the Proposed Path Loss Model

The coverage probability represents the probability that the UE's SINR is above a predesignated threshold γ:

$$p^{\text{cov}}(\lambda,\gamma) = \Pr[\text{SINR} > \gamma], \tag{4.7}$$

where the SINR is computed by

$$\text{SINR} = \frac{P\zeta(r)h}{I_r + N_0}, \tag{4.8}$$

where h is the Rician distributed channel gain and P and N_0 refer to the transmission power of each BS and the additive white Gaussian noise (AWGN) power at the typical UE, respectively. The aggregated interference from all non-serving BSs is denoted by I_r and is defined as

$$I_r = \sum_{i:\, b_i \in \Phi \setminus b_o} P\beta_i g_i, \tag{4.9}$$

where b_o denotes to the serving BS, and b_i, β_i and g_i refer to the i-th interfering BS, the path loss associated with b_i and the Rician fading channel gain associated with b_i, respectively.

For a specific λ, the ASE in bps/Hz/km^2 can be expressed as

$$A^{\text{ASE}}(\lambda,\gamma_0) = \lambda \int_{\gamma_0}^{\infty} \log_2(1+\gamma) f_\Gamma(\lambda,\gamma)\, d\gamma, \tag{4.10}$$

where γ_0 denotes the minimum working SINR for the considered SCN, and $f_\Gamma(\lambda,\gamma)$ represents the PDF of SINR for a specific value of λ observed at the typical UE.

The PDF of SINR is then computed as

$$f_\Gamma(\lambda,\gamma) = \frac{\partial\left(1 - p^{\text{cov}}(\lambda,\gamma)\right)}{\partial\gamma}. \tag{4.11}$$

In the following, Theorem 1 is presented which is used to obtain the $p^{\text{cov}}(\lambda,\gamma)$ based on the proposed path loss model in (4.3). Note that for tractability of analysis, an interference limited scenario where $I_r \gg N_0$ is considered.

Theorem 1. *Considering the path loss model in (4.3), $p^{cov}(\lambda,\gamma)$ is computed as*

$$p^{cov}(\lambda,\gamma) = \sum_{n=1}^{N}\left(T_n^L + T_n^{NL}\right), \tag{4.12}$$

where $T_n^L = \int_{d_{n-1}}^{d_n} Pr\left[\frac{P\zeta_n^L(r)h}{I_r} > \gamma\right] f_{R,n}^L(r)\,dr$, $T_n^{NL} = \int_{d_{n-1}}^{d_n} Pr\left[\frac{P\zeta_n^{NL}(r)h}{I_r} > \gamma\right] f_{R,n}^{NL}(r)\,dr$, and d_0 and d_N are equal to 0 and ∞. $f_{R,n}^L(r)$ and $f_{R,n}^{NL}(r)$ are defined by

$$\begin{aligned} f_{R,n}^{L}(r) &= \exp\left(-\int_0^{r_1}\left(1-Pr^L(u)\right)2\pi u\lambda du\right)\times\exp\left(-\int_0^{r}Pr^L(u)\,2\pi u\lambda du\right) \\ &\quad \times Pr_n^L(r)\times 2\pi r\lambda, \quad (d_{n-1}<r\le d_n), \end{aligned} \tag{4.13}$$

and

$$\begin{aligned} f_{R,n}^{NL}(r) &= \exp\left(-\int_0^{r_2}Pr^L(u)\,2\pi u\lambda du\right)\times\exp\left(-\int_0^{r}\left(1-Pr^L(u)\right)2\pi u\lambda du\right) \\ &\quad \times\left(1-Pr_n^L(r)\right)\times 2\pi r\lambda, \quad (d_{n-1}<r\le d_n), \end{aligned} \tag{4.14}$$

noteworthy that r_1 *and* r_2 *can be determined as*

$\underset{r_1}{arg}\left\{\zeta^{NL}(r_1)=\zeta_n^L(r)\right\}$ *and* $\underset{r_2}{arg}\left\{\zeta^{L}(r_2)=\zeta_n^{NL}(r)\right\}$*, respectively.*

Furthermore, $Pr\left[\frac{P\zeta_n^L(r)h}{I_r}>\gamma\right]$ *and* $Pr\left[\frac{P\zeta_n^{NL}(r)h}{I_r}>\gamma\right]$ *are respectively computed by*

$$\Pr[\frac{P\zeta_n^L(r)h}{I_r}>\gamma]=\sum_{k=0}^{\infty}\sum_{m=0}^{k}J(m,k)\;\gamma^{k-m}(-1)^{k-m}\frac{\partial^{k-m}\mathscr{L}_{I_r}(\frac{\gamma}{P\zeta_n^L(r)})}{\partial\gamma^{k-m}} \tag{4.15}$$

and

$$\Pr[\frac{P\zeta_n^{NL}(r)h}{I_r}>\gamma]=\sum_{k=0}^{\infty}\sum_{m=0}^{k}J(m,k)\;\gamma^{k-m}(-1)^{k-m}\frac{\partial^{k-m}\mathscr{L}_{I_r}(\frac{\gamma}{P\zeta_n^{NL}(r)})}{\partial\gamma^{k-m}} \tag{4.16}$$

where $\mathscr{L}_{I_r}(s)$ *is the Laplace transform of RV* I_r *evaluated at s.*

See Appendix B-1.

In Theorem 1, for a certain r, $\Pr\left[\frac{P_t\zeta_n^L(r)h}{I_r}>\gamma\right]$ in (4.15) and $\Pr\left[\frac{P_t\zeta_n^{NL}(r)h}{I_r}>\gamma\right]$ in (4.16) compute the coverage probability for LoS signal transmission and that for NLoS transmission, respectively. The rational behind such expressions is that the h follows a Rician distribution, whose CDF is $-\sum_{k=0}^{\infty}\sum_{m=0}^{k}J(m,k)\;h^{k-m}e^{-h}+1$.

4.5 Study of a 3GPP Special Case

As a special case for Theorem 1, the following path loss function, $\zeta(r)$, is considered which is adopted by the 3rd Generation Partnership Project (3GPP) [69]. This path loss function is compatible with ultra-dense small cell networks, because both the exponential path loss function in [69] and the LOS probability function in [114] are only valid for small cell BSs. Another key reason to adopt a 3GPP path loss model is that 3GPP plays a major role in taking the entire industry forward and the channel models discussed in the 3GPP standards have been agreed upon by all of the major telecommunication companies in the world. Therefore, the fact that the 3GPP path loss model can be considered as a special case of the proposed path loss model in this chapter validates the practicality of the proposed model.

$$\zeta(r) = \begin{cases} A^{\mathrm{L}} r^{-\alpha^{\mathrm{L}}}, & \text{with probability } \mathrm{Pr}^{\mathrm{L}}(r) \\ A^{\mathrm{NL}} r^{-\alpha^{\mathrm{NL}}}, & \text{with probability } \left(1 - \mathrm{Pr}^{\mathrm{L}}(r)\right) \end{cases}, \tag{4.17}$$

which for sake of simplicity and without any loss of generality uses a linear LOS probability function [114] of $\mathrm{Pr}^{\mathrm{L}}(r)$ defined as

$$\mathrm{Pr}^{\mathrm{L}}(r) = \begin{cases} 1 - \frac{r}{d_1}, & 0 < r \leq d_1 \\ 0, & r > d_1 \end{cases}, \tag{4.18}$$

where steepness of $\mathrm{Pr}^{\mathrm{L}}(r)$ is defined by the parameter d_1. It can be commented that the 3GPP special case assumes a 2 piece path loss model and hence the upper bound N in (4.12) is 2. According to Theorem 1 and considering the mentioned 3GPP case, $p^{\mathrm{cov}}(\lambda,\gamma)$ can be computed as $p^{\mathrm{cov}}(\lambda,\gamma) = \sum\limits_{n=1}^{2} \left(T_n^{\mathrm{L}} + T_n^{\mathrm{NL}}\right)$ where $\zeta_1^{\mathrm{L}}(r) = \zeta_2^{\mathrm{L}}(r) = A^{\mathrm{L}} r^{-\alpha^{\mathrm{L}}}$, $\zeta_1^{\mathrm{NL}}(r) = \zeta_2^{\mathrm{NL}}(r) = A^{\mathrm{NL}} r^{-\alpha^{\mathrm{NL}}}$, $\mathrm{Pr}_1^{\mathrm{L}}(r) = 1 - \frac{r}{d_1}$, and $\mathrm{Pr}_2^{\mathrm{L}}(r) = 0$. Note that studying the linear LOS probability function not only allows obtaining more tractable results, but also helps to deal with more complicated path loss models in practice, as they can be approximated by piecewise linear functions. In the following, T_1^{L}, T_1^{NL}, T_2^{L}, and T_2^{NL} are presented, respectively.

4.5.1 The Computation of T_1^{L}

From Theorem 1, T_1^{L} is computed as

$$\begin{aligned} T_1^{\mathrm{L}} &= \int_0^{d_1} \sum_{k=0}^{\infty} \sum_{m=0}^{k} J(m,k)\, \gamma^{k-m} (-1)^{k-m} \frac{\partial^{k-m} \mathscr{L}_{I_r}\left(\frac{\gamma}{P\zeta_n^{L}(r)}\right)}{\partial \gamma^{k-m}} f_{R,1}^{\mathrm{L}}(r)\, dr \\ &\overset{(a)}{=} \int_0^{d_1} \sum_{k=0}^{\infty} \sum_{m=0}^{k} J(m,k)\, \gamma^{k-m} (-1)^{k-m} \frac{\partial^{k-m} \mathscr{L}_{I_r}\left(\frac{\gamma r^{\alpha^{\mathrm{L}}}}{PA^{\mathrm{L}}}\right)}{\partial \gamma^{k-m}} f_{R,1}^{\mathrm{L}}(r)\, dr, \end{aligned} \tag{4.19}$$

where $\zeta_1^{\mathrm{L}}(r) = A^{\mathrm{L}} r^{-\alpha^{\mathrm{L}}}$ from (4.17) is plugged into the step (a) of (4.19) and $\mathscr{L}_{I_r}(s)$ represents the Laplace transform of RV I_r evaluated at s.

In (4.19), according to Theorem 1 and (4.18), $f_{R,1}^{\mathrm{L}}(r)$ is computed as

$$\begin{aligned} f_{R,1}^{\mathrm{L}}(r) &= \exp\left(-\int_0^{r_1} \lambda \frac{u}{d_1} 2\pi u du\right) \exp\left(-\int_0^{r} \lambda \left(1-\frac{u}{d_1}\right) 2\pi u du\right) \left(1-\frac{r}{d_1}\right) 2\pi r\lambda \\ &= \exp\left(-\pi\lambda r^2 + 2\pi\lambda \left(\frac{r^3}{3d_1} - \frac{r_1^3}{3d_1}\right)\right) \left(1-\frac{r}{d_1}\right) 2\pi r\lambda, \quad (0 < r \leq d_1), \quad (4.20) \end{aligned}$$

where $r_1 = \left(\frac{A^{\mathrm{NL}}}{A^{\mathrm{L}}}\right)^{\frac{1}{\alpha^{\mathrm{NL}}}} r^{\frac{\alpha^{\mathrm{L}}}{\alpha^{\mathrm{NL}}}}$.

Moreover, in order to compute $\mathscr{L}_{I_r}\left(\frac{\gamma r^{\alpha^{\mathrm{L}}}}{PA^{\mathrm{L}}}\right)$ in (4.19) for the range of $0 < r \leq d_1$, Lemma 1 is proposed.

Lemma 1. *$\mathscr{L}_{I_r}\left(\frac{\gamma r^{\alpha^{\mathrm{L}}}}{PA^{\mathrm{L}}}\right)$ in the range of $0 < r \le d_1$ can be computed by*

$$
\begin{aligned}
&\mathscr{L}_{I_r}\left(\frac{\gamma r^{\alpha^{\mathrm{L}}}}{PA^{\mathrm{L}}}\right) = \\
&\exp\left(-2\pi\lambda\,\left(\rho_1\left(\alpha^L, 1, (1-K)\left(\gamma r^{\alpha^{\mathrm{L}}}\right)^{-1}, d_1\right) - \rho_1\left(\alpha^L, 1, (1-K)\left(\gamma r^{\alpha^{\mathrm{L}}}\right)^{-1}, r\right)\right)\right) \\
&\times\ \exp\Bigg(-2\pi\lambda\,\Bigg(\rho_1\left(\alpha^L, \alpha^L+1, (1-K)\left(\gamma r^{\alpha^{\mathrm{L}}}\right)^{-1}, d_1\right) \\
&-\ \rho_1\left(\alpha^L, \alpha^L+1, (1-K)\left(\gamma r^{\alpha^{\mathrm{L}}}\right)^{-1}, r\right)\Bigg)\Bigg) \\
&\times\ \exp\Bigg(\frac{2\pi\lambda}{d_0}\left(\gamma r^{\alpha^{\mathrm{L}}}\right)^{-1}\left(1-K-e^{-K}\right)\Bigg(\rho_1\left(\alpha^L, 2, (1-K)\left(\gamma r^{\alpha^{\mathrm{L}}}\right)^{-1}, d_1\right) \\
&-\ \rho_1\left(\alpha^L, 2, (1-K)\left(\gamma r^{\alpha^{\mathrm{L}}}\right)^{-1}, r\right)\Bigg)\Bigg) \\
&\times\ \exp\Bigg(\frac{2\pi\lambda}{d_0}\left(\gamma r^{\alpha^{\mathrm{L}}}\right)^{-1}\left(1-K-e^{-K}\right)\Bigg(\rho_1\left(\alpha^L, \alpha^L+2, (1-K)\left(\gamma r^{\alpha^{\mathrm{L}}}\right)^{-1}, d_1\right) \\
&-\ \rho_1\left(\alpha^L, \alpha^L+2, (1-K)\left(\gamma r^{\alpha^{\mathrm{L}}}\right)^{-1}, r_1\right)\Bigg)\Bigg) \\
&\times\ \exp\Bigg(\frac{-2\pi\lambda}{d_0}\Bigg(\rho_1\left(\alpha^{NL}, 2, (1-K)\left(\frac{\gamma A^{\mathrm{NL}}}{A^{\mathrm{L}}} r^{\alpha^{\mathrm{L}}}\right)^{-1}, d_1\right) \\
&-\ \rho_1\left(\alpha^{NL}, 2, (1-K)\left(\frac{\gamma A^{\mathrm{NL}}}{A^{\mathrm{L}}} r^{\alpha^{\mathrm{L}}}\right)^{-1}, r_1\right)\Bigg)\Bigg) \\
&\times\ \exp\Bigg(\frac{-2\pi\lambda}{d_0}\left(\frac{\gamma A^{\mathrm{NL}}}{A^{\mathrm{L}}} r^{\alpha^{\mathrm{L}}}\right)^{-1}\left(1-K-e^{-K}\right)\Bigg(\rho_1\left(\alpha^{NL}, \alpha^{NL}+2, (1-K)\left(\frac{\gamma A^{\mathrm{NL}}}{A^{\mathrm{L}}} r^{\alpha^{\mathrm{L}}}\right)^{-1}, d_1\right) \\
&-\ \rho_1\left(\alpha^{NL}, \alpha^{NL}+2, (1-K)\left(\frac{\gamma A^{\mathrm{NL}}}{A^{\mathrm{L}}} r^{\alpha^{\mathrm{L}}}\right)^{-1}, r_1\right)\Bigg)\Bigg) \\
&\times\ \exp\left(-2\pi\lambda\rho_2\left(\alpha^{NL}, 1, (1-K)\left(\frac{\gamma A^{\mathrm{NL}}}{A^{\mathrm{L}}} r^{\alpha^{\mathrm{L}}}\right)^{-1}, d_1\right)\right) \\
&\times\ \exp\Bigg(-2\pi\lambda\left(\frac{\gamma A^{\mathrm{NL}}}{A^{\mathrm{L}}} r^{\alpha^{\mathrm{L}}}\right)^{-1}\left(1-K-e^{-K}\right) \\
&\rho_2\left(\alpha^{NL}, \alpha^{NL}+1, (1-K)\left(\frac{\gamma A^{\mathrm{NL}}}{A^{\mathrm{L}}} r^{\alpha^{\mathrm{L}}}\right)^{-1}, d_1\right)\Bigg), \qquad (0 < r \le d_1)
\end{aligned}
\tag{4.21}
$$

where

$$\rho_1(\alpha,\beta,t,d)=\left[\frac{d^{(\beta+1)}}{\beta+1}\right]{}_2F_1\left[1,\frac{\beta+1}{\alpha};1+\frac{\beta+1}{\alpha};-td^{\alpha}\right], \tag{4.22}$$

and

$$\rho_2(\alpha,\beta,t,d)=\left[\frac{d^{-(\alpha-\beta-1)}}{t(\alpha-\beta-1)}\right]{}_2F_1\left[1,1-\frac{\beta+1}{\alpha};2-\frac{\beta+1}{\alpha};-\frac{1}{td^{\alpha}}\right],(\alpha>\beta+1), \tag{4.23}$$

where ${}_2F_1[\cdot,\cdot;\cdot;\cdot]$ *is the hyper-geometric function [115].*

See Appendix B-2.

It is important to note that the Laplace term computed by Lemma 1, gives the probability that the first-piece LOS signal power exceeds the aggregate interference power by a factor of at least γ.

Overall, T_1^{L} is evaluated as

$$T_1^{\mathrm{L}}=\int_0^{d_1}\sum_{k=0}^{\infty}\sum_{m=0}^{k}J(m,k)\,\gamma^{k-m}(-1)^{k-m}\frac{\partial^{k-m}\mathscr{L}_{I_r}\left(\frac{\gamma r^{\alpha^{\mathrm{L}}}}{PA^{\mathrm{L}}}\right)}{\partial\gamma^{k-m}}f_{R,1}^{\mathrm{L}}(r)\,dr, \tag{4.24}$$

where $f_{R,1}^{\mathrm{L}}(r)$ and $\mathscr{L}_{I_r}\left(\frac{\gamma r^{\alpha^{\mathrm{L}}}}{PA^{\mathrm{L}}}\right)$ are given by (4.20) and (4.21), respectively.

4.5.2 The Computation of T_1^{NL}

From Theorem 1, T_1^{NL} is computed as

$$\begin{aligned}T_1^{\mathrm{NL}}&=\int_0^{d_1}\sum_{k=0}^{\infty}\sum_{m=0}^{k}J(m,k)\,\gamma^{k-m}(-1)^{k-m}\frac{\partial^{k-m}\mathscr{L}_{I_r}\left(\frac{\gamma}{P\zeta_n^{NL}(r)}\right)}{\partial\gamma^{k-m}}f_{R,1}^{\mathrm{NL}}(r)\,dr\\&\overset{(a)}{=}\int_0^{d_1}\sum_{k=0}^{\infty}\sum_{m=0}^{k}J(m,k)\,\gamma^{k-m}(-1)^{k-m}\frac{\partial^{k-m}\mathscr{L}_{I_r}\left(\frac{\gamma r^{\alpha^{\mathrm{NL}}}}{PA^{\mathrm{NL}}}\right)}{\partial\gamma^{k-m}}f_{R,1}^{\mathrm{NL}}(r)\,dr,\end{aligned} \tag{4.25}$$

where $\zeta_1^{\mathrm{NL}}(r)=A^{\mathrm{NL}}r^{-\alpha^{\mathrm{NL}}}$ from (4.17) is plugged into the step (a) of (4.25).

In (4.25), according to Theorem 1 and (4.18), $f_{R,1}^{\mathrm{NL}}(r)$ can be written as

$$\begin{aligned}f_{R,1}^{\mathrm{NL}}(r)&=\exp\left(-\int_0^{r_2}\lambda\mathrm{Pr}^{\mathrm{L}}(u)\,2\pi u du\right)\\&\quad\times\exp\left(-\int_0^{r}\lambda\left(1-\mathrm{Pr}^{\mathrm{L}}(u)\right)2\pi u du\right)\left(\frac{r}{d_1}\right)2\pi r\lambda,\quad(0<r\le d_1),\end{aligned} \tag{4.26}$$

where $r_2 = \left(\frac{A^{\mathrm{L}}}{A^{\mathrm{NL}}}\right)^{\frac{1}{\alpha^{\mathrm{L}}}} r^{\frac{\alpha^{\mathrm{NL}}}{\alpha^{\mathrm{L}}}}$. In the following, the cases of $0 < r_2 \le d_1$ and $r_2 > d_1$ are discussed separately.

If $0 < r_2 \le d_1$, i.e., $0 < r \le y_1 = d_1^{\frac{\alpha^{\mathrm{L}}}{\alpha^{\mathrm{NL}}}} \left(\frac{A^{\mathrm{NL}}}{A^{\mathrm{L}}}\right)^{\frac{1}{\alpha^{\mathrm{NL}}}}$, the $f_{R,1}^{\mathrm{NL}}(r)$ is calculated as

$$\begin{aligned} f_{R,1}^{\mathrm{NL}}(r) &= \exp\left(-\int_0^{r_2} \lambda \left(1-\frac{u}{d_1}\right) 2\pi u du\right) \exp\left(-\int_0^{r} \lambda \frac{u}{d_1} 2\pi u du\right) \left(\frac{r}{d_1}\right) 2\pi r \lambda \\ &= \exp\left(-\pi\lambda r_2^2 + 2\pi\lambda \left(\frac{r_2^3}{3d_1} - \frac{r^3}{3d_1}\right)\right) \left(\frac{r}{d_1}\right) 2\pi r\lambda,\ (0 < r \le y_1). \end{aligned} \tag{4.27}$$

Otherwise, if $r_2 > d_1$, i.e., $y_1 < r \le d_1$, $f_{R,1}^{\mathrm{NL}}(r)$ is calculated as

$$\begin{aligned} f_{R,1}^{\mathrm{NL}}(r) &= \exp\left(-\int_0^{d_1} \lambda \left(1-\frac{u}{d_1}\right) 2\pi u du\right) \exp\left(-\int_0^{r} \lambda \frac{u}{d_1} 2\pi u du\right) \left(\frac{r}{d_1}\right) 2\pi r \lambda \\ &= \exp\left(-\frac{\pi\lambda d_1^2}{3} - \frac{2\pi\lambda r^3}{3d_1}\right) \left(\frac{r}{d_1}\right) 2\pi r\lambda, \quad (y_1 < r \le d_1). \end{aligned} \tag{4.28}$$

In the following, Lemma 2 is proposed to compute $\mathscr{L}_{I_r}\left(\frac{\gamma r^{\alpha^{\mathrm{NL}}}}{PA^{\mathrm{NL}}}\right)$ in (4.25) for the range of $0 < r \le d_1$. Note that, the computation of $\mathscr{L}_{I_r}\left(\frac{\gamma r^{\alpha^{\mathrm{NL}}}}{PA^{\mathrm{NL}}}\right)$ will also be performed in the two ranges of $0 < r_2 \le d_1$ and $r_2 > d_1$ separately.

Lemma 2. $\mathscr{L}_{I_r}\left(\frac{\gamma r^{\alpha^{\mathrm{NL}}}}{PA^{\mathrm{NL}}}\right)$ *in the range of* $0 < r \le d_1$ *is considered separately for two different cases, i.e.,* $0 < r \le y_1$ *and* $y_1 < r \le d_1$.

$$
\begin{aligned}
&\mathscr{L}_{I_r}\left(\frac{\gamma r^{\alpha^{\mathrm{NL}}}}{PA^{\mathrm{NL}}}\right)= \\
&\exp\Bigg(-2\pi\lambda\,\Bigg(\rho_1\Bigg(\alpha^{L},1,(1-K)\left(\frac{\gamma A^{\mathrm{L}}}{A^{\mathrm{NL}}}r^{\alpha^{\mathrm{NL}}}\right)^{-1},d_1\Bigg) \\
&-\,\rho_1\Bigg(\alpha^{L},1,(1-K)\left(\frac{\gamma A^{\mathrm{L}}}{A^{\mathrm{NL}}}r^{\alpha^{\mathrm{NL}}}\right)^{-1},r_2\Bigg)\Bigg)\Bigg) \\
&\times\,\exp\Bigg(-2\pi\lambda\,\Bigg(\rho_1\Bigg(\alpha^{L},\alpha^{L}+1,(1-K)\left(\frac{\gamma A^{\mathrm{L}}}{A^{\mathrm{NL}}}r^{\alpha^{\mathrm{NL}}}\right)^{-1},d_1\Bigg) \\
&-\,\rho_1\Bigg(\alpha^{L},\alpha^{L}+1,(1-K)\left(\frac{\gamma A^{\mathrm{L}}}{A^{\mathrm{NL}}}r^{\alpha^{\mathrm{NL}}}\right)^{-1},r_2\Bigg)\Bigg)\Bigg) \\
&\times\,\exp\Bigg(\frac{2\pi\lambda}{d_0}\left(\frac{\gamma A^{\mathrm{L}}}{A^{\mathrm{NL}}}r^{\alpha^{\mathrm{NL}}}\right)^{-1}\left(1-K-e^{-K}\right)\Bigg(\rho_1\Bigg(\alpha^{L},2,(1-K)\left(\frac{\gamma A^{\mathrm{L}}}{A^{\mathrm{NL}}}r^{\alpha^{\mathrm{NL}}}\right)^{-1},d_1\Bigg) \\
&-\,\rho_1\Bigg(\alpha^{L},2,(1-K)\left(\frac{\gamma A^{\mathrm{L}}}{A^{\mathrm{NL}}}r^{\alpha^{\mathrm{NL}}}\right)^{-1},r_2\Bigg)\Bigg)\Bigg) \\
&\times\,\exp\Bigg(\frac{2\pi\lambda}{d_0}\left(\frac{\gamma A^{\mathrm{L}}}{A^{\mathrm{NL}}}r^{\alpha^{\mathrm{NL}}}\right)^{-1}\left(1-K-e^{-K}\right)\Bigg(\rho_1\Bigg(\alpha^{L},\alpha^{L}+2,(1-K)\left(\frac{\gamma A^{\mathrm{L}}}{A^{\mathrm{NL}}}r^{\alpha^{\mathrm{NL}}}\right)^{-1},d_1\Bigg) \\
&-\,\rho_1\Bigg(\alpha^{L},\alpha^{L}+2,(1-K)\left(\frac{\gamma A^{\mathrm{L}}}{A^{\mathrm{NL}}}r^{\alpha^{\mathrm{NL}}}\right)^{-1},r_2\Bigg)\Bigg)\Bigg) \\
&\times\exp\Bigg(\frac{-2\pi\lambda}{d_0}\bigg(\rho_1\bigg(\alpha^{NL},2,(1-K)\left(\gamma r^{\alpha^{\mathrm{NL}}}\right)^{-1},d_1\bigg) \\
&-\,\rho_1\bigg(\alpha^{NL},2,(1-K)\left(\gamma r^{\alpha^{\mathrm{NL}}}\right)^{-1},r\bigg)\bigg)\Bigg) \\
&\times\,\exp\Bigg(\frac{-2\pi\lambda}{d_0}\left(\gamma r^{\alpha^{\mathrm{NL}}}\right)^{-1}\left(1-K-e^{-K}\right)\bigg(\rho_1\bigg(\alpha^{NL},\alpha^{NL}+2,(1-K)\left(\gamma r^{\alpha^{\mathrm{NL}}}\right)^{-1},d_1\bigg) \\
&-\,\rho_1\bigg(\alpha^{NL},\alpha^{NL}+2,(1-K)\left(\gamma r^{\alpha^{\mathrm{NL}}}\right)^{-1},r\bigg)\bigg)\Bigg) \\
&\times\,\exp\bigg(-2\pi\lambda\,\rho_2\bigg(\alpha^{NL},1,(1-K)\left(\gamma r^{\alpha^{\mathrm{NL}}}\right)^{-1},d_1\bigg)\bigg) \\
&\times\,\exp\bigg(-2\pi\lambda\left(\gamma r^{\alpha^{\mathrm{NL}}}\right)^{-1}\left(1-K-e^{-K}\right) \\
&\rho_2\bigg(\alpha^{NL},\alpha^{NL}+1,(1-K)\left(\gamma r^{\alpha^{\mathrm{NL}}}\right)^{-1},d_1\bigg)\bigg)\qquad\left(0<r\le y_1\right),
\end{aligned}
\tag{4.29}
$$

and

$$
\begin{aligned}
&\mathscr{L}_{I_r}\left(\frac{\gamma r^{\alpha^{\mathrm{NL}}}}{PA^{\mathrm{NL}}}\right) = \\
&\exp\left(\frac{-2\pi\lambda}{d_0}\left(\rho_1\left(\alpha^{NL},2,(1-K)\left(\gamma r^{\alpha^{\mathrm{NL}}}\right)^{-1},d_1\right)-\rho_1\left(\alpha^{NL},2,(1-K)\left(\gamma r^{\alpha^{\mathrm{NL}}}\right)^{-1},r\right)\right)\right) \\
&\times\ \exp\Bigg(\frac{-2\pi\lambda}{d_0}\left(\gamma r^{\alpha^{\mathrm{NL}}}\right)^{-1}\left(1-K-e^{-K}\right)\Bigg(\rho_1\left(\alpha^{NL},\alpha^{NL}+2,(1-K)\left(\gamma r^{\alpha^{\mathrm{NL}}}\right)^{-1},d_1\right) \\
&-\ \rho_1\left(\alpha^{NL},\alpha^{NL}+2,(1-K)\left(\gamma r^{\alpha^{\mathrm{NL}}}\right)^{-1},r\right)\Bigg)\Bigg) \\
&\times\ \exp\Bigg(-2\pi\lambda\ \rho_2\left(\alpha^{NL},1,(1-K)\left(\gamma r^{\alpha^{\mathrm{NL}}}\right)^{-1},d_1\right)\Bigg) \\
&\times\ \exp\Bigg(-2\pi\lambda\left(\gamma r^{\alpha^{\mathrm{NL}}}\right)^{-1}\left(1-K-e^{-K}\right) \\
&\rho_2\left(\alpha^{NL},\alpha^{NL}+1,(1-K)\left(\gamma r^{\alpha^{\mathrm{NL}}}\right)^{-1},d_1\right)\Bigg) \qquad (y_1<r\leq d_1),
\end{aligned}
\tag{4.30}
$$

where $\rho_1(\alpha,\beta,t,d)$ *and* $\rho_2(\alpha,\beta,t,d)$ *are defined in (4.22) and (4.23), respectively.*

See Appendix B-3.

It is important to note that the Laplace term computed by Lemma 2, gives the probability that the first-piece NLOS signal power exceeds the aggregate interference power by a factor of at least γ.

Overall, T_1^{NL} is evaluated as

$$
\begin{aligned}
T_1^{\mathrm{NL}} \;=\;& \int_0^{y_1}\sum_{k=0}^{\infty}\sum_{m=0}^{k} J(m,k)\,\gamma^{k-m}(-1)^{k-m}\frac{\partial^{k-m}\mathscr{L}_{I_r}\left(\frac{\gamma r^{\alpha^{\mathrm{NL}}}}{PA^{\mathrm{NL}}}\right)}{\partial\gamma^{k-m}} f_{R,1}^{\mathrm{NL}}(r)\,|0<r\leq y_1]dr \\
&+\int_{y_1}^{d_1}\sum_{k=0}^{\infty}\sum_{m=0}^{k} J(m,k)\,\gamma^{k-m}(-1)^{k-m}\frac{\partial^{k-m}\mathscr{L}_{I_r}\left(\frac{\gamma r^{\alpha^{\mathrm{NL}}}}{PA^{\mathrm{NL}}}\right)}{\partial\gamma^{k-m}} f_{R,1}^{\mathrm{NL}}(r)\,|y_1<r\leq d_1]dr,
\end{aligned}
\tag{4.31}
$$

where based on the distance r, $f_{R,1}^{\mathrm{NL}}(r)$ is computed using (4.27) and (4.28), and $\mathscr{L}_{I_r}\left(\frac{\gamma r^{\alpha^{\mathrm{NL}}}}{PA^{\mathrm{NL}}}\right)$ is given by (4.29) and (4.30), respectively.

4.5.3 The Computation of T_2^{L}

From Theorem 1, T_2^{L} is computed as

$$T_2^{\mathrm{L}} = \int_{d_1}^{\infty} \sum_{k=0}^{\infty} \sum_{m=0}^{k} J(m,k)\, \gamma^{k-m} (-1)^{k-m} \frac{\partial^{k-m} \mathscr{L}_{I_r}\left(\frac{\gamma}{P\zeta_n^{L}(r)}\right)}{\partial \gamma^{k-m}} f_{R,2}^{\mathrm{L}}(r)\, dr. \tag{4.32}$$

It is important to note that the Laplace term in (4.32), gives the probability that the second-piece LOS signal power exceeds the aggregate interference power by a factor of at least γ. According to Theorem 1 and (4.18), $f_{R,2}^{\mathrm{L}}(r)$ can be calculated by

$$\begin{aligned} f_{R,2}^{\mathrm{L}}(r) &= \exp\left(-\int_0^{r_1} \lambda \left(1-\Pr^{\mathrm{L}}(u)\right) 2\pi u du\right) \exp\left(-\int_0^{r} \lambda \Pr^{\mathrm{L}}(u)\, 2\pi u du\right) \times 0 \times 2\pi r \lambda \\ &= 0, \quad (r > d_1). \end{aligned} \tag{4.33}$$

4.5.4 The Computation of T_2^{NL}

From Theorem 1, T_2^{NL} is computed as

$$\begin{aligned} T_2^{\mathrm{NL}} &= \int_{d_1}^{\infty} \sum_{k=0}^{\infty} \sum_{m=0}^{k} J(m,k)\, \gamma^{k-m} (-1)^{k-m} \frac{\partial^{k-m} \mathscr{L}_{I_r}\left(\frac{\gamma}{P\zeta_n^{NL}(r)}\right)}{\partial \gamma^{k-m}} f_{R,1}^{\mathrm{NL}}(r)\, dr \\ &\overset{(a)}{=} \int_{d_1}^{\infty} \sum_{k=0}^{\infty} \sum_{m=0}^{k} J(m,k)\, \gamma^{k-m} (-1)^{k-m} \frac{\partial^{k-m} \mathscr{L}_{I_r}\left(\frac{\gamma r^{\alpha^{\mathrm{NL}}}}{PA^{\mathrm{NL}}}\right)}{\partial \gamma^{k-m}} f_{R,1}^{\mathrm{NL}}(r)\, dr, \end{aligned} \tag{4.34}$$

where $\zeta_2^{\mathrm{NL}}(r) = A^{\mathrm{NL}} r^{-\alpha^{\mathrm{NL}}}$ from (4.17) is plugged into the step (a) of (4.34).

Furthermore, based on Theorem 1 and (4.18), $f_{R,2}^{\mathrm{NL}}(r)$ is computed as

$$\begin{aligned} f_{R,2}^{\mathrm{NL}}(r) &= \exp\left(-\int_0^{d_1} \lambda \left(1-\frac{u}{d_1}\right) 2\pi u du\right) \exp\left(-\int_0^{d_1} \lambda \frac{u}{d_1} 2\pi u du - \int_{d_1}^{r} \lambda 2\pi u du\right) 2\pi r \lambda \\ &= \exp\left(-\pi \lambda r^2\right) 2\pi r \lambda, \quad (r > d_1). \end{aligned} \tag{4.35}$$

In the following, Lemma 3 is proposed in order to to calculate $\mathscr{L}_{I_r}\left(\frac{\gamma r^{\alpha^{\mathrm{NL}}}}{PA^{\mathrm{NL}}}\right)$ in (4.34) for the range of $r > d_1$.

Lemma 3. *$\mathscr{L}_{I_r}\left(\frac{\gamma r^{\alpha^{\mathrm{NL}}}}{PA^{\mathrm{NL}}}\right)$ in the range of $r > d_1$ can be computed as*

$$\begin{aligned}
\mathscr{L}_{I_r}\left(\frac{\gamma r^{\alpha^{\mathrm{NL}}}}{PA^{\mathrm{NL}}}\right) &= \\
\exp\left(-2\pi\lambda\,\rho_2\left(\alpha^{NL},1,(1-K)\left(\gamma r^{\alpha^{\mathrm{NL}}}\right)^{-1},d_1\right)\right) &\times \exp\Big(-2\pi\lambda\left(\gamma r^{\alpha^{\mathrm{NL}}}\right)^{-1}\left(1-K-e^{-K}\right) \\
\rho_2\left(\alpha^{NL},\alpha^{NL}+1,(1-K)\left(\gamma r^{\alpha^{\mathrm{NL}}}\right)^{-1},d_1\right)\Big), &\quad (r > d_1), \qquad (4.36)
\end{aligned}$$

where $\rho_2(\alpha,\beta,t,d)$ is defined in (4.23).

See Appendix B-4.

It is important to note that the Laplace term computed by Lemma 3, gives the probability that the second-piece NLOS signal power exceeds the aggregate interference power by a factor of at least γ.

Overall, T_2^{NL} is evaluated as

$$T_2^{\mathrm{NL}} = \int_{d_1}^{\infty} \sum_{k=0}^{\infty}\sum_{m=0}^{k} J(m,k)\,\gamma^{k-m}(-1)^{k-m}\frac{\partial^{k-m}\mathscr{L}_{I_r}\left(\frac{\gamma r^{\alpha^{\mathrm{NL}}}}{PA^{\mathrm{NL}}}\right)}{\partial\gamma^{k-m}} f_{R,1}^{\mathrm{NL}}(r)\,dr. \qquad (4.37)$$

where $f_{R,2}^{\mathrm{NL}}(r)$ and $\mathscr{L}_{I_r}\left(\frac{\gamma r^{\alpha^{\mathrm{NL}}}}{PA^{\mathrm{NL}}}\right)$ are computed by (4.35) and (4.36), respectively.

4.5.5 The Results of $p^{\mathrm{cov}}(\lambda,\gamma)$ and $A^{\mathrm{ASE}}(\lambda,\gamma_0)$

Based on the obtained derivations given in (4.24), (4.31), and (4.37), the probability of coverage can be written as

$$p^{\mathrm{cov}}(\lambda,\gamma) = T_1^{\mathrm{L}} + T_1^{\mathrm{NL}} + T_2^{\mathrm{NL}}, \qquad (4.38)$$

Plugging $p^{\mathrm{cov}}(\lambda,\gamma)$ into (4.11), the area spectral efficiency $A^{\mathrm{ASE}}(\lambda,\gamma_0)$ is obtained.

4.6 Simulation and Discussion

In this section, we use numerical results to to study the performance of dense small cell networks under Rician fading channel. The simulation settings is presented in Table 4.1.

Table 4.1 Simulation Settings

Parameter	Value [80]
α^{L}	2.09
α^{NL}	3.75
A^{L}	$10^{-10.38}$
A^{NL}	$10^{-14.54}$
d_1	0.3 km
P	24 dBm
N_0	-95 dBm

4.6.1 Validation of the Analytical Results of $p^{\mathrm{cov}}(\lambda,\gamma)$ for 3GPP Case

Fig. 4.2 shows the results of $p^{\mathrm{cov}}(\lambda,\gamma)$ for different SINR thresholds of $\gamma = 0$ dB and $\gamma = 3$ dB. It should be mentioned that Fig. 4.2 also shows the analytical results assuming a single-slope path loss model based on [107] which does not differentiate the LOS and NLOS transmissions. Note that in [107] the path loss exponent is $\alpha = \alpha^{\mathrm{NL}} = 3.75$.

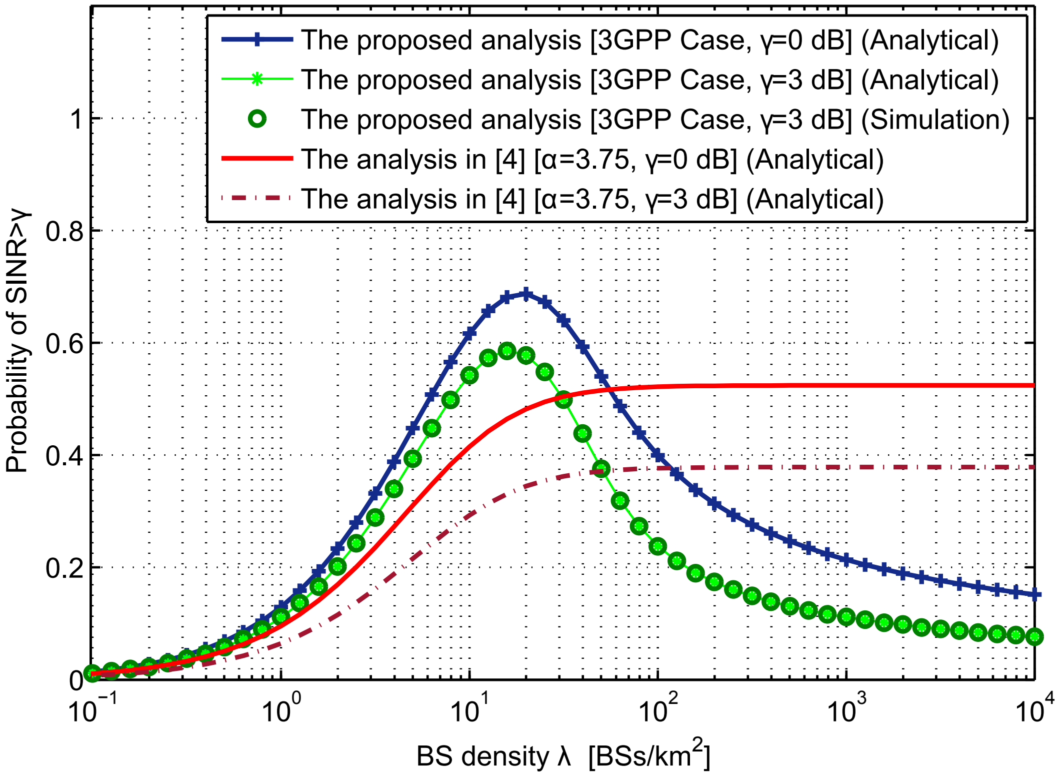

Fig. 4.2 The probability of coverage probability versus the BS density for 3GPP Case with various SINR thresholds.

First, it is important to note that the theoretical analysis results match well with the simulation results, and hence the theoretical results are only shown in the sequel. Fig. 4.2 shows that the probability of coverage in the case of Rician fading follows the same trend as in the case of Rayleigh fading presented in [113]. More specifically, the probability of coverage initially increases as the BS density increases. However, once the BS density exceeds a certain threshold, i.e., $\lambda > \lambda_1$ $(i.e., \lambda_1 = 100\frac{\text{BSs}}{\text{km}^2}$ in Fig. 4.2), the probability of coverage starts to decline. This can be explained as follows. When the BS density is lower than λ_1, the network behaviour is noise limited and thus there is a rapid increase in coverage probability with the BS density. However, once the network becomes denser and the density of BSs is larger than λ_1, then a large number of interfering signals transit from NLOS to LOS, and hence the increase in interference power cannot be counterbalanced by the increase in signal power, which was already LOS. Note that further densification beyond λ_1 results in slower decline rate in coverage probability, since both signals corresponding to interfering and serving BSs are LOS dominated.

Comparing the probability of coverage results assuming Rician fading with those in [113] that have considered Rayleigh fading, it can be concluded that the impact of Rician fading on the probability of coverage is negligible. The difference in coverage probability is less than 0.02 for all BS densities. This is because the NLOS to LOS transition is in the order of 15-20 dB according to the 3GPP path loss functions [80], while that of Rayleigh to Rician is in the order of $\sim$ 3 dB. Hence, Rayleigh or Rician fading makes little difference against this abrupt change of interference strength. Comparing the results of the proposed piecewise path loss model to those by [107], it is realized that the coverage probability given by [107] first starts to increase with the BS density because using a larger number of BSs leads to a better coverage in noise-limited networks. Then, when λ is further increased, i.e., $\lambda > 10^2$ BSs/km^2, the network becomes interference-limited and so the coverage probability behaves as independent of λ. The reason for this behaviour is that when a path loss model with a single path loss exponent is used, the increase in interference power is counterbalanced by the increase in signal power and, therefore, the increase in BS density does not impact the coverage probability [107].

In next subsection, the trend of ASE performance will be investigated based on the expression of the ASE in (4.10).

4.6.2 Discussion on the Analytical Results of $A^{\mathrm{ASE}}(\lambda, \gamma_0)$ for 3GPP Case

Fig. 4.3 shows the ASE for different SINR thresholds of $\gamma = 0$ dB and $\gamma = 3$ dB. Note that the ASE results are derived based on the results from the probability of coverage presented in (4.10). Similar to the observed trend for the probability of coverage, the ASE trend also shows three phases. In the first phase, when the BS density is lower than λ_1, the ASE increases with the BS density as coverage holes are mitigated. In the second phase, when the BS density exceeds λ_1, the ASE suffers from a slower growth pace or even a decrease due to the decline in probability of coverage originated by the transition of a large number of interfering signals from NLOS to LOS. In the third phase, when all interfering signals has transited to LOS, the ASE starts to linearly increase with BS density since the network has become statistically stable with all interfering and serving BSs being LOS dominated. In particular, the decrease in ASE due to increase in the BS density λ emphasizes the important impact of the proposed distance dependent path loss model that takes into account both NLOS and LOS transmissions.

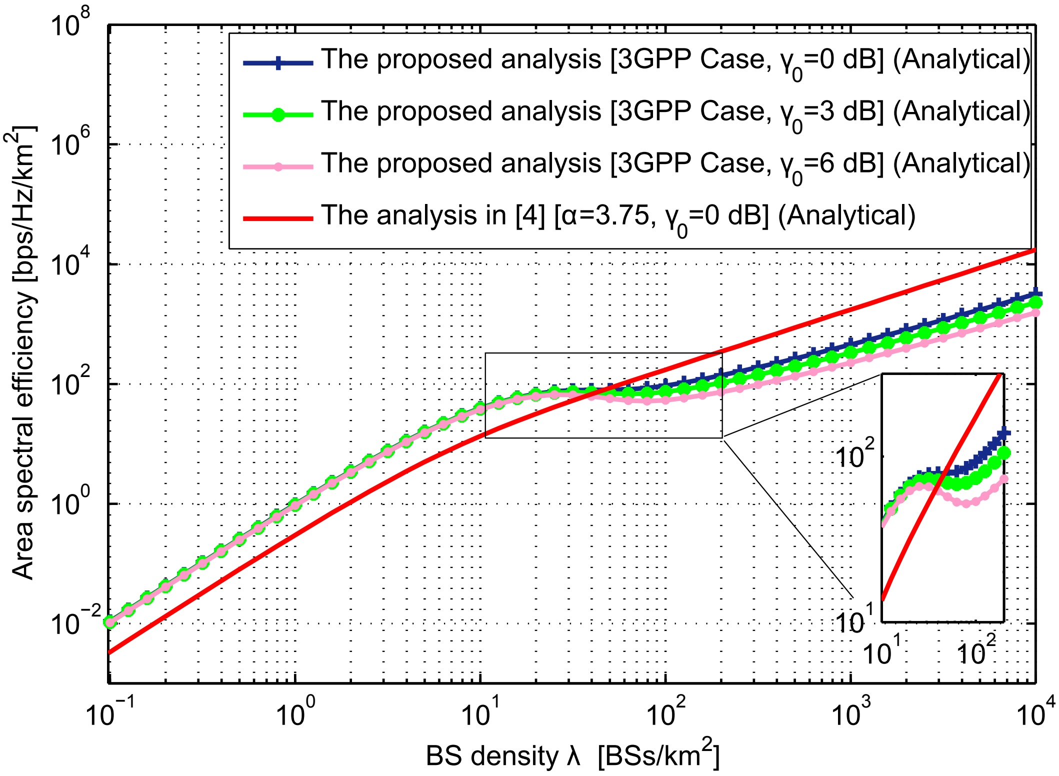

Fig. 4.3 The area spectral efficiency versus the BS density for 3GPP Case with various SINR thresholds.

Comparing the ASE results as shown in Fig. 4.3 which assume Rician fading with those in [113] that have considered Rayleigh fading, it can be concluded that the impact of Rician fading on the ASE is negligible with a peak Rician to Rayleigh gain of about 1.02x at a BS density of 15.85 $\frac{BSs}{km^2}$. The reason of this conclusion has been explained before, i.e., the power variation of the NLOS to LOS transition is in the order of 15-20 dB according to the 3GPP path loss functions [80], while that of Rayleigh to Rician is in the order of $\sim$ 3 dB. Hence, Rayleigh or Rician fading makes little difference against this abrupt change of interference strength. Comparing to the results of $A^{\mathrm{ASE}}(\lambda, \gamma_0)$ with the analytical results in [107] assuming $\gamma_0 = 0\,\mathrm{dB}$, it is perceived that the analysis from [107] indicates that when the small cell network is dense enough, i.e., $\lambda \geq 10^2\,\mathrm{BSs/km^2}$, the ASE linearly increases with λ. This can be explained considering that when λ is sufficiently large and for a given γ, the $p^{\mathrm{cov}}(\lambda, \gamma)$ is independent of λ [107]. In the following, the implications can be summarized as:

- ***Remark 1:*** It is perceived that when the density of small cell BSs exceeds a certain threshold λ_0, the ASE may suffer from a slow growth or even a decrease due to the rapid reduction in the network coverage probability.

- ***Remark 2:*** This observation is particularly important for practical deployments of dense small cell networks from two perspectives: *(i)* The BS density of about tens to hundreds BSs/km^2 refers to the path from 4G to 5G where the ASE may suffer from a slow growth or even a decrease. Assuming that λ has been estimated of several to tens of BSs/km^2 in 4G [69], [116] and tens to hundreds or even thousands of BSs/km^2 in 5G [117], it is imperative to present cost-effective deployment strategies of ultra-dense small cell networks for the commercial success of future 5G networks, *(ii)* Near-field path loss exponents, i.e., $\alpha^{\mathrm{L}} < 2$ or $\alpha^{\mathrm{NL}} < 2$ do not set any limitation on the obtained results. Also, note that the parameters that were considered have been recommended by the 3GPP standards benefit and hence the results take advantage of practical values which helps for cost-effective deployment strategies of ultra-dense small cell networks for the commercial success of future 5G networks.

- ***Remark 3:*** As the density of small cell BSs goes beyond λ_1, an almost linear growth in ASE is observed. This can be used to determine an optimum BS density threshold for the future 5G ultra-dense small cell networks [117].

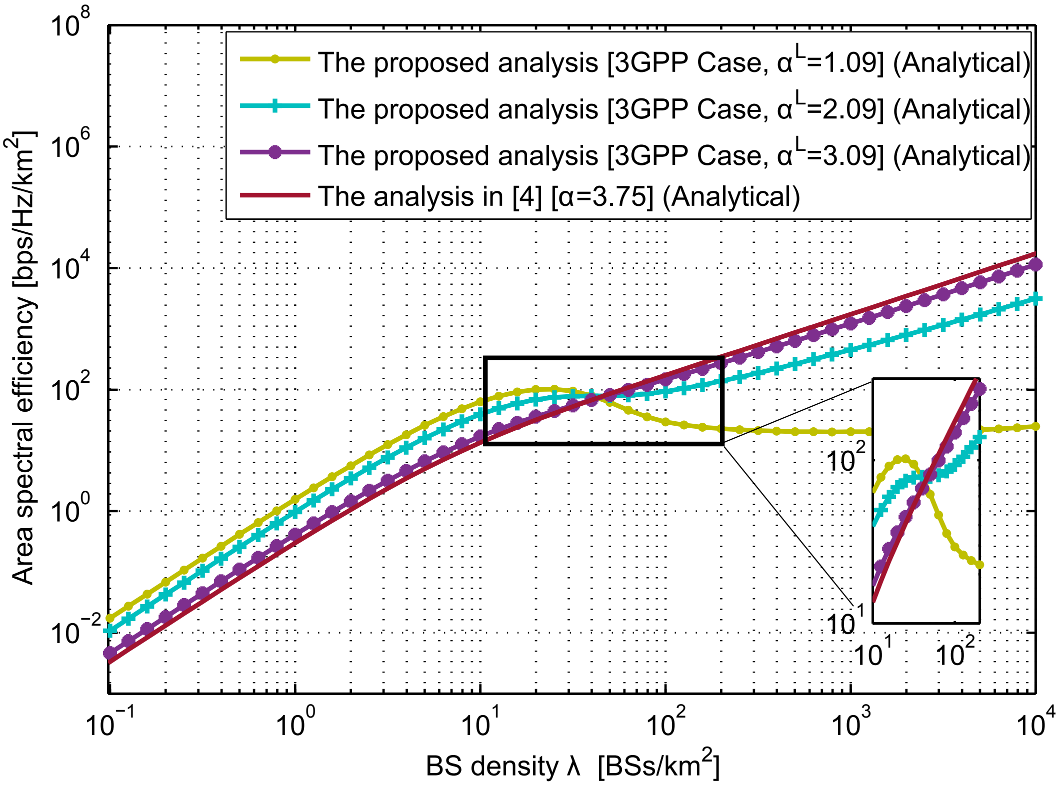

Fig. 4.4 The area spectral efficiency versus the BS density for 3GPP Case with SINR threshold and with various LoS path loss exponents.

4.6.3 Discussion on Various Values of α^{L} for 3GPP Case

Fig. 4.4 shows the ASE performance for SINR threshold of $\gamma_0 = 0\,\mathrm{dB}$ assuming various values of α^{L} as $\alpha^{\mathrm{L}} = 1.09$ and $\alpha^{\mathrm{L}} = 3.09$. Moreover, it compares the results with those from [107] in which $\alpha^{\mathrm{NL}} = 3.75$ has been considered.

Fig. 4.4 demonstrates that when the difference between the LOS path loss exponent α^{L} and NLOS path loss exponent α^{NL} becomes larger, due to a more drastic transition of interference from NLOS transmission to LOS transmission the slow growth or the decrease of ASE at $\lambda \in [\lambda_0, \lambda_1]$ BSs/km^2 ($\lambda_0 \approx 20\,$BSs/km^2 and $\lambda_1 \approx 10^2\,$BSs/km^2) is more prominent. Specifically, a considerable decrease in the ASE performance is observed at $\lambda \in [\lambda_0, \lambda_1]$ BSs/km^2 when α^{L} is allocated a near-field path loss exponent such as 1.09 [110] and it is important to emphasize that ASE performance can hardly recover beyond λ_1. The difference between these results and those in [110] is mainly attributed to the different definitions of ASE in [110] and in the definition of ASE presented in (4.10) which is also able capturing the phenomena where the ASE performance also experiences a decrease even when $\alpha^{\mathrm{L}} \geq 2$. Note that [110] assumed a deterministic rate which does not depend on the actual value of SINR and is based on γ_0 for the typical UE. However, the definition of ASE presented in (4.10) takes into account the actual value of SINR which represents a more realistic scenario. However, this comes at the cost of increase in the complexity of analysis since the analysis in this chapter used one more fold of numerical integral compared with [110]. Therefore, the following implication can be included as:

- ***Remark 4:*** The performance of ASE is dependent on the LOS and the NLOS path loss functions characteristics. Indeed, a larger difference between the LOS and the NLOS path loss exponents will cause a more drastic transition of interference from the NLOS transmission to the LOS transmission and hence the ASE suffers more at $\lambda \in [\lambda_0, \lambda_1]$ BSs/km^2.

4.6.4 Performance Comparison of Hexagonal and Poisson BS Deployment

In terms of BS deployment in cellular networks, the BS locations are usually modelled either according to the traditional deterministic hexagonal grid model which was discussed and exploited in chapters 2 and 3, or according to the Poisson model which refers to a random BS deployment and was discussed in this chapter. The hexagonal BS deployment is considered to be more pertinent and represents an extreme in terms of regularity and uniformity of coverage, however, it does not allow analytical techniques for the study of the SINR-based characteristics. On the contrary, the Poisson model is able to model the irregularities of the network and represents a worst case scenario due to its complete randomness property. Moreover, the Poisson model allows to derive the SINR distribution at an arbitrary location considering the random channel effects such as multi-path fading and shadowing. Considering the two BS deployment scenarios, it is important to observe the network performance in terms of coverage probability using the proposed path loss model. Fig. 4.5 shows that both hexagonal and PPP deployment layout follow the same performance trend, where the probability of coverage first increases with BS density, however, once the BS density exceeds a certain threshold, due to transition of many interfering signals from NLOS to LOS, the coverage probability starts to decline. As discussed earlier, PPP deployment represents the worst case scenario and hence the reason for the better performance of hexagonal layout.

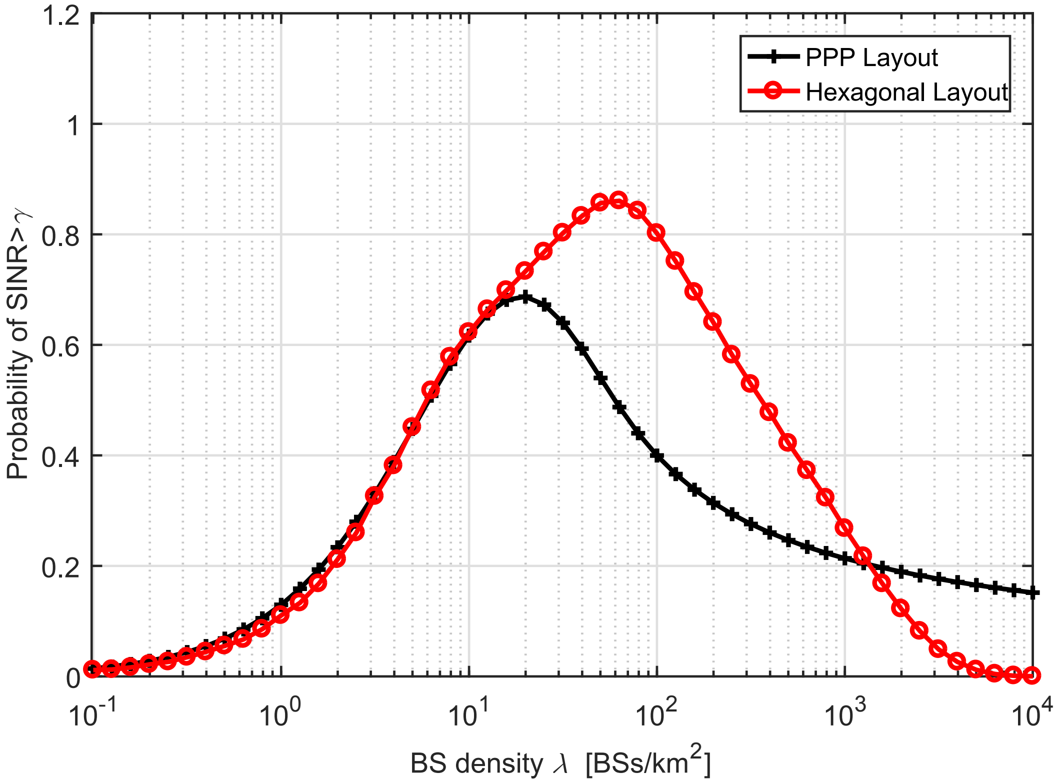

Fig. 4.5 Comparison of coverage probability versus the BS density for Hexagonal and Poisson Point Process BS deployments.

4.6.5 Discussion of the Value of Theoretical Analysis

While theoretical derivations do not have straightforward and compact expressions, this has to be pointed out that computer based simulations are nearly infeasible when looking at a practical ultra-dense network with a tremendous number of BSs, millions of them. The complexity of computer based simulations quickly become prohibitive, with running times of around a month for the discussed scenario in this paper. In more details, the required time to perform the computer based simulations for BS densities of $\lambda \geq 10^3$ BSs/km^2 is very long, and it becomes almost infeasible for BS densities of $\lambda \geq 10^5$ BSs/km^2. For instance, for BS density of $\lambda = 10^6$ BSs/km^2, it takes a minimum of twenty seven days to plot smooth curves using computer based simulations in comparison to five days using the theoretical derivations. In contrast, the complexity of the theoretical analysis remains independent of the BS density, thanks to the numerical integration derived in this paper, i.e., the complexity is not a function of the BS density and so the results can be obtained much faster.

4.7 Conclusion

In this chapter, it has been discussed that most theoretical studies on small cell networks have only considered simple path loss models that do not differentiate LOS and NLOS transmissions and hence have come to the conclusion that neither the number of small cells nor the number of cell tiers changes the coverage probability in interference-limited fully-loaded cellular networks. However, in ultra-dense small cell networks due to decrease in the distance between UEs and BSs, the probability of LOS transmission is increased which causes a transition from NLOS transmission to LOS transmission which can notably change the previous conclusion. To capture the impact of LOS-to-NLOS transition in ultra-dense small cell networks, a novel piecewise path loss model that features piecewise path loss functions with probabilistic LOS and NLOS transmissions has been proposed. Moreover, in terms of multi-path fading, a distance-dependent Rician fading channel with variant Rician K factor has been exploited for the first time to investigate the combined impacts of the *distance based path loss model and multi-path fading* on the performance of ultra-dense small cell networks. It has been shown through theoretical analysis and simulation results that Rician fading as a more realistic multi-path model for ultra-dense small cell networks has a negligible impact on the system performance in terms of both coverage probability and area spectral efficiency compared to Rayleigh one. This important finding, indicates that in ultra-dense small cell networks where the UE and BS are deployed at the same height, the LOS/NLOS path loss characteristics and *not the multi-path fading* ones dominate the performance. The results further demonstrate that in ultra-dense small cell networks, when the BS density exceeds a certain threshold, due to NLOS to LOS transition of a large number of interference signals, the SINR degrades and so the coverage probability starts to decline for a given BS density range and *multi-path fading* does not help to mitigate the SINR degradation. This major finding proves that in ultra-dense small cell networks and unlike traditional macrocell networks, the small cell BS density has a prominent impact on network performance and how to cost-efficiently march across this undesirable BS density range is crucial for the deployment of future 5G networks.

Chapter 5

Diversity Pulse Shaped Transmission in Dense Small Cell Networks

5.1 Introduction

It has been discussed in previous chapters that network densification has the potential to increase the network capacity with the number of deployed cells [117]. It is also well known that exploiting spatial multiplexing of MIMO technology has the potential to increase the network capacity by the minimum number of transmit/receive antennas [118]. However, it is not clear whether both technologies can be exploited simultaneously. Indeed, due to increased spatial correlation among different channel pairs of a MIMO system employed in a dense small cell network, spatial multiplexing suffers and hence the UE's throughput cannot be enhanced by the minimum number of transmit/receive antennas. In response to the urge to investigate new transmission techniques, diversity pulse shaped transmission is proposed as a new technology in order to enhance the user throughput and thus counterbalance the loss of spatial multiplexing. The main contributions of this chapter are summarized as follows:

- A correlated MIMO channel model is proposed and its mathematical model is derived that is able to capture the impact of the spacing between antenna elements at both UE and BS as well as the distance between UE and BS on the spatial correlation of the channel.
- The fundamentals of delayed pulse shaping transmission at the transmitter and fractionally spaced equalizer at the receiver are elaborated and analytical results are obtained to demonstrate how a virtual MIMO channel with improved condition number is generated.

- The analytical derivations and simulation results for the diversity pulse shaped transmission as a novel transmission technique are presented and it is shown that for any arbitrary size MIMO system, DPST can almost enhance the UE throughput by the minimum number of transmit/receive antennas and hence compensate for the loss of spatial multiplexing gain in ultra-dense small cell networks.

5.2 MIMO in Dense Small Cell Networks

One flavour of MIMO technology is spatial multiplexing, which allows simultaneous transmission of independent data streams from different transmit antennas, eventually enhancing the network capacity by the minimum number of transmit/receive antennas [90]. However, applying spatial multiplexing to ultra-dense small cell networks is challenging due to the different propagation conditions when compared to macrocell networks. For instance, in macrocell networks, spatial multiplexing gain typically improves when the MIMO channel benefits from sufficient environment scattering enabling different channel pairs to be uncorrelated. In contrast, in ultra-dense small cell networks, spatial multiplexing gains may be limited due to channel pairs being correlated. Two phenomena contribute to this channel spatial correlation. Firstly, due to proximity of UE and BS, there is a high probability of LOS communication (the channel can even be prone to only LOS communication as the ISD is decreased). Secondly, the antennas at both UE and BS may be placed very closely to each other ($\sim$ half wavelength). This spatial correlation causes the communication channel to be ill-conditioned, which lowers the number of independent parallel data streams that can be simultaneously multiplexed and decoded. As a result, UE's throughput is significantly degraded in comparison to macrocell networks,and thus spatial reuse might be traded for spatial multiplexing when densifying the network. In order to compensate for the loss of spatial multiplexing gain and enhance the UE's throughput over correlated MIMO channels in an ultra-dense small cell network, diversity pulse shaped transmission (DPST) is proposed as a novel transmission technique, which exploits distinct pulse shapes to modulate data streams of adjacent antennas [119].

DPST suggests that the signals corresponding to adjacent antenna elements should be shaped with distinct band limited pulse shaping filters to generate diversity. The filters are here characterised by *deterministic delays*, meaning that the transmission of one antenna with respect to its adjacent one is delayed by a deterministic amount. This leads to inter-symbol interference (ISI) in the time domain, which in turn generates diversity. It is important to note that the deterministic delay must be a *fraction of the symbol period* in order to allow the UE receiver to resolve the multiple delayed replicas of the transmitted data stream within

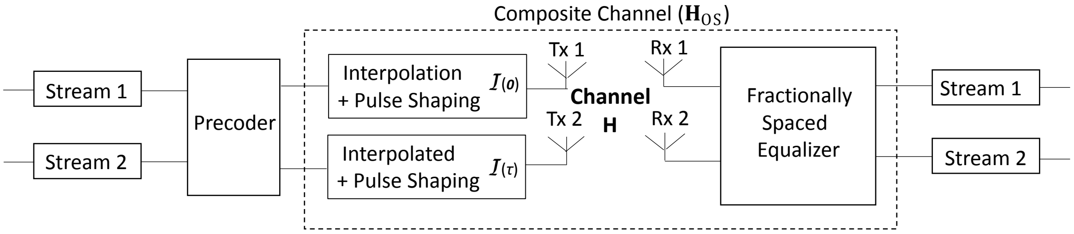

Fig. 5.1 DPST block diagram. The fractional delay τ is introduced to ensure that the effective channel between transmit-receive pairs is well-conditioned.

the symbol period (in contrast to overlapping replicas in correlated scenarios), and hence distinguish between the transmissions of different transmit antennas.

For simplicity, a 2×2 MIMO setup is considered. In this case, the receive antennas would observe antenna 1 to transmit its data streams with symbol period T_s as well as antenna 2 to transmit its data stream with delay τ with respect to antenna 1, while being sampled at T_s where $0 < \tau < T_s$. This implies that in a LOS scenario and assuming that the receiver is synchronised to T_s (ignoring the bulk delays), the receive antennas would observe a direct path from antenna 1 with data stream 1 as well as a delayed path from antenna 2 with data stream 2, with the latter being corrupted by ISI where the generated ISI helps to diversify the different channel pairs. In order to account for the increased ISI in one of the streams, it is proposed to use a fractionally spaced equaliser (FSE) at the UE, which operates on the precoded data streams and wireless channel output and eventually improves the UE's throughput in ultra-dense small cell networks [120]. In order to ensure a reasonable estimate of multi-path signals, minimum mean squared error (MMSE) is used to design the equaliser.

It is shown that the combined arrangement of DPST based on pulse shaping diversity and deterministic delay as well as oversampled receiver improves the overall dimensionality of the transmitted multi-antenna data streams viewed by the receiver and consequently enhances the data rates. Note that while the modelling is restricted to a 2×2 MIMO case, DPST can be applied to arbitrary sized antenna arrays. It is further discussed the optimisation of the deterministic delay that results in the least correlation among channel pairs. Moreover, the performance of DPST is evaluated in a single tier hexagonal small cell layout, considering downlink communications. In more detail, the degradation of SINR and UE throughput due to spatial correlation for 2×2 and 4×4 MIMO systems at different ISDs, i.e., 20 m, 50 m and 100 m, is quantified and then it is demonstrated that the proposed DPST leads to significant gains, e.g., for an ISD of 50 m, DPST provides a 50%-tile SINR improvement of 10.5 dB and 12 dB in 2×2 and 4×4 MIMO systems, respectively, and enhance the UE throughput by approximately 2x and 4x in 2×2 and 4×4 MIMO systems, respectively.

5.3 Channel Correlation Model in Ultra-Dense Small Cell Networks

The performance of a MIMO systems is highly dependent on different channel pairs being spatially uncorrelated. In correlated channel scenarios, different transmit-receive antenna pairs will undergo similar channel conditions, and as a result the multi-path components corresponding to different pairs may not be resolvable by the UE [121]. Thus, correlated channels have reduced degrees of freedom, leading to reduced throughputs as detailed in [122] [123].

The Rician multi-path fading model is used in order to capture the impact of LOS communication in ultra-dense small cell networks. The channel variations due to UE mobility are not considered, since ultra-dense small cell networks are designated to provide coverage to static UEs.

The Rician MIMO channel for N_t transmit antennas and N_r receive antennas can be represented using an $N_r \times N_t$ matrix $\mathbf{H}$ as

$$\mathbf{H} = \sqrt{\frac{K}{K+1}}\mathbf{H}_i{}^{\text{LOS}} + \sqrt{\frac{1}{K+1}}\mathbf{H}_s{}^{\text{NLOS}}, \tag{5.1}$$

where K is the Rician K factor, and $\mathbf{H}_i{}^{\text{LOS}}$ and $\mathbf{H}_s{}^{\text{NLOS}}$ are the unit LOS MIMO channel matrix and the correlated NLOS MIMO channel matrix, respectively. In chapter 3, a distance dependant Rician K factor based on the probability of LOS in micro urban environments was presented, which offers a transition from Rician to Rayleigh fading as UEs locate further away from the BSs and the LOS component gradually decades. Worth noting that as the ISD reduces, the LOS component becomes more dominant, which leads to a larger correlation among the different transmit-receive channel pairs. The distance dependant Rician K factor has been expressed as

$$\text{K} = \begin{cases} 32 & \text{if } d < 18m \\ 140.10 \times \exp(-0.107 \times d) & \text{otherwise,} \end{cases} \tag{5.2}$$

where d denotes the distance between the UE and BS [124]. To model the correlated NLOS channel matrix, the Kronecker model is used, which captures the correlation among the channel pairs due to the spacing between antenna elements [125] at both UE and BS. $\mathbf{R}_R$ and $\mathbf{R}_T$ are derived as the $N_r \times N_t$ correlation matrices at the receiver and transmitter sides, respectively. A detailed discussion on derivation of correlation coefficient between any two channel pairs as a function of the spacing between antenna elements is presented in the Appendix C.

The correlated NLOS MIMO channel ${\mathbf{H}_s}^{\text{NLOS}}$ can therefore be expressed as

$$ {\mathbf{H}_s}^{\text{NLOS}} = {\mathbf{R}_R}^{\frac{1}{2}} \mathbf{H}_w {\mathbf{R}_T}^{\frac{1}{2}}, \tag{5.3} $$

where $\mathbf{H}_w$ is the $N_r \times N_t$ spatially white MIMO channel. Plugging (5.3) into (5.1), the correlated Rician MIMO channel is derived as

$$ \mathbf{H} = \sqrt{\frac{K}{K+1}} {\mathbf{H}_i}^{\text{LOS}} + \sqrt{\frac{1}{K+1}} \mathbf{R}_R^{\frac{1}{2}} \mathbf{H}_w \mathbf{R}_T^{\frac{1}{2}} \tag{5.4} $$

Note that the dependency of spatial correlation on UE-BS distance as well as antenna spacing is attributed to the Rician K factor and the Kronecker product of transmit/receive correlation matrices, respectively. Applying singular value decomposition (SVD), the $N_r \times N_t$ channel $\mathbf{H}$ can be written as $\mathbf{H} = \mathbf{U}\Sigma\mathbf{V}^{\text{H}}$ where $\mathbf{U}$ and $\mathbf{V}$ are $N_r \times N_r$ and $N_t \times N_t$ unitary matrices, respectively and Σ is a $N_r \times N_t$ diagonal matrix as shown in (5.5). The diagonal entries λ_l $(l = 1, 2, \cdots, L)$ where $L = min(N_r, N_t)$ denote the singular values of the channel $\mathbf{H}$ in the descending order.

$$ \Sigma = \begin{pmatrix} \lambda_1 & 0 & \cdots & 0 \\ 0 & \lambda_2 & \cdots & 0 \\ \vdots & \vdots & \ddots & \vdots \\ 0 & 0 & \cdots & \lambda_L \end{pmatrix} \tag{5.5} $$

The condition number ($\mathscr{K}$) of the channel is defined as the ratio of the maximum to minimum singular values $\mathscr{K} = \frac{\lambda_1}{\lambda_L}$, and is referred to as a metric to denote the quality of the independent streams of the wireless channel [126]. $\mathscr{K} \approx 1$ implies no correlation between channel pairs, and as long as $\mathscr{K}$ is less than 10, the channel is regarded as well-conditioned, and can be leveraged to extract the unitary vectors of the channel for precoding and spatial multiplexing purposes.

For simplicity - in an $N_r = 2$ and $N_t = 2$ setup, the singular values corresponding to each transmit antenna can be approximated as

$$ \begin{aligned} \lambda_1 \approx & -\frac{|h_{1,1}\, h_{2,2} - h_{1,2}\, h_{2,1}|^2}{{a_{1,1}}^2 + {a_{1,2}}^2 + {a_{2,1}}^2 + {a_{2,2}}^2} + {a_{1,1}}^2 + {a_{1,2}}^2 \\ & + {a_{2,1}}^2 + {a_{2,2}}^2 \\ \lambda_2 \approx & \frac{|h_{1,1} h_{2,2} - h_{1,2} h_{2,1}|^2}{{a_{1,1}}^2 + {a_{1,2}}^2 + {a_{2,1}}^2 + {a_{2,2}}^2} \end{aligned} \tag{5.6} $$

where $a_{i,j}$ denotes the amplitude gain of $h_{i,j}$, which refers to channel from the j-th transmit antenna to the i-th receive antenna [127]. The 2×2 wireless channel can be decomposed into its $L = 2$ singular channels, and if both λ_1 and λ_2 are sufficiently large, the corresponding parallel channels can be exploited to convey the specific data streams and the capacity C can be computed as the sum of the corresponding singular channels' capacities as follows

$$C = \log_2 \left[\det \left(\mathbf{I}_L + \frac{\rho}{N_0}\mathbf{H}\mathbf{H}^H\right)\right] = \sum_{l=1}^{L} \log_2 \left(1 + \frac{\rho\lambda_l}{L}\right), \tag{5.7}$$

where ρ is the SINR at each receiver branch and N_0 is the receiver noise power [127].

However, in the correlated 2×2 MIMO channel, λ_2 will be minimal implying that the corresponding singular channel cannot be used to transmit its data stream. This leads to the condition number $\mathscr{K}$ to be considerably larger than 10, and therefore the channel becomes ill-conditioned and spatial multiplexing gain suffers. In next section, a new transmission scheme to tackle this issue is proposed.

5.4 Delayed Pulse Shaping Transmission

In the 2×2 MIMO system, DPST works by shaping the data stream of the second antenna with respect to first antenna such that in DL communications the multi-path components corresponding to the second antenna arrive at the UE at a later time instant than those corresponding to the first antenna, aiming to enhance the diversity among the *fractionally delayed* multi-path components of the closely placed transmit antennas. Fig. 5.1 shows the block diagram of DPST in a 2×2 setup.

The impact of the *deterministic fractional delay* on enhancing the diversity of the channel by means of ISI generation is similar to the outcome of faster than Nyquist (FTN) signalling [128] [129] [130]. In FTN communications, a non-orthogonal sampling kernel is used to allow for signalling above the Nyquist limit, and hence data streams are sampled and transmitted at a fraction of symbol period, eventually leading to an improvement in communication rates at the cost of a more complicated receiver design to combat the introduced ISI through oversampling. In traditional cases, by using an orthogonal sampling kernel, there is only a single non-zero component of the transmitted signal. However, in FTN the signals are transmitted at above the Nyquist rate and the intentionally generated ISI results in enhanced system capacity at the expense of a more complex receiver.

The additional *fractional delay* that is applied to the transmission of the second antenna in DPST also generates *deterministic ISI* in the system [131], which suggests the analogy between DPST and FTN in terms of generation of controlled ISI. Fig. 5.2 intuitively shows

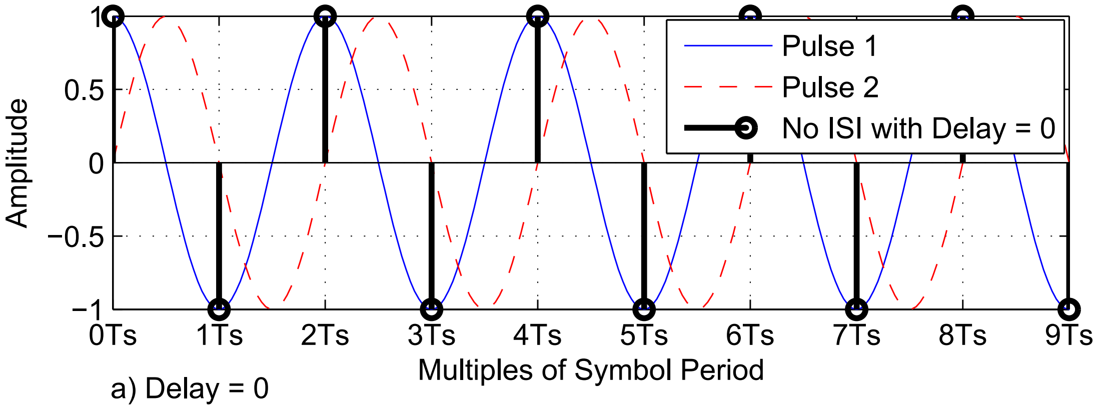

a) Delay = 0

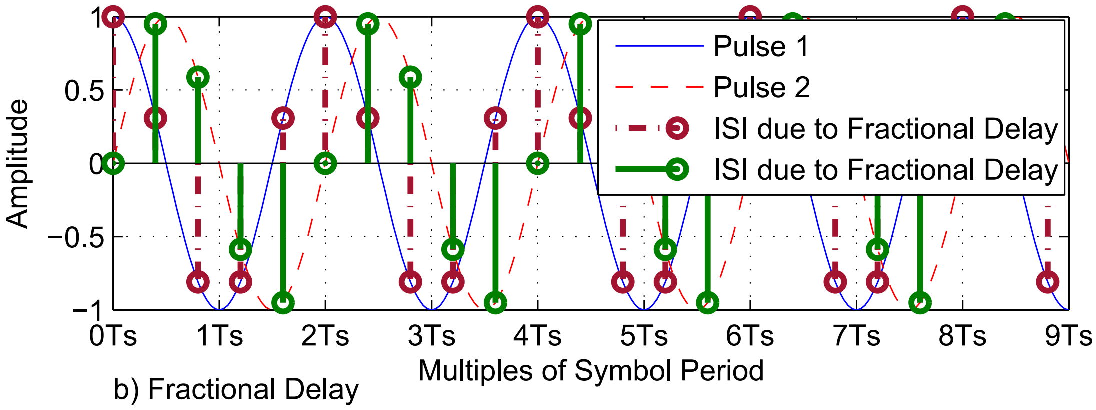

b) Fractional Delay

Fig. 5.2 Integral and non-integral sampling effect on DPST.

the implication of DPST. In Fig. 5.2(a), the signals are sampled at integral multiples of symbol period with an orthogonal sampling kernel, while in Fig. 5.2(b), signals are sampled at non-integral multiples of symbol period. In the latter case and in contrast with the former, at each sampling instant, there are multiple non-zero samples viewed by the sampling kernel, which shows how at each sampling point the pulses interfere and hence ISI is generated. As a result of the generated ISI in the system, the sampled channel impulse response $h[nT_s]$ will no longer follow the Nyquist zero ISI criterion presented in (5.8) with n being an integer. The generated ISI is then exploited to increase the diversity of the wireless channel seen between the transmit and receive antennas pairs, implying reduced correlation among different channel pairs viewed by the receiver.

$$h[nT_s] = \begin{cases} 1 & n = 0 \\ 0 & n \neq 0 \end{cases} \tag{5.8}$$

5.4.1 MIMO Link Model with Pulse Shaping

The deterministic transmission delay τ must be a fraction of the transmitted signal period T_s, i.e., $0 < \tau < T_s$, where T_s is normalised to be 1. The received signal can be expressed as

$$\begin{bmatrix} x_1(t) \\ x_2(t) \end{bmatrix} = \begin{bmatrix} h_{1,1}(t) & h_{1,2}(t) \\ h_{2,1}(t) & h_{2,2}(t) \end{bmatrix} * \begin{bmatrix} s_1(t) \\ s_2(t+\tau) \end{bmatrix} \tag{5.9}$$

$$\mathbf{x}(t) = \mathbf{H}(t) * \mathbf{s}(t) \tag{5.10}$$

where $\mathbf{H}(t)$ is the continuous time version of the 2×2 correlated MIMO channel, $s_1(t)$ and $s_2(t)$ are the signals transmitted by first and second transmit antennas, respectively, while $x_1(t)$ and $x_2(t)$ are the signals received by first and second receive antennas, respectively. In order to implement the fractional delay τ, the transmit data streams are oversampled/interpolated as shown in the following

$$\begin{bmatrix} x_1(t) \\ x_2(t) \end{bmatrix} = \begin{bmatrix} h_{1,1}(t) & h_{1,2}(t) \\ h_{2,1}(t) & h_{2,2}(t) \end{bmatrix} * \left(\begin{bmatrix} \mathscr{I}(0)s_1(t) & 0 \\ 0 & \mathscr{I}(\tau)s_2(t) \end{bmatrix} \right) \tag{5.11}$$

where $\mathscr{I}(0)$ and $\mathscr{I}(\tau)$ are $N \times M$ interpolation matrices that are applied to the first and second transmit antennas, respectively. $\mathscr{I}_{\mathrm{Tx}}$ refers to the $2N \times 2M$ interpolation matrix encompassing the interpolation matrices at both transmit antennas where M denotes the length of input signals with period T_s, R is the oversampling ratio at the transmitter and $N = MR$ [132].

The modelling of oversampled analogue signals follows [132], and the elements of $N \times M$ interpolation matrix are obtained as

$$\mathscr{I}_{nm} = \mathrm{sinc}\left(\frac{n(\frac{T_s}{N}) + \tau - m(\frac{T_s}{M})}{\frac{T_s}{M}} \right) \quad \begin{cases} m = 1, 2, ..., M \\ n = 1, 2, ..., N \end{cases} \tag{5.12}$$

It is evident that the interpolation matrix corresponding to antenna 1 has no time offset, while the one corresponding to antenna 2 is offset by time τ to account for delayed pulse shaping. Exploiting the interpolating filters might give rise to the following question: Does DPST require an excess bandwidth in order to overcome the rank deficiency of the channel? Note that in order to apply the fractional delay, the interpolation and delay at the transmitter occurs in the radio frequency (RF) domain, which does not depend on the sampling frequency. DPST aims to squeeze more data bits (simultaneous transmission/reception of independent data streams) at the cost of enhanced ISI, and therefore it does not require any additional bandwidth, implying that the throughput per bandwidth increase will be constant.

The delay τ plays a key role in DPST performance. When the delay $\tau = 0$, the expression presented in (5.11) collapses into the initial ill-conditioned wireless channel $\mathbf{H}$. Alternatively, for integral multiples of $\tau = kT_s$ ($k = 1, 2, ...$), integral DPST provides a cyclic shift of transmitted data streams at the receiver. This integral delay can be interpreted as a variation of cyclic delay diversity (CDD), which does not lead to spatial multiplexing gain. To further explain, the BS pulse shaping filter shapes the pulses so that the zero-crossings at the output of the receiving filter take place at integral multiples of T_s. Therefore, when sampling is performed at integral multiples of T_s, only one pulse is non-zero and the rest are zeros, complying with the original rule of orthogonality.

For fractionally delayed values of $\tau \neq kT_s$ ($k = 1, 2, ...$), the matrix $\mathscr{I}(\tau)$ becomes a block diagonal matrix operating on the streams of the input sequence $\{s_2[1], s_2[2], \cdots s_2[k]\}$ which correspond to the second transmit antenna. As a result, the signals corresponding to adjacent antenna elements are shaped with distinct pulse shaping filters. Note that this will introduce ISI in time domain, which increases the order of the composite channel between the transmit and receive streams, as shown in Fig. 5.1. On the contrary to integral delay, fractional delay prompts the pulses not to be orthogonal any more, which leads to different non-zero pulses at sampling points, and therefore the pulses are interfering with each other (introducing ISI). It is worth noting that the transmitted signals by antenna 1 and antenna 2 are not matched any more, and thus the corresponding signal degradation is taken into account. Moreover, in case of sinc pulse shaping, even a very small fractional delay introduces ISI terms, which is exploited to enhance the diversity among different channel pairs.

5.4.2 Receiver Design Considerations - Fractionally Spaced Equalisation

The sinc interpolation shown in (5.11) can be interchanged and alternatively represented as

$$\begin{bmatrix} x_1(t) \\ x_2(t) \end{bmatrix} = \left(\begin{bmatrix} h_{1,1}(t) & h_{1,2}(t) \\ h_{2,1}(t) & h_{2,2}(t) \end{bmatrix} * \begin{bmatrix} \mathscr{I}(0) & 0 \\ 0 & \mathscr{I}(\tau) \end{bmatrix} \right) \begin{bmatrix} s_1(t) \\ s_2(t+\tau) \end{bmatrix} \tag{5.13}$$

Assuming that ultra-dense small cell networks are interference-limited, the noise term is ignored and so the received signal at antennas 1 and 2 can be rewritten as

$$\begin{bmatrix} x_1(t) \\ x_2(t) \end{bmatrix} = \begin{bmatrix} \mathscr{I}(0) * h_{1,1}(t) & \mathscr{I}(\tau) * h_{1,2}(t) \\ \mathscr{I}(0) * h_{2,1}(t) & \mathscr{I}(\tau) * h_{2,2}(t) \end{bmatrix} \begin{bmatrix} s_1(t) \\ s_2(t) \end{bmatrix} \tag{5.14}$$

At the receiver side, to comply with DPST requirement, the receiver must operate at a rate significantly greater than the symbol period. This is in order to be consistent with the interpolation stage at the transmitter as well as to mitigate the ISI. For this purpose, fractionally spaced equaliser (FSE) is used, which is a finite impulse response (FIR) filter and the spacing between its taps is a fraction of symbol period. FSE is implemented by sampling the received signals P times (typically $P \geq 2$) within the time interval $t \in (kT_s, [k+1]T_s]$ where $t = (k + \frac{1}{P})T_s$ and is stacked as a $P \times 1$ vector, i.e.,

$$\begin{bmatrix} x_1(t = kT_s) \\ \vdots \\ x_1(t = (k + \frac{P-1}{P})T_s) \end{bmatrix} = \underbrace{\mathscr{I}_{\mathrm{R}} \begin{bmatrix} \mathscr{I}(0) * h_{1,1}(t) \\ \mathscr{I}(\tau) * h_{1,2}(t) \end{bmatrix}^T}_{\mathbf{H}_{1,os}[k]} \begin{bmatrix} s_1(t) \\ s_2(t) \end{bmatrix} \tag{5.15}$$

$$\mathbf{x}_{1,os}[k] = \mathbf{H}_{1,os}[k]\ \mathbf{s}[k] \tag{5.16}$$

$$\begin{bmatrix} x_2(t = kT_s) \\ \vdots \\ x_2(t = (k + \frac{P-1}{P})T_s) \end{bmatrix} = \underbrace{\mathscr{I}_{\mathrm{R}} \begin{bmatrix} \mathscr{I}(0) * h_{2,1}(t) \\ \mathscr{I}(\tau) * h_{2,2}(t) \end{bmatrix}^T}_{\mathbf{H}_{2,os}[k]} \begin{bmatrix} s_1(t) \\ s_2(t) \end{bmatrix} \tag{5.17}$$

$$\mathbf{x}_{2,os}[k] = \mathbf{H}_{2,os}[k]\ \mathbf{s}[k] \tag{5.18}$$

where $\mathbf{s}[k] = \mathbf{s}(t = kT_s)$ and $\mathbf{x}_{1,os}$ and $\mathbf{x}_{2,os}$ are the interpolated signals at the first and second receive antennas, respectively, which are $P \times 1$ vectors. $\mathscr{I}_R$ is the $(N \times P) \times N$ oversampling matrix at each receiver antenna. Note that for consistency with the interpolated pulse shaping at transmitter, *sinc interpolation* as shown in (5.19) is also exploited at the receiver. From a receiver perspective, the signals from the two transmit antennas are observed at kT_s and $kT_s + \tau$ ($k = 1, 2, \ldots$), respectively. It is important to realise that the triggered diversity can be only extracted by the receiver if it is operating in an oversampled domain. Moreover, exploiting an oversampled receiver allows the UE to suppress the ISI using an equalizer.

$$\mathscr{I}_{pn} = \mathrm{sinc}\left(\frac{p(\frac{T_s}{P \times N}) - n(\frac{T_s}{N})}{\frac{T_s}{N}} \right) \quad \begin{cases} n = 1, 2, \ldots, N \\ p = 1, 2, \ldots, P \times N \end{cases} \tag{5.19}$$

Stacking the $P \times 1$ vectors $\mathbf{x}_{1,os}[k]$ and $\mathbf{x}_{2,os}[k]$ from both receive antennas, gives

$$\mathbf{x}_{os}[k] = \begin{bmatrix} \mathbf{x}_{1,os}[k] \\ \mathbf{x}_{2,os}[k] \end{bmatrix} = \begin{bmatrix} \mathbf{H}_{1,os} \\ \mathbf{H}_{2,os} \end{bmatrix} * \mathbf{s}[k] = \mathbf{H}_{os} * \mathbf{s}[k] \tag{5.20}$$

It can be understood from (5.20) that due to fractionally delayed interpolated pulse shaping, the diversity of the channel is enhanced because the columns of $\mathbf{H}_{1,\mathrm{os}}$ and $\mathbf{H}_{2,\mathrm{os}}$

are independent of each other. This indicates that the rank of the composite channel $\mathbf{H}_{\mathrm{os}}$ is greater than 1. It is also noticed that the composite channel matrix $\mathbf{H}_{\mathrm{os}}$ is a tall matrix, which becomes a full rank column matrix subject to the sufficient pulse shaping diversity. Moreover, it has to be indicated that while SINR at a given sampling instant can be degraded due to pulses interfering with each other, the overall SINR after receiver equalisation can still be large enough by exploiting the pulse diversity to allow decoding.

From the receiver point of view, the combined effect of DPST and FSE enhances the degrees of freedom and reduces the correlation between different pairs of the composite channel $\mathbf{H}_{\mathrm{os}}$. This composite channel $\mathbf{H}_{os}$ can be represented as

$$\mathbf{H}_{\mathrm{os}} = \mathscr{I}_{\mathrm{Rx}}(\mathbf{H} * \mathscr{I}_{\mathrm{Tx}}), \tag{5.21}$$

where $\mathscr{I}_{\mathrm{Tx}}$ and $\mathscr{I}_{\mathrm{Rx}}$ are $2N \times 2M$ and $2P \times 2N$ matrices that are comprised of the interpolation matrices at both antennas at the transmitter and receiver sides, respectively. It is worth reminding that the deterministic fractional delay is incorporated in $\mathscr{I}_{\mathrm{Tx}}$.

5.4.3 Matrix Dimension Reduction and Power Normalizsation

Due to the interpolation stages involved at both transmitter and receiver sides, the composite channel matrix $\mathbf{H}_{\mathrm{os}}$ is of larger dimensions than $\mathbf{H}$. To downsize $\mathbf{H}_{\mathrm{os}}$ with respect to $\mathbf{H}$, the composite channel is decomposed using SVD as $\mathbf{H}_{\mathrm{os}} = \mathbf{U}_{\mathrm{os}}\Sigma_{\mathrm{os}}\mathbf{V}_{\mathrm{os}}^{\mathrm{H}}$, and since $\mathbf{H}$ refers to a 2×2 MIMO channel matrix, $\mathbf{U}_{\mathrm{os}}$ and $\mathbf{V}_{\mathrm{os}}$ only take the first two columns and rows, respectively, in the sequel.

$$\mathbf{H}_{\mathrm{R}} = \mathbf{U}_{\mathrm{os}}(:,1:2)^{\mathrm{H}}\,\mathbf{H}_{\mathrm{os}}\,\mathbf{V}_{\mathrm{os}}(1:2\,,:)^{\mathrm{H}} \tag{5.22}$$

The downsized channel $\mathbf{H}_{\mathrm{R}}$ must also be normalised with respect to the initial channel $\mathbf{H}$. The normalised channel is then obtained as

$$\mathbf{H}_{\mathrm{N}} = \mathbf{H}_{\mathrm{R}} \times \frac{\| \mathbf{H} \|_2}{\| \mathbf{H}_{\mathrm{R}} \|_2}, \tag{5.23}$$

where $\| \; \|$ is the Frobenius norm.

Prior to downsizing, there are still some redundancy in the channel matrix $\mathbf{H}_{\mathrm{os}}$. However, when the dimension of the channel is reduced, the residual small singular values are removed, and, therefore, the condition number of the channel $\mathbf{H}_{\mathrm{R}}$ witnessed by the receiver is improved. Overall, the diversity enhancement of the virtual MIMO channel $\mathbf{H}_{\mathrm{N}}$ is attributed to

- the introduction of deterministic fractional delay realised though distinct interpolated pulse shapes,
- the higher order channel observed at the receiver due to fractionally spaced equaliser and the elimination of the residual singular values.

5.4.4 Precoding and Detection

As discussed in 5.4.1 and 5.4.2, the virtual channel $\mathbf{H}_\mathrm{N}$ benefits from enhanced diversity.

At the transmitter, in order to perform precoding, SVD precoding is selected as $\mathbf{H}_\mathrm{N} = \mathbf{U}_\mathrm{N}\Sigma_\mathrm{N}\mathbf{V}_\mathrm{N}^\mathrm{H}$, and extract the first two columns of $\mathbf{V}_\mathrm{N}$ to generate the precoding matrix denoted by $\mathbf{W}$ where $\mathbf{W} = \mathbf{V}_\mathrm{N}(:,1:2)$. The precoding matrix is then subject to power scaling since it must not violate the BS transmission power constraint, i.e.,

$$\mathbf{W} = \sqrt{P_\mathrm{BS}} \times \rho \times \mathbf{W}, \tag{5.24}$$

where P_BS is the BS transmit power and ρ is the power scaling ratio. The precoded channel $\mathbf{H}_\mathrm{eq}$ is then defined as $\mathbf{H}_\mathrm{eq} = \mathbf{H}_\mathrm{N}\mathbf{W}$.

At the receiver side, minimum mean squared error (MMSE) equaliser is exploited, which is defined as

$$\mathbf{F}^\mathrm{MMSE} = \begin{bmatrix} f_{1,1} & f_{1,2} \\ f_{2,1} & f_{2,2} \end{bmatrix} = \mathbf{H}_\mathrm{eq}^\mathrm{H}(\mathbf{H}_\mathrm{eq}\mathbf{H}_\mathrm{eq}^\mathrm{H} + \Phi + N_0\mathbf{I})^{-1}, \tag{5.25}$$

where N_0 is the noise power and Φ is the inter-cell interference covariance matrix at the receiver denoted as $\Phi = \mathrm{E}\{\mathbf{v}\mathbf{v}^\mathrm{H}\}$ where $\mathbf{v} = [v_1\ v_2]^T$.

The SINR corresponding to data streams one and two are then computed as

$$SINR_{x_1}^\mathrm{Receive} = \frac{|f_{1,1}h_{1,1} + f_{1,2}h_{2,1}|^2}{I_{x_1} + N_0(|f_{1,1}|^2 + |f_{2,1}|^2)}, \tag{5.26}$$

$$SINR_{x_2}^\mathrm{Receive} = \frac{|f_{2,1}h_{1,2} + f_{2,2}h_{2,2}|^2}{I_{x_2} + N_0(|f_{1,2}|^2 + |f_{2,2}|^2)} \tag{5.27}$$

where I_{x_1} and I_{x_2} refer to the interferences at first and second receive antennas, and are defined as $|f_{1,1}h_{1,2} + f_{1,2}h_{2,2}|^2 + \mathrm{E}\{|f_{1,1}v_1 + f_{1,2}v_2|^2\}$ and $|f_{2,1}h_{1,1} + f_{2,2}h_{2,1}|^2 + \mathrm{E}\{|f_{2,1}v_1 + f_{2,2}v_2|^2\}$, respectively.

The transmitted data streams can be thus estimated using $\mathbf{F}^\mathrm{MMSE}$ operating on the received signals as

$$\hat{\mathbf{s}}[k] = \mathbf{F}^\mathrm{MMSE}(\mathbf{U}_\mathrm{os}^\mathrm{H}\mathbf{H}_\mathrm{os} * \mathbf{s}[k]) \tag{5.28}$$

Despite that ultra-dense small cell networks are assumed to be interference limited, the DPST requirement for a receiver to operate in an oversampled domain according to 5.4.2 can give rise to the question of the oversampling impact on the noise signal and accordingly on the overall performance. Note that it is assumed that the signal is band limited which is corrupted by thermal and quantisation noise. However, oversampling only modifies the quantisation noise, and does not alter any thermal noise terms and hence the noise spectral density does not change.

5.4.5 Differentiation with Cyclic Delay Diversity

Cyclic delay diversity (CDD) [133] [134] [135] is known as a diversity technique used in LTE for spatial multiplexing applications aiming to enhance the diversity between different data streams. In CDD, different antennas transmit a cyclically shifted version of the same signal to achieve a diversity gain [136]. The cyclic shift in time domain is equivalent to phase shift in frequency domain, and offers the same impact as frequency diversity.

It is important to emphasise that DPST differs from CDD. On the contrary to CDD, in DPST each antenna transmits its own individual signal, which is modulated with a distinct pulse shape and then transmitted with a fractional real delay with respect to its former antenna, requiring to redesign the precoder and the receiver. However, according to [137], in CDD, the signal is not truly delayed, but cyclically shifted among the transmit antennas. While it might be projected that the fractional delay in time domain is translated into phase shift in frequency domain, the functionality of DPTS is different from techniques that aim to mitigate the correlation through phase rotation precoding techniques [138]. Owing to the fractional delay and interpolated pulse shaping, DPST injects deterministic ISI in order to increase the diversity among different channel pairs followed by an oversampled receiver to extract such diversity.

Having discussed the difference between DPST and CDD, it is also necessary to point out that while exploiting antenna polarisation at the transmitter is an effective technique in MIMO systems, it is usually limited to two transmit antennas [139]. Conversely, DPST can be applied to larger MIMO systems once the set of optimised fractional delays are acquired and applied to the transmit antennas.

5.4.6 Challenges associated with DPST

DPST benefits from singular value decomposition (SVD) which is not particularly practical since the complexity of finding the SVD of $N_t \times N_r$ matrix is of order $O(N_r N_t^2)$ if $N_r \geq N_t$ and requires a significant amount of feedback which is subject to channel estimation error and hence can degrade the performance of DPST. Moreover, considering the complexity of the DPST and the requirement to tune the optimum deterministic delay, the significant performance gain may only be feasible when there is no NLOS communication between UE and BS and the channel is prone to single LOS communication which might be the case in specific ultra-dense small cell deployment scenarios. However, the presence of NLOS communication between the UE and BS improves the channel initial condition number and this will degrade the again achieved through implementation of DPST.

5.5 Optimisation of Deterministic Delay in DPST

To optimise the deterministic delay, it is suggested that the performed FSE at the receiver is not considered as part of DPST delay optimisation. FSE is integrated into the DPST receiver design, and therefore is treated independently.

The optimisation aims to diagonalise the covariance matrix $\mathbf{R}_\mathrm{x}$ corresponding to the fractionally delayed interpolated pulse shaped channels associated with both transmit antennas $\mathbf{H}_\mathrm{Tx}$, i.e., a fully diagonal covariance matrix has only non-zero elements on its main diagonal and the rest of its elements are zero. Thinking in this line, the optimum delay aims to maximise each of the diagonal elements of the $\mathbf{R}_\mathrm{x}$ to 1, while minimising all non-diagonal elements. As a matter of fact, the optimisation attempts to jointly maximise the auto-correlation, while minimising the cross-correlation of the transmit antennas fractionally delayed interpolated pulse shaped channel covariance matrix.

$$\mathbf{H}_{\mathrm{Tx},1} = \mathbf{H}(:\,,\,1) * \mathscr{I}(0) = \begin{bmatrix} h_{1,1} \\ h_{2,1} \end{bmatrix}^{\mathrm{T}} * \begin{bmatrix} \mathscr{I}_{11}(0) & \mathscr{I}_{12}(0) & \cdots & \mathscr{I}_{1M}(0) \\ \mathscr{I}_{21}(0) & \mathscr{I}_{22}(0) & \cdots & \mathscr{I}_{2M}(0) \\ \vdots & \vdots & \ddots & \vdots \\ \mathscr{I}_{N1}(0) & \mathscr{I}_{N2}(0) & \cdots & \mathscr{I}_{NM}(0) \end{bmatrix} \tag{5.29}$$

$$\mathbf{H}_{\mathrm{Tx},2} = \mathbf{H}(:\,,\,2) * \mathscr{I}(\tau) = \begin{bmatrix} h_{1,2} \\ h_{2,2} \end{bmatrix}^{\mathrm{T}} * \begin{bmatrix} \mathscr{I}_{11}(\tau) & \mathscr{I}_{12}(\tau) & \cdots & \mathscr{I}_{1M}(\tau) \\ \mathscr{I}_{21}(\tau) & \mathscr{I}_{22}(\tau) & \cdots & \mathscr{I}_{2M}(\tau) \\ \vdots & \vdots & \ddots & \vdots \\ \mathscr{I}_{N1}(\tau) & \mathscr{I}_{N2}(\tau) & \cdots & \mathscr{I}_{NM}(\tau) \end{bmatrix} \tag{5.30}$$

where the components of $\mathscr{I}_{nm}(\tau)$ are computed based on (5.12). The corresponding covariance matrix $\mathbf{R}_\mathrm{x}(\tau)$ is thus defined as

$$\mathbf{H}\mathrm{Tx} = \begin{bmatrix}\mathbf{H}_{\mathrm{Tx},1} & \mathbf{H}_{\mathrm{Tx},2}\end{bmatrix}^T \tag{5.31}$$

$$\mathbf{R}_{\mathrm{X}}(\tau) = \mathbf{H}_{\mathrm{Tx}}\ \mathbf{H}_{\mathrm{Tx}}^{\mathrm{T}} = \begin{bmatrix} \mathbf{r}_{x_{1,1}}(\tau) & \mathbf{r}_{x_{1,2}}(\tau) & \cdots & \mathbf{r}_{x_{1,P}}(\tau) \\ \mathbf{r}_{x_{2,1}}(\tau) & \mathbf{r}_{x_{2,2}}(\tau) & \cdots & \mathbf{r}_{x_{2,P}}(\tau) \\ \vdots & \vdots & \ddots & \vdots \\ \mathbf{r}_{x_{P,1}}(\tau) & \mathbf{r}_{x_{P,2}}(\tau) & \cdots & \mathbf{r}_{x_{P,P}}(\tau) \end{bmatrix} \tag{5.32}$$

The optimisation problem can then be formulated as

$$\begin{aligned} &\operatorname{argmax}\ \mathbf{r}_{x,i,i} = 1\ \forall\, i = 1,2,...,P \\ &\textit{subject to} \begin{cases} \operatorname{argmin}\ \mathbf{r}_{x,i,j}\ \ \forall\, i,j = 1,2,...,P\ \ i \neq j \\ \tau < T_s \end{cases} \end{aligned} \tag{5.33}$$

For antenna arrays of more than two antennas, the optimisation is modified since adjacent transmit antennas could be subject to non-identical fractional delays. Consequently, the optimisation becomes a multi-variate one that aims at finding the Pareto set of fractional delays corresponding to each transmit antenna that leads to the channel with least correlation. In this case, (5.31) can be obtained as

$$\mathbf{H}_{\mathrm{Tx},u\ (u\ =\ 2,3,...,U)} = \mathbf{H}(:\ ,\ u)\ *\ \mathscr{I}(\tau_u) \tag{5.34}$$

$$\mathbf{H}_{\mathrm{Tx}} = \begin{bmatrix}\mathbf{H}_{\mathrm{Tx},1} & \mathbf{H}_{\mathrm{Tx},2} & \cdots & \mathbf{H}_{\mathrm{Tx},K}\end{bmatrix}^T \tag{5.35}$$

where τ_u refers to the fractional delay imposed to the transmission of u-th transmit antenna and U is the total number of transmit antennas.

Note that an optimum delay will result in a channel, whose singular values all exist within the interval $[1-\varepsilon\ ,\ 1+\varepsilon]$ where $\varepsilon \in (0,1)$. This is a hard problem since a polynomial cannot be found to formulate the problem. Moreover, since an existing NP-complete problem cannot be encoded into this, it is concluded that this is an NP hard problem. Considering that this is an NP hard problem, there is no efficient, general purpose methods that can be exploited. Since the fractional delay τ is a one dimensional element, a brute force search over discrete values of τ can provide us with a reasonably accurate estimate.

5.6 Simulation and Discussion

A single tier hexagonal layout consisting of seven small cell BSs in a $500m \times 500m$ scenario with different ISDs is considered to observe the impact of DPST on various degrees of network densification. The central cell is designated as the serving cell and the remaining six cells are considered as interferers. Downlink communication is only considered and it is assumed that all the small cell BSs operate in the 2 GHz band. Macrocell BSs are assumed to operate in a different frequency band and are not considered in this performance evaluation. To capture the enhanced spatial correlation due to densification, the ISDs of 20 m, 50 m, and 100 m are takedn into account. Each small cell consists of an array of two and four transmit antennas, and only serves a single UE in one frequency resource. The UE also has two and four antennas, thus forming 2×2 and 4×4 MIMO systems, respectively. Spacings of 0.25λ and 0.1λ between antenna elements of both arrays at UE and BS for the 2×2 and 4×4 systems are assumed, respectively where λ refers to the wavelength corresponding to the operating frequency. The input signal consists of 10 samples with an oversampling ratio of 2. The focus is on a single frequency resource case, and antenna gain, path loss, lognormal shadowing and multi-path Rician fast fading are included in SINR computation. The path loss model that is used is the microcell urban model defined in [89], which includes both the LOS and NLOS components. At the receiver, MMSE receive filter is used. Note that closed-loop precoding is considered. Note that in the legend of the figures, "corr" represents the correlated channel scenario and "corr+DPST" refers to the scenario that DPST is applied to the correlated channel model.

In the following, it is first shown how spatial correlation as a result of densification degrades the effective SINR and UE throughput. Then the simulation results for DPST are provided, and it is shown how it can considerably enhance the effective SINR as well the UE throughput.

5.6.1 Performance Degradation versus Densification

To show the performance degradation due to densification, the effective SINR and UE throughput CDFs of 2×2 and 4×4 MIMO systems under both uncorrelated and correlated multi-path fading channel conditions are compared. When considering uncorrelated multi-path channel, the channel taps are Rayleigh distributed, while for correlated scenarios, the channel model presented in Section 5.3 is used, which captures the impacts of UE-BS distance and the spacing between antenna elements on spatial correlation.

Fig. 5.3(a) compares the effective SINR CDF of a 2×2 MIMO system when using uncorrelated and correlated multi-path fading channels at different ISDs. When considering uncorrelated scenarios, it can be observed that the SINR CDF worsens with the lower ISD. This is because the path loss of interfering signals transit from NLOS to LOS interference with the densification, and therefore, the interference grows faster than the carrier signal [140]. When considering correlated channel scenarios, the SINR CDF further worsens since a new degree of channel correlation is introduced through the multi-path domain resulting in an ill-conditioned channel. At ISDs of 20 m, 50 m and 100 m, the difference in 50%-tile effective SINR between the uncorrelated and correlated scenarios is about 4 dB, 4.85 dB and 6.3 dB, respectively. Worth noting that as network becomes denser, the difference in 50%-tile effective SINR between the uncorrelated and correlated channels decreases. This is because at very low ISDs, the LOS path loss dominates the SINR and hence the impact of spatial correlation and consequently the multi-path fading becomes more trivial. Fig. 5.3(b) presents a similar comparison in terms of UE throughput CDF of uncorrelated and correlated channels. At ISDs of 20 m, 50 m and 100 m the gain of the 50%-tile UE throughput from uncorrelated to correlated scenarios is about 1.92x, 1.78x and 1.65x, respectively.

Figs. 5.4(a) and 5.4(b) show the same performance comparisons for a 4×4 MIMO system, which can potentially take advantage of upper bound of 4 in terms of the channel degrees of freedom. In terms of effective SINR, at ISDs of 20 m, 50 m and 100 m, the difference at 50%-tile effective SINR between the uncorrelated and correlated systems is about 4.5 dB, 6.8 dB and 10.45 dB, respectively. In terms of UE throughput, at ISDs of 20 m, 50 m and 100 m the gain of the 50%-tile UE throughput from uncorrelated to correlated scenarios is about 3.4x, 3.05x and 1.96x, respectively. It is worth noting that as the dimension of MIMO system increases, due to channel higher degrees of freedom the uncorrelated over correlated gain increases.

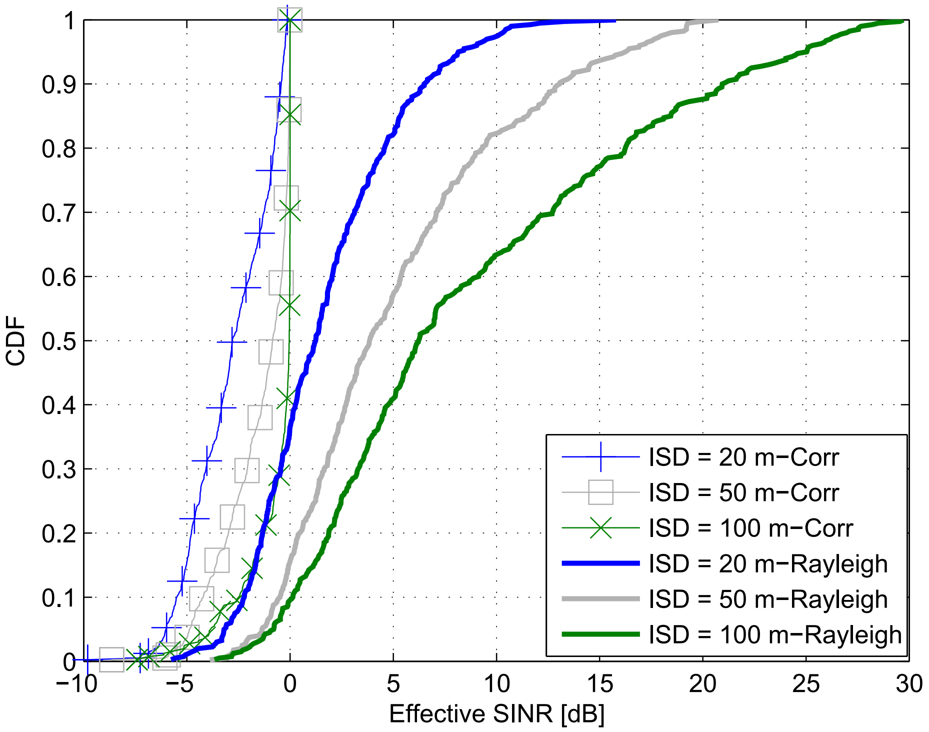

(a) Effective SINR CDF.

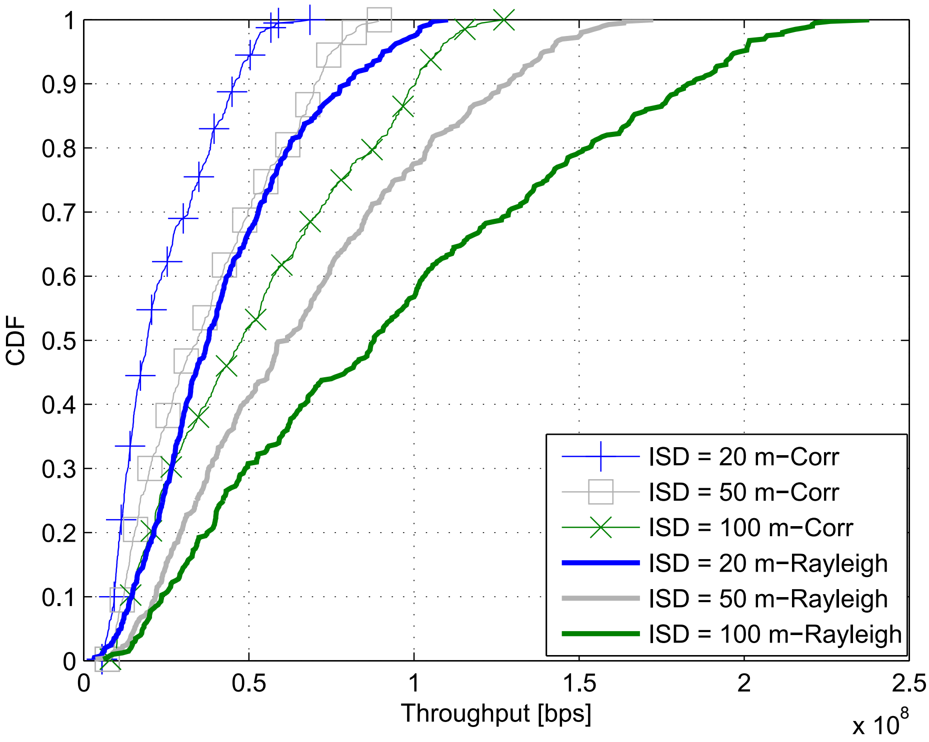

(b) UE throughput CDF.

Fig. 5.3 SINR and throughput CDFs comparison of correlated and Rayleigh channels for a 2x2 MIMO.

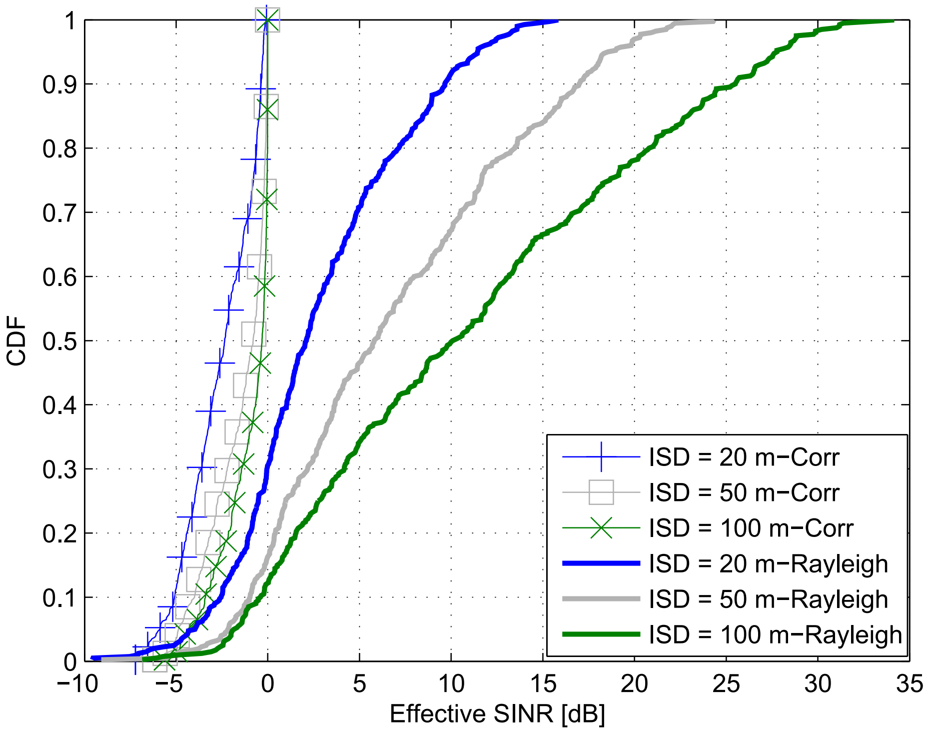

(a) Effective SINR CDF.

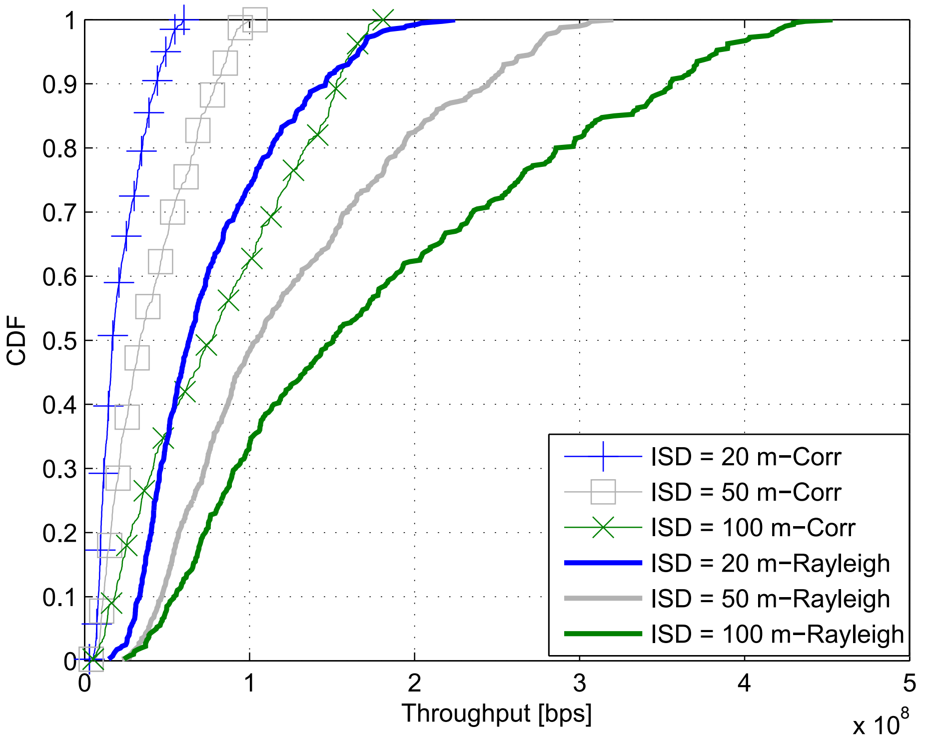

(b) UE throughput CDF.

Fig. 5.4 SINR and throughput CDFs comparison of correlated and Rayleigh channels for a 4x4 MIMO.

5.6.2 Performance Enhancement by DPST

It was shown that the reinforced spatial correlation due to network densification significantly lowers the effective SINR and UE throughput. Indeed, it was realised that when channel suffers from larger correlation due to discussed causes, the UE receiver is only able to decode the data stream transmitted by the first transmit antenna and fails to decode the data streams sent by the remaining antennas.

In the sequel, DPST is applied to the correlated channel presented in Section 5.3 to perceive how enhanced diversity among channel pairs (as an outcome of increased ISI due to fractional delay and oversampled receiver) impacts the channel condition number from the receiver perspective. Note that in DPST each transmit antenna is subject to a specific fractional delay with respect to its former one, which is determined according to Section 5.5. As discussed, the optimisation seeks to get the Pareto set of fractional deterministic delays corresponding to each transmit antenna that results in the least correlated effective channel. In the 2×2 MIMO, the optimum fractional delay is 0.5 nsec, whereas in the 4×4 MIMO the optimum Pareto set of fractional delays is [0.25 nsec, 0.45 nsec, 1.5 nsec] applied to second, third and forth transmit antennas. Furthermore, the performance of DPST is also compared with respect to the optimistic channel, which benefits from channel condition number ($\mathscr{K}$) equals to 1. This refers to the optimal channel condition where all the channels are orthogonal, and hence the UE throughput can be enhanced by the minimum number of transmit/receiver antennas.

Figs. 5.6(a) and 5.6(b) compare the effective SINR and UE throughput CDFs for a 2×2 MIMO system where DPST is applied to the correlated channel. Results show that at all tested ISDs, DPST can significantly improve the effective SINR and UE throughput with respect to the case of no DPST, offering a very close to optimal performance. The attained 50%-tile SINR improvement by DPST with respect to correlated scenario – where no DPST is applied – at ISDs of 20 m, 50 m and 100 m is about 6.7 dB, 10.2 dB and 13.6 dB, respectively. At all respective ISDs, DPST performance is only about 0.14 dB away from the optimum performance.

Note that this significant performance enhancement by DPST is because through the optimisation of deterministic delay, DPST is able to lower the condition number of the virtual channel as close as possible to 1. Accordingly, DPST is also able to boost the UE throughput by almost 1.93x at all respective ISDs, which is less than 1.03 away from optimum performance. This implies that even at very low ISDs, where the channel struggles with high degree of spatial correlation, DPST remarkably enhances the UE throughput through lowering the channel condition number. Note that the choice of optimum delay plays a key role in DPST performance. Fig. 5.5 shows that in a 2×2 MIMO system and at ISDs of 20 m, 50 m and 100 m, the optimum delay boosts the UE throughput by 1.95x, 1.86x, 1.4x with respect to non-optimum delay of 1.5 nsec.

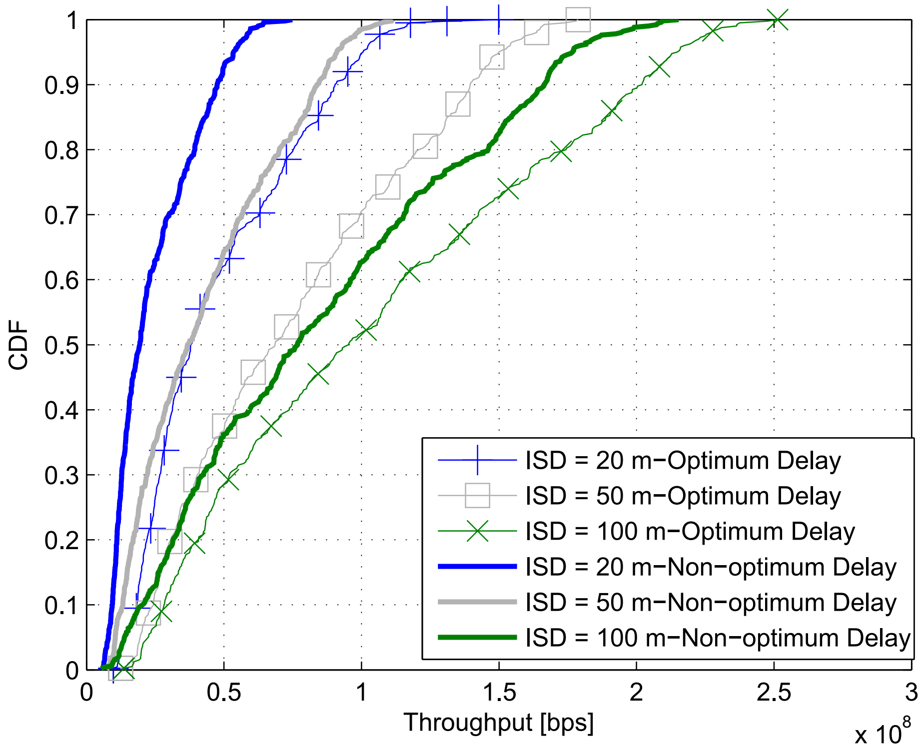

Fig. 5.5 Impact of optimum and non-optimum delays on UE throughput CDF.

Similarly, Figs. 5.7(a) and 5.7(b) compare the performance of a 4×4 MIMO system. Likewise, DPST enhances the effective SINR and UE throughput. In more detail, at ISDs of 20 m, 50 m and 100 m, DPST enhances the 50%-tile wideband SINR with respect to the correlated channel by 9.6 dB, 12.6 dB and 14.8 dB, respectively. However, the extent of improvement with respect to optimum scenario ($\mathscr{K} = 1$) differs from that of the 2×2 MIMO system. Performance from the optimum is about 0.15 dB, 0.8 dB and 1 dB away at respective ISDs. In terms of the UE throughput, it can perceived that UE throughput is enhanced by about 3.76x when DPST is exploited and the difference between DPST and optimum scenarios at all ISDs is about 1.13x.

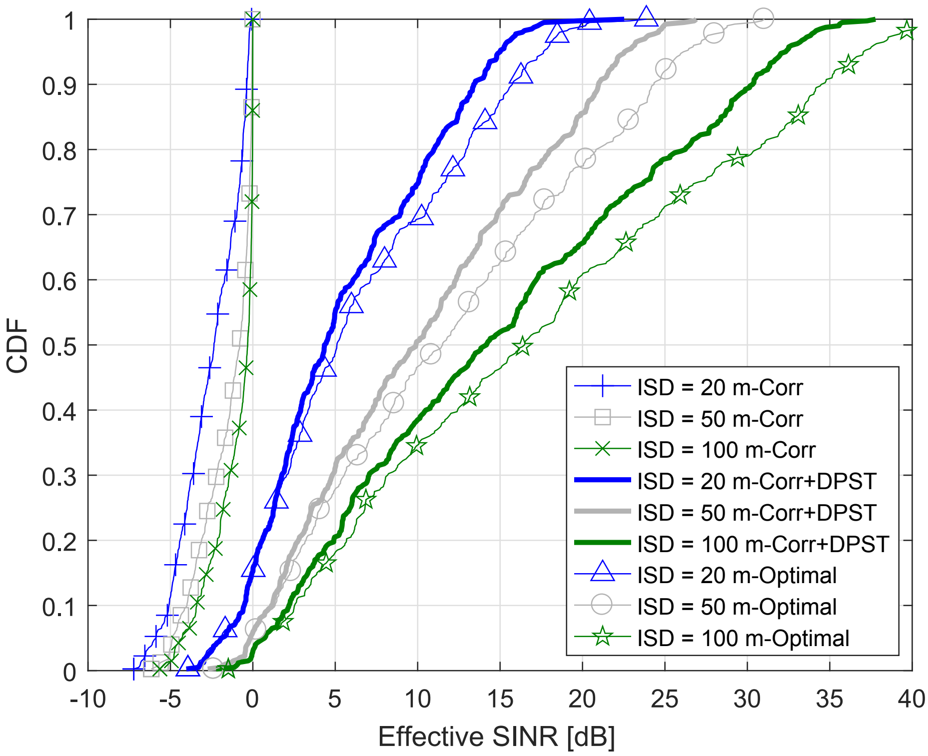

(a) Effective SINR CDF.

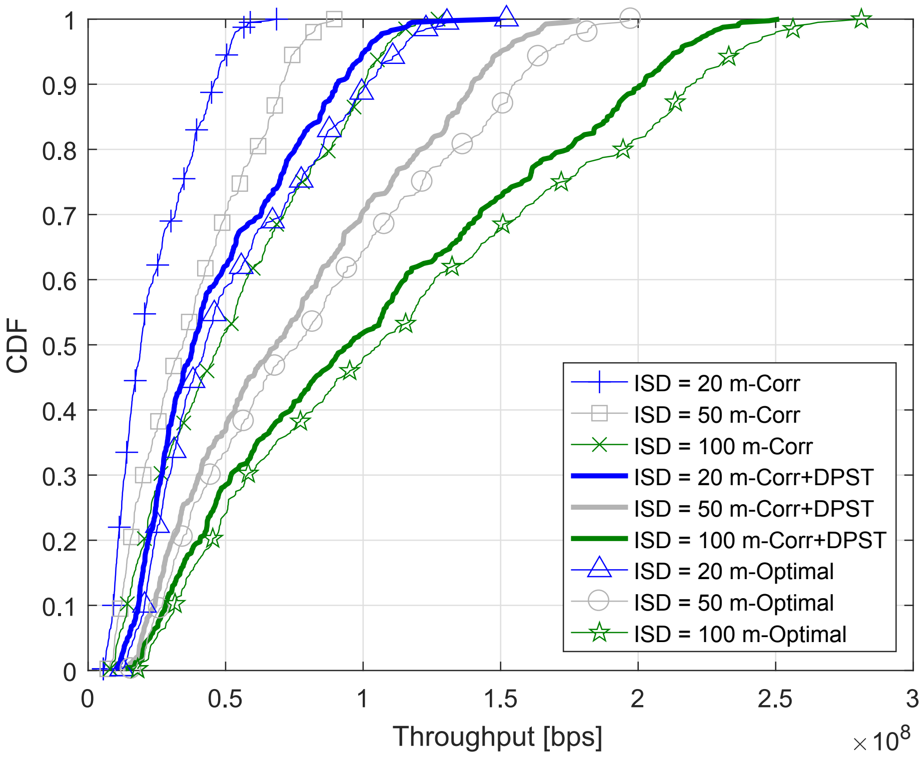

(b) UE throughput CDF.

Fig. 5.6 SINR and throughput CDFs comparison of correlated, DPST and optimum channel conditions for a 2x2 MIMO.

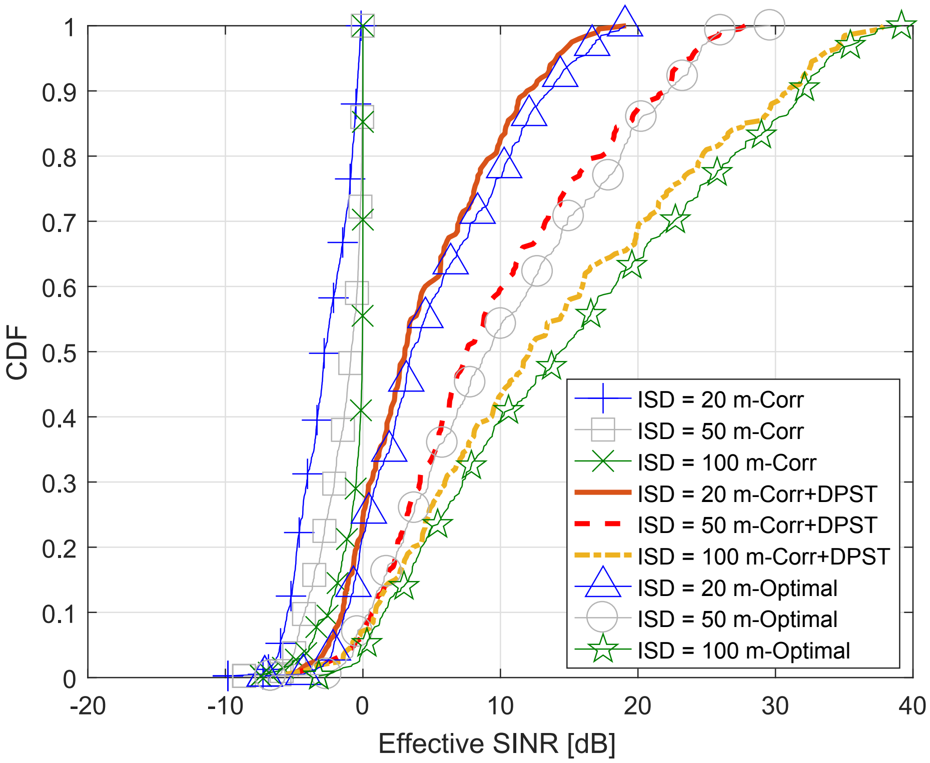

(a) Effective SINR CDF.

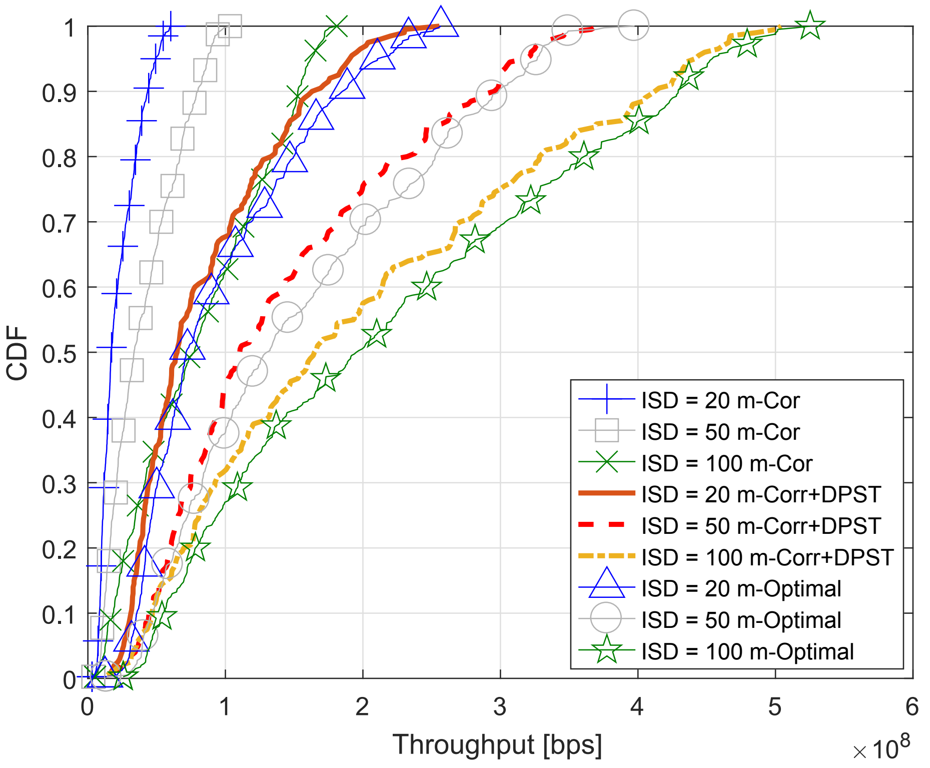

(b) UE throughput CDF.

Fig. 5.7 SINR and throughput CDFs comparison of correlated, DPST and optimum channel conditions for a 4x4 MIMO.

Table 5.1 Performance comparison under different channel condition

Channel Status	**Channel Rank**	**Channel Condition Number**
LOS channel (Default)	1	∞
2×2 Rayleigh	2	4.45
2×2 DPST	2	1.31
2×2 Optimum	2	1
4×4 Rayleigh	4	9.35
4×4 DPST	4	1.42
4×4 Optimum	4	1

Table 5.1 summarizes the rank and condition number of different channel scenarios. Beware that DPST refers to the virtual channel attained after applying DPST with optimum deterministic fractional delay to the correlated channel. Also, it must be stated that the condition number is obtained over an average of 10000 different realisations of the channel type. As shown in table 5.1, the system performance when the DPST channel is used outperforms that of the Rayleigh channel. While Rayleigh channel offers a well conditioned channel, it is still far from the optimal channel (condition numbers of 4.45 and 9.35 for 2×2 and 4×4 MIMO systems, respectively). In contrast, the combined effects of the i) optimised deterministic fractional delay interpolated with sinc pulse shaping and the ii) the oversampled receiver helps DPST to forcefully converge to a virtual channel with a condition number of close to 1.

5.7 Conclusion

In this chapter, it has been discussed that in ultra-dense small cell networks, the presence of spatial channel correlation is an obstacle to achieve spatial multiplexing gain. Therefore, a model for the channel correlation, which captures the effects of both UE-BS distance and antenna spacing as the main sources of spatial correlation has been proposed. It has been shown that in ultra-dense small cell networks, due to enhanced spatial correlation, it is almost impossible to simultaneously transmit and decode multiple data stream and hence achieve spatial multiplexing gain. In order to overcome this challenge, a new transmission scheme referred to as diversity pulse shaped transmission (DPST) has been proposed for the first time that modulates the transmission of adjacent antennas at the transmitter with distinct interpolated shaped pulses which are offset by a deterministic delay which must be a fraction of symbol period. At the receiver side, DPST takes advantage of fractionally spaced equaliser (FSE) that operates in the oversampled domain to extract the enhanced channel diversity. The combined effects of DPST and FSE is able to significantly enhance the diversity among the channel pairs, and thus generates a virtual MIMO channel with reduced correlation among its pairs from the receiver perspective. It has been shown that DPST can reduce the channel condition number close to one and, therefore, enhance the UE throughput by 1.93x and 3.76x in 2×2 and 4×4 MIMO systems, respectively.

Chapter 6

Conclusions and Future Work

6.1 Conclusion

This dissertation focused on understanding different challenges associated with ultra-dense small cell networks as well as its implications as a key paradigm in development of the next generation of mobile communications. In the following, the main contributions of chapters 2-5 are summarized.

- In chapter 2, it was discussed that at least a 100 × network capacity increase would be required to meet the exponentially increasing traffic demands over the next decade. For the first time, an in-depth survey was conducted on network densification, the use of higher frequency bands, and spectral efficiency enhancement techniques as the three main paradigms to drive the capacity enhancement to not only bring further common understanding, but also to analyse their potential gains and limitations. An outdoor simulation scenario of 500 m × 500 m was considered where small cell BSs were placed in a uniform hexagonal grid with different ISDs resulting in different number of small cell BSs per square km. The impact of idle mode capabilities at the small cell BSs as well as UE density and distribution and cell-edge SNR target were also studied. Extensive simulation results were performed under various simulation settings aiming to provide some insights on Pareto set of network configurations that can achieve the desired average UE throughput of 1 Gbps for the next generation of mobile communications. A key observation from simulations results was that densifying further than the 1 UE per small cell BS sweet spot requires an exponential increase in investment to achieve a diminishing logarithmic capacity gain through signal quality enhancement, implying that when the network is dense enough, a large number of small cell BSs have to be added to the network to enhance the UE throughput in a noticeable manner, which may not be cost effective. It was further discovered that beamforming gains are larger at cell-edge of larger cell sizes and that activation of idle mode at small cell BSs with no active UE can significantly mitigate interference and hence allows the UE SINR to be greatly boosted with the cell density. As a major remark, it was emphasised that idle mode capability must be utilized in future small cell BSs in order for mobile operators to realize the remarkable gains of network densification. Finally, the simulation results showed that for a realistic non-uniformly distributed UE density of 300 active UE per square km, the average UE throughput of 1 Gbps can be achieved with an ISD of 75 m, 500 MHz bandwidth and 4 antennas per small cell BS. The results of this chapter have been published in [P1].

- In chapter 3, it was discussed that scheduling has been perceived as an effective technique to efficiently use the available spectrum and improve network throughput in macrocell scenarios with a large number of UEs per macrocell BS. In particular, proportional fair scheduler has been used as an appealing scheduling technique that offers a good trade-off between maximising throughput and improving fairness among UEs with diverse channel conditions. However, in ultra-dense small cell networks, not only UEs are located closer to their serving BSs, but also the number of UEs per active BS is considerably reduced and, therefore, it is necessary to investigate whether proportional fair scheduling is efficient for ultra-dense small cell networks. For the first time, the performances of different scheduling algorithms were analysed under different densification levels and some fundamental tradeoffs of network densification were presented. Considering the high density of BSs and the relative proximity of UEs to their serving BSs in ultra-dense small cell networks, novel models were proposed for both small scale Rician fading K factor and cross-correlation large scale shadow fading to more accurately capture the impact of densification on the performance of scheduling algorithms. The analysis demonstrated that as the cell size reduces, multi-user diversity gains also vanish and serving more UEs does not bring any further gain in cell throughput. As major remark, it was proved that the channel-dependent proportional fair scheduling gains over channel-independent round robin scheduling are only $(\approx 10\%)$ at low ISDs and hence round robin scheduling may be a better choice in dense small cell deployments considering its considerably lower complexity. This conclusion has a significant impact in the manufacturing of small cell BSs where the digital signal processing cycles saved due to the adoption of round robin scheduling, can be used to adopt more advanced idle mode algorithms. The results of this chapter have been published in [P1] and [P6].

- In chapter 3, it was also discussed that deployment of small cell BSs in large numbers, i.e., tens of millions, would lead to massive power consumption and, therefore, energy efficiency of ultra-dense small cell deployments must be carefully investigated to allow the deployment of sustainable networks. Using the power model developed by the GreenTouch project, a comprehensive survey was conducted on the power consumption of different small cell BS sizes (different ISDs) assuming different number of antennas and various idle mode states. In addition to the slow idle mode and the shut-down mode models provided by the GreenTouch project, two futuristic idle modes were also proposed, where their energy consumption were 15% and 0% of the GreenTouch slow idle mode power consumption model. A key finding was that for any given idle mode, increasing the number of antennas at the small cell BS always decreases the energy efficiency since the performance gain provided by adding a new antenna through beamforming is not large enough to cope with the increase in power consumption due to addition of a new antenna chain at the small cell BS. This is particularly important since in macrocell networks, adding a new antenna chain does not lead to a large increase in the total power consumption of the BS. The simulation results Comparison of different idle modes associated with different energy consumptions demonstrated that the lower the power consumption in the idle mode, the larger the energy efficiency of the network and so the network energy efficiency only increases with densification if the energy consumption in idle mode is (0%). This major observation indicates that the only way to enhance the energy efficiency of ultra-dense small cell networks is to develop advanced idle mode capabilities where the small cell BS has zero power consumption from the energy grid in the idle mode. In this regard, the use of energy harvesting technologies such as thermoelectric and mechanical energy harvesting based on vibration energy harvesting techniques in the context of small cell networks was proposed which are able to provide minimal power to keep the small cell BS alive when it is in idle mode. The results of this chapter have been published in [P1].

- In chapter 4, it was discussed that most studies on small cell networks have considered simplistic single slope path loss models that do not differentiate LOS and NLOS transmissions and hence have concluded that coverage probability would linearly increase with BS density. However, in ultra-dense small cell networks, the small distances between UEs and BSs bring a change in the channel characteristics, which in turn may significantly impact the network performance, i.e., the channel may become LOS dominated. Moreover, most studies have considered Rayleigh fading for LOS communication, which is an oversimplification, as the multi-path fading in LOS transmission is well known to be non-Rayleigh distributed. In this regard, for the first time a practical distance dependent Rician fading with a variant Rician K factor was exploited along with a novel piecewise multi slope path loss model that features piecewise path loss functions with probabilistic LOS and NLOS transmissions. Analytical results were derived for the coverage probability and area spectral efficiency and it was demonstrated that coverage probability first increases as BS density increases, but as network becomes denser and exceeds a certain BS density, due to transition of many interfering signals from NLOS to LOS, the SINR degrades and so the coverage probability declines. It was further proved that conditioned on negligible difference between the deployment height of small cell BS and the average UE height, the impact of multi-path fading on the overall system performance is minor, and multi-path fading does not help to mitigate the performance loss brought by the NLOS-to-LOS transition of many interfering signals. This important remark proved that in ultra-dense small cell networks (and in contrary to macrocell networks), the coverage probability does not linearly increase with BS density and the small cell BS density does matter. This key conclusion shed new insights on the design and deployment of future ultra-dense small cell networks in order to cost-efficiently march across the undesirable BS density. The results of this chapter have been published in [P3] and [P5].

- In chapter 5, it was discussed that one flavour of MIMO technology is spatial multiplexing which refers to simultaneous transmission of independent data streams from different transmit antennas in order to eventually enhance the network capacity by the minimum number of transmit/receive antennas. Spatial multiplexing is conditioned based on the availability of distinct propagation paths for each transmit/receive pair. However, applying MIMO technology to ultra-dense small cell networks to achieve spatial multiplexing gain is nearly impossible due to channel pairs being highly correlated as a result of different propagation conditions in comparison to macrocell networks. In order to compensate for the loss of spatial multiplexing gain and enhance the UE's throughput over correlated MIMO channels in ultra-dense small cell networks, diversity pulse shaped transmission (DPST) was proposed for the first time as a novel transmission technique, whose combined arrangement based on pulse shaping diversity and deterministic delay as well as oversampled receiver through fractionally spaced equalizer (FSE) significantly enhances the diversity among the channel pairs. From the receiver perspective, the combined effect of DPST and FSE generates a virtual channel with reduced correlation among channel pairs that improves the overall dimensionality of the transmitted multi-antenna data streams. Consequently, DPST is able to compensate for the loss of spatial multiplexing gain in ulta-dense small cell networks and enhances the data rates by almost the minimum number of transmit/receive antennas.

The performance of DPST in a single tier hexagonal small cell layout was evaluated assuming 2×2 and 4×4 MIMO setups and it was proved that DPST can enhance the UE throughput by approximately 2× and 4×, respectively. The results of this chapter have been published in [P2] and [P7].

6.2 Future Research Directions

There are many interesting future research directions of the work presented in this thesis. In chapter 1, some of the challenges that are faced on the way towards the deployment of ultra-dense small cell networks were discussed. Moreover, in the remainder of this chapter, two topics are discussed and a brief overview of them are provided.

6.2.1 Dense Small Cell Millimetre Wave Frequency Networks

Millimetre wave (mmWave) communication is considered as one of the enabling technologies for the next generation of mobile communications. An interesting feature of mmWave systems, is that due to very high frequency (30-300 GHz) the corresponding wavelength is very small and such a decrease in wavelength reduces the size of antennas and, therefore, allows to pack large antenna arrays within the limited space at both the BS and UE. Large antenna arrays can provide the beamforming gain required to overcome the high path loss at mmWave frequencies, i.e., the path loss at 30 GHz is almost 20 dB larger than path loss at 3 GHz. However, dense small cell networks are considered to be interference limited and hence there is an inevitable need for new interference mitigation techniques exploiting the existing large antenna arrays. This opens up new research venues, i.e., organization of adjacent small cell BSs for cooperative transmission using beamforming and smooth handovers between mmWave small cells. Due to the presence of a hybrid array architecture at the BS in dense mmWave networks, partial zero forcing receiver can also be exploited as a strategy to simultaneously mitigate the interference while enhancing the desired signal strength. However, when an interferer is cancelled, the array gain is reduced. Therefore, an important challenge to tackle is how to keep a balance between boosting the desired signal strength while mitigating the interference.

6.2.2 Backhaul Energy Efficiency of Dense Small Cell Networks

One of the key challenges in small cell backhaul is the backhaul capacity because backhaul capacity must not constrain the small cell capacity and it should also be able to support the busy hour traffic and have enough margin to cover its future growth and statistical variation.

In addition to the capacity requirement of small cell backhaul, the backhaul energy efficiency is an important research topic that can limit the performance of dense small cell networks. There have been studies that have shown that backhaul energy efficiency start to decline once the density of deployed small cell BSs exceed a certain threshold. While it is perceived that densification can enhance the area spectral efficiency of the network, this comes at the cost of backhaul energy efficiency degradation. Therefore, there must be in-depth research to investigate the performance of backhaul energy efficiency versus densification at different frequency bands. As a result, since both the backhaul energy efficiency and the backhual capacity should not be limiting factors to the performance of small cell BSs, a future research endeavour is to determine the adaptive pareto set of parameters (degree of densification, backhaul solution, etc) that optimize the integrated access and backhaul network performance.

References

[1] MobiForge. Global mobile statistics 2014 Part A: Mobile subscribers; handset market share; mobile operators, 2014.

[2] Tim Berners-Lee. *Weaving the Web: The Original Design and Ultimate Destiny of the World Wide Web*. HarperBusiness, Nov. 2000.

[3] Ian McCulloh, Helen Armstrong, and Anthony Johnson. *Social Network Analysis with Applications*. John Wiley & Sons Ltd, Jul. 2013.

[4] T. Halonen, J. Romero, and J. Melero. *GSM, GPRS and EDGE performance: evolution towards 3G/UMTS*. John Wiley & Sons Ltd, 2004.

[5] Dapeng Wu, Student Member, Yiwei Thomas Hou, Wenwu Zhu, Ya qin Zhang, Jon M. Peha, and Senior Member. Streaming video over the Internet: approaches and directions. *IEEE Transactions on Circuits and Systems for Video Technology*, 11: 282–300, 2001.

[6] E. Setton, Taesang Yoo, Xiaoqing Zhu, A Goldsmith, and B. Girod. Cross-Layer Design of Ad-Hoc Networks for Real-Time Video Streaming. *IEEE Wireless Communications*, 12(4):59–65, Aug. 2005. ISSN 1536-1284. doi: 10.1109/MWC.2005.1497859.

[7] Qualcom. The 1000x Mobile Data Challenge: More Spectrum, More Small Cells, More Indoor Cells and Higher Efficiency. http://www.qualcomm.com/.

[8] Cisco. Cisco visual networking index: Global mobile data traffic forecast update, 2014 – Global Mobile Data Traffic Forecast Update, 2014-2019. White paper, Feb. 2015.

[9] A. Damnjanovic, J. Montojo, Yongbin Wei, Tingfang Ji, Tao Luo, M. Vajapeyam, Taesang Yoo, Osok Song, and D. Malladi. A survey on 3GPP heterogeneous networks. *IEEE Wireless Communications Magazine*, 18(3):10 –21, Jun. 2011. ISSN 1536-1284. doi: 10.1109/MWC.2011.5876496.

[10] David López-Pérez, Ismail Güvenç, Guillaume de la Roche, Marios Kountouris, Tony Q.S. Quek, and Jie Zhang. Enhanced Inter-Cell Interference Coordination Challenges in Heterogeneous Networks. *IEEE Wireless Communications Magazine*, 18(3):22–31, Jun. 2011.

[11] Small Cell Forum. Small Cell Market Status Dec 2012. White paper, Dec. 2012.

[12] V. Chandrasekhar, J. G. Andrews, and A. Gatherer. Femtocell Networks: A Survey. *IEEE Communications Magazine*, 46(9):59–67, Sept. 2008. ISSN 0163-6804. doi: 10.1109/MCOM.2008.4623708.

[13] Holger Claussen, Lester Tse Wee Ho, and Louis Gwyn Samuel. An overview of the femtocell concept. *Bell Labs Tech. J.*, 13(1):221–245, May 2008.

[14] David López-Pérez, Alvaro Valcarce, Guillaume de la Roche, and Jie Zhang. OFDMA Femtocells: A Roadmap on Interference Avoidance. *IEEE Communications Magazine*, 47(9):41–48, Sep. 2009.

[15] D. López-Pérez, Xiaoli Chu, and I Guvenc. On the Expanded Region of Picocells in Heterogeneous Networks. *IEEE Journal of Selected Topics in Signal Processing (J-STSP)*, 6(3):281–294, Jun. 2012. ISSN 1932-4553. doi: 10.1109/JSTSP.2012.2190381.

[16] ArrayComm & William Webb. Ofcom, 2007.

[17] John D. Hobby and Holger Claussen. Deployment options for femtocells and their impact on existing macrocellular networks. *Bell Labs Tech. J.*, 13(4):145–160, Feb. 2009.

[18] Guillaume de la Roche, Alvaro Valcarce, David López-Pérez, and Jie Zhang. Access Control Mechanisms for Femtocells. *IEEE Communications Magazine*, 48(1):33–39, Jan. 2010.

[19] D. López-Pérez, I Guvenc, and Xiaoli Chu. Mobility Management Challenges in 3GPP Heterogeneous Networks. *IEEE Communications Magazine*, 50(12):70–78, Dec. 2012. ISSN 0163-6804. doi: 10.1109/MCOM.2012.6384454.

[20] Young-Han Nam, Boon Loong Ng, K. Sayana, Yang Li, Jianzhong Zhang, Younsun Kim, and Juho Lee. Full-Dimension MIMO (FD-MIMO) for Next Generation Cellular Technology. *IEEE Communications Magazine*, 51(6):172–179, Jun. 2013. ISSN 0163-6804. doi: 10.1109/MCOM.2013.6525612.

[21] Ling Xie, Lihua Li, and Xingwang Li. Sum rate analysis of multicell mu-mimo with 3d user distribution and base station tilting. In *IEEE Vehicular Technology Conference (VTC 2014-Fall)*, pages 1–6, Sep. 2014. doi: 10.1109/VTCFall.2014.6966194.

[22] B.E. Priyanto, S. Kant, F. Rusek, Sha Hu, Jianjun Chen, and C. Wugengshi. Robust ue receiver with interference cancellation in lte advanced heterogeneous network. In *IEEE Vehicular Technology Conference (VTC 2013-Fall)*, pages 1–7, Sep. 2013. doi: 10.1109/VTCFall.2013.6692396.

[23] Yifeng Xie, Hui Zhang, Yingshan Li, Liang Feng, and Mengmeng Ji. Analysis of coverage probability for cooperative heterogeneous network. In *IEEE Vehicular Technology Conference (VTC 2013-Fall)*, pages 1–5, Sep. 2013. doi: 10.1109/VTCFall.2013.6692101.

[24] Hua Wang, C. Rosa, and K. Pedersen. Analysis of carrier deployment strategies for lte-a hetnets with multicell cooperation. In *IEEE Vehicular Technology Conference (VTC 2014-Fall)*, pages 1–5, Sep. 2014. doi: 10.1109/VTCFall.2014.6965874.

[25] Philip Sorrells. Wrestling with the Data Tsunami Indoors. White paper, Mar. 2014.

[26] ETSI MCC. Draft Report of 3GPP TSG RAN WG1 #77. Technical report, 3GPP TSG RAN WG1 Meeting #77, Seoul, Korea, May 2014.

[27] H. Ishii, Y. Kishiyama, and H. Takahashi. A novel architecture for lte-b: C-plane/u-plane split and phantom cell concept. In *IEEE Global Telecommunications Conference (GLOBECOM)*, pages 624–630, Dec. 2012. doi: 10.1109/GLOCOMW.2012.6477646.

[28] Xiuqiang Xu, Gaoning He, Shunqing Zhang, Yan Chen, and Shugong Xu. On Functionality Separation for Green Mobile Networks: Concept Study over LTE. *IEEE Communications Magazine*, 51(5):82–90, May 2013. ISSN 0163-6804. doi: 10.1109/MCOM.2013.6515050.

[29] A. Zakrzewska, D. Lopez-Perez, S. Kucera, and H. Claussen. Dual Connectivity in LTE HetNets with Split Control- and User-Plane. In *IEEE Global Telecommunications Conference (GLOBECOM)*, pages 391–396, Dec. 2013. doi: 10.1109/GLOCOMW.2013.6825019.

[30] 3GPP RP 132069. New Work Item Description: Dual Connectivity for LTE, 3GPP TSG-RAN Meeting 62. Technical report, 3GPP, 2013.

[31] H. Claussen, I. Ashraf, and L. T. W. Ho. Dynamic idle mode procedures for femtocells. *Bell Labs Tech. J.*, 15:95–116, 2010.

[32] I. Ashraf, F. Boccardi, and L. Ho. SLEEP mode techniques for small cell deployments. *IEEE Communications Magazine*, 49(8):72–79, Aug. 2011. ISSN 0163-6804. doi: 10.1109/MCOM.2011.5978418.

[33] Rouzbeh Razavi and Holger Claussen. Urban Small Cell Deployments: Impact on the Network Energy Consumption. In *IEEE Wireless Communications and Networking Conference (WCNC)*, Paris, France, Apr. 2012.

[34] Zukang Shen, A. Khoryaev, E. Eriksson, and Xueming Pan. Dynamic uplink-downlink configuration and interference management in TD-LTE. *IEEE Communications Magazine*, 50(11):51–59, Nov. 2012. ISSN 0163-6804. doi: 10.1109/MCOM.2012.6353682.

[35] Ming Ding, David López-Pérez, W. Chen, and A. Vasilakos. Dynamic TDD Transmissions in Homogeneous Small Cell Networks. In *IEEE International Conference on Communications (ICC)*, Sydney, Australia, Jun. 2014.

[36] Ming Ding, David López-Pérez, R. Xue, W. Chen, and A. Vasilakos. Small Cell Dynamic TDD Transmissions in Heterogeneous Networks. In *IEEE International Conference on Communications (ICC)*, Sydney, Australia, Jun. 2014.

[37] Weilei Wang, Pinyi Ren, Qinghe Du, and Li Sun. Robust detection with stable throughput over ill-conditioned channels for high-order mimo systems. In *IEEE Vehicular Technology Conference (VTC 2013-Fall)*, pages 1–5, Sep. 2013. doi: 10.1109/VTCFall.2013.6692392.

[38] M. Sawahashi, T. Kawamura, and Y. Kakishima. Csi reference signal multiplexing using carrier frequency swapping for fdd high-order mimo sdm. In *IEEE Vehicular Technology Conference (VTC 2014-Fall)*, pages 1–5, Sep. 2014. doi: 10.1109/VTCFall.2014.6965928.

[39] A.I. Sulyman, A.T. Nassar, M.K. Samimi, G.R. MacCartney, T.S. Rappaport, and A. Alsanie. Radio propagation path loss models for 5g cellular networks in the 28 ghz and 38 ghz millimeter-wave bands. *IEEE Communications Magazine*, 52(9):78–86, Sep. 2014. ISSN 0163-6804. doi: 10.1109/MCOM.2014.6894456.

[40] T.S. Rappaport, Shu Sun, R. Mayzus, Hang Zhao, Y. Azar, K. Wang, G.N. Wong, J.K. Schulz, M. Samimi, and F. Gutierrez. Millimeter wave mobile communications for 5g cellular: It will work! *IEEE Access*, 1:335–349, 2013. ISSN 2169-3536. doi: 10.1109/ACCESS.2013.2260813.

[41] A. Ghosh, T.A. Thomas, M.C. Cudak, R. Ratasuk, P. Moorut, F.W. Vook, T.S. Rappaport, G.R. MacCartney, Shu Sun, and Shuai Nie. Millimeter-wave enhanced local area systems: A high-data-rate approach for future wireless networks. *IEEE Journal on Selected Areas in Communications*, 32(6):1152–1163, Jun. 2014. ISSN 0733-8716. doi: 10.1109/JSAC.2014.2328111.

[42] F. Rusek, D. Persson, Buon Kiong Lau, E.G. Larsson, T.L. Marzetta, O. Edfors, and F. Tufvesson. Scaling Up MIMO: Opportunities and Challenges with Very Large Arrays. *IEEE Signal Processing Magazine*, 30(1):40–60, Jan. 2013. ISSN 1053-5888. doi: 10.1109/MSP.2011.2178495.

[43] E. Larsson, O. Edfors, F. Tufvesson, and T. Marzetta. Massive MIMO for Next Generation Wireless Systems. *IEEE Communications Magazine*, 52(2):186–195, Feb. 2014. ISSN 0163-6804. doi: 10.1109/MCOM.2014.6736761.

[44] Qualcomm. Importance of serving cell selection in heterogeneous networks (R1-100701), Jan. 2010.

[45] H.-S. Jo, Y. J. Sang, P. Xia, and J. G. Andrews. Outage probability for heterogeneous cellular networks with biased cell association. In *IEEE Global Telecommunications Conference (GLOBECOM)*, Houston, TX, Dec. 2011.

[46] 3GPP TS 36.133. Evolved Universal Terrestrial Radio Access (E-UTRA); Requirements for support of radio resource management. v.12.6.0, Dec. 2015.

[47] Alcatel-Lucent, Ericsson, et.al. CR on ABS definition (R2-111701), Feb. 2011.

[48] Ismail Güvenç. Capacity and fairness analysis of heterogeneous networks with range expansion and interference coordination. *IEEE Communications Letters*, PP(99):1 – 4, Sep. 2011.

[49] Arvind Merwaday, Sayandev Mukherjee, and Ismail Guvenc. Capacity analysis of LTE-Advanced HetNets with reduced power subframes and range expansion. *EURASIP Journal on Wireless Communications and Networking*, Nov. 2014.

[50] Supratim Deb, Pantelis Monogioudis, and Jerzy Miernik James P. Seymour. Algorithms for Enhanced Inter-Cell Interference Coordination (eICIC) in LTE HetNets. *IEEE/ACM Transactions on Networking*, accepted for publication in a future issue of this journal, 2013.

[51] B. Soret and K.I. Pedersen. Macro Cell Muting Coordination for Non-Uniform Topologies in LTE-A HetNets. In *IEEE Vehicular Technology Conference (VTC Fall)*, Sep. 2013. doi: 10.1109/VTCFall.2013.6692277.

[52] Chris Nicoll. 3G and 4G Small Cells Create Big challenges for MNOs. Analysis Mason, Mar. 2013.

[53] SCF049: Backhaul technologies for small cells (Release 4)s. Small Cell Forum, Feb. 2014.

[54] A. H. Jafari, D. Lopez-Perez, H. Song, H. Claussen, L. Ho, and J. Zhang. Small cell backhaul: Challenges and prospective solutions. *EURASIP Journal on Wireless Communications and Networking*, pages 1–18, Aug. 2015.

[55] Ulf Gustavsson, Cesar Sanchez-Perez, Thomas Eriksson, Fredrik Athley, Giuseppe Durisi, Per Landin, Katharina Hausmair, Christian Fager, and Lars Svensson. On the Impact of Hardware Impairments on Massive MIMO. In *IEEE Global Telecommunications Conference (GLOBECOM)*, Austin, Texas, Dec. 2014.

[56] J. Jose, A. Ashikhmin, T.L. Marzetta, and S. Vishwanath. Pilot Contamination and Precoding in Multi-Cell TDD Systems. *IEEE Transactions on Wireless Communications*, 10(8):2640–2651, Aug. 2011. ISSN 1536-1276. doi: 10.1109/TWC.2011.060711.101155.

[57] K. T. Truong and Jr. R. W. Heath. Effects of Channel Aging in Massive MIMO Systems. *Journal of Communications and Networks, Special Issue on Massive MIMO*, 15(4):338–351, Aug. 2013.

[58] L. Chun-Hung and X. Feng. Network Coding for Two-Way Relaying: Rate Region, Sum Rate and Opportunistic Scheduling. In *IEEE International Conference on Communications (ICC)*, pages 1044–1049, May 2008.

[59] L. Huaping, P. Popovski, E. de Carvalho, Y. Zhao, and F. Sun. Four-way relaying in wireless cellular systems. *IEEE Wireless Communications Letters*, 2(4):403–406, Aug. 2013.

[60] Jani Puttonen, Niko Kolehmainen, Tero Henttonen, and Jorma Kaikkonen. On idle mode mobility state detection in evloved UTRAN. In *Proc. IEEE International Conference on Information Technology: New Generations*, pages 1195–1200, Las Vegas, NV, Apr. 2009.

[61] 3GPP TR 36.842. Study on Small Cell Enhancements for E-UTRA and E-UTRAN; Higher layer aspects. v.12.0.0, Jan. 2014.

[62] Holger Claussen, Lester Tse Wee Ho, and Louis Gwyn Samuel. Financial analysis of a pico-cellular home network deployment. In *Proc. IEEE International Conference on Communications (ICC)*, pages 5604–5609, Glasgow, UK, June 2007.

[63] Holger Claussen, Lester Tse Wee Ho, and Florian Pivit. Self-optimization of femtocell coverage to minimize the increase in core network mobility signalling. *Bell Labs Tech. J.*, 14(2):155–184, Aug. 2009.

[64] R. Razavi, L. Ho, H. Claussen, and D. Lopez-Perez. Improving Small Cell Performance through Switched Multi-element Antenna Systems in Heterogeneous Networks. *IEEE Transactions on Vehicular Technology*, PP(99):1–1, 2014. ISSN 0018-9545. doi: 10.1109/TVT.2014.2348319.

[65] M. Amirijoo, P. Frenger, F. Gunnarsson, H. Kallin, J. Moe, and K. Zetterberg. Neighbor Cell Relation List and Physical Cell Identity Self-Organization in LTE. In *IEEE International Conference on Communications (ICC)*, pages 37–41, May 2008. doi: 10.1109/ICCW.2008.12.

[66] Guolin Sun, Jie Chen, Wei Guo, and K.J.R. Liu. Signal processing techniques in network-aided positioning: A survey of state-of-the-art positioning designs. *IEEE Signal Processing Magazine*, 22(4):12–23, Jul. 2005. ISSN 1053-5888. doi: 10.1109/MSP.2005.1458273.

[67] Imran Ashraf, Lester Tse Wee Ho, and Holger Claussen. Improving energy efficiency of femtocell base stations via user activity detection. In *Proc. IEEE Wireless Communciations and Networking Conference (WCNC)*, Sydney, Australia, Apr. 2010.

[68] ETSI MCC. Draft Report of 3GPP TSG RAN WG1 #75. Technical report, Nov. 2013.

[69] 3GPP TR 36.828. Further enhancements to LTE Time Division Duplex (TDD) for Downlink-Uplink (DL-UL) interference management and traffic adaptatio. v.11.0.0, Jun. 2012.

[70] Ming Ding, David López-Pérez, W. Chen, and A. Vasilakos. Analysis on the SINR Performance of Dynamic TDD in Homogeneous Small Cell Networks. In *IEEE Global Telecommunications Conference (GLOBECOM)*, Austin, Texas, Dec. 2014.

[71] L. Li, A. H. Jafari, X. Chu, and J. Zhang. Simultaneous transmission opportunities for LTE-LAA small cells coexisting with wifi in unlicensed spectrum. In *IEEE International Conference on Communications (ICC)*, May 2016.

[72] AM. Cavalcante, E. Almeida, R.D. Vieira, F. Chaves, R.C.D. Paiva, F. Abinader, S. Choudhury, E. Tuomaala, and K. Doppler. Performance Evaluation of LTE and Wi-Fi Coexistence in Unlicensed Bands. In *IEEE Vehicular Technology Conference (VTC Spring)*, pages 1–6, Jun. 2013. doi: 10.1109/VTCSpring.2013.6692702.

[73] 3GPP TR 36.889. Feasibility Study on Licensed-Assisted Access to Unlicensed Spectrum. Technical report, 3GPP, 2014.

[74] ETSI MCC. Draft Report of 3GPP workshop on LTE in unlicensed spectrum. Technical report, 3GPP workshop on LTE in unlicensed spectrum, Sophia Antipolis, France, Jun. 2014.

[75] J. Deissner and G.P. Fettweis. A Study on Hierarchical Cellular Structures with Inter-Layer Reuse in an Enhanced GSM Radio Network. In *IEEE International Workshop on Mobile Multimedia Communications (MoMuC '99)*, pages 243–251, 1999. doi: 10.1109/MOMUC.1999.819497.

[76] C. E. Shannon. A mathematical theory of communication. *Bell System Tech. J.*, 27: 379–423, Jul. 1948.

[77] J. G. Andrews, F. Baccelli, and R. K. Ganti. A tractable approach to coverage and rate in cellular networks. *IEEE Transactions on Communications*, 59(11):3122–3134, Nov. 2011.

[78] S. Mukherjee. Distribution of Downlink SINR in Heterogeneous Cellular Networks. *IEEE Journal on Selected Areas in Communications (JSAC)*, 30(3):575–585, Apr. 2012.

[79] 3GPP TR 36.814. Evolved Universal Terrestrial Radio Access (E-UTRA); Further advancements for E-UTRA Physical layer aspects. Technical Report v 1.0.0, 3GPP-TSG R1.

[80] 3GPP TSG RAN, TR 25.996 v10.0.0, "TR 36.828 (V11.0.0): Further enhancements to LTE Time Division Duplex (TDD) for Downlink-Uplink (DL-UL) interference management and traffic adaptation, Jun. 2012.

[81] Y. Kishiyama, A Benjebbour, T. Nakamura, and H. Ishii. Future Steps of LTE-A: Evolution Toward Integration of Local Area and Wide Area Systems. *IEEE Wireless Communications*, 20(1):12–18, Feb. 2013. ISSN 1536-1284. doi: 10.1109/MWC.2013.6472194.

[82] F. Gustafsson and F. Gunnarsson. Mobile positioning using wireless networks: possibilities and fundamental limitations based on available wireless network measurements. *IEEE Signal Processing Magazine*, 22(4):41–53, Jul. 2005. ISSN 1053-5888. doi: 10.1109/MSP.2005.1458284.

[83] K. Klessig and V. Suryaprakash. Spatial Traffic Modelling for Architecture Evolution. Green Touch.

[84] Farooq Khan. *LTE for 4G Mobile Broadband: Air Interface Technologies and Performance*. University Cambridge Press, 2009.

[85] 3GPP TS 36.211. Evolved Universal Terrestrial Radio Access (E-UTRA); Physical channels and modulation. v.12.2.0, Jul. 2014.

[86] Pramod Viswanath, David N. C. Tse, and Rajiv Laroia. Opportunistic beamforming using dumb antennas. *IEEE Trans. Inf. Theory*, 48(5):1277–1294, Jun. 2002.

[87] Constantine A. Balanis. *Antenna Theory: Analysis and Design*. John Wiley & Sons Ltd, 2005.

[88] Xiaoli Chu, David López-Pérez, Yang Yang, and Fredrik Gunnarsson. *Heterogeneous Cellular Networks: Theory, Simulation and Deployment*. University Cambridge Press, 2013.

[89] 3rd Generation Partnership Project (3GPP). http://www.3gpp.org.

[90] Farooq Khan. *LTE for 4G Mobile Broadband Air Interface Technologies and Performance*. University Cambridge Press, 2009. ISBN 9780521882217.

[91] M. Sharif and B. Hassibi. A comparison of time-sharing, dpc, and beamforming for mimo broadcast channels with many users. *IEEE Transactions on Communications.*, 55(1):11–15, Jan. 2007. ISSN 0090-6778. doi: 10.1109/TCOMM.2006.887480.

[92] T. Bu, Li Li, and R. Ramjee. Generalized proportional fair scheduling in third generation wireless data networks. In *25th IEEE International Conference on Computer Communications (INFOCOM)*, pages 1–12, Apr. 2006. doi: 10.1109/INFOCOM.2006.145.

[93] Erwu Liu and K.K. Leung. Proportional fair scheduling: Analytical insight under rayleigh fading environment. In *IEEE Wireless Communications and Networking Conference (WCNC)*, pages 1883–1888, Mar. 2008. doi: 10.1109/WCNC.2008.335.

[94] G. Mongha, K.I. Pedersen, I.Z. Kovacs, and P.E. Mogensen. QoS Oriented Time and Frequency Domain Packet Schedulers for The UTRAN Long Term Evolution. In *IEEE Vehicular Technology Conference, 2008.*, pages 2532 –2536, May 2008. doi: 10.1109/VETECS.2008.557.

[95] A Jalali, R. Padovani, and R. Pankaj. Data throughput of cdma-hdr a high efficiency-high data rate personal communication wireless system. In *IEEE 51st Vehicular Technology Conference (VTC 2000-Spring)*, volume 3, pages 1854–1858 vol.3, 2000. doi: 10.1109/VETECS.2000.851593.

[96] Holger Claussen. Future Cellular Networks. Alcatel-Lucent, Apr. 2012.

[97] Congzheng Han et al. Green radio: radio techniques to enable energy-efficient wireless networks. *IEEE Communications Magazine*, 49(6):46–54, Jun. 2011. ISSN 0163-6804. doi: 10.1109/MCOM.2011.5783984.

[98] Bjorn Debaillie Claude Desset and Filip Louagie. Flexible Power Model of Future Base Stations: System Architecture Breakdown and Parameters. Green Touch.

[99] K. C. Chen G. P. Fettweis and R. Tafazoli. Green radio: Energy efficiency in wireless networks. *Journal of Communications and Networks*, 12(2):99–102, Apr. 2010. ISSN 1229-2370. doi: 10.1109/JCN.2010.6391365.

[100] W. Guo and T. O’Farrell. Green cellular network: Deployment solutions, sensitivity and tradeoffs. In *2011 Wireless Advanced*, pages 42–47, Jun. 2011. doi: 10.1109/WiAd.2011.5983283.

[101] P. Loskot B. Badic, T. O’Farrrell and J. He. Energy efficient radio access architectures for green radio: Large versus small cell size deployment. In *2009 IEEE 70th Vehicular Technology Conference Fall*, pages 1–5, Sep. 2009. doi: 10.1109/VETECF.2009.5379035.

[102] Declan O’Donoghue, Valeria Nico, Ronan Frizzell, Gerard Kelly, and Jeff Punch. A multiple-degree-of-freedom velocity-amplified vibrational energy harvester: Part a — experimental analysis. *Proceedings of the American Society of Mechanical Engineers*, 2, Sep. 2014.

[103] Valeria Nico, Declan O'Donoghue, Ronan Frizzell, Gerard Kelly, and Jeff Punch. A multiple degree-of-freedom velocity-amplified vibrational energy harvester: Part b — modelling. *Proceedings of the American Society of Mechanical Engineers*, 8, Sep. 2014.

[104] K. Divya and J. Oestergaard. Battery Energy Storage Technology for Power Systems — an Overview. *Electric Power Systems Research J.*, 79(4):511–520, 2009.

[105] M. Haenggi. *Stochastic Geometry for Wireless Networks*. Cambridge University Press, 2012.

[106] H. S. Dhillon, R. Ganti, F. Baccelli, and J.G. Andrews. Modeling and analysis of k-tier downlink heterogeneous cellular networks. *IEEE Journal on Selected Areas in Communications*, 30(3):550–560, Apr. 2012.

[107] J. G. Andrews, F. Baccelli, and R. K. Ganti. A tractable approach to coverage and rate in cellular networks. *IEEE Transactions on Wireless Communications*, 59(11): 3122–3134, Nov. 2011.

[108] T. Bai, R. Vaze, and R. W. Heath. Analysis of blockage effects on urban cellular networks. *IEEE Transactions on Wireless Communications*, 13(9):5070–5083, Sep. 2014.

[109] J. Ling and D. Chizhik. Capacity scaling of indoor pico-cellular networks via reuse. *IEEE Communications Letters*, 16(2):231–233, Feb. 2012.

[110] X. Zhang and J. G. Andrews. Downlink cellular network analysis with multi-slope path loss models. *IEEE Transactions on Wireless Communications*, 63(5):1881–1894, Mar. 2015.

[111] T. Bai and R. W. Heath Jr. Coverage and rate analysis for millimeter wave cellular networks. *IEEE Transactions on Wireless Communications*, 14(2):1100–1114, Oct. 2014.

[112] C. Galiotto, N. K. Pratas, N. Marchetti, and L. Doyle. A stochastic geometry framework for los/nlos propagation in dense small cell networks. In *IEEE International Conference on Communications (ICC)*, pages 2851–2856, Jun. 2015. doi: 10.1109/ICC.2015.7248759.

[113] M. Ding, P. Wang, D. Lopez-Perez, G. Mao, and Z Lin. Performance impact of los and nlos transmissions in small cell networks. *Wireless Communications, submitted to IEEE Transactions on*. URL http://arxiv.org/pdf/1503.04251.pdf.

[114] Spatial Channel Model AHG, "Subsection 3.5.3, Spatial Channel Model Text Description V6.0,", Apr. 2003.

[115] I.S. Gradshteyn and I.M. Ryzhik. *Table of Integrals, Series, and Products (7th Ed.)*. Academic Press, 2007.

[116] H. Holma and A. Toskala. *LTE for UMTS - OFDMA and SC-FDMA Based Radio Access*. John Wiley & Sons Ltd., 2009.

[117] D. Lopez-Perez, M. Ding, H. Claussen, and A. H. Jafari. Towards 1 Gbps/UE in cellular systems: understanding ultra-Dense small cell deployment. In *IEEE Communications Surveys and Tutorials*, Jun. 2015.

[118] J. Akhtar and D. Gesbert. Spatial multiplexing over correlated mimo channels with a closed-form precoder. *IEEE Transactions on Wireless Communications*, 4(5):2400–2409, Sep. 2005. ISSN 1536-1276. doi: 10.1109/TWC.2005.853915.

[119] A. H. Jafari, V. Venkateswaran, D. Lopez-Perez, and J. Zhang. Pulse shaping diversity to enhance throughput in ultra-dense small cell networks. In *IEEE 17th Workshop on Signal Processing Advances in Wireless Communications (SPAWC-2016)*, Jul. 2016.

[120] J.R. Treichler, I. Fijalkow, and C.R. Johnson. Fractionally spaced equalizers. *IEEE Signal Processing Magazine*, 13(3):65–81, May 1996. ISSN 1053-5888. doi: 10.1109/79.489269.

[121] M.T. Ivrlc, W. Utschick, and J.A. Nossek. Fading correlations in wireless mimo communicatin systems. *IEEE Journal on Selected Areas in Communications*, 21(5): 819–828, Jun. 2003. ISSN 0733-8716. doi: 10.1109/JSAC.2003.810348.

[122] A. M. Tulino, A. Lozano, and S. Verdu. Impact of antenna correlation on the capacity of multiantenna channels. *IEEE Transactions on Information Theory*, 51(7):2491–2509, Jul. 2005. ISSN 0018-9448. doi: 10.1109/TIT.2005.850094.

[123] D. Chizhik, F. Rashid-Farrokhi, J. Ling, and A. Lozano. Effect of antenna separation on the capacity of blast in correlated channels. *IEEE Communications Letters*, 4(11): 337–339, Nov. 2000. ISSN 1089-7798. doi: 10.1109/4234.892194.

[124] A.H. Jafari, D. Lopez-Perez, M. Ding, and J. Zhang. Study on Scheduling Techniques for Ultra Dense Small Cell Networks. In *IEEE Vehicular Technology Conference (VTC Fall)*, Boston, USA, Sep. 2015.

[125] C. Oestges. Validity of the kronecker model for mimo correlated channels. In *IEEE 63rd Vehicular Technology Conference (VTC Spring)*, volume 6, pages 2818–2822, May 2006. doi: 10.1109/VETECS.2006.1683382.

[126] Ravindra B. Bapat, Steve J. Kirkland, K. Manjunatha Prasad, and Simo Puntanen. *Combinatorial Matrix Theory and Generalized Inverses of Matrices*. Springer, 2013. ISBN 9788132210528.

[127] Jiyun Shen, Y. Oda, T. Furuno, T. Maruyama, and T. Ohya. A novel approach for capacity improvement of 2x2 mimo in los channel using reflectarray. In *IEEE 73rd Vehicular Technology Conference (VTC Spring)*, pages 1–5, May 2011. doi: 10.1109/VETECS.2011.5956339.

[128] J.B. Anderson, F. Rusek, and V. Owall. Faster-than-nyquist signaling. *Proceedings of the IEEE*, 101(8):1817–1830, Aug. 2013. ISSN 0018-9219. doi: 10.1109/JPROC.2012.2233451.

[129] F. Rusek and J.B. Anderson. Constrained capacities for faster-than-nyquist signaling. *IEEE Transactions on Information Theory*, 55(2):764–775, Feb. 2009. ISSN 0018-9448. doi: 10.1109/TIT.2008.2009832.

[130] A.D. Liveris and C.N. Georghiades. Exploiting faster-than-nyquist signaling. *IEEE Transactions on Communications*, 51(9):1502–1511, Sep. 2003. ISSN 0090-6778. doi: 10.1109/TCOMM.2003.816943.

[131] A. Sheikholeslami, D. Goeckel, and H. Pishro-Nik. Artificial intersymbol interference (isi) to exploit receiver imperfections for secrecy. In *IEEE International Symposium on Information Theory Proceedings (ISIT)*, pages 2950–2954, Jul. 2013. doi: 10.1109/ISIT.2013.6620766.

[132] V. Venkateswaran and A.-J. van der Veen. Multichannel SigmaDelta ADCs with integrated feedback beamformers to cancel interfering communication signals. *IEEE Transactions on Signal Processing*, 59(5):2211–2222, May 2011. ISSN 1053-587X. doi: 10.1109/TSP.2011.2109954.

[133] S. Plass, A. Dammann, and S. Sand. An overview of cyclic delay diversity and its applications. In *IEEE 68th Vehicular Technology Conference (VTC Fall)*, pages 1–5, Sep. 2008. doi: 10.1109/VETECF.2008.133.

[134] W.C.Y. Lee. The most spectrum-efficient duplexing system: Cdd. *IEEE Communications Magazine*, 40(3):163–166, Mar. 2002. ISSN 0163-6804. doi: 10.1109/35.989781.

[135] S. Plass and A. Dammann. Cellular cyclic delay diversity for next generation mobile systems. In *IEEE 64th Vehicular Technology Conference (VTC Fall)*, pages 1–5, Sep. 2006. doi: 10.1109/VTCF.2006.125.

[136] G. Bauch and T. Abe. On the parameter choice for cyclic delay diversity based precoding with spatial multiplexing. In *IEEE Global Telecommunications Conference (Globecom)*, pages 1–6, Nov. 2009. doi: 10.1109/GLOCOM.2009.5426062.

[137] E. de Carvalho M. I. Rahman, S. S. Das and R. Prasad. Spatial multiplexing in ofdm systems with cyclic delay diversity. In *IEEE 65th Vehicular Technology Conference (VTC Spring)*, pages 1491–1495, Apr. 2007. doi: 10.1109/VETECS.2007.311.

[138] Chuanlian Ma. Mitigation of transmit correlation for mimo spatial multiplexing through phase rotation precoding. In *International Conference on Consumer Electronics, Communications and Networks (CECNet)*, pages 1398–1401, Apr. 2011. doi: 10.1109/CECNET.2011.5768230.

[139] D. Gesbert, M. Shafi, Da-Shan Shiu, P.J. Smith, and A. Naguib. From theory to practice: an overview of mimo space-time coded wireless systems. *IEEE Journal on Selected Areas in Communications*, 21(3):281–302, Apr. 2003. ISSN 0733-8716. doi: 10.1109/JSAC.2003.809458.

[140] M. Ding, P. Wang, D. López-Pérez, G. Mao, and Z. Lin. Performance impact of LoS and NLoS transmissions in dense cellular networks. *IEEE Transactions on Wireless Communications*, 15(3):2365–2380, Mar. 2016. ISSN 1536-1276. doi: 10.1109/TWC.2015.2503391.

[141] H. Claussen and L. T. W. Ho. Multi-carrier Cell Structures with Angular Offset. In *IEEE Personal, Indoor and Mobile Radio Communications (PIMRC)*, pages 1–6, Sydney, Australia, Sept. 2012.

[142] Hon Tat Hui. Multiple Antennas for MIMO Communciations-Channel Correlation. NUS/ECE.

Appendix A

Ultra Dense Small Cell Network Simulation Setup

The simulated environment in chapters 2 and 3 and their corresponding channel gains are calculated in form of matrices, representing a two dimensional gain map with a given resolution [141]. The overall gain is calculated as a sum of individual gains in decibels for each small cell BS m at each location as

$$G_m[\mathrm{dB}] = G_{\mathrm{A},m}[\mathrm{dB}] + G_{\mathrm{P},m}[\mathrm{dB}] + G_{\mathrm{S},m}[\mathrm{dB}], \tag{A.1}$$

where $G_{\mathrm{A},m}[\mathrm{dB}]$ is the antenna gain, $G_{\mathrm{P},m}[\mathrm{dB}]$ is the path gain (loss) and $G_{\mathrm{S},m}[\mathrm{dB}]$ is the shadow fading gain (loss).

The antenna gain $G_{\mathrm{A},m}[\mathrm{dB}]$ represents the gain resulting from focussing the antenna beam towards one direction. In this case, a vertical dipole array with four elements spaced by $0.6\,\lambda_c$ is used (see Fig. A.1 (a)), where the combined gain of the horizontal and vertical antenna patterns together with the vertical array factor gain is calculated as:

$$G^{\mathrm{a}}(\varphi,\theta)[\mathrm{dB}] = G^{\mathrm{a}}_{\mathrm{M}}[dBi] + G^{\mathrm{a}}_{\mathrm{H}}(\varphi)[dB] + G^{\mathrm{a}}_{\mathrm{V}}(\theta)[dB] + G^{\mathrm{a,array}}_{\mathrm{V}}(\theta)[dB], \tag{A.2}$$

where φ and θ are the angles of arrival in the horizontal and vertical planes with respect to the main beam direction, respectively, $G^{\mathrm{a}}_{\mathrm{M}}$, $G^{\mathrm{a}}_{\mathrm{H}}(\varphi)$ and $G^{\mathrm{a}}_{\mathrm{V}}(\theta)$ are the maximum antenna gain, the horizontal attenuation offset of one antenna element of the array, and the vertical attenuation offset of one antenna element of the array, respectively, and $G^{\mathrm{a,array}}_{\mathrm{V}}(\theta)$ is the vertical array factor gain. It is important to mention that the vertical dipole array helps to create a pattern similar to downtilt effect of a dipole where the main lobe is pointed a bit

Fig. A.1 (a) Vertical dipole array with four elements spaced by 0.6 λ_c (b) Horizontal array of vertical dipoles with four elements spaced by 0.6 λ_c used for beamforming.

downwards to reduce the interference to small cell BSs further away, resulting in improved performance compared to a standard dipole.

The horizontal and vertical attenuation offsets of one antenna element of the array can be respectively modelled as:

$$G^{\mathrm{a}}_{\mathrm{H}}(\varphi)[\mathrm{dB}] = 0, \tag{A.3}$$

and

$$G^{\mathrm{a}}_{\mathrm{V}}(\theta)[\mathrm{dB}] = 20\log_{10}\left(\frac{\cos\left(\frac{\pi}{2}\cos\left(\theta+\frac{\pi}{2}\right)\right)}{\sin\left(\theta+\frac{\pi}{2}\right)}\right), \tag{A.4}$$

while the vertical array factor gain $G^{\mathrm{a,array}}_{\mathrm{V}}(\theta)$ can be modelled as:

$$G^{\mathrm{a,array}}_{\mathrm{V}}(\theta) = \sum_{n=1}^{N_t} a(n)\mathrm{e}^{(j(n-1)\times 2\pi d_\varepsilon(-\sin(\theta))+\delta_{\mathrm{phase}})}, \tag{A.5}$$

where N_t is the number of antenna elements in the vertical array, d_ε is the spacing between antenna elements in wavelength, $a(n)$ is the normalised voltage of antenna element n, and δ_{phase} is the phase increment within antenna elements in radian (see Table A.1). Note that the horizontal array factor gain in the horizontal plane depends on the beamforming weights used, and those are specified by the used standardised LTE code book beamforming [84].

Fig. A.2(a) shows the vertical and horizontal gain patterns of *ONE vertical dipole array with four elements that are spaced by 0.6* λ_c where the maximum gain is around 7 dBi. As

Table A.1 Typical parameters of a dipole array

Parameter	**Value**
N_t	4
$G_{\mathrm{M}}^{\mathrm{a}}$	2.15 dBi
d_ε	0.6 wavelength
$a(n)$	[0.97 1.077 1.077 0.86]
δ_{phase}	1.658 radian

previously mentioned, the *similar to downtilt effect* reduces the interference to the small cell BSs that are further away and results in improved performance in comparison to using a standard dipole. Fig. A.2(b) also shows the spatial antenna gain for the simulation area in dBi. In particular, considering the 500 m × 500 m simulation area, A.2(b) shows how the gain of the vertical dipole is received within the entire simulation area. Assuming that BS is located at the origin, it is seen that as the distance to the BS is increased, the antenna gain reduces.

It is also important to note that the proposed configuration was optimised for a given ISD and antenna height, and results in a given certain downtilt. In order to keep the resulting downtilt fixed, the height of the antenna is changed with the ISD. The longer the ISD, the higher the antenna height.

The path gain (loss) $G_{\mathrm{P},m}[\mathrm{dB}]$ represents the gain between a transmitter and a receiver located in this case outdoors for the given environment. The path gain (loss) is modelled as an expected gain value composed of LOS gain, NLOS gain and a LOS probability as

$$G_{\mathrm{P},m}[\mathrm{dB}] = P_{\mathrm{l}}(d[\mathrm{m}])[\cdot] \times G_{\mathrm{Pl}}(d[\mathrm{m}])[\mathrm{dB}] + (1 - P_{\mathrm{l}}(d[\mathrm{m}])) \times G_{\mathrm{Pn}}(d)[\mathrm{dB}]. \tag{A.6}$$

The LOS probability $P_{\mathrm{l}}(d)[.]$ for a propagation distance d is based on [79], with an additional spline interpolation for a smooth transition, the resulting LOS $G_{\mathrm{Pl}}(d)[\mathrm{dB}]$ and NLOS $G_{\mathrm{Pn}}(d)[\mathrm{dB}]$ path gains for a propagation distance d are calculated using the 3GPP urban micro (UMi) models [79]. Note that d is computed in the 3D space. The small cell BS transmit power $P_{\mathrm{tx},m}[\mathrm{mW}]$ is calculated to achieve an average targeted SNR at the cell-edge of $\gamma^{\mathrm{edge}}[\mathrm{dB}] = 9$, 12 or 15 dB as

$$P_{\mathrm{tx},m}[\mathrm{dBm}] = P_{\mathrm{N}}[\mathrm{dBm}] + G_{\mathrm{P},m,\mathrm{edge}}[\mathrm{dB}] + \gamma^{\mathrm{edge}}[\mathrm{dB}]. \tag{A.7}$$

where $P_{\mathrm{N}}[\mathrm{dBm}]$ is the noise power in dBm, and $G_{\mathrm{P},m,\mathrm{edge}}[\mathrm{dB}]$ is the path gain (loss) from BS m to its cell-edge, which is $\frac{\sqrt{3}}{2}$ of the ISD.

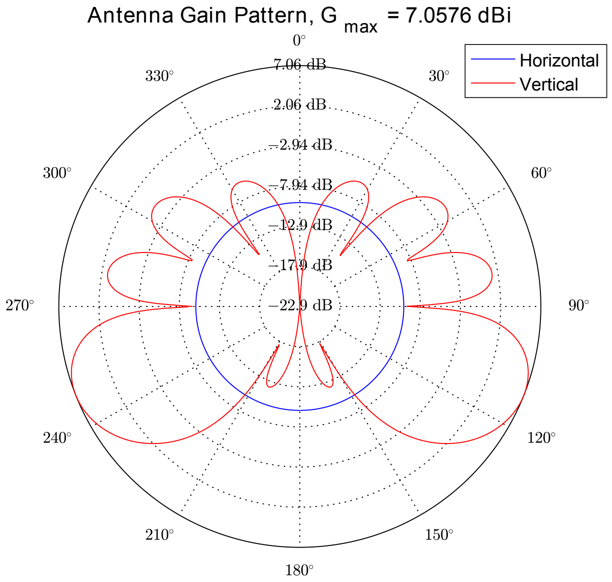

(a) Gain pattern of vertical dipole with four elements.

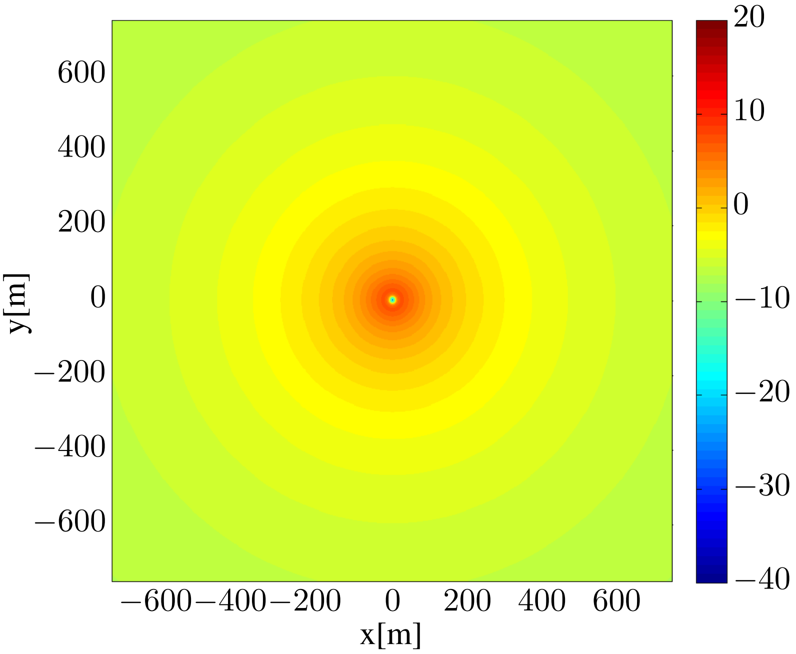

(b) Spatial antenna gains.

Fig. A.2 Gain characteristics of the 4 element vertical dipole array.

The received power from each small cell BS m at each UE u is calculated using $P_{\mathrm{tx},m}[\mathrm{mW}]$ and the overall gain $G_{m,u}$ as

$$P_{\mathrm{rx},m,u}[\mathrm{dBm}] = P_{\mathrm{tx},m}[\mathrm{dBm}] + G_{m,u}[\mathrm{dB}]. \tag{A.8}$$

The SINR of UE u when served by small cell BS m is

$$\gamma_{m,u}[\mathrm{dB}] = \frac{P_{\mathrm{rx},m,u}[\mathrm{mW}]}{\left(\sum_{n=1}^{M} P_{\mathrm{rx},n,u}[\mathrm{mW}]\right) - P_{\mathrm{rx},m,u}[\mathrm{mW}] + P_{\mathrm{N}}[\mathrm{mW}]}, \tag{A.9}$$

where M is the total number of small cell BS transmitting in the studied frequency band.

From the SINRs and assuming a round robin scheduling, the throughput of UE u can be calculated as

$$C_u = \frac{C(\gamma_{m,u})}{U}, \tag{A.10}$$

where $C(\gamma_{m,u})$ is the SINR to throughput mapping and U is the number of UEs served by small cell BS m. The mapping used here is the Shannon-Hartley theorem presented in (2.1) in chapter 2 with an operation point 3.5 dB from the optimum capacity, and there is no cap for the modulation and coding scheme (MCS).

Also note that throughput performance statistics are collected over 150 simulation runs from UE connected to the small cell BS in the scenario, with independent UE location and shadow fading realisations. Extra tiers of small cell BSs outside the scenario were added to avoid border effects.

Appendix B

Proofs of Theorems and Lemmas presented in Chapter 4

B.1 Proof of Theorem 1

To compute $p^{\mathrm{cov}}(\lambda,\gamma)$, it is first needed to compute the distance PDFs for the events that the typical UE located at the origin is associated with a BS with either a LOS or NLOS path.

Recalling from (4.7) and (4.8), the $p^{\mathrm{cov}}(\lambda,\gamma)$ can be computed as

$$\begin{aligned}
p^{\mathrm{cov}}(\lambda,\gamma) &\overset{(a)}{=} \int_{r>0} \Pr\left[\mathrm{SINR}>\gamma | r\right] f_R(r)\,dr \\
&= \int_{r>0} \Pr\left[\frac{P\zeta(r)h}{I_r}>\gamma\right] f_R(r)\,dr \\
&= \int_0^{d_1} \Pr\left[\frac{P\zeta_1^{\mathrm{L}}(r)h}{I_r}>\gamma\right] f_{R,1}^{\mathrm{L}}(r)\,dr + \int_0^{d_1} \Pr\left[\frac{P\zeta_1^{\mathrm{NL}}(r)h}{I_r}>\gamma\right] f_{R,1}^{\mathrm{NL}}(r)\,dr \\
&\quad + \cdots \\
&\quad + \int_{d_{N-1}}^{\infty} \Pr\left[\frac{P\zeta_N^{\mathrm{L}}(r)h}{I_r}>\gamma\right] f_{R,N}^{\mathrm{L}}(r)\,dr + \int_{d_{N-1}}^{\infty} \Pr\left[\frac{P\zeta_N^{\mathrm{NL}}(r)h}{I_r}>\gamma\right] f_{R,N}^{\mathrm{NL}}(r)\,dr \\
&\overset{\triangle}{=} \sum_{n=1}^{N} \left(T_n^{\mathrm{L}}+T_n^{\mathrm{NL}}\right),
\end{aligned} \tag{B.1}$$

where $f_{R,n}^{\mathrm{L}}(r)$ and $f_{R,n}^{\mathrm{NL}}(r)$ refer to the piece-wise densities of the RVs R_n^{L} and R_n^{NL}, respectively. R_n^{L} and R_n^{NL} also denote the distances that the UE is associated with a BS with a LOS path and a NLOS path, respectively with the corresponding events being assumed to be disjoint. Furthermore, it is worth reminding that T_n^{L} and T_n^{NL} are piecewise functions which were defined as $T_n^{\mathrm{L}} = \int_{d_{n-1}}^{d_n} \Pr\left[\frac{P\zeta_n^{\mathrm{L}}(r)h}{I_r} > \gamma\right] f_{R,n}^{\mathrm{L}}(r)\,dr$ and $T_n^{\mathrm{NL}} = \int_{d_{n-1}}^{d_n} \Pr\left[\frac{P\zeta_n^{\mathrm{NL}}(r)h}{I_r} > \gamma\right] f_{R,n}^{\mathrm{NL}}(r)\,dr$, respectively with d_0 and d_N referring to 0 and ∞.

$$f_R(r) = \begin{cases} f_{R,1}(r) = \begin{cases} f_{R,1}^{\mathrm{L}}(r), & \text{the UE is associated with an LOS BS} \\ f_{R,1}^{\mathrm{NL}}(r), & \text{the UE is associated with an NLOS BS} \end{cases}, & 0 \le r \le d_1 \\ f_{R,2}(r) = \begin{cases} f_{R,2}^{\mathrm{L}}(r), & \text{the UE is associated with an LOS BS} \\ f_{R,2}^{\mathrm{NL}}(r), & \text{the UE is associated with an NLOS BS} \end{cases}, & d_1 < r \le d_2 \\ \vdots & \vdots \\ f_{R,N}(r) = \begin{cases} f_{R,N}^{\mathrm{L}}(r), & \text{the UE is associated with a BS with LOS link} \\ f_{R,N}^{\mathrm{NL}}(r), & \text{the UE is associated with a BS with NLOS link} \end{cases}, & r > d_{N-1} \end{cases}. \tag{B.2}$$

In the following, two events are presented in order to calculate $f_{R,n}^{\mathrm{L}}(r)$ in (B.1).

- Event B^{L}: The BS that is located at distance X^{L} is the nearest BS the UE with a LOS path. According to [107], the complementary CDF (CCDF) of X^{L} is written as $\bar{F}_X^{\mathrm{L}}(x) = \exp\left(-\int_0^x \Pr^{\mathrm{L}}(u)\,2\pi u\lambda du\right)$.The PDF of X^{L} can then be obtained by taking the derivative of $\left(1 - \bar{F}_X^{\mathrm{L}}(x)\right)$ with regard to x as

$$f_X^{\mathrm{L}}(x) = \exp\left(-\int_0^x \Pr^{\mathrm{L}}(u)\,2\pi u\lambda du\right) \Pr^{\mathrm{L}}(x)\,2\pi x\lambda. \tag{B.3}$$

- Event C^{NL} is conditional on the corresponding value of X^{L}: Assuming $X^{\mathrm{L}} = x$, the UE is associated with the BS located at distance X^{L} that corresponds to the nearest BS to the UE with a LOS path, giving the smallest path loss (i.e., the largest $\zeta(r)$) from such BS to the UE. To ensure that the UE is associated with such LOS BS located at distance $X^{\mathrm{L}} = x$, there must not be any BS that has a NLOS path inside the disk centered on the UE with a radius of $x_1 < x$ to outperform such LOS BS which is located at distance $X^{\mathrm{L}} = x$, where x_1 satisfies $x_1 = \underset{x_1}{arg}\left\{\zeta^{\mathrm{NL}}(x_1) = \zeta^{\mathrm{L}}(x)\right\}$. According to [107], the conditional probability of C^{NL} on condition of $X^{\mathrm{L}} = x$ is

$$\Pr\left[C^{\mathrm{NL}} \middle| X^{\mathrm{L}} = x\right] = \exp\left(-\int_0^{x_1} \left(1 - \Pr^{\mathrm{L}}(u)\right) 2\pi u\lambda du\right). \tag{B.4}$$

It is noteworthy that it is guaranteed by Event B^{L} that the path loss value $\zeta^{\mathrm{L}}(x)$ associated with *an arbitrary BS with LOS path* is always smaller than that associated with *the considered BS with LOS path* located at distance $X^{\mathrm{L}} = x$. Moreover, conditional on $X^{\mathrm{L}} = x$, it is guaranteed by Event $C^{N\mathrm{L}}$ that the path loss value $\zeta^{\mathrm{NL}}(x)$ associated with *an arbitrary BS with NLOS path* is always smaller than that associated with *the considered BS with LOS path* located at distance x.

Another Event that has to be taken into account is the one that the UE is associated with a BS with a LOS path where the BS is placed at distance R^{L}. The CCDF of R^{L}, denoted by $\bar{F}_R^{\mathrm{L}}(r)$, is derived as

$$\begin{aligned}
\bar{F}_R^{\mathrm{L}}(r) &= \Pr\left[R^{\mathrm{L}} > r\right] \\
&\overset{(a)}{=} \mathrm{E}_{[X^{\mathrm{L}}]}\left\{\Pr\left[R^{\mathrm{L}} > r \middle| X^{\mathrm{L}}\right]\right\} \\
&= \int_0^{+\infty} \Pr\left[R^{\mathrm{L}} > r \middle| X^{\mathrm{L}} = x\right] f_X^{\mathrm{L}}(x)\,dx \\
&\overset{(b)}{=} \int_0^{r} 0 \times f_X^{\mathrm{L}}(x)\,dx + \int_r^{+\infty} \Pr\left[C^{\mathrm{NL}} \middle| X^{\mathrm{L}} = x\right] f_X^{\mathrm{L}}(x)\,dx \\
&= \int_r^{+\infty} \Pr\left[C^{\mathrm{NL}} \middle| X^{\mathrm{L}} = x\right] f_X^{\mathrm{L}}(x)\,dx, \qquad \text{(B.5)}
\end{aligned}$$

where $\mathbb{E}_{[X]}\{\cdot\}$ in the step (a) of (B.5) denotes the expectation operation which takes the expectation over the variable X and validity of the step (b) of (B.5) is because $\Pr\left[R^{\mathrm{L}} > r \middle| X^{\mathrm{L}} = x\right] = 0$ when $0 < x \leq r$ and the conditional event $\left[R^{\mathrm{L}} > r \middle| X^{\mathrm{L}} = x\right]$ is equivalent to the conditional event $\left[C^{\mathrm{NL}} \middle| X^{\mathrm{L}} = x\right]$ when $x > r$. In order to obtain the PDF of R^{L}, the derivative of $\left(1 - \bar{F}_R^{\mathrm{L}}(r)\right)$ can be taken with regard to r which results in

$$f_R^{\mathrm{L}}(r) = \Pr\left[C^{\mathrm{NL}} \middle| X^{\mathrm{L}} = r\right] f_X^{\mathrm{L}}(r). \qquad \text{(B.6)}$$

Considering the distance range of $(d_{n-1} < r \leq d_n)$, the segment of $f_{R,n}^{\mathrm{L}}(r)$ can be extracted from $f_R^{\mathrm{L}}(r)$ as

$$\begin{aligned}
f_{R,n}^{\mathrm{L}}(r) \;=\; &\exp\left(-\int_0^{r_1}\left(1 - \Pr^{\mathrm{L}}(u)\right) 2\pi u\lambda\,du\right) \\
&\times \exp\left(-\int_0^{r} \Pr^{\mathrm{L}}(u)\, 2\pi u\lambda\,du\right) \Pr_n^{\mathrm{L}}(r)\, 2\pi r\lambda, \quad (d_{n-1} < r \leq d_n), \qquad \text{(B.7)}
\end{aligned}$$

where $r_1 = \underset{r_1}{arg}\left\{\zeta^{\mathrm{NL}}(r_1) = \zeta_n^{\mathrm{L}}(r)\right\}$.

Having obtained $f_{R,n}^{\mathrm{L}}(r)$, the next is to evaluate $\Pr\left[\frac{P\zeta_n^{\mathrm{L}}(r)h}{I_r} > \gamma\right]$ in (B.1) as

$$\Pr[\frac{P\zeta_n^L(r)h}{I_r} > \gamma] = 1 - \Pr[\frac{P\zeta_n^L(r)h}{I_r} < \gamma] \qquad \text{(B.8)}$$

where $\Pr[\frac{P\zeta_n^L(r)h}{I_r} > \gamma]$ and $\Pr[\frac{P\zeta_n^L(r)h}{I_r} < \gamma]$ indeed refer to the CCDF and CDF of SINR, respectively. Note that, an interference limited scenario is considered, which is a feasible assumption in small cell networks.

The interference is normalized with respect to $P\zeta_n^L(r)$ and therefore the normalized interference is defined as $I_{rn} = \frac{I_r}{P\zeta_n^L(r)}$. Hence, (B.8) can be expressed as

$$\Pr[\frac{h}{I_{rn}} > \gamma] = 1 - \Pr[\frac{h}{I_{rn}} < \gamma] \tag{B.9}$$

Subsequently, the coverage probability can be computed as

$$\Pr[\frac{h}{I_{rn}} > \gamma] = 1 - \int\int_{\frac{x}{y}<\gamma} f_h(x) f_{I_{rn}}(y)\, dx\, dy = 1 - \int_0^\infty F_h(\gamma y) f_{I_{rn}}(y)\, dy \tag{B.10}$$

where $f_h(x)$ and $F_h(x)$ denote the PDF and CDF of random variable h, respectively. Assuming that the random variable h is Rician distributed, its PDF is given by

$$f_h(x) = \frac{(K+1)e^{-K}}{\bar{x}}\, exp(-\frac{(K+1)x}{\bar{x}})\, I_0(\sqrt{\frac{4K(K+1)x}{\bar{x}}}) \tag{B.11}$$

where K refers to the Rician K factor, I_0 is the zero-th order first kind modified Bessel function and $\bar{x}$ refers to the expectation of h. Applying the series expansion from [115], the $f_h(x)$ can be expressed as

$$f_h(x) = \exp(-K-x) \sum_{k=0}^{\infty} \frac{(Kx)^k}{(k!)^2} \tag{B.12}$$

and therefore, the CDF of RV h can be derived from its PDF as

$$\begin{aligned} F_h(x) &= e^{-K} \sum_{k=0}^{\infty} \frac{K^k}{(k!)^2} \left(e^{-x} \sum_{m=0}^{k} (-1)^{2m+1}\, m!\, \binom{k}{m} x^{k-m} + k! \right) \\ &= -\sum_{k=0}^{\infty}\sum_{m=0}^{k} J(m,k)\, x^{k-m} e^{-x} + \sum_{k=0}^{\infty} \frac{K^k}{k!} e^{-K} \\ &= -\sum_{k=0}^{\infty}\sum_{m=0}^{k} J(m,k)\, x^{k-m} e^{-x} + 1 \end{aligned} \tag{B.13}$$

where $J(m,k) = \frac{e^{-K}K^k m! \binom{k}{m}}{(k!)^2}$ and $\sum\limits_{k=0}^{\infty} \frac{K^k}{k!} = e^K$ based on the combination of Taylor series.

By replacing (B.13) in (B.10), the coverage probability can be derived as

$$\begin{aligned}\Pr[\frac{h}{I_{rn}} > \gamma] &= \sum_{k=0}^{\infty}\sum_{m=0}^{k} J(m,k) \int_0^{\infty} (y\gamma)^{k-m} e^{-y\gamma} f_{I_{rn}}(y)\, dy\} \\ &= \sum_{k=0}^{\infty}\sum_{m=0}^{k} J(m,k)\, \gamma^{k-m} Q(\gamma, k-m) \qquad \text{(B.14)}\end{aligned}$$

where $Q(\tau,n) = \int_0^{\infty} y^n e^{-y\tau} f_{I_{rn}}(y)dy = (-1)^n \frac{\partial^n \mathscr{L}_{I_{rn}}(\tau)}{\partial \tau^n}$ and $n \in [0,\infty]$.

The coverage probability can be presented as

$$\Pr[\frac{h}{I_{rn}} > \gamma] = \sum_{k=0}^{\infty}\sum_{m=0}^{k} J(m,k)\, \gamma^{k-m} (-1)^{k-m}\, \frac{\partial^{k-m} \mathscr{L}_{I_{rn}}(\gamma)}{\partial \gamma^{k-m}} \qquad \text{(B.15)}$$

Plugging $I_r = I_{rn}\, P\zeta_n^L(r)$ into (B.15), the coverage probability can be derived as

$$\Pr[\frac{P\zeta_n^L(r) h}{I_r} > \gamma] = \sum_{k=0}^{\infty}\sum_{m=0}^{k} J(m,k)\, \gamma^{k-m} (-1)^{k-m}\, \frac{\partial^{k-m} \mathscr{L}_{I_r}(\frac{\gamma}{P\zeta_n^L(r)})}{\partial \gamma^{k-m}} \qquad \text{(B.16)}$$

where $\mathscr{L}_{I_r}(s)$ is the Laplace transform of RV I_r evaluated at s.

Similarly, $f_{R,n}^{\mathrm{NL}}(r)$ in (B.1) can also be computed. In this regard, the following two events are defined.

- Event B^{NL}: The nearest BS with a NLOS path to the UE, is located at distance X^{NL}. Similar to (B.3), the PDF of X^{NL} is given by

$$f_X^{\mathrm{NL}}(x) = \exp\left(-\int_0^x \left(1-\Pr^{\mathrm{L}}(u)\right) 2\pi u\lambda du\right) \left(1-\Pr^{\mathrm{L}}(x)\right) 2\pi x\lambda. \qquad \text{(B.17)}$$

- Event C^{L} conditional on the corresponding value of X^{NL}: Assuming $X^{\mathrm{NL}} = x$, the UE is associated with the BS located at distance X^{NL} that corresponds to nearest BS to the UE with a NLOS path, giving the smallest path loss (i.e., the largest $\zeta(r)$) from such BS to the UE. Consequently, there must not be any BS that has a LOS path inside the disk centered on the UE with a radius of $x_2 < x$, where x_2 satisfies $x_2 = \underset{x_2}{arg}\left\{\zeta^{\mathrm{L}}(x_2) = \zeta^{\mathrm{NL}}(x)\right\}$. Similar to (B.4), the conditional probability of C^{L} on condition of $X^{\mathrm{NL}} = x$ can be expressed as

$$\Pr\left[C^{\mathrm{L}} \middle| X^{\mathrm{NL}} = x\right] = \exp\left(-\int_0^{x_2} \Pr^{\mathrm{L}}(u)\, 2\pi u\lambda du\right). \qquad \text{(B.18)}$$

Another Event that must be taken into account is the one that the UE is associated with a BS with a NLOS path and such BS is placed at distance R^{NL}. Similar to (B.5), the CCDF of R^{NL}, denoted by $\bar{F}_R^{\mathrm{NL}}(r)$, can be computed as

$$\begin{aligned}\bar{F}_R^{\mathrm{NL}}(r) &= \Pr\left[R^{\mathrm{NL}} > r\right] \\ &= \int_r^{+\infty} \Pr\left[C^{\mathrm{L}} \middle| X^{\mathrm{NL}} = x\right] f_X^{\mathrm{NL}}(x)\, dx. \end{aligned} \tag{B.19}$$

The PDF of R^{NL} can be obtained by taking the derivative of $\left(1 - \bar{F}_R^{\mathrm{NL}}(r)\right)$ with regard to r which results in

$$f_R^{\mathrm{NL}}(r) = \Pr\left[C^{\mathrm{L}} \middle| X^{\mathrm{NL}} = r\right] f_X^{\mathrm{NL}}(x). \tag{B.20}$$

Considering the distance range of $(d_{n-1} < r \le d_n)$, the segment of $f_{R,n}^{\mathrm{NL}}(r)$ from $f_R^{\mathrm{NL}}(r)$ can be derived as

$$\begin{aligned} f_{R,n}^{\mathrm{NL}}(r) &= \exp\left(-\int_0^{r_2} \Pr^{\mathrm{L}}(u)\, 2\pi u\lambda du\right) \\ &\times \exp\left(-\int_0^{r} \left(1 - \Pr^{\mathrm{L}}(u)\right) 2\pi u\lambda du\right) \left(1 - \Pr_n^{\mathrm{L}}(r)\right) 2\pi r\lambda, (d_{n-1} < r \le d_n) \end{aligned} \tag{B.21}$$

where $r_2 = \underset{r_2}{arg}\left\{\zeta^{\mathrm{L}}(r_2) = \zeta_n^{\mathrm{NL}}(r)\right\}$.

Similarly, $\Pr\left[\frac{P\zeta_n^{\mathrm{NL}}(r)h}{I_r} > \gamma\right]$ can be derived as

$$\Pr\left[\frac{P\zeta_n^{\mathrm{NL}}(r)h}{I_r} > \gamma\right] = \sum_{k=0}^{\infty}\sum_{m=0}^{k} J(m,k)\, \gamma^{k-m}(-1)^{k-m}\frac{\partial^{k-m}\mathscr{L}_{I_r}\left(\frac{\gamma}{P\zeta_n^{NL}(r)}\right)}{\partial\gamma^{k-m}}. \tag{B.22}$$

B.2 Proof of Lemma 1

In the following, $\mathscr{L}_{I_r}(s)$ in the range of $0 < r \le d_1$ is derived as

$$\begin{aligned} \mathscr{L}_{I_r}(s) &= \mathbb{E}_{[I_r]}\left\{\exp(-sI_r) \middle| 0 < r \le d_1\right\} \\ &= \mathbb{E}_{[\Phi,\{\beta_i\},\{g_i\}]}\left\{\exp\left(-s\sum_{i\in\Phi/b_o} P\beta_i g_i\right) \middle| 0 < r \le d_1\right\} \\ &\overset{(a)}{=} \exp\left(-2\pi\lambda\int_r^{\infty}\left(1 - \mathbb{E}_{[g]}\left\{\exp(-sP\beta(u)g)\right\}\right) udu \middle| 0 < r \le d_1\right), \end{aligned} \tag{B.23}$$

where the step (a) of (B.23) is obtained from [107].

Considering that $0 < r \leq d_1$, $\mathrm{E}_{[g]}\{\exp(-sP\beta(u)g)\}$ in (B.23) must take into account the interference from both the LOS and NLoS paths. Note that the random varibale g follows Rician distribution. Therefore, $\mathscr{L}_{I_r}(s)$ can be expressed as

$$\begin{aligned}\mathscr{L}_{I_r}(s) \;&=\; \exp\left(-2\pi\lambda \int_r^{d_1} \left(1-\frac{u}{d_1}\right)[1-\mathrm{E}_{[g]}\exp\left(-sPA^L u^{-\alpha^L} g\right)]\; udu\right) \\ &\times\exp\left(-2\pi\lambda \int_{r_1}^{d_1} \frac{u}{d_1}[1-\mathrm{E}_{[g]}\exp(-sPA^{NL}u^{-\alpha^{NL}}g)]\; udu\right) \\ &\times\exp\left(-2\pi\lambda \int_{d_1}^{\infty}[1-\mathrm{E}_{[g]}\exp(-sPA^{NL}u^{-\alpha^{NL}}g)]udu\right) \qquad \text{(B.24)}\end{aligned}$$

For sake of presentation, $sPA^L u^{-\alpha^L}$ is denoted by M and hence $\mathrm{E}_{[g]}\{\exp(-Mg)\}$ is computed as

$$\mathrm{E}_{[g]}\exp(-Mg) = \int_0^{\infty} \exp(-Mg)\,\exp(-K-g)\,\sum_{k=0}^{\infty}\frac{(Kg)^k}{(k!)^2}\,dg \qquad \text{(B.25)}$$

where $\exp(-K-g)\sum_{k=0}^{\infty}\frac{(Kg)^k}{(k!)^2}$ denotes the PDF of random variable g. According to Taylor series, it is perceived that $\sum_{k=0}^{\infty}\frac{K^k}{k!} = e^K$ and hence, (B.25) can be written as

$$\begin{aligned}\mathrm{E}_{[g]}\{\exp(-Mg)\} \;&=\; \int_0^{\infty}\exp(-Mg)\exp(-K-g)\exp(Kg)\,dg \\ &=\; \exp(-K)\int_0^{\infty}\exp(-g(1+M-K))\,dg = \frac{\exp(-K)}{1+M-K} \qquad \text{(B.26)}\end{aligned}$$

Plugging $M = sPA^L u^{-\alpha^L}$, the term $1-\mathrm{E}_{[g]}\exp(-sPA^L u^{-\alpha^L} g)$ is derived as

$$1-\mathrm{E}_{[g]}\exp(-sPA^L u^{-\alpha^L} g) = \frac{1+(sPA^L)^{-1}u^{\alpha^L} - K(sPA^L)^{-1}u^{\alpha^L} - (e^K sPA^L)^{-1}u^{\alpha^L}}{1+(sPA^L)^{-1}u^{\alpha^L} - K(sPA^L)^{-1}u^{\alpha^L}} \qquad \text{(B.27)}$$

Similarly, the term $1-\mathrm{E}_{[g]}\{\exp(-sPA^{NL}u^{-\alpha^{NL}}g)\}$ is computed and therefore, (B.24) is written as

$$\begin{aligned}
\mathscr{L}_{I_r}(s) \;\; = & \\
\exp\Bigg(-2\pi\lambda \int_{r}^{d_1} \left(1-\frac{u}{d_1}\right) & \left(\frac{1+(sPA^{L})^{-1}u^{\alpha^{L}} - K(sPA^{L})^{-1}u^{\alpha^{L}} - (e^{K}sPA^{L})^{-1}u^{\alpha^{L}}}{1+(sPA^{L})^{-1}u^{\alpha^{L}} - K(sPA^{L})^{-1}u^{\alpha^{L}}} \right) udu \Bigg) \\
\times \exp\Bigg(-2\pi\lambda \int_{r_1}^{d_1} \frac{u}{d_1} & \left(\frac{1+(sPA^{NL})^{-1}u^{\alpha^{NL}} - K(sPA^{NL})^{-1}u^{\alpha^{NL}} - (e^{K}sPA^{NL})^{-1}u^{\alpha^{NL}}}{1+(sPA^{NL})^{-1}u^{\alpha^{NL}} - K(sPA^{NL})^{-1}u^{\alpha^{NL}}} \right) udu \Bigg) \\
\times \exp\Bigg(-2\pi\lambda \int_{d_1}^{\infty} & \left(\frac{1+(sPA^{NL})^{-1}u^{\alpha^{NL}} - K(sPA^{NL})^{-1}u^{\alpha^{NL}} - (e^{K}sPA^{NL})^{-1}u^{\alpha^{NL}}}{1+(sPA^{NL})^{-1}u^{\alpha^{NL}} - K(sPA^{NL})^{-1}u^{\alpha^{NL}}} \right) udu \Bigg)
\end{aligned} \tag{B.28}$$

Plugging $s = \frac{\gamma r^{\alpha^{\mathrm{L}}}}{PA^{\mathrm{L}}}$ into (B.28), and considering the definition of $\rho_1(\alpha,\beta,t,d)$ and $\rho_2(\alpha,\beta,t,d)$ in (4.22) and (4.23), $\mathscr{L}_{I_r}\left(\frac{\gamma r^{\alpha^{\mathrm{L}}}}{PA^{\mathrm{L}}}\right)$ can be obtained as shown in (4.21).

B.3 Proof of Lemma 2

Similar to Appendix B.2, $\mathscr{L}_{I_r}\left(\frac{\gamma r^{\alpha^{\mathrm{NL}}}}{PA^{\mathrm{NL}}}\right)$ is derived in the range of $0 < r \le y_1$ as

$$\begin{aligned}
\mathscr{L}_{I_r}(\frac{\gamma r^{\alpha^{\mathrm{NL}}}}{PA^{\mathrm{NL}}}) \;\; = & \\
\exp\Bigg(-2\pi\lambda \int_{r_2}^{d_1} (1-\frac{u}{d_1}) & \frac{1+(\frac{\gamma r^{\alpha^{\mathrm{NL}}}}{PA^{\mathrm{NL}}}PA^{L})^{-1}u^{\alpha^{L}} - K(\frac{\gamma r^{\alpha^{\mathrm{NL}}}}{PA^{\mathrm{NL}}}PA^{L})^{-1}u^{\alpha^{L}} - (e^{K}\frac{\gamma r^{\alpha^{\mathrm{NL}}}}{PA^{\mathrm{NL}}}PA^{L})^{-1}u^{\alpha^{L}}}{1+(\frac{\gamma r^{\alpha^{\mathrm{NL}}}}{PA^{\mathrm{NL}}}PA^{L})^{-1}u^{\alpha^{L}} - K(\frac{\gamma r^{\alpha^{\mathrm{NL}}}}{PA^{\mathrm{NL}}}PA^{L})^{-1}u^{\alpha^{L}}})udu \Bigg) \\
\times \exp\Bigg(-2\pi\lambda \int_{r}^{d_1} \frac{u}{d_1} & \frac{1+(\frac{\gamma r^{\alpha^{\mathrm{NL}}}}{PA^{\mathrm{NL}}}PA^{NL})^{-1}u^{\alpha^{NL}} - K(\frac{\gamma r^{\alpha^{\mathrm{NL}}}}{PA^{\mathrm{NL}}}PA^{NL})^{-1}u^{\alpha^{NL}} - (e^{K}\frac{\gamma r^{\alpha^{\mathrm{NL}}}}{PA^{\mathrm{NL}}}PA^{NL})^{-1}u^{\alpha^{NL}}}{1+(\frac{\gamma r^{\alpha^{\mathrm{NL}}}}{PA^{\mathrm{NL}}}PA^{NL})^{-1}u^{\alpha^{NL}} - K(\frac{\gamma r^{\alpha^{\mathrm{NL}}}}{PA^{\mathrm{NL}}}PA^{NL})^{-1}u^{\alpha^{NL}}} udu \Bigg) \\
\times \exp\Bigg(-2\pi\lambda \int_{d_1}^{\infty} & \frac{1+(\frac{\gamma r^{\alpha^{\mathrm{NL}}}}{PA^{\mathrm{NL}}}PA^{NL})^{-1}u^{\alpha^{NL}} - K(\frac{\gamma r^{\alpha^{\mathrm{NL}}}}{PA^{\mathrm{NL}}}PA^{NL})^{-1}u^{\alpha^{NL}} - (e^{K}\frac{\gamma r^{\alpha^{\mathrm{NL}}}}{PA^{\mathrm{NL}}}PA^{NL})^{-1}u^{\alpha^{NL}}}{1+(\frac{\gamma r^{\alpha^{\mathrm{NL}}}}{PA^{\mathrm{NL}}}PA^{NL})^{-1}u^{\alpha^{NL}} - K(\frac{\gamma r^{\alpha^{\mathrm{NL}}}}{PA^{\mathrm{NL}}}PA^{NL})^{-1}u^{\alpha^{NL}}} udu \Bigg) \\
& .
\end{aligned} \tag{B.29}$$

Similarly, $\mathscr{L}_{I_r}\left(\frac{\gamma r^{\alpha^{\mathrm{NL}}}}{PA^{\mathrm{NL}}}\right)$ in the range of $y_1 < r \le d_1$ can be calculated by

$$
\begin{aligned}
&\mathscr{L}_{I_r}\left(\frac{\gamma r^{\alpha^{\mathrm{NL}}}}{PA^{\mathrm{NL}}}\right) \quad = \\
&\exp\left(-2\pi\lambda\int_r^{d_1}\frac{u}{d_1}\frac{1+(\frac{\gamma r^{\alpha^{\mathrm{NL}}}}{PA^{\mathrm{NL}}}PA^{NL})^{-1}u^{\alpha^{NL}}-K(\frac{\gamma r^{\alpha^{\mathrm{NL}}}}{PA^{\mathrm{NL}}}PA^{NL})^{-1}u^{\alpha^{NL}}-(e^{K}\frac{\gamma r^{\alpha^{\mathrm{NL}}}}{PA^{\mathrm{NL}}}PA^{NL})^{-1}u^{\alpha^{NL}}}{1+(\frac{\gamma r^{\alpha^{\mathrm{NL}}}}{PA^{\mathrm{NL}}}PA^{NL})^{-1}u^{\alpha^{NL}}-K(\frac{\gamma r^{\alpha^{\mathrm{NL}}}}{PA^{\mathrm{NL}}}PA^{NL})^{-1}u^{\alpha^{NL}}}udu\right) \\
&\times \exp\left(-2\pi\lambda\int_{d_1}^{\infty}\frac{1+(\frac{\gamma r^{\alpha^{\mathrm{NL}}}}{PA^{\mathrm{NL}}}PA^{NL})^{-1}u^{\alpha^{NL}}-K(\frac{\gamma r^{\alpha^{\mathrm{NL}}}}{PA^{\mathrm{NL}}}PA^{NL})^{-1}u^{\alpha^{NL}}-(e^{K}\frac{\gamma r^{\alpha^{\mathrm{NL}}}}{PA^{\mathrm{NL}}}PA^{NL})^{-1}u^{\alpha^{NL}}}{1+(\frac{\gamma r^{\alpha^{\mathrm{NL}}}}{PA^{\mathrm{NL}}}PA^{NL})^{-1}u^{\alpha^{NL}}-K(\frac{\gamma r^{\alpha^{\mathrm{NL}}}}{PA^{\mathrm{NL}}}PA^{NL})^{-1}u^{\alpha^{NL}}}udu\right) \\
&,
\end{aligned}
\tag{B.30}
$$

The proof is concluded by plugging (4.22) and (4.23) into (B.29) and (B.30).

B.4 Proof of Lemma 3

Considering only NLOS interference, $\mathscr{L}_{I_r}\left(\frac{\gamma r^{\alpha^{\mathrm{NL}}}}{PA^{\mathrm{NL}}}\right)$ in the range of $r > d_1$ can be derived as

$$
\begin{aligned}
&\mathscr{L}_{I_r}(\frac{\gamma r^{\alpha^{\mathrm{NL}}}}{PA^{\mathrm{NL}}}) \quad = \\
&\exp\left(-2\pi\lambda\int_{d_1}^{\infty}(\frac{1+(\frac{\gamma r^{\alpha^{\mathrm{NL}}}}{PA^{\mathrm{NL}}}PA^{NL})^{-1}u^{\alpha^{NL}}-K(\frac{\gamma r^{\alpha^{\mathrm{NL}}}}{PA^{\mathrm{NL}}}PA^{NL})^{-1}u^{\alpha^{NL}}-(e^{K}\frac{\gamma r^{\alpha^{\mathrm{NL}}}}{PA^{\mathrm{NL}}}PA^{NL})^{-1}u^{\alpha^{NL}}}{1+(\frac{\gamma r^{\alpha^{\mathrm{NL}}}}{PA^{\mathrm{NL}}}PA^{NL})^{-1}u^{\alpha^{NL}}-K(\frac{\gamma r^{\alpha^{\mathrm{NL}}}}{PA^{\mathrm{NL}}}PA^{NL})^{-1}u^{\alpha^{NL}}})udu\right) \\
&.
\end{aligned}
\tag{B.31}
$$

where $(r > d_1)$. The proof is concluded by plugging (4.23) into (B.31).

Appendix C

Correlated Multiple Input Multiple Output Channel Model

A MIMO system is considered with N_t transmit and N_r receive antennas with corresponding antenna spacings of d_t and d_r, respectively. It is understood that the correlated Rician channel can be decomposed to LOS and NLOS matrices. Considering the correlated NLOS MIMO channel, the degree of spatial correlation between any two transmit-receive pair in a $N_r \times N_t$ MIMO is computed as

$$\rho_{ij,pq} = \frac{E[h_{i,j}h^*_{p,q}]}{\sqrt{E[h_{i,j}h^*_{i,j}]E[h_{p,q}h^*_{p,q}]}} \quad \begin{cases} i,p = 1,2,...,N_r \\ j,q = 1,2,...,N_t \end{cases} \tag{C.1}$$

where $h_{i,j}$ is the channel from j-th transmit antenna to i-th receive antenna and E refers to the expectation operation.

For sake of clarity, a 2×2 MIMO system is only considered, for which the channel matrix is given as

$$\mathbf{H} = \begin{bmatrix} h_{1,1}(t) & h_{1,2}(t) \\ h_{2,1}(t) & h_{2,2}(t) \end{bmatrix} \tag{C.2}$$

From (C.1), the spatial correlation coefficient between channel pairs, $h_{1,1}$ and $h_{2,2}$ is

$$\rho_{11,22} = \frac{E[h_{1,1}h^*_{2,2}]}{\sqrt{E[h_{1,1}h^*_{1,1}]E[h_{2,2}h^*_{2,2}]}} \tag{C.3}$$

To derive the correlation coefficient as a function of antenna spacing, the channel gains are modelled as the ratio of received output voltage $\mathbf{v}_{out}$ to the transmitted input voltage

$\mathbf{v}_{in}$. Noteworthy that the transmitted input voltage is assumed identical for all transmit antennas [142].

$$\begin{bmatrix} v_{out,1}(t) \\ v_{out,2}(t) \end{bmatrix} = \begin{bmatrix} h_{1,1}(t) & h_{1,2}(t) \\ h_{2,1}(t) & h_{2,2}(t) \end{bmatrix} * \begin{bmatrix} v_{in}(t) \\ v_{in}(t) \end{bmatrix} \tag{C.4}$$

$$\begin{bmatrix} v_{out,1}(t) \\ v_{out,2}(t) \end{bmatrix} = \begin{bmatrix} v_{out,1,1}(t) + v_{out,1,2}(t) \\ v_{out,2,1}(t) + v_{out,2,2}(t) \end{bmatrix} \tag{C.5}$$

$$\mathbf{v}_{out}(t) = \mathbf{H}(t)\mathbf{v}_{in}(t) \tag{C.6}$$

where $v_{out,i,j}$ refers to the signal received by i-th receive antenna from j-th transmit antenna, respectively. The correlation coefficient between $h_{1,1}$ and $h_{2,2}$ is therefore written as

$$\rho_{11,22} = \frac{E[v_{out,1,1}v^*_{out,2,2}]}{\sqrt{E[v_{out,1,1}v^*_{out,1,1}]E[v_{out,2,2}v^*_{out,2,2}]}} \tag{C.7}$$

For simplicity, the numerator of (C.7) is only computed, reminding that its denominator can be derived in the same way. Considering that electric voltage can be computed as the integral of electric field over the path taken, the numerator of (C.7) is written as

$$\begin{aligned} E[v_{out,1,1}v^*_{out,2,2}] &= E\Bigg[\Bigg[\frac{-1}{I}\int_0^{2\pi}\int_0^{l} I(z)(\int_0^{2\pi} e_1(\phi)d\phi)E_1(\varphi)dzd\varphi\Bigg]\Bigg[\frac{-1}{I}\int_0^{2\pi}\int_0^{l} I(z) \\ &\quad (\int_0^{2\pi} e_2(\phi)d\phi)E_2(\varphi)dzd\varphi\Bigg]^*\Bigg] \\ &= \left(\frac{-1}{I^2}\right)\Bigg[\int_0^{l}\int_0^{l} I(z)I^*(z)dzE\Bigg[\left(\int_0^{2\pi} e_1(\phi)d\phi\int_0^{2\pi} e_2^*(\phi)d\phi^*\right) \\ &\quad \left(\int_0^{2\pi} E_1(\varphi)d\varphi\int_0^{2\pi} E_2(\varphi^{'}\right)d\varphi^{'})\Bigg]dz^*\Bigg] \end{aligned} \tag{C.8}$$

where I is the induced current in the antennas, E_1 and E_2 refer to incident fields at the receive antennas and e_1 and e_2 are the far fields generated by the transmit antennas. φ and ϕ also denote the angle of departure (AoD) from transmit antennas and angle of arrival (AoA) at receive antennas, respectively. Due to different spatial locations of the antennas, $e_2(\phi)$ and $E_2(\varphi)$ are modeled as $e_0e^{jd_tcos(\phi)}$ and $E_0e^{jd_rcos(\varphi)}$, respectively where $e_1(\phi) = e_0$ and $E_1(\varphi) = E_0$. Note that e_0 and E_0 follow Rayleigh distribution.

$$\begin{aligned}
E[v_{out,1,1}v^*_{out,2,2}] &= \left(\frac{-1}{I^2}\right)\left[\int_0^l\int_0^l I(z)I^*(z)dzdz^*\right]E\left[\left(\int_0^{2\pi}e_0\int_0^{2\pi}e_0e^{jd_tcos(\phi^*)}d\phi^*\right)\right. \\
&\left.\left(\int_0^{2\pi}E_0\int_0^{2\pi}E_0e^{jd_rcos(\varphi^{'})}d\varphi^{'}\right)\right] \\
&= \left(\frac{-1}{I^2}\right)\left[\int_0^l\int_0^l I(z)I^*(z)dzdz^*\right]E\left[\int_0^{2\pi}\int_0^{2\pi}e_0^2\,E_0^2\,e^{jd_tcos(\phi^*)}\right. \\
&\left. d\phi^*\,e^{jd_rcos(\varphi^{'})}d\varphi^{'}\right] \qquad \text{(C.9)}
\end{aligned}$$

Intuitively, the two inner integrals represent the auto-correlation functions of the two Rayleigh distributed variables, e_0 and E_0. Provided that the auto-correlation function of Rayleigh distribution can be modeled by Bessel function, it is derived that

$$E[v_{out,1,1}v^*_{out,2,2}] = (\frac{-1}{I^2})[\int_0^l\int_0^l I(z)I^*(z)dzdz^*]\;J_0(2\pi d_t)J_0(2\pi d_r) \qquad \text{(C.10)}$$

where J_0 is the zero-th order first kind Bessel function. The denominator of (C.7) can be expanded likewise and therefore it can be shown that in a MIMO system with N_t and N_r transmit and receive antennas spaced by d_t and d_r, the correlation coefficient between any two channel pairs is computed as

$$\rho_{ij,pq} = J_0(2\pi d_t|q-j|)J_0(2\pi d_r|p-i|) \quad \begin{cases} i,p = 1,2,...,N_r \\ j,q = 1,2,...,N_t \end{cases} \qquad \text{(C.11)}$$

where $||$ denotes the absolute operation. Having computed the correlation coefficient between any two channel pairs, the transmit and receive correlation matrices denoted by $\mathbf{R}_T$ and $\mathbf{R}_R$, respectively, are derived which take into account the impact of antenna spacing. This is used to determine the correlated channel model presented in (5.4) in chapter 5 that considers both the UE-BS distance and the spacing between antenna elements at both UE and BS.